

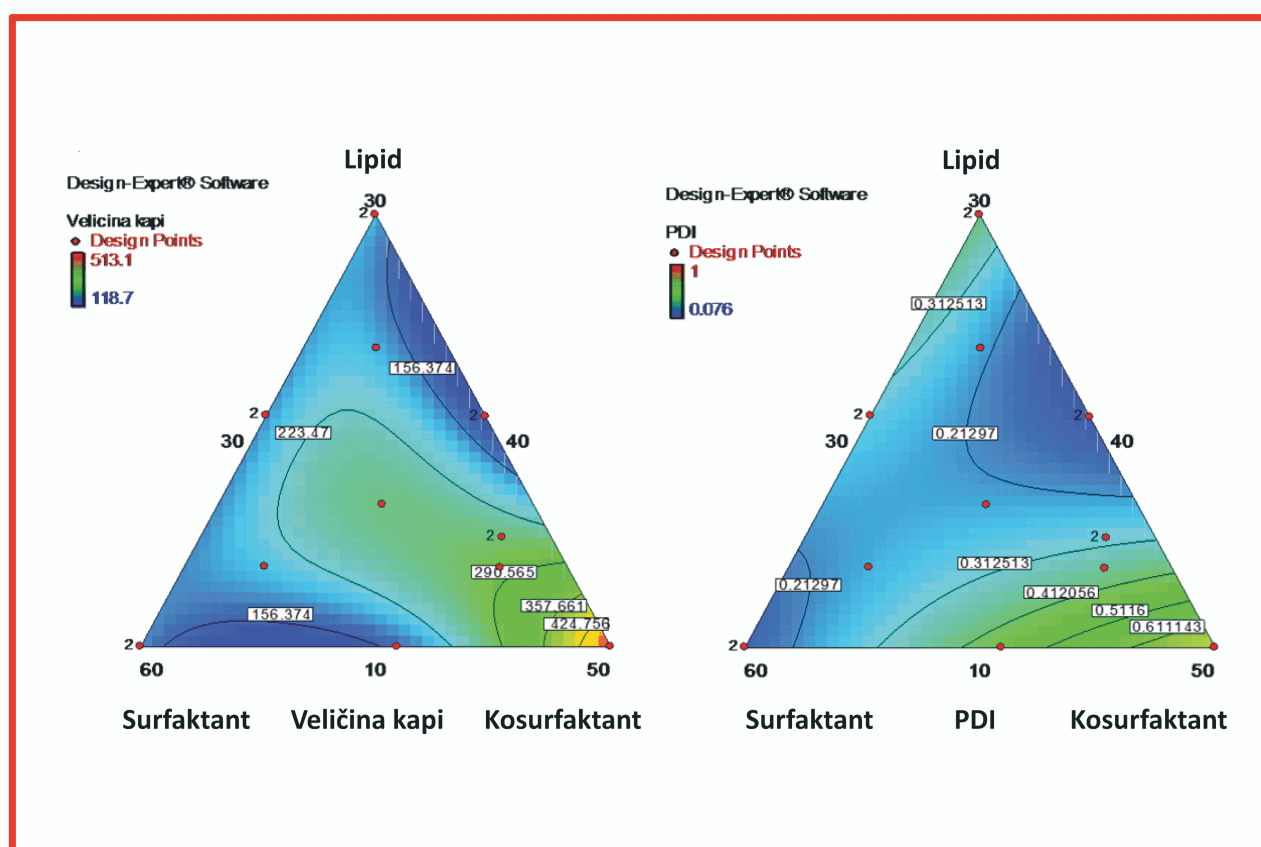
5

Hemijska industrija

Vol. 70

časopis Saveza hemijskih inženjera Srbije

Chemical Industry



Aktivnosti Saveza hemijskih inženjera Srbije pomažu:



MINISTARSTVO PROSVETE, NAUKE I
TEHNOLOŠKOG RAZVOJA REPUBLIKE
SRBIJE



Tehnološko-metalurški fakultet
Univerziteta u Beogradu, Beograd



Prirodno-matematički fakultet Univerziteta
u Novom Sadu, Novi Sad



Hemijski fakultet
Univerziteta u Beogradu
Beograd



Institut za tehnologiju nuklearnih i drugih
mineralnih sirovina, Beograd



Institut za opštu i fizičku hemiju,
Beograd



Tehnološki fakultet Univerziteta
u Novom Sadu, Novi Sad



NU Institut za hemiju,
tehnologiju i metalurgiju
Univerziteta u Beogradu,
Beograd



Hipol a.d., Odžaci



Tehnološki fakultet Univerziteta
u Nišu, Leskovac



Fakultet tehničkih nauka,
Kosovska Mitrovica



Chemical Industry

Химическая промышленность

Hemijska industrija

Časopis Saveza hemijskih inženjera Srbije
Journal of the Association of Chemical Engineers of Serbia
Журнал Союза химических инженеров Сербии

VOL. 70

Beograd, septembar–oktobar 2016

Broj 5

Izdavač

Savez hemijskih inženjera Srbije
Beograd, Kneza Miloša 9/1

Glavni urednik

Bojana Obradović

Urednici

Katarina Jeremić, Ivana Banković-Ilić, Maja Obradović,
Dušan Mijin, Mirjana Ristić, Zorica Knežević Jugović

Članovi uredništva

Nikolaj Ostrovski, Milorad Cakić, Željko Čupić, Katarina Jeremić, Miodrag Lazić, Slobodan Petrović, Milovan Purenović, Aleksandar Spasić, Dragoslav Stoiljković, Radmila Šećerov-Sokolović, Slobodan Šerbanović, Nikola Nikačević, Svetomir Milojević

Članovi uredništva iz inostranstva

Dragomir Bukur (SAD), Jiri Hanika (Češka Republika),
Valerij Meshalkin (Rusija), Ljubiša Radović (SAD),
Constantinos Vayenas (Grčka)

Likovno-grafičko rešenje naslovne strane

Ivana Drvenica

Redakcija

11000 Beograd, Kneza Miloša 9/1
Tel/fax: 011/3240-018
E-pošta: shi@ache.org.rs
www.ache.org.rs

Izlazi dvomesečno, rukopisi se ne vraćaju

Za izdavača

Tatijana Duduković

Sekretar redakcije

Slavica Desnica

Izdavanje časopisa pomaže

Republika Srbija, Ministarstvo prosvete, nauke i
tehnološkog razvoja

Uplata pretplate i oglasnog prostora vrši se na tekući račun Saveza hemijskih inženjera Srbije, Beograd, broj 205-2172-71, Komercijalna banka a.d., Beograd

Kompjuterska priprema

Vladimir Panić

Štampa

Razvojno-istraživački centar grafičkog inženjerstva,
Tehnološko-metalurški fakultet, Univerzitet u
Beogradu, Karnegijeva 4, 11000 Beograd

Indeksiranje

Radovi koji se publikuju u časopisu *Hemijska Industrija* indeksiraju se preko *Thompson Reuters Scietific®* servisa *Science Citation Index - Expanded™* i *Journal Citation Report (JCR)*

SADRŽAJ/CONTENTS

- Darko M. Božović, Vladimir M. Simić, Dragan S. Radulović, Filip B. Abramović, Slobodan S. Radusinović, **Carbonate filler resources of the Bjelopavlići area, Montenegro** 493
- Miroslav Đ. Kukučka, Nikoleta M. Kukučka, **Groundwater nano-filtration process efficiency improvement with additional concentrate membrane treatment** 501
- Jasmina V. Bašić, Branka M. Ivković, Slavica Stevanović, Anđelka Lazarević, Zorica B. Vujić, **Određivanje lipofilnosti 2'-hidroksihalkona primenom RP-HPLC metode / Determination of the lipophilicity of 2'-hydroxychalcones by RP-HPLC method**..... 511
- Marija A. Marković, Aleksandra S. Daković, George E. Rottinghaus, Mirjana D. Stojanović, Vera T. Dondur, Milan M. Kragović, Zvonko P. Gulišija, **Adsorpcija aflatoksina B₁ na prirodnim alumosilikatima – koncentratu montmorilonita i zeolitu** 519
- Marko Z. Krstić, Svetlana R. Ibrić, **Primena dizajna smeše u formulaciji i karakterizaciji čvrstih samo-nanoemulgujućih terapijskih sistema sa karbamazepinom / Application of mixture experimental design in formulation and characterization of solid self-nanoemulsifying drug delivery systems containing carbamazepine** 525
- Lato Pezo, Milada Pezo, Aca Jovanović, Nenad Kosanić, Aleksandar Petrović, Ljubinko Lević, **Granular flow in static mixers by coupled DEM/CFD approach** 539
- Saša J. Brzić, Gordana S. Uščumlić, Mirjana V. Dimić, Miloš Tomić, Vesna Ž. Rodić, Bojana Z. Fidanovski, **Viscoelastic behaviour of carboxyl-terminated (butadiene-co-acrylonitrile)-based composite propellant binder containing polyglycidyl-type bonding agent**..... 547
- Vladimir M. Tomović, Nikola Z. Stanišić, Marija R. Jokanović, Žarko S. Kevrešan, Branislav V. Šojić, Snežana B. Škaljac, Igor B. Tomašević, Aleksandra B. Martinović, Aleksandra R. Despotović, Danijela Z. Šuput, **Meat quality of Swallow-Belly Mangulica pigs reared under intensive production system and slaughtered at 100 kg live weight** 557
- Remy M.K. Vala, Donbebe Wankasi, Ezekiel D. Dikio, **Morphology and adsorption of chromium ion on uranium 1,2,4,5-benzotetracarboxylic acid metal organic framework (MOF)** 565
- Dalibor B. Jovanović, Predrag N. Stojisavljević, Sveta G. Cvetanović, Dušan S. Rajić, Radovan M. Karkalić, Negovan D. Ivanković, Željko B. Senić, **Testing of the functional garments with microencapsulated phase-change material in simulated high temperature conditions** 573

SADRŽAJ nastavak
CONTENTS continued

Nikola I. Gligorijević, Vesna Ž. Rodić, Saša Ž. Živković, Bojan M. Pavković, Momčilo M. Nikolić, Stevan M. Kozomara, Sredoje D. Subotić, Mechanical characterization of composite solid rocket propellant based on hydroxy-terminated polybutadiene	581
Elizabeth Erasmus, The influence of thermal treatment on properties of kaolin	595

Carbonate filler resources of the Bjelopavlići area, Montenegro

Darko M. Božović¹, Vladimir M. Simić², Dragan S. Radulović³, Filip B. Abramović⁴, Slobodan S. Radusinović¹

¹Geological survey, Podgorica

²University of Belgrade, Faculty of Mining and Geology, Belgrade

³Institute for Technology of Nuclear and other Mineral Raw Materials, Belgrade

⁴City Administration, Secretariat for Environmental Protection, Direction for Waste Management, Belgrade

Abstract

Carbonate filler is an important mineral commodity, with rather diverse industrial applications. The Bjelopavlići area in Montenegro is rich in chemically pure limestone, which was preliminary explored in the field, and further its mineralogical, petrographic, geochemical and technological properties were studied. The obtained results have proven the high quality of limestone from the studied deposits, as it can be used for paints and varnishes, rubber and plastics, metallurgy, foundry, sugar, fertilizers and animal feed industry. Several deposits have very pure limestone, that can be also used for paper, glass, pharmaceutical industry and soil neutralisation. The potential resources of high quality limestone are around 23 million tons.

Keywords: limestone, filler, geochemistry, application, resources.

Available online at the Journal website: <http://www.ache.org.rs/HI/>

PROFESSIONAL PAPER

UDC 552.541(497.16):66:550.4

Hem. Ind. 70 (5) 493–500 (2016)

doi: 10.2298/HEMIND150325054B

The carbonate resources of the Bjelopavlići area (Fig. 1) comprise dimension (decorative) stone, aggregate rock, and filler grade carbonate. Their unique feature is that all those industrial types of stone are made of extremely pure limestone, which means that all fully and/or partially explored and analysed deposits can be used as source of filler, even for very demanding markets.

The most important deposits of dimension (decorative) stone in Montenegro are located in the region of Bjelopavlići (area of Danilovgrad and Spuž), where eight deposits have been explored: Visočica, Maljat, Klikovača, Vinići, Radujev krš, Suk, Slatina and Jovanovići, with proven balanced geological reserves of over 23 Mt. The centre for stone processing is in the nearby town of Danilovgrad. One aggregate rock quarry named Sađavac was also explored. All these deposits were preliminary explored in the last five years as potential source of calcium-carbonate filler [1–4], including several new occurrences: Lalevići, Pješivački do and Mali Garač. Possibility of using limestone from the Visočica deposit in paper production was already studied [5]. The goal of this paper was to characterise and prove the high quality of studied limestone as potential source of filler.

Geological background

The most significant deposits of high purity limestone have been discovered within the Upper Creta-

ceous carbonate sediments [6] of the High Karst zone (the Bjelopavlići area). High karst covers the central and southwestern parts of Montenegro. This tectonic unit consists of two sub-units: Old Montenegrin and Kuč thrust. Both units, which are separated by a regional dislocation known as Kuč thrust, have a very complex tectonic structure.

Limestones of Senonian age, present in the coastal and central part of Montenegro, were formed mostly on carbonate platform, and consist of bedded to massive limestone, dolomitic limestone and dolomite, with rudists and foraminiferae. Bedded to massive limestone is predominantly bioclastic floatstone to bioclastic grainstone, occasionally with small intraclasts (Visočica), wackestone-packstone (Klikovača) and very subordinately mudstone as cement (Visočica).

High quality Senonian limestone is underlain by Turonian limestone and dolomite, and overlain by Paleogene flysch of the Zeta valley, comprised of marlstone, shale and sandstone with lenses and layers of breccia and conglomerate [6].

EXPERIMENTAL

Samples for mineralogical, geochemical and technological analyses were collected from each deposit, taking into account the differences in macroscopic composition of stone in order to be fully representative. Samples from each deposit weighted 80–100 kg. Representative rock pieces were taken to prepare thin sections for optical microscopy and scanning electron microscopy, and the remaining material of each sample was crushed in laboratory jaw crusher Denver Model Colo 4"x6". After splitting, 5 kg of material was taken

Correspondence: V.M. Simić, University of Belgrade, Faculty of Mining and Geology, Đušina 7, Belgrade, Serbia.

E-mail: vladimir.simic@rgf.bg.ac.rs

Paper received: 25 March, 2015

Paper accepted: 16 September, 2015

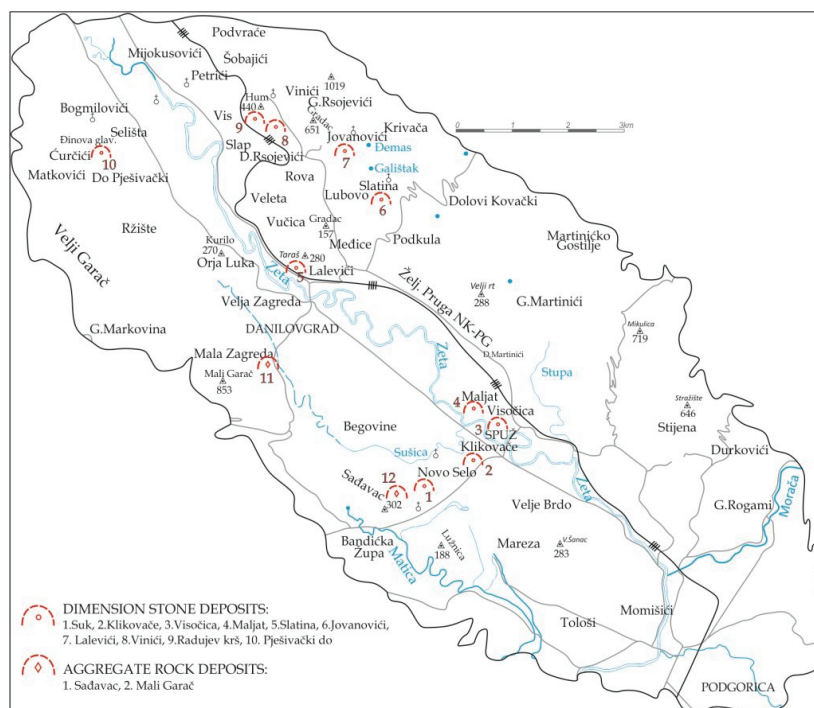


Figure 1. Orientation map with studied limestone deposits.

for laboratory analyses, pulverised in agate stone pulveriser “KHD Humboldt Wedag” and packed in plastic bags and properly marked. Duplicate of each sample has been kept at the Geological Survey in Podgorica.

Mineralogical and technological studies, either on rock pieces or powder, included optical microscopy, X-ray powder diffraction (XRD) and scanning electron microscopy (SEM), differential thermal and thermogravimetric analyses (DTA and TGA), determination of moisture, whiteness, specific weight, oil absorption, water absorption, and pH determination. For XRD and SEM analyses two samples were taken from Visočica deposit and Klikovača deposit.

XRD analyses were performed on Ital Structure APD2000 diffractometer with 2θ range of $5\text{--}60^\circ$, step 0.02° , and retention time of 0.5 s, using $\text{CuK}\alpha$ 1.54178 Å). SEM analysis were done using a JEOL JSM-6610LV scanning electron microscope (SEM) coupled with energy-dispersive X-Max Large area analytical silicon drifted spectrometer (Oxford). The samples were covered by gold using a sputter machine type BALTEC-SCD-005. The analyses were done under acceleration voltage of 20 kV, a beam current of 20 nA and a spot size of 1 μm . Tungsten filament was used as a beam source. Appropriate internal and external standards were used for the analyses. Detection limit for most elements was $\sim 0.1\%$.

DTA and TGA analyses were done on all samples using Netzsch-simultaneous thermal analysis – STA 409 EP, heating speed of $\Delta T = 10^\circ\text{C}/\text{min}$, in temperature

interval from 20 do 1000 $^\circ\text{C}$. Sample mass for analyses was 100 mg.

Geochemical analyses were done at AcmeLabs in Vancouver, Canada. 250 g of rock samples were previously crushed, split and pulverised to 200 mesh. Macro-elements were analysed by XRF (including Lecco C and S) employing fusion techniques to completely decompose the material and provide total element concentrations. Trace elements were analysed by ICP-MS method after multi-acid digestion. Detection limits are given in Table 1.

Table 1. Detection limits of analytical methods

Element	Detection limit, %	Upper limit, %	Element	Detection limit, mg/kg
SiO_2	0.01	100	As	0.5
TiO_2	0.01	50	Be	1
Al_2O_3	0.01	100	Cd	0.1
Fe_2O_3	0.01	100	Co	0.2
CaO	0.01	100	Cu	0.1
MgO	0.01	100	Hg	0.01
Na_2O	0.01	100	Mo	0.1
K_2O	0.01	100	Ni	0.1
MnO	0.01	93	Pb	0.1
P_2O_5	0.01	100	Se	0.5
Cr_2O_3	0.01	10	Sb	0.1
LOI	0.10	–	Th	0.2
C_{total}	0.02	100	U	0.1
S_{total}	0.02	100		

Determination of whiteness was done on 20 g of each sample previously pulverised to 100 % below 63 µm and compared to standard whiteness MgO = 100 %. Oil absorption was analysed on dried 5 g samples with flaxseed oil with specific mass of 0.928 g/cm³, while water absorption was done on dried 20 g samples with distilled water. pH values were determined on 10 g samples of limestone mixed in 100 cm³ vessel with distilled water for one hour. After that pH was measured by CONSORT C830 instrument, which was previously calibrated to pH 7 and 10 using standard buffer solutions for corresponding pH values. Moisture was determined after heating to 105 °C till constant mass, specific weight was determined using pycnometer in xylene.

RESULTS AND DISCUSSION

Mineralogical and petrographic analyses revealed that studied limestone differs in structure and texture, with variations from boundstone, rudstone and floatstone, to grainstone and, subordinately wackestone, packstone and mudstone (Fig. 2).

SEM analyses revealed that Visočica limestone is extremely pure, with no visible metallic minerals, while Klikovača limestone contains Fe-mineral (most probably hydroxide due to the film-like appearance), but also Bi-bearing mineral (Fig. 3). However, the total amount of impurities is rather low as seen from geochemistry of stone (Tables 2 and 3) as well as XRD analyses (Fig. 4).

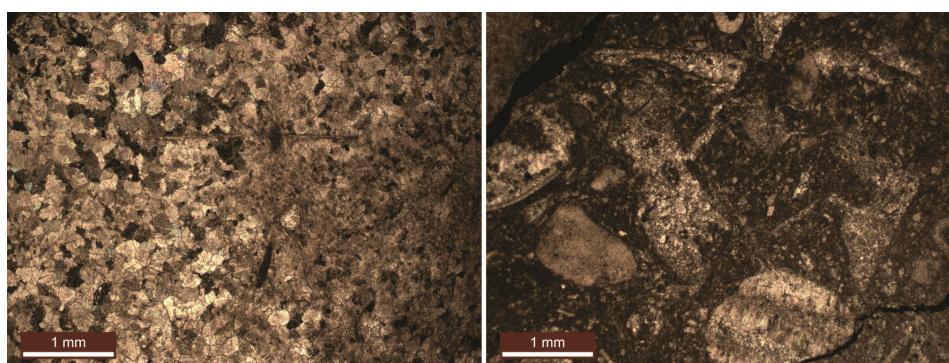


Figure 2. Photomicrographs of limestone from the Visočica deposit: grainstone (left image) and bioclastic packstone (right image).

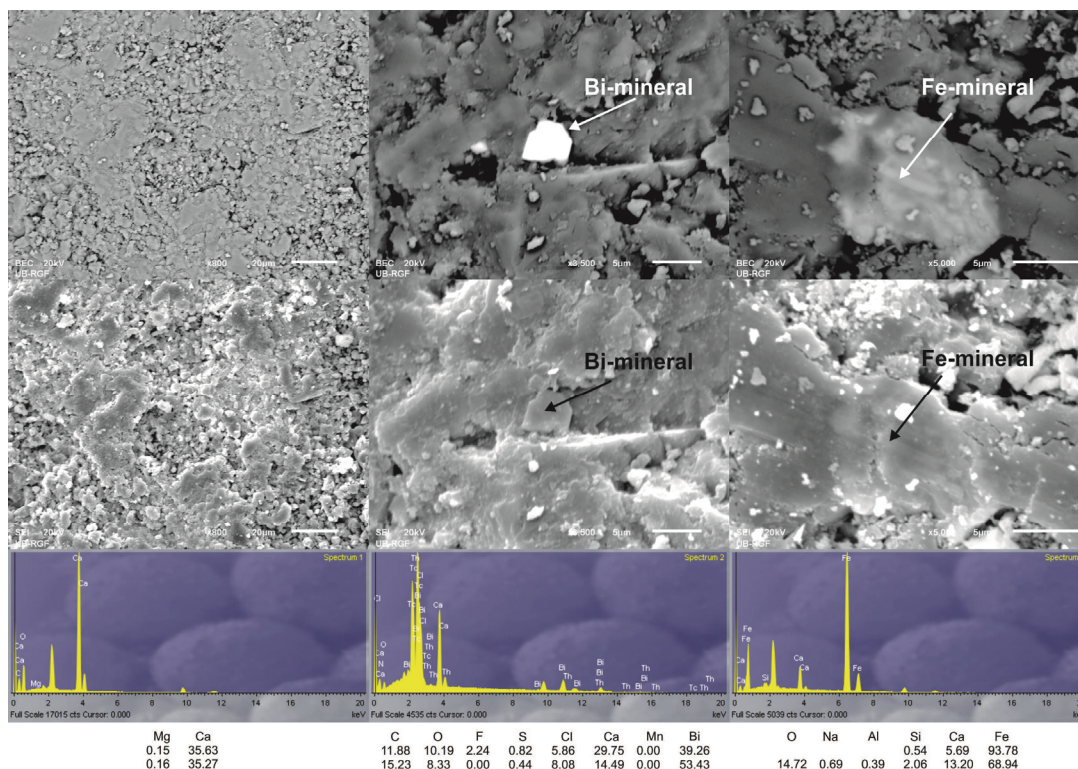


Figure 3. SEM images of limestone from the Visočica (1) with none of the metallic minerals and Klikovača deposits (2 and 3) displaying metallic minerals; semiquantitative chemistry of analysed points is given below the images (in %).

Table 2. Chemical composition (in %) of limestone from the Bjelopavlići area

Site	SiO ₂	TiO ₂	Al ₂ O ₃	Fe ₂ O ₃	CaO	MgO	Na ₂ O	K ₂ O	MnO	P ₂ O ₅	Cr ₂ O ₃	LOI	SUM	C _{total}	S _{total}
Suk	0.20	<0.01	0.04	0.06	55.84	0.34	<0.01	<0.01	<0.01	<0.01	<0.001	43.73	100.20	12.48	<0.02
Klikovača	0.10	<0.01	0.02	0.02	55.60	0.33	<0.01	<0.01	<0.01	<0.01	<0.001	43.76	99.84	12.26	<0.02
Sađavac	<0.10	<0.01	<0.01	0.03	54.84	0.67	<0.01	<0.01	<0.01	<0.01	0.003	43.87	99.47	12.28	0.03
Mali Garač	0.10	<0.01	0.03	0.02	55.04	0.70	<0.01	<0.01	<0.01	<0.01	0.002	43.88	99.79	12.44	0.03
Slatina	<0.10	<0.01	<0.01	<0.01	55.67	0.34	<0.01	<0.01	<0.01	<0.01	0.002	43.62	99.63	12.36	<0.02
Maljat	<0.10	<0.01	<0.01	0.03	55.58	0.27	<0.01	<0.01	<0.01	0.01	<0.001	43.27	99.22	12.48	<0.02
Vinici	<0.10	<0.01	<0.01	0.01	56.04	0.27	<0.01	<0.01	<0.01	<0.01	<0.001	43.39	99.70	12.39	<0.02
Visočica	<0.10	<0.01	0.01	0.02	56.13	0.28	<0.01	<0.01	<0.01	<0.01	0.003	43.40	99.86	12.36	<0.02
Pješivački do	<0.10	<0.01	<0.01	<0.01	55.27	0.56	<0.01	<0.01	<0.01	<0.01	0.003	43.67	99.52	12.47	0.02
Lalevići	0.10	<0.01	0.05	0.03	55.73	0.50	<0.01	<0.01	0.02	0.03	<0.001	43.76	100.20	12.26	0.02
Jovanovići	0.10	<0.01	0.03	0.02	55.43	0.53	<0.01	<0.01	0.01	0.03	0.001	43.72	99.89	12.39	0.02
Radujev krš	<0.10	<0.01	<0.01	0.01	55.84	0.28	<0.01	<0.01	<0.01	<0.01	0.006	43.57	99.72	12.22	<0.02

Table 3. Potentially toxic trace elements content (in mg/kg) in limestone from the Bjelopavlići area

Site	As	Be	Cd	Co	Cu	Hg	Mo	Ni	Pb	Se	Sb	Th	U
Suk	<0.5	<1	0.2	0.6	0.2	<0.01	<0.1	0.1	1.2	<0.5	0.1	<0.2	1.4
Klikovača	<0.5	<1	0.1	1.2	<0.1	<0.01	<0.1	0.2	1.1	<0.5	0.1	<0.2	0.7
Sađavac	<0.5	<1	0.2	0.4	0.1	<0.01	0.2	0.5	0.6	<0.5	<0.1	<0.2	1.3
Mali Garač	0.8	<1	0.2	0.6	0.1	<0.01	0.2	0.9	0.7	<0.5	<0.1	<0.2	1.4
Slatina	0.6	<1	0.4	0.5	<0.1	<0.01	<0.1	1.1	0.5	<0.5	<0.1	<0.2	0.9
Maljat	<0.5	<1	0.3	0.3	0.3	<0.01	<0.1	<0.1	0.2	<0.5	<0.1	<0.2	0.7
Vinici	<0.5	<1	0.2	0.8	<0.1	<0.01	<0.1	<0.1	0.2	<0.5	<0.1	<0.2	<0.1
Visočica	0.6	<1	0.2	0.7	0.1	<0.01	<0.1	0.8	0.1	<0.5	<0.1	<0.2	0.4
Pješivački do	<0.5	<1	0.3	0.2	<0.1	<0.01	<0.1	<0.1	0.2	<0.5	<0.1	<0.2	1.6
Lalevići	0.9	<1	0.2	1.0	0.3	0.02	<0.1	1.1	0.5	<0.5	<0.1	<0.2	1.2
Jovanovići	1.1	<1	0.3	0.7	0.2	0.01	<0.1	1.2	0.4	<0.5	<0.1	<0.2	1
Radujev krš	<0.5	<1	<0.1	<0.2	<0.1	<0.01	<0.1	0.7	0.1	<0.5	<0.1	<0.2	0.1

DTA and TGA, performed on all studied samples, confirmed that all limestones are very pure and, as the thermal curves were similar, only two are shown (Fig. 4).

Geochemical analyses (Table 2) revealed rather high purity of all studied limestone samples with CaCO₃ content of over 98 %, and small variations in MgO. The content of all other components is very low.

Potentially toxic trace elements (Table 3) show as well extremely low concentrations, particularly As, Cd, and Pb being below the most rigid requirements, enabling utilization of limestone in most demanding filler products like food industry [7] and pharmacy.

The basic parameters for using limestone as filler measured on investigated limestone are given in Table 4.

The current production of several products based on chemically pure limestone is from the Visočica quarry only, and filler is used for mechanical plaster, ceramic and marble adhesives, and glue for demit facades. By development of the chemical industry and the improvement of production technology, industry in Montenegro can significantly expand the possibilities to use carbonate fillers in various industrial branches: con-

struction industry, paint and varnish industry, pharmaceutical and cosmetic industry, food industry, rubber industry, paper industry, industry of cables, polyvinyl chloride, and fertilisers. Very promising application of limestone filler in Montenegro is in cement and concrete industry. Namely, concrete with a high limestone filler content with suitable particle size distribution generally improves strength characteristics of concrete compared to the usual concrete with the same water/cement ratio and cement type [8–12]. The favourable opportunity is that quarry waste can be used for concrete mixtures [13]. That industry does not require extremely pure limestone, but the relatively cheap product.

As seen from the Table 5, limestone from several deposits can be used in practically all industrial branches without major limitations, while the other deposits can be used as a source of limestone for less demanding production. Further geological exploration and complete characterisation of limestone shall be conducted according to the existing regulations, but keeping in mind the potential usage of material. That should inc-

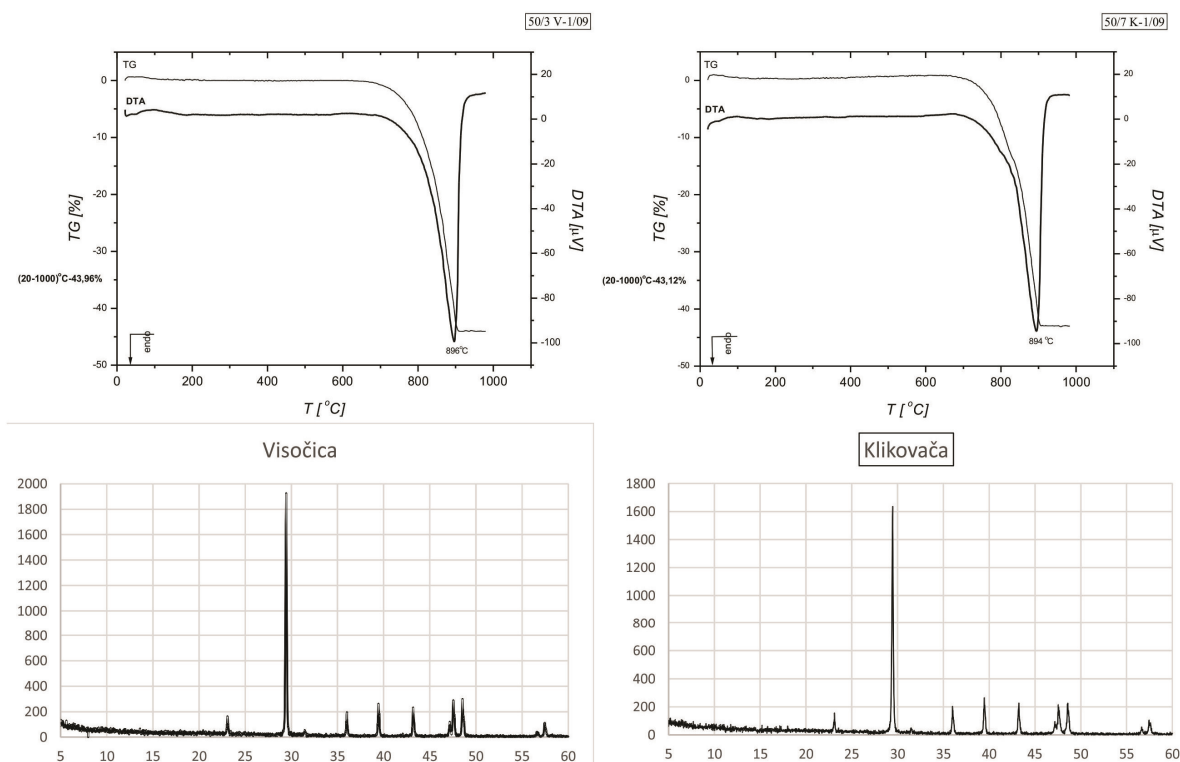


Figure 4. DTA, TGA and XRD curves of limestone from the Visočica and Klikovača deposits, displaying values for pure calcite.

Table 4. Basic technological parameters of limestone from the Bjelopavlići area

Deposit	Whiteness MgO-100%, %	Moisture %	Specific weight g/cm ³	Oil absorption %	Water absorption %	pH
Pješivački do	87.60	0.043	2.632	13.90	15.50	9.35
Radujev krš	93.50	0.051	2.726	12.00	15.50	9.20
Visočica	91.60	0.018	2.654	14.40	19.20	9.35
Suk	85.90	0.039	2.691	14.20	18.50	9.33
Sađavac	80.00	0.039	2.622	11.80	16.00	9.56
Slatina	91.90	0.046	2.689	14.60	19.50	9.34
Klikovača	84.90	0.064	2.654	13.90	19.00	9.39
Lalevići	84.50	0.022	2.632	11.80	15.50	9.33
Vinići	92.20	0.073	2.671	13.70	19.00	9.51
Maljat	93.40	0.087	2.681	13.00	19.20	9.40
Mali Garač	85.30	0.042	na.	11.80	15.80	na.
Jovanovići	85.80	0.045	2.679	11.80	15.00	9.35

lude much more analyses in order to define different grades of limestone that may be used in the most rational and sustainable way.

Limestone from the Bjelopavlići area as high quality raw material can be compared to other well known limestone resources in Serbia that can be used as coated filler in production of PVC products [14]. The importance of recycling dust from marble production, which would be economically rather important for the studied area, was discussed in recent years [15,16].

Although majority of papers dealing with detailed geochemistry of limestone is more geologically oriented [17–21], study in Canada [22] resulted in estimation of resources potential for industrial uses of limestone based on chemistry among the other criteria.

The overall economic potential of limestone fillers from the Bjelopavlići area is clearly visible from Table 6, where limestone resources are summarised. The most promising deposits for filler production are the actual dimension stone deposits, where the average block (and product) yield is around 20 %, while the rest is at

Table 5. Potential application of limestone from Bjelopavlići area based on preliminary tests. Y – yes, N – no, L – limited, VL – very limited

Deposit	Paints & varnishes	Paper	Rubber & PVC	Glass	Metal-lurgy	Foundry	Phar-macy	Sugar	Animal feed	Ferti-lizers	Soil neutralisation
Limitations	Whiteness		Chemistry			Whiteness			LOI	Chemistry P ₂ O ₅ , MgO, Cr	
Radujev krš	Y	Y	Y	L	Y	Y	Y	Y	Y	Y	Y
Visočica	Y	Y	Y	L	Y	Y	Y	Y	Y	Y	Y
Slatina	Y	L	Y	L	Y	Y	Y	Y	Y	L	Y
Vinići	Y	Y	Y	L	Y	Y	Y	Y	Y	Y	Y
Maljat	Y	Y	Y	L	Y	Y	Y	Y	Y	Y	Y
Klikovača	Y	VL	Y	L	Y	Y	N	Y	Y	L	N
Lalevići	Y	VL	Y	L	Y	Y	N	Y	Y	L	L
Suk	Y	VL	Y	L	Y	Y	N	Y	Y	L	Y
Sađavac	Y	N	Y	L	Y	Y	N	Y	Y	L	N
Pješivački do	Y	VL	Y	L	Y	Y	N	Y	Y	L	Y
Mali Garač	Y	VL	Y	L	Y	Y	N	Y	Y	L	Y
Jovanovići	Y	VL	Y	L	Y	Y	N	Y	Y	L	N

Table 6. Resources of the stone and block mass of explored deposits; measured resources (000 m³), JORC reporting

Deposit	Category (national reporting scheme)				Block yield %	Block mass 000 m ³
	A	B	C ₁	A+B+C ₁		
Suk	202	306	434	942	16.20	153
Klikovače	185	524	519	1228	25.00	307
Visočica	-	897	-	897	22.00	197
Maljat	376	635	868	1879	23.00	432
Slatina		234	291	525		
Jovanovići	251	592	1720	2563		
Vinići	348	347	645	1340	15.00	201
Radujev Krš	-	9	34	43	16.00	7
Sađavac		3285	1362	4647		Aggregate rock

the moment not fully (or at all) utilised as either filler, or any other product.

In Montenegro the market for filler is rather low, but due to the relatively close sea harbour and direct railway connection as precondition for cheap transport, the possibilities for increasing the sales of this type of products in the future are open. One of the potential markets could be eventually Belgrade region in Serbia, which has no sources of high quality special aggregates on its territory [23]. However, the utilisation of studied limestone deposits will require a lot of planning at different levels and countries [24–26].

CONCLUSION

The first complex study of potential limestone resources for filler grade quality was performed on twelve deposits in the Bjelopavlići area in Montenegro. The obtained results have proven the high quality of limestone from the studied deposits, as it can be used

for paints and varnishes, rubber and plastics, metal-lurgy, foundry, sugar production, fertilizers and animal feed industry. Several deposits have very pure limestone, that can be also used for paper, glass, pharmaceutical industry and soil neutralisation. We would like to stress again that these are preliminary results based on representative samples from each studied deposit. Further exploration should prove the quality of different grades of limestone and shall also require more sensitive and precise analytical methods for Cr, P, F and some other components. The economic potential of limestone fillers from the Bjelopavlići area is high, and the most promising deposits for filler production are the actual dimension stone deposits, where the average block (and product) yield is around 20%, while the rest can be used for filler production.

Acknowledgement

This paper is the result of the project titled “Potential of Cretaceous limestone in Montenegro as

source of carbonate fillers” financed by the Ministry of Economy of the Republic of Montenegro. This research was partly financed by the Ministry of Education, Science and Technological Development of the Republic of Serbia, Project OI176016, which is gratefully acknowledged. This paper also used materials and experiences resulted from the SARMa project (SEE/A/151/2.4/X) and SNAP-SEE project (SEE/D/0167/2.4/X), which were both financed by the European Commission.

REFERENCES

- [1] D. Božović, Godišnji izvještaj o izvršenim radovima po projektu Potencijalnost krednih krečnjaka u Crnoj Gori kao sirovine za proizvodnju karbonatnih punila, Zavod za geološka istraživanja, Podgorica, 2007 (in Serbian).
- [2] D. Božović, Godišnji izvještaj o izvršenim radovima po projektu Potencijalnost krednih krečnjaka u Crnoj Gori kao sirovine za proizvodnju karbonatnih punila (područje Bjelopavlića), Zavod za geološka istraživanja, Podgorica, 2010 (in Serbian).
- [3] D. Božović, Završni izvještaj o izvršenim radovima po projektu Potencijalnost krednih krečnjaka u Crnoj Gori kao sirovine za proizvodnju karbonatnih punila, Zavod za geološka istraživanja, Podgorica, 2011 (in Serbian).
- [4] M. Pajović, S. Radusinović, Mineralne sirovine Crne Gore, in: Crna Gora u XXI stoleću – u eri kompetitivnosti, životna sredina i održivi razvoj, Crnogorska akademija nauka i umjetnosti, Podgorica, Posebna izdanja 72/2, 2010, pp. 237–282 (in Serbian).
- [5] M. Krgović, N. Blagojević, N. Blagojević, Comparative possibilities of using limestone „Visočica“ and dolomite „Virpazar“ as fillers in paper production, *Hem. Ind.* **58** (2004) 228–231.
- [6] M. Živaljević, M. Pajović, V. Đokić, Tumač za osnovnu geološku kartu SFRJ, list Titograd, Savezni geološki zavod Beograd, 1967 (in Serbian).
- [7] EFSA Panel on Food Additives and Nutrient Sources added to Food (ANS), Scientific Opinion on reevaluation of calcium carbonate (E 170) as a food additive, *EFSA J.* **9**(7) 2318 (2011) 73. Available online: www.efsa.europa.eu/efsajournal.htm
- [8] T. Subbulakshmi, B. Vidivelli, Mechanical Properties of High Performance Concrete in Incorporating with Quarry Wastes, *IJEAT* **3** (2014) 231–236.
- [9] H.S.B. Nagabhushana, Use of crushed rock powder as replacement of fine aggregate in mortar and concrete, *Indian J. Sci. Techn.* **4** (2011) 917–922.
- [10] R.B.A. Alshahwany, Effect of Partial Replacement of Sand with Limestone Filler on Some Properties of Normal Concrete, *Al-Rafidain Eng.* **19** (2009) 37–48.
- [11] N. Voglis, G. Kakali, E. Chaniotakis, S. Tsvivilis, Portland-limestone cements. Their properties and hydration compared to those of other composite cements, *Cem. Concr. Compos.* **27** (2005) 191–196.
- [12] V. Bonavetti, H. Donza, G. Menendez, O. Cabrera, E.F. Irassar, Limestone filler cement in low w/c concrete: A rational use of energy, *Cem. Concr. Res.* **33** (2003) 865–871.
- [13] Md. Safiuddin, S.N. Raman, M.F.M. Zain, Utilization of quarry waste fine aggregate in concrete mixtures, *J. Appl. Sci. Res.* **3** (2007) 202–208.
- [14] S. Mihajlović, Ž. Sekulić, M. Petrov, Coated limestone as a filler for the production of PVC products, *Hem. Ind.* **59** (2004) 32–35 (In Serbian).
- [15] G. Marras, G. Siotto, J.L. Parra, N. Careddu, Potential applications of waste material deriving from marble processing plants. In: Ersoy, M., Çelik, M.Y., Yesilkaya, L. (Eds.), in *Proc. 7th International Marble and Natural Stones Congress of Turkey (Mersem VII)*, 14–15 October 2010, Afyonkarahisar, Turkey, , 2010, pp. 55-61.
- [16] N. Careddu, G. Marras, G. Siotto, Recovery of sawdust resulting from marble processing plants for future uses in high value-added products, *J.Clean. Prod.* **84** (2014) 533–539.
- [17] S.H.H. Azizi, G.M. Shabestari, A. Khazaei, Petrography and geochemistry of Paleocene–Eocene limestones in the Ching-dar syncline, eastern Iran, *Geosci. Frontiers* **5** (2014) 429–438.
- [18] K. Babu, R. Prabhakaran, P. Subramanian, B.Selvaraj, Geochemical Characterization of Garudamangalam Limestone Cretaceous of Ariyalur Tamilnadu, India, *Int. J. Geol. Agric. Environ. Sci.* **2** (2014) 17–22.
- [19] M.M. El Kammar, Geochemical characterization of Middle Eocene sediments in Helwan area, Greater Cairo, Egypt, *Life Science Journal* **10** (2013) 170–178.
- [20] J. Madhavaraju, Y.I. Lee, Geochemistry of the Dalmiapuram Formation of the Uttatur Group (Early Cretaceous), Cauvery basin, southeastern India: Implications on provenance and paleo-redox conditions, *Rev. Mex. Cien. Geol.* **26** (2009) 380–394.
- [21] G.J. Bowen, A.L. Daniels, B.B. Bowen, Paleoenvironmental isotope geochemistry and paragenesis of lacustrine and palustrine carbonates, Flagstaff formation, central Utah, U.S.A., *J.Sediment. Res.* **78** (2008) 162–174.
- [22] M.C. Birchard, M.A. Rutka, F.R. Brunton, Lithofacies and Geochemistry of the Lucas Formation in the Subsurface of Southwestern Ontario: A High-Purity Limestone and Potential High-Purity Dolostone Resource, Ontario Geological Survey, Open File Report **6137** (2004) 180.
- [23] V. Simić, D. Životić, Z. Miladinović, Aggregates Supply in Serbia. In: G. Žibret and S. Šolar, Eds., *Sustainable Aggregates Resource Management, Abstract and Short Paper Book*, Ljubljana, Geol. Survey Slov. (2011), 26–27.
- [24] G. Tiess, F. Chalkiopoulou, Sustainable Aggregates Resource Management and Sustainable Supply Mix at the Regional, National and Transnational Level, SARMa Project, 2011, p. 61 (<http://www.sarmaproject.eu>).
- [25] Z. Agioutantis, K. Komnitsas, M. Steiakis, S. Mavrigianakis, F. Stathogianni, F. Chalkiopoulou, K. Hatzilazaridou, A. Moltre, M. Valbusa, S. Bobba, G. A. Blengini, Data and Analysis Methodologies for Aggregates Planning: In support of best practices in Sustainable Aggregates Planning, SNAP-SEE Project, <http://>

//www.snapsee.eu, doi: 10.5474/snapsee-WP4-EN, 2014.

SNAP-SEE Project, <http://www.snapsee.eu>, doi: 10.5474/snapsee-WP5-EN, 2014.

[26] Z. Horváth, S. Miko, K. Sári, Ž. Dedić, A Vision of Best Practices for Aggregates Planning in South East Europe,

IZVOD

RESURSI KARBONATNIH PUNILA NA PODRUČJU BJELOPAVLICA, CRNA GORA

Darko M. Božović¹, Vladimir M. Simić², Dragan S. Radulović³, Filip B. Abramović⁴, Slobodan S. Radusinović¹

¹*JU Zavod za geološka istraživanja, Podgorica*

²*Univerzitet u Beogradu – Rudarsko–geološki fakultet, Beograd*

³*Institut za tehnologiju nuklearnih i drugih mineralnih sirovina, Beograd*

⁴*Gradska uprava grada Beograda, Sekretarijat za zaštitu životne sredine, Direkcija za upravljanje otpadom, Beograd*

(Stručni rad)

Karbonatna punila predstavljaju veoma važnu mineralnu sirovinu koja se može upotrebiti u različitim industrijskim granama. Područje Bjelopavlića u Crnoj Gori odlikuje se prisustvom mineraloški i hemijski veoma čistih krečnjaka, koji su dosada istraživani uglavnom kao arhitektonsko-građevinski i tehnički građevinski kamen. Istraživani krečnjaci su senonske starosti, slojeviti do masivni, izgrađeni od različitih varijeteta – bioklastičnih sparita i mikrita, uglavnom sa rudistima i foraminiferama. Uzorci za proučavanja (težine 80–100 kg) uzeti su iz svih istraživanih ležišta uzimajući u obzir makroskopski sastav stenske mase zbog reprezentativnosti. Zatim su iz njih izdvojeni manji komadi krečnjaka za potrebe izrade preparata za ispitivanja na optičkom i skenirajućem elektronskom mikroskopu. Ostatak uzoraka iz svakog ležišta je izdrobljen, homogenizovan i pulverizovan. Mineraloško–petrografska i tehnološka ispitivanja obuhvatila su optičku mikroskopiju, skenirajuću elektronsku mikroskopiju (SEM) i rendgensku difrakciju praha na dva izabrana uzorka iz ležišta Visočica i Klikovača, diferencijalno-termičke i termogravimetrijske analize (DTA i TGA), određivanje sadržaja vlage, beline, specifične težine, apsorpciju ulja i vode i određivanje pH. Geohemijska ispitivanja urađena su u AcmeLabs u Kanadi i to makro elementi XRF metodom (C i S Lecco metodom), a mikroelementi ICP-MS metodom. Istraživanja i ispitivanja dvanaest ležišta i pojava krečnjaka pokazala su visok kvalitet ove mineralne sirovine, pri čemu se krečnjak iz svih ležišta može upotrebiti u industriji boja i lakova, gume i plastike, metalurgiji, livarstvu, proizvodnji šećera, mineralnih đubriva i stočnoj hrani. Nekoliko ležišta i pojava sadrže veoma kvalitetan krečnjak koji se može upotrebiti i u industriji papira, stakla, farmaciji i neutralizaciji zemljišta. Potencijalni mineralni resursi procenjeni su na oko 23 miliona tona. U slučaju relativno jeftinog transporta postoji mogućnost snabdevanja i tržišta Srbije (pa i Beograda) agregatom za punila visokog kvaliteta.

Ključne reči: Krečnjak • Punila • Geohemija • Primena • Resursi

Groundwater nanofiltration process efficiency improvement with additional concentrate membrane treatment

Miroslav Đ. Kukučka, Nikoleta M. Kukučka

EnviroTech d.o.o., Kikinda, Serbia

Abstract

Nanofiltration (NF) of waste water originated from nanofiltration drinking water plant stationed in town of Kikinda (Northern Serbia) was investigated. Experiments on removal characteristics of nanofiltration membranes when exposed to influent rich in arsenic and natural organic matter under different flux and transmembrane pressure (TMP) conditions were conducted in order to obtain drinking water from waste water and reduce total amount of waste water. Applied NF membranes showed remarkable removal characteristics. Also, obtained result for concentrate yield, an indicator of reduced concentrate amount, of 8.89% under optimum flux value presents considerable amount of reclaimed drinking water. Calculated empirical and theoretical concentration factors quotients were indicated to probable accumulation of some inlet water components at NF membrane surface. Based on the obtained results that nanofiltration membranes remove natural organic matter, arsenic, ammonia and sodium with high efficiencies of around 98, 96, 80 and 93%, respectively, the conceptual design of drinking water plant for City of Kikinda was defined and presented.

Keywords: nanofiltration, water reclamation, concentrate yield, arsenic, humic matter, concentration factor.

Available online at the Journal website: <http://www.ache.org.rs/HI/>

SCIENTIFIC PAPER

UDC 628.3(497.11):66.067.1:628.16

Hem. Ind. 70 (5) 501–509 (2016)

doi: 10.2298/HEMIND150627056K

Membrane processes are currently considered to be one of the best separation technologies for water and wastewater treatment. Nanofiltration has been a rapidly expanding field leading to significant innovations in the last decade especially for aqueous effluents treatment in various industries. About 75% of the total market share of NF membranes worldwide is dominated by water demineralization and wastewater treatment applications [1]. NF is widely used for production of clean and pollutants free drinking water around the world [2–4]. Regardless, NF concentrate disposal presents a great problem because of its quality and quantity [5]. Even though the properties of NF membranes are improving every day in means of materials, resistance and recovery rates [6–8], the matter of concentrate discharge is still present.

Reclamation of membrane processes concentrates separated during desalination of sea or fresh water presented a big challenge in many previous investigations [9–11]. There are also numerous studies dedicated to water reclamation from waste water plants [12–14] in order to reuse obtained product for instance for irrigation [15].

In the Northern part of Serbia – Vojvodina, where the investigations were conducted, the main source of drinking water is unprocessed groundwater. The prob-

lem is that the quality of groundwater is not suitable for human consumption, according to local regulations [16]. More correctly speaking, water from approximately 45% public wells has elevated levels of arsenic. Second problem of Vojvodina's groundwater is natural organic matter (NOM) which concentration exceeds maximum tolerable level (MTL) [16] in majority of groundwater used for human consumption. There were many previous investigations based on application of adsorption and other processes for removal of groundwater arsenic and NOM. Strong base macroporous ion exchange resin was successfully applied for adsorption of As and NOM from chlorinated and non-chlorinated groundwater [17]. Since NOM is precursor of disinfection by products formation, adsorption of organics from the groundwater onto resin significantly decreases the possibilities of trihalomethanes arising [18]. The role of individual NOM fractions on changes in trihalomethanes and haloacetic acids formation during coagulation with iron chloride and a combination of polyaluminium chloride and iron chloride was determined. Results showed that most of the dissolved organic carbon (68%) in the raw water comes from the fulvic acid fraction, yielding 41% of the total trihalomethane precursors and 21% of the total haloacetic acid precursors [19]. Laboratory scale electrocoagulation/flotation reactor was successfully applied for removal of high concentrations of natural organic matter and arsenic from groundwater [20]. Based on the obtained results,

Correspondence: M.Đ. Kukučka, Sterije Popovića 42, Kikinda Serbia.

E-mail: miroslav@envirotech.rs

Paper received: 27 June, 2015

Paper accepted: 30 September, 2015

conceptual design of drinking water plant for City of Kikinda was presented.

The electrocoagulation/flocculation reactor at the optimum operational conditions was able to remove 93% of arsenic and 70% of dissolved organic carbon, comparing with raw groundwater [19].

Arsenic can be removed from water in greater percentage when it is present in organic form. It is found in literature that As, if present in natural organic matter-rich water, has ability to make complex compounds with anions of NOM as ligands [21]. Yu and a group of authors investigated effects of ion concentration and natural organic matter on arsenic(V) removal by nanofiltration under different transmembrane pressures using four different types of NF membranes [22]. It is shown that the removal efficiency of arsenic was influenced by ion concentration, TMP, and the presence of NOM.

Therefore, topic that interested authors was behavior of NF membranes when exposed to influent containing high levels of arsenic and humic matter. Aim of this work was to obtain drinking water from the NF concentrate, to investigate influence of transmembrane pressure on NF membranes functionality as well as to study influence of water flux on NF concentrate yield.

MATERIALS AND METHODS

Description of experiment location

Experiments were conducted in northern Serbia (Vojvodina) in the town of Kikinda (45.84° North, 20.45° East). The water-bearing formations in Vojvodina were formed during the final phase of existence of the Pannonian Sea [23]. In this region, the arsenic rich waters have a characteristic yellow color, a specific taste, and increased arsenic concentrations range from 0.040 to 0.380 mg/L [24–26] as well as elevated NH₄-N (ammonia – AM) and sodium level. The yellow color is due to the presence of undesirable organic (humic) matter. Measured physicochemical parameters in groundwater exceeds MTL [16] as presented: NOM, expressed as KMnO₄ consumption (*COD*, mg KMnO₄/L): 28.65; As [μg/L]: 18.07; Na [mg/L]: 206.90; NH₄-N [mg/L]: 2.07. This water is without any treatment being used as a source of drinking water in majority of nearby settlements.

Design of the pilot plant and operating conditions

Nanofiltration concentrate was obtained from the industrial NF plant, used for production of drinking water from groundwater according to local regulations [16]. NF plant operated under water flux ($J = 25.76 \text{ L}/(\text{h m}^2)$), and contained nanofiltration membranes type CSM NE8040-90 manufactured by Torey Chemical

Korea Inc. [27]. Inlet groundwater flow rate in the first step of nanofiltration was 13,500 L/h. The actual permeate and concentrate flow rates produced in NF plant were 11,500 and 2,000 L/h, respectively. Industrial NF plant permeate (NFP1) physicochemical composition is in accordance with the local regulations for drinking water [16] and it is used as a drinking water on investigated location. For this investigations NF plant concentrate (NFC1), which is usually discharged into the sewage, was treated on a self-made NF pilot plant (NFPP) at different flux conditions. Scheme of NFPP is given in Figure 1. NFPP has been designed for optimal permeate flow rate of 700 L/h, and contained three NF membranes (CSM NE4040-90, Torey Chemical Korea Inc. [28]) in two-array operating regime. As can be seen from the Figure 1, a part of the concentrate produced on NFPP (NFC2) was recirculated and joined with NFC1 – making feed water flow in order to reduce wastewater quantity. Because of this, values of *COD*, As, Na and AM in NFC1 were proportionality calculated with respect to inlet and recirculation flow rates. Experiments were conducted while the hydraulic conditions of the NFPP were operable. After first experimental procedure membranes were chemically cleaned using Clean-in-place method. Cleaning lasted for 2 h and it was done using 0.1% solution of NaOH. At the end of cleaning process solution was dark yellow color with foam appearance on the solution surface. Experimental procedure was repeated two more times. All presented results of groundwater and effluents are the mean values of measured parameters from three experimental procedures.

Physicochemical methods and analytical instruments used in the water analyses

General water quality parameters for the groundwater and effluent, such as *COD*, and arsenic, were determined by standard analytical methods [29]. Total arsenic and sodium was determined by atomic absorption spectrophotometry on a Varian AA 240FS. The total arsenic as well as sodium content was determined by the VGA technique on a Varian/VGA-77. Ammonium nitrogen content was determined by standard spectrophotometric Nessler method on instrument Hanna C-100. The TOC was measured on an Analytik Jena/Multi N/C 2100 instrument.

Calculation of experimental parameters

Operational parameters including inlet flow, permeate flow and concentrate flow were monitored during the study. Pressures between the feed and permeate side were detected by a pressure meter. According to the pressures, a transmembrane pressure that presents a force needed for filtration process to occur can be calculated using Eq. (1), where p_f , p_c , and p_p are influent, concentrate and permeate pressure, respectively.

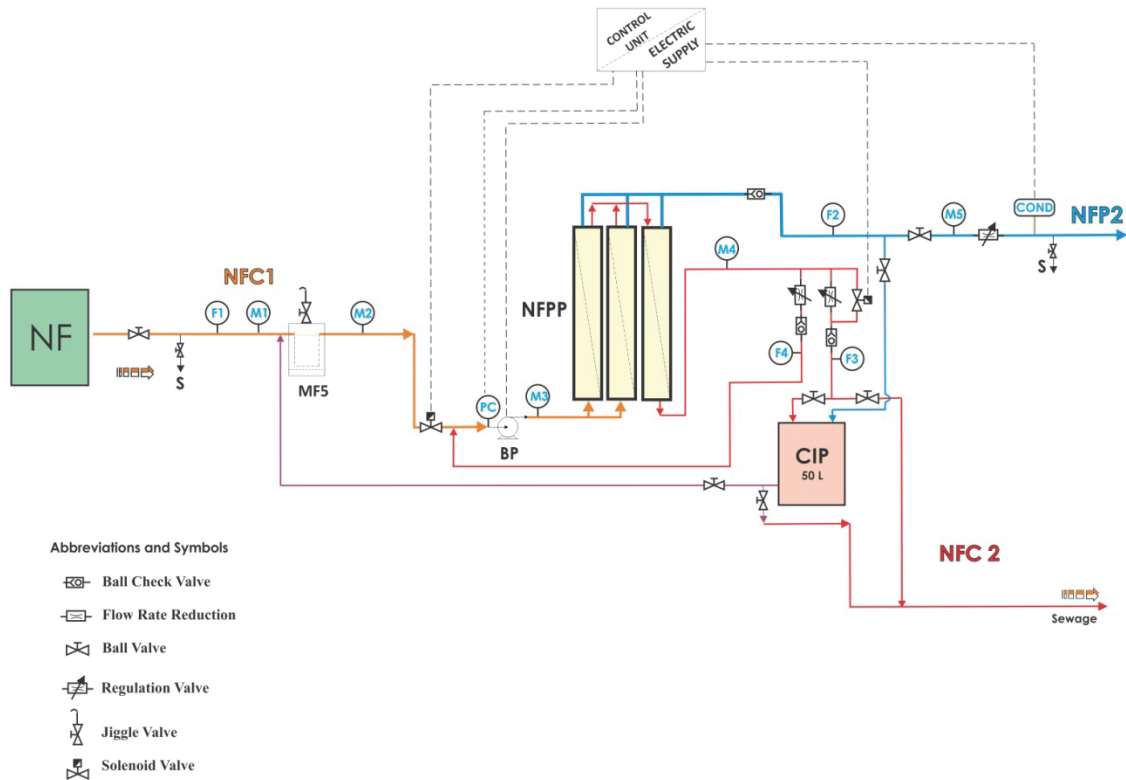


Figure 1. Scheme of the NF pilot plant (NF – industrial NF plant; NFC1 – concentrate after first step of nanofiltration; MF5 – micro-filter of 5 mm; BP – booster pump; NFPP – NF pilot plant; CIP – clean in place unit; M1–5 – pressure gauge; PC – automatic pressure unit; F1–4 – continuous flowmeter; COND – conductivity meter; S – sampling tap; NFC1 – permeate after second step of nanofiltration; NFC2 – concentrate after second step of nanofiltration).

Calculation of membrane flux J (L/hm²) is given in Eq. (2), where Q_p presents permeate flow (L/h), and A presents effective membrane area (m²):

$$TMP = \frac{p_f + p_c}{2} - p_p \quad (1)$$

$$J = \frac{Q_p}{A} \quad (2)$$

Flow rate of permeate produced per flow rate of feed water presents membrane recovery that is calculated as follows:

$$R = 100 \frac{Q_p}{Q_f} \quad (3)$$

where: Q_f – feed water flow (L/h).

Removal efficiency (η) can be expressed using Eq. (4), where c_p and c_f are concentrations of measured component in permeate and feed, respectively, in mg/L:

$$\eta = 100 \left(1 - \frac{c_p}{c_f} \right) \quad (4)$$

Concentration of measured parameters in the concentrate, c_c (mg/L), can be calculated using expression

(5), where Q_c is volumetric flow (L/h) of concentrate stream [30]:

$$c_c = \frac{(Q_f c_f) - (Q_p c_p)}{Q_c} \quad (5)$$

The concentration factor (CF , the ratio of the concentration of a component in concentrate and feed) can be calculated from the mass balance for each measured water component [30]:

$$CF = \frac{c_c}{c_f} = \frac{Q_f}{Q_c} \left[1 - R \frac{c_p}{c_f} \right] \quad (6)$$

Concentrate yield, which was calculated using expression (7), is used to show percentage of feed flow rate that is converted to concentrate stream:

$$Y_c = 100 \frac{Q_c}{Q_f} \quad (7)$$

RESULTS AND DISCUSSION

Concentrate nanofiltration was very effective while COD and arsenic concentration in the permeate produced on the NFPP were below the maximum tolerable values [16]. Influence of the transmembrane pressure

on the relative removal of measured parameters in NFC2 is shown on Figure 2. As can be seen, removal of all measured parameters with the increase of TMP was progressing in a constant way, with slight decrease of c/c_f values with TMP increase (where c and c_f present concentration of measured parameters in feed and NFC2, respectively). Also, values of c/c_f for *COD*, *TOC*, and *As* below 0.5 indicate that the experimental membranes showed excellent removal characteristics. Mean values of *As*, *TOC* and *COD* in P were 2.6 $\mu\text{g/L}$, 0.33 mg/L , and 1.7 $\text{mg KMnO}_4/\text{L}$, respectively, while average values of *Na* is 56.66 mg/L and ammonia were 1.14 mg/L . It can be concluded from obtained results that experimental NF membranes showed excellent arsenic and *COD* removal characteristics which is proven by the fact that concentrations of all measured parameters

are below the MTL, except the ammonia value, which slightly exceeds MTL, according to local regulations [16].

Influence of flux values on the membrane rejection is shown in Figure 3. Increase in ammonia removal efficiency was observed with the flux increase, while the mean value of membrane rejection ($\bar{\eta}$) for ammonia was 80.40%. Membranes exhibited similar constant behavior in regard to *COD*, *TOC*, *As* and *Na* removal, with $\bar{\eta}$ of 98.23, 98.73, 96.74 and 93.45%, respectively.

$Y_{c,\text{total}}$ value (total percentage of produced concentrate after both steps) as well as R_{total} (total recovery after both steps) are given in Figure 4. Concentrate yield after the first step of the nanofiltration was 18.52% and the recovery valued 81.48%. $Y_{c,\text{total}}$ values had decreasing trend with TMP increase. Also total recovery increase was observed. Optimum transmem-

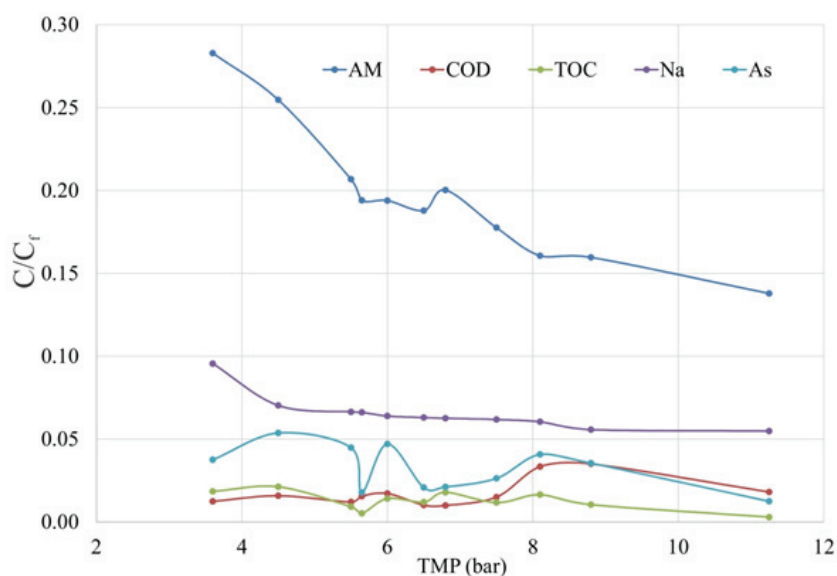


Figure 2. Influence of TMP on the removal of investigated physicochemical parameters in the permeate obtained from NFC2.

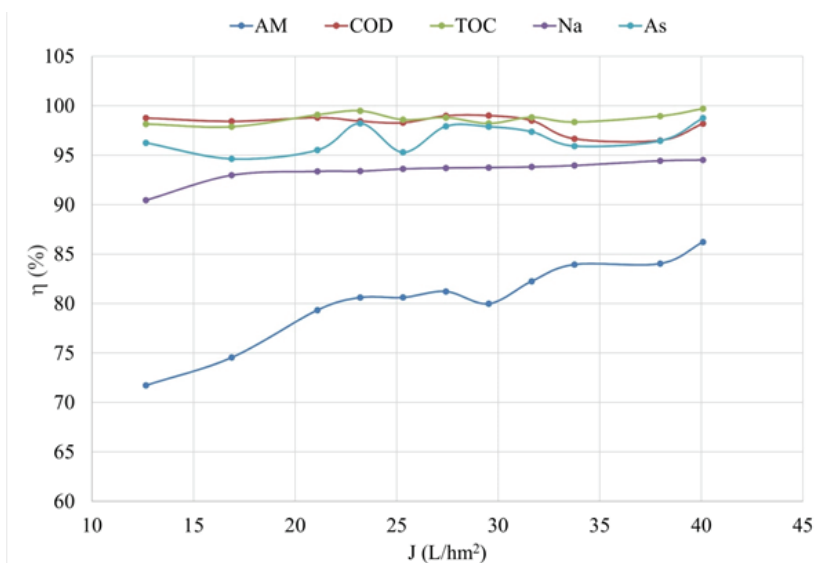


Figure 3. Changes in measured parameters removal efficiency with flux values increase.

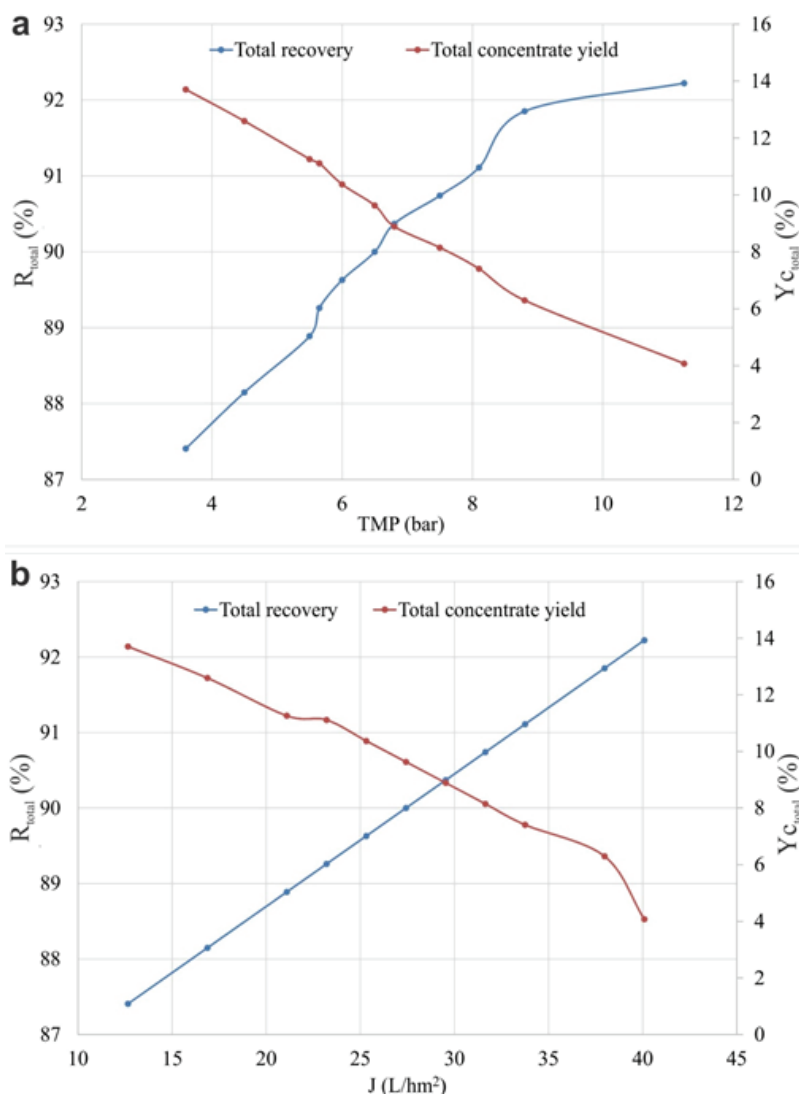


Figure 4. Transmembrane pressure (a) and flux (b) influence on total concentrate yield and total recovery values.

brane pressure and membrane flux were between 6.5–7.5 bar and ~ 30 L/hm², respectively, which was in accordance with observed intercepts in Fig. 4a and b. Obtained R_{total} was 90.37% and $Y_{\text{c,total}}$ was 8.89% which is significantly lower than presented in previous results [30].

Equation (5) was used to calculate theoretical values of parameters in the concentrate. Concentration factor (expression (6)) was calculated for theoretically obtained results (CF_{th}) and empirically measured values in the concentrate (CF_{ex}). Both concentration factors for different parameters at optimal flux value are given in Table 1. The best and the worst CF_{ex} vs. CF_{th} relative accordance of around 9 and 20% were evident in the case of arsenic and TOC, respectively.

$CF_{\text{ex}}/CF_{\text{th}}$ quotient was established as real concentration factor CF_r and it defined passage of some water constituents through, *i.e.*, their accumulation on the membrane surface. CF_r values are presented in Table 2

Table 1. Theoretically obtained and empirically measured concentration factors at optimal flux value

Parameter	AM	COD	TOC	Na	As
CF_{th}	2.05	2.16	2.16	2.13	2.15
CF_{ex}	2.41	2.50	1.79	2.55	2.36

and showed that all values greater than 1 ensigned good passage of inlet water constituents to the concentrate without or small accumulation on the membrane surface. For fluxes greater than 31 L/hm² all CF_r values were less than 1. Exceptions were data for TOC which for all flux amounts valued lesser than 1, what denoted to probably high content of chemically non-easily oxidable organics. The similar values less and close to 1 were obtained for arsenic which ensigns the possibility of predominant organically bonded arsenic species. CF_r values for ammonia, easy oxidable organics as COD and sodium were in flux range until 31 L/hm² greater than 1, and did not show any affinity to accu-

multate onto membrane surface. Higher fluxes contributed to CF_r decrease below 1, when all determined parameters could potentially be accumulated in the membrane pores.

Table 2. Measured parameters CF_r quotient changes in the dependence of flux

$J / L h^{-1} m^{-2}$	AM	COD	TOC	Na	As
12.66	1.31	1.47	0.75	1.12	0.78
16.88	1.32	1.30	0.88	1.48	0.64
21.10	1.40	1.42	0.75	1.40	0.61
23.21	1.40	1.33	0.86	1.41	1.34
25.32	1.34	1.24	0.85	1.36	0.58
27.43	1.22	1.23	0.80	1.27	1.15
29.54	1.18	1.16	0.83	1.20	1.09
31.65	1.18	0.91	0.78	1.11	1.04
33.76	1.09	0.94	0.74	1.05	1.09
37.97	0.97	0.84	0.72	0.92	0.88
40.08	0.67	0.67	0.54	0.63	0.68

As mentioned, membranes were chemically cleaned, and COD, TOC, As, Na and ammonia concentrations were not of interest for this work and were not measured in cleaning solution. Yet, appearance of yellow-brown color established by visual method confirmed data presented in Table 2, that part of humic matter along with other measured parameters were accumulated on the surface of the membrane.

Conceptual design of drinking water plant for City of Kikinda

Described two step nanofiltration of groundwater and further concentrate nanofiltration results were the base for preliminary design of potable water plant (PWP) assigned to supply of City of Kikinda citizens. Input data for dimensioning of PWP capacity are presented in Table 3.

Data presented in Table 3, accompanied with described nanofiltration results were the base for preliminary design of PWP presented in Tables 4 and 5.

Groundwaters under pressure of well pumps pass through double fineness microfilter protective cartridges of 20 and 5 μm to NF booster pumps which increase the pressure to 8 bar. First step nanofiltration process consists of two parallel interconnected NF plants. Obtained permeate, NFP1, flows to the collecting tank of 3,000 m^3 volume by previous disinfection with sodium hypochlorite. Separated concentrate NFC1 flows to additional filtration process into the third NF plant. Secondly originated permeate, NFP2, join the NFP1 permeate stream, and NFC2 as a total concentrate is disposed to the recipient. Complete two step NF process does not required any chemicals in service regime, but only for temporary membranes chemical cleaning.

The PWP nanofiltration equipment installing space required small area of $\sim 300 m^2$, plus reservoir needed area of $\sim 1,300 m^2$, sized to $\sim 25 m \times 50 m \times 4 m$ as a width, length and height, respectively. The pure drinking water reserve of $\sim 3,000 m^3$ is enough for 12 h

Table 3. Essential input data for preliminary design of PWP

Population (people)	Daily consumption L/capita	Water demand m^3/d	Average hourly consumption m^3/h ; L/s	Maximal hourly consumption m^3/h ; L/s
37,676	150	5,651.40	235.46; 65.41	353.21; 98.12

Table 4. PWP water balance

Feed water L/s	NFP1 L/s	NFC1 L/s	NFP2 L/s	Total permeate L/s	Total concentrate L/s
110	89.65	20.35	9.76	99.41	10.59

Table 5. Technical and economic overview of PWP construction and maintenance

Position	First NF step	Second NF step
Installed electric power, kW	140	35
Number of NE-8040 membranes	288	72
Number of pressure membrane vessels	48	12
Specific electric power consumption, kWh/ m^3	0.321	–
Building required, m^2	~ 300	–
Net capacity, m^3/d	7,064.20	–
Net capacity, m^3/y	2,578,433	–
Capital investment, €	~ 2.2 million	–
Price of drinking water vs. maintenance costs, €/ m^3	~ 0.1	–

continual supplying of citizens, as well as for 8 h of maximal hourly consumption demand. The graphical abstract of the conceptual design which presents 3D view of nanofiltration plant as a part of PWP is shown in Figure 5.

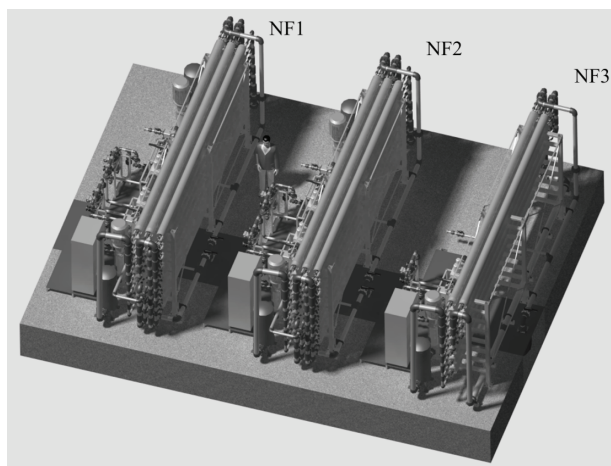


Figure 5. 3D view of NF drinking water plant.

The Figure 5 presents two first step nanofiltration units (NF1 and NF2) for groundwater purification and the third unit (NF3) designed for NFC1 treatment. In comparison of plant dimensions with the displayed worker average height, it could be seen that the main part of PWP does not required big space.

CONCLUSION

Pilot plant used in this study showed great ability to reduce amount of disposable NF concentrate. Arsenic and *COD* values in permeate from second step of the experiment were below *MTL*, according to local regulation and could be mixed with the first step permeate to increase total drinking water yield for almost 9%.

Concentrate nanofiltration exhibited high rejection of all determined water parameters, *i.e.*, ammonia more than 80%, and *COD*, *TOC*, *Na* and *As* for over 90%.

Results showed that obviously high organic matter and arsenic amounts in the same solution can be successfully removed by nanofiltration force. At the base of these data investigated concentrate nanofiltration was in the same time wastewater treatment and potable water preparation by mean of physical process without usage of any chemical. Established CF_r quotient is excellent indicator for degree of potential accumulation of water constituents on membrane surface during desalination. Analysis of obtained CF_r values for all investigated water constituents proved that only organic matter coupled with arsenic species definitely was accumulated in membrane pores which could evoke potential fouling.

Obtained results are obviously important contribution to modern trends of preserving natural resources of fresh water. Taking into consideration amount of reduced concentrate, authors suggest application of obtained desalination procedure and results to a large scale membrane plants for drinking water conditioning. Based on the obtained results, conceptual design of drinking water plant for City of Kikinda was presented.

REFERENCES

- [1] M. Gagliardi, Global markets and technologies for nanofiltration, in: BCC Research, Wellesley, MA, 2014, pp. 132.
- [2] I. Mijatović, M. Matošić, B.H. Černeha, D. Bratulić, Removal of natural organic matter by ultrafiltration and nanofiltration for drinking water production, *Desalination* **169** (2004) 223–230.
- [3] I. Vergili, Application of nanofiltration for the removal of carbamazepine, diclofenac and ibuprofen from drinking water sources, *J. Environ. Manage.* **127** (2013) 177–187.
- [4] A.R. Costa, M.N.d. Pinho, Performance and cost estimation of nanofiltration for surface water treatment in drinking water production, *Desalination* **196** (2006) 55–65.
- [5] N. Kukučka, Engineering design of nanofiltration modules for the reduction of organic matter and arsenic from the groundwater aquifer, Ph.D. Thesis, Faculty of Technical Sciences, Novi Sad, 2013, p. 152.
- [6] H. Runlin, Formation and characterization of (melamine–TMC) based thin film composite NF membranes for improved thermal and chlorine resistances, *J. Memb. Sci.* **425–426** (2013) 176–181.
- [7] W. Fang, R.Wang, S. Chou, L. Setiawan, A.G. Fane, Composite forward osmosis hollow fiber membranes: Integration of RO- and NF-like selective layers to enhance membrane properties of anti-scaling and anti-internal concentration polarization., *J. Memb. Sci.* **394–395** (2012) 140–150.
- [8] P. Marchetti, A. Butté, A.G. Livingston, An improved phenomenological model for prediction of solvent permeation through ceramic NF and UF membranes, *J. Memb. Sci.* **415–416** (2012) 444–458.
- [9] A.Y. Bagastyo, J. Keller, D.J. Batstone, Size fractionation characterisation of removed organics in reverse osmosis concentrates by ferric chloride, *Water Sci. Technol.* **63** (2011) 1795–1800.
- [10] X. Xu, L. Lin, C. Papelis, M. Myint, T.Y. Cath, P. Xu, Use of drinking water treatment solids for arsenate removal from desalination concentrate, *J. Colloid Interface Sci.* **445** (2015) 252–261.
- [11] P. Xu, M. Capito, T.Y. Cath, Selective removal of arsenic and monovalent ions from brackish water reverse osmosis concentrate, *J. Hazardous Mat.* **260** (2013) 885–891.
- [12] F.C. Kent, K. Farahbakhsh, B. Mahendran, M. Jaklewicz, S.N. Liss, H. Zhou, Water reclamation using reverse osmosis: Analysis of fouling propagation given tertiary

- membrane filtration and MBR pretreatments, *J. Memb. Sci.* **382** (2011) 328–338.
- [13] J. Kim, F.A. DiGiano, R.D. Reardon, Autopsy of high-pressure membranes to compare effectiveness of MF and UF pretreatment in water reclamation, *Water Res.* **42** (2008) 697–706.
- [14] J. Meier, T. Melin, Wastewater reclamation by the PAC-NF process, *Desalination* **178** (2005) 27–40.
- [15] S. Shanmuganathan, S. Vigneswaran, T.V. Nguyen, P. Loganathan, J. Kandasamy, Use of nanofiltration and reverse osmosis in reclaiming micro-filtered biologically treated sewage effluent for irrigation, *Desalination* **364** (2015) 119–125.
- [16] Local regulations on drinking water quality (1998–1999).
- [17] M. Kukučka, N. Kukučka, Effect of Extremely High Specific Flow Rates on the Ion-Exchange Resin Sorption Characteristics, in: A. Kilislioglu (Ed.), *Ion Exchange – Studies and Applications*, Intech, Rijeka, 2015, pp. 73–102.
- [18] M.M. Vidović, B. Milovanović, I.S. Trajković, J.G. Momić, I. Tomić, Reduction of Trihalomethanes Forming Potential by Adsorption of Natural Organic Matter on Ionic Exchange Resins, *J. Water Resource Prot.* **2** (2010) 137–142.
- [19] E. Mohora, S. Rončević, J. Agbaba, A. Tubić, M. Mitić, M. Klačnja, B. Dalmacija, Removal of arsenic from groundwater rich in natural organic matter (NOM) by continuous electrocoagulation/flocculation (ECF), *Sep. Purif. Technol.* **136** (2014) 150–156.
- [20] E. Mohora, S. Rončević, B. Dalmacija, J. Agbaba, M. Watson, E. Karlović, M. Dalmacija, Removal of natural organic matter and arsenic from water by electrocoagulation/flotation continuous flow reactor, *J. Hazardous Mat.* **235–236** (2012) 257–264.
- [21] P. Warwick, E. Inam, N. Evans, Arsenic's Interaction with Humic Acid, *Environ. Chem.* **2** (2005) 119–124.
- [22] Y. Yu, C. Zhao, Y. Wang, W. Fan, Z. Luan, Effects of ion concentration and natural organic matter on arsenic(V) removal by nanofiltration under different transmembrane pressures, *J. Environ. Sci.* **25** (2013) 302–307.
- [23] Z. Nikić, M. Vidović, Hydrogeological conditions and quality of ground waters in northern Banat, Pannonian basin., *Environ. Geol.* **52** (2007) 1075–1084.
- [24] M. Vasiljević, Possibility of Using Groundwaters for the Needs of Water Supply of the Settlements and Industry in the Pannonian Basin (Banat and Bačka), Ph.D. Thesis, University of Belgrade, 1999.
- [25] M. Kukučka, N. Kukučka, M. Vojinović-Miloradov, Ž. Tomić, M. Šiljeg, A novel approach to determine a resin's sorption characteristics for the removal of natural organic matter and arsenic from groundwater, *Water Sci. Technol.* **11** (2011) 726–736.
- [26] M. Kukučka, N. Kukučka, M. Vojinović-Miloradov, Ž. Tomić, M. Šiljeg, Effect of extremely high specific flow rates on the removal of NOM and arsenic from groundwater with an ion-exchange resin: A pilot-scale study in northern Serbia, *J. Environ. Sci. Health, A* **46** (2011) 952–959.
- Toray, Product Specification Sheet/Model CSM NE8040-90, 2012, pp. 1, 2.
- [27] Toray, Product Specification Sheet/Model CSM NE4040-90, 2012, pp. 1, 2
- [28] Standard Methods for the Examination of Water and Wastewater, 19th ed., American Public Health Association Publications, Washington DC, 1995.
- [29] B. Van der Bruggen, L. Lejon, C. Vandecasteele, Reuse, Treatment, and Discharge of the Concentrate of Pressure-Driven Membrane Processes, *Environ. Sci. Technol.* **37** (2003) 3733–3738.

IZVOD

POVEĆANJE EFIKASNOSTI NANOFILTRACIONOG PROCESA PRERADE PODZEMNE VODE DODATNIM MEMBRANSKIM TRETMANOM KONCENTRATA

Miroslav Đ. Kukučka, Nikoleta M. Kukučka

EnviroTech d.o.o., Sterije Popovića 42, Kikinda, Srbija

(Naučni rad)

U radu je prikazan tretman otpadne vode (koncentrata) iz nanofiltracionog uređaja za proizvodnju pijaće vode kapaciteta proizvodnje permeata od 11.500 L/h. U cilju dobijanja pijaće vode iz koncentrata kao i smanjenja količine otpadne vode izrađen je nanofiltracioni pilot uređaj, neto kapaciteta permeata 700 L/h pri optimalnom fluksu od ~ 30 L/(h m²). Ispitivane su mogućnosti uklanjanja visokih koncentracija arsena, prirodnih organskih materija preko lako oksidujućih (COD) i ukupnih organskih materija (TOC), natrijuma i amonijaka (AM) iz influenta pri različitim fluksevima i transmembranskim pritiscima. Nanofiltracijom koncentrata na pilot uređaju je značajno smanjen sadržaj navedenih sastojaka što preko srednjih vrednosti efikasnosti uklanjanja ($\bar{\eta}$) iznosi: $\bar{\eta}_{As} = 96,74\%$, $\bar{\eta}_{COD} = 98,23\%$, $\bar{\eta}_{TOC} = 98,73\%$, $\bar{\eta}_{Na} = 93,45\%$, $\bar{\eta}_{AM} = 80,40\%$. Na osnovu dobijenih rezultata u radu je predstavljen konceptualni dizajn postrojenja za kondicioniranje vode za grad Kikinda. Srednje vrednosti koncentracija As, TOC, i COD u proizvedenom permeatu su iznosile 2,6 µg/L, 0,33 mg/L i 1,7 mg KMnO₄/L, redom, dok su srednje vrednosti za Na i amonijak iznosile 56,66 i 1,14 mg/L, redom. S obzirom na to da su svi mereni parametri u permeatu ispod maksimalno dozvoljene koncentracije može se zaključiti da se primenjene membrane mogu uspešno koristiti za dobijanje pijaće vode iz voda sa visokim sadržajem organskih materija i arsena. Izuzetak je amonijak čija koncentracija u permeatu minimalno premašuje maksimalno dozvoljenu koncentraciju. U radu su takođe ispitivani koncentracioni faktori za svaki mereni parametar. Koncentracioni faktori su određivani teorijski i empirijski, a prikazan je i njihov odnos pomoću kojeg je bilo moguće odrediti pojavu nastajanja naslaga na membranama. Na osnovu prinosa koncentrata i iskorišćenja membrana utvrđen je procenat smanjenja količine otpadne vode. Pri optimalnim vrednostima fluksa i transmembranskog pritiska od ~ 30 L/(h m²) i 6,5–7,5 bar, redom, dobijene su vrednosti prinosa koncentrata i iskorišćenja membrana od 8,89% i 90,37%, redom, što označava povećanje iskorišćenja membranskih procesa na oba uređaja zajedno i smanjanja količine koncentrata za $\sim 9\%$.

Ključne reči: Nanofiltracija • Ušteda vode
• Prinos koncentrata • Arsen • Huminske materije • Koncentracioni faktor

Određivanje lipofilnosti 2'-hidroksihalkona primenom RP-HPLC metode

Jasmina V. Bašić¹, Branka M. Ivković², Slavica Stevanović³, Anđelka Lazarević¹, Zorica B. Vujić²

¹Visoka zdravstvena škola strukovnih studija u Beogradu, Srbija

²Farmaceutski fakultet, Univerzitet u Beogradu, Srbija

³Tehnološko–metalurški fakultet, Univerzitet u Beogradu, Srbija

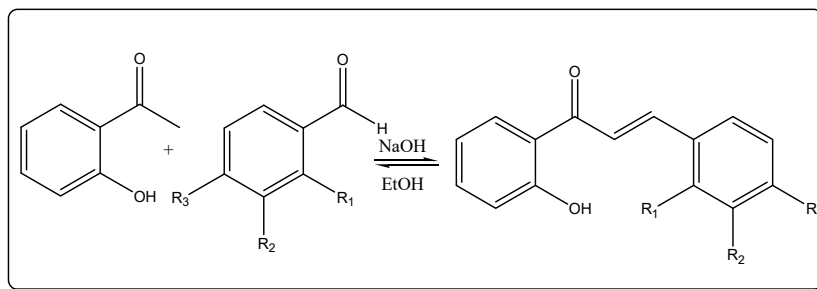
Izvod

Lipofilnost dvanaest sintetisanih halkona, čiji je prsten B *orto*, *meta* ili *para* monosupstituisan alkil, oksialkil grupama ili halogenom određena je u uslovima reversno-fazne tečne hromatografije uz upotrebu oktadecil-modifikovanog (RP-18) silika-gela kao stacionarne faze i dvokomponentne smeše metanol/voda kao mobilne faze. Linearna zavisnost $\log k'$ vrednosti od zapreminskog udela metanola u mobilnoj fazi, utvrđena je za sva ispitivana jedinjenja, sa visokom vrednošću korelacionog koeficijenta ($r > 0,99$). Ekstrapolacijom dobijene prave na 0% udela metanola dobijena je vrednost faktora kapaciteta za hromatografski sistem u kom bi mobilnu fazu predstavljala voda ($\log k_w$). Za pet standardnih supstanci, hemijski sličnih halkonima pod istim eksperimentalnim uslovima određene su $\log k_w$ vrednosti i korelisane sa literaturno dostupnim $\log P$ vrednostima za data jedinjenja. Na osnovu formirane standardne krive, izračunate su vrednosti $\log P_{EXP}$ za sintetisane halkone. Da bi se izvršila procena relevantnosti eksperimentalno dobijenih $\log P$ vrednosti halkona, linearnom regresionom analizom, izvršena je korelacija $\log P_{EXP}$ vrednostima sa $\log P$ vrednostima izračunatim primenom različitih računskih programa. Statistički parametri zavisnosti pokazali su da je primenom programa ChemOffice postignuto najbolje slaganje rezultata, što ukazuje na to da je ovaj program pogodan za izračunavanje $\log P$ vrednosti novosintetisanih halkona kao i jedinjenja, strukturno sličnih halkonima.

Ključne reči: halkoni, lipofilnost, HPLC.

Dostupno na Internetu sa adrese časopisa: <http://www.ache.org.rs/HI/>

Halkoni su prirodni proizvodi biljnog porekla, rasprostranjeni u voću, povrću, začinicima i čajevima, a nastaju kao intermedijeri u sintezi flavonoida i flavanona koju katalizuje enzim halkon sintaza. Hemijski gledano, halkoni predstavljaju *seco* flavonoidne strukture kod kojih su dva aromatična prstena povezana preko α,β -nezasićenog ketonskog mosta. Derivati su 1,3-diaril-2-propen-1-ona i u novije vreme dobijaju polusintetski ili totalnom sintezom [1] u reakciji aldolne kondenzacije (Claisen–Schmidt reakcija), slika 1.



Slika 1. Šema sinteze halkona.

Figure 1. Scheme synthesis of chalcones.

Preписка: J.Bašić, Visoka zdravstvena škola strukovnih studija u Beogradu, cara Dušana 285, 11000 Beograd, Srbija.

E-pošta: basic.jasmina23@gmail.com

Rad primljen: 26. april, 2015

Rad prihvaćen: 13. oktobar, 2015

Halkoni imaju širok spektar bioloških aktivnosti: antiinflamatornu [1–3], antibakterijsku [1,2,4,5], fungicidnu [1,2], antiproliferativnu [1,2,6,7], tuberkulozatsku [1,8] i druge, ali i nisku selektivnost koja ograničava kliničku primenu ovih jedinjenja [1].

Mehanizam njihovog citotoksičnog, mutagenog i antikancerogenog delovanja je poznat i ogleda se u vezivanju za nukleinske kiseline slično alkilirajućim agensima [1].

Mehanizmi antibakterijskog i antifungalnog dejstva halkona nisu u potpunosti razjašnjeni. Neke studije su pokazale da različiti halkonski derivati deluju na nivou ćelijske membrane mikroorganizama izazivajući njenu destrukciju. Pretpostavlja se da različita osetljivost

NAUČNI RAD

UDK 547.81:544.722.123:543.544

Hem. Ind. 70 (5) 511–518 (2016)

doi: 10.2298/HEMIND150426057B

pojedinih sojeva mikroorganizama na citotoksično dejstvo halkona potiče od razlike u mehanizmu destrukcije ćelijske membrane. Smatra se da ove razlike nastaju usled različite orijentacije molekula unutar ćelijske membrane, kao i različitog afiniteta halkona prema membrani ćelija [9]. Takođe, dosadašnje studije su pokazale da halkoni svoju antimikrobnu aktivnost ispoljavaju zahvaljujući prisustvu α, β -nezasićenog karbonilnog niza u molekuli koji stupa u reakciju sa sulfhidrilnim grupama enzima i drugih proteina (Majklova adicija) [10–12]. U ovoj reakciji enonska funkcionalna grupa ima funkciju akceptora elektrona. Majklova adicija je olakšana prisustvom elektronakceptorskih (EA) grupa u *para* položaju u prstenu B halkona, dok prisustvo elektrondonorskih (ED) grupa na istom položaju otežava ovu reakciju. Ipak, Boeck i saradnici [10] pokazali su da *p*-nitrohalkon (nitro grupa ima jak EA efekat) pokazuje istu ili manju aktivnost u odnosu na *p*-hlorohalkon (hloro grupa, ima slab EA efekat) i *p*-metilhalkon (metil grupa ima ED efekat). Dosada izvedene QSAR studije halkona, pokazale su da prisustvo hidroksilnih grupa čini ovu klasu jedinjenja potentnijim za antimikrobno dejstvo [1,11], mada nije utvrđeno kako njihov broj i položaj utiče na aktivnost halkona [1]. Halkoni takođe ispoljavaju svoje dejstvo vezivanjem za DNA mikroorganizama, ali je pokazano da DNA ne predstavlja glavni ciljni molekul njihovog intracelularnog dejstva [9].

Da bi se razjasnili farmakodinamski mehanizmi, kao i farmakokinetičke osobine nosivih jedinjenja, važno je poznavati njihove fizičko-hemijske osobine među kojima najznačajnu ulogu ima lipofilnost molekula. Ovaj parametar ima važnu ulogu u transportu molekula kroz biološke sisteme i može uticati na formiranje kompleksa između samog molekula i biomolekula (receptora) u organizmu. Lipofilnost se izražava preko podeonog koeficijenta (P), odnosno njegove logaritamske vrednosti ($\log P$). Vrednost $\log P$, kao mera lipofilnosti, trenutno se najviše koristi u medicinskoj hemiji i molekularnoj farmakologiji, gde je formirana baza podataka $\log P$ vrednosti. Lipofilnost molekula se, pored direktnog određivanja metodom mućkanja (*shake flask method*), može odrediti i indirektnim eksperimentalnim metodama kao što su: hromatografija na obrnutim fazama, micelarna/mikroemulziona elektrokinetička hromatografija, potenciometrijska metoda, metoda filter probe i druge.

Visokoefikasna tačna hromatografija na reverznim fazama (RP-HPLC – *Reversed Phase High Pressure Liquid Chromatography*) je široko zastupljena u određivanju $\log P$ vrednosti koja se dalje koriste u QSRR i QSAR studijama.

U QSRR modelima od hromatografskih retencionih parametara koristi se logaritamska vrednost faktora kapaciteta, $\log k$ vrednost, kao retencionog faktora [16], koja se može izračunati iz izraza:

$$k = (t_R - t_0)/t_0 \quad (1a)$$

$$\log k = \log (t_R - t_0)/t_0 \quad (1b)$$

gde je t_R retenciono vreme ispitivane supstance, a t_0 retenciono vreme rastvarača. Vrednost $\log k$ se može korelisati sa udelom organske komponente u mobilnoj fazi, a dobijena zavisnost se može prikazati jednačinom prave:

$$\log k = \log k_w + b\phi \quad (2)$$

gde je $\log k_w$ odsečak prave, b nagib prave, a ϕ udeo organske komponente u mobilnoj fazi. Kao mera lipofilnosti koristi se vrednost $\log k_w$, koja se dobija ekstrapolacijom na nulu koncentracije organske komponente. S obzirom na to da se retencija određuje u dvokomponentnoj (voda/organski rastvarač) mobilnoj fazi koja može biti različitog sastava, ekstrapolacija je uobičajeni postupak standardizacije hromatografskih parametara. $\log k_w$ predstavlja retenciju supstance u vodi čime se uticaj organskog rastvarača u mobilnoj fazi svodi na minimum. Jedino pitanje koje se i kroz literaturu provlači je, koji model najprikladnije definiše zavisnost retencionih parametara i sastava mobilne faze. U upotrebi su dva modela, linearni i kvadratni. Pokazano je da za mobilnu fazu metanol-voda, oba modela daju vrlo slične rezultate, a da se ekstrapolirane vrednosti statistički bitno ne razlikuju. Suprotno tome, kod mobilne faze acetonitril-voda javlja se statistički značajna razlika između izračunatih vrednosti po linearnom i kvadratnom modelu [17]. S obzirom na to da se u većini slučajeva najbolje korelacije između $\log P$ i $\log k_w$ postižu primenom linearnog modela sa mobilnom fazom metanol-voda, za određivanje lipofilnosti molekula kao mobilna faza najčešće se koristi smeša ova dva rastvarača pri čemu se udeo organske komponente nalazi u opsegu od 30 do 80%.

Pored eksperimentalnih metoda, za određivanje $\log P$ vrednosti često se koriste računarske metode. Danas postoji veliki broj softverskih paketa koji se koriste za izračunavanje lipofilnosti molekula [18–20].

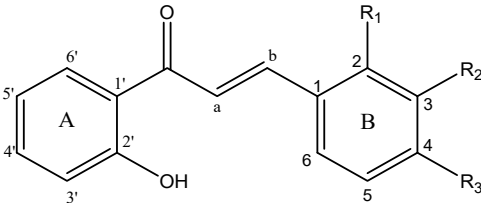
U prethodnim studijama lipofilnosti halkona upotrebom RP-HPLC metode, određene su $\log k_w$ vrednosti koje su korišćene u QSAR studijama antimalarijske [21] i antiplazmodijalne aktivnosti [22] ovih jedinjenja, ali nisu određivane njihove $\log P$ vrednosti.

U ovom radu upotrebom RP-HPLC metode, određene su $\log P$ vrednosti dvanaest sintetisanih halkona čiji je prsten B *orto*, *meta* ili *para* monosupstituisan halogenima ($-F$, $-Cl$, CF_3), alkil ($-CH_3$) ili oksialkil ($-OCH_3$) grupama.

EKSPERIMENTALNI DEO

Hemikalije i reagensi. a) hemijska struktura ispitivanih halkona kao i njihovi hemijski nazivi prikazani su u tabeli 1.

Tabela 1. Strukture ispitivanih halkona
Table 1. Structure of studied chalcones



Br.	R ₁	R ₂	R ₃	Mol. formula	M _R	Hemijski naziv
1	H	H	F	C ₁₅ H ₁₁ FO ₂	242,25	(E)-3-(4-Fluorofenil)-1-(2-hidroksifenil)prop-2-en-1-on
2	H	F	H	C ₁₅ H ₁₁ FO ₂	242,25	(E)-3-(3-Fluorofenil)-1-(2-hidroksifenil)prop-2-en-1-on
3	F	H	H	C ₁₅ H ₁₁ FO ₂	242,25	(E)-3-(2-Fluorofenil)-1-(2-hidroksifenil)prop-2-en-1-on
4	H	H	OH	C ₁₅ H ₁₂ O ₃	240,25	(E)-1-(2-Hidroksifenil)-3-(4-hidroksifenil)prop-2-en-1-on
5	H	OH	H	C ₁₅ H ₁₂ O ₃	240,25	(E)-1-(2-Hidroksi-fenil)-3-(3-hidroksi-fenil)prop-2-en-1-on
6	OH	H	H	C ₁₅ H ₁₂ O ₃	240,25	(E)-1,3-Bis-(2-hidroksi-fenil)prop-2-en-1-on
7	H	H	CH ₃	C ₁₆ H ₁₄ O ₂	238,28	(E)-1-(2-Hidroksifenil)-3- <i>p</i> -tolilprop-2-en-1-on
8	H	CH ₃	H	C ₁₆ H ₁₄ O ₂	238,28	(E)-1-(2-Hidroksifenil)-3- <i>m</i> -tolilprop-2-en-1-on
9	CH ₃	H	H	C ₁₆ H ₁₄ O ₂	238,28	(E)-1-(2-Hidroksifenil)-3- <i>o</i> -tolilprop-2-en-1-on
10	OCH ₃	H	H	C ₁₆ H ₁₄ O ₃	254,28	(E)-1-(2-Hidroksifenil)-3-(2-metoksifenil)prop-2-en-1-on
11	CF ₃	H	H	C ₁₆ H ₁₁ F ₃ O ₂	292,25	(E)-1-(2-Hidroksifenil)-3-(2-(trifluorometil)fenil)prop-2-en-1-on
12	Cl	H	H	C ₁₅ H ₁₁ ClO ₂	258,70	(E)-3-(2-Hlorofenil)-1-(2-hidroksifenil)prop-2-en-1-on

b) standardne supstance: 4-hidroksibenzaldehid, Merck, Nemačka, salicilaldehid, Merck, Nemačka, 2-metoksi-4-alilfenol (eugenol), Merck, Nemačka, mentol, Merck, Nemačka i 2,3,4,5,6-pentahlorofenol, Sigma Aldrich, Nemačka.

c) rastvarači korišćeni u pripremi mobilne faze: metanol HPLC čistoće, Sigma–Aldrich, Nemačka, dejonizovana voda, HPLC čistoće.

HPLC analiza. Određivanje lipofilnosti sintetisanih halkona izvedeno je na tečnom hromatograf HP 1200 Hewlett-Packard, sa DAD detektorom, a prikupljeni podaci obrađeni su u ChemStation programu (Agilent Technologies, SAD). Za ispitivana jedinjenja i standardne supstance, izvršena je izokratska hromatografska analiza u hromatografskom sistemu koga čine: Zorbax Eclipse XDB-C18, 4,6 mm×150 mm, 5 μm kolona (Agilent Technologies, SAD) čija je temperatura podešena na 30 °C sa mobilnom fazom koju čini smeša voda–metanol u yapremninskim odnosima 75:25, 70:30, 65:35, 60:40 i 55:45, pri protoku od 1,2 mL/min.

Injektovana zapremina rastvora ispitivanih halkona i standardnih jedinjenja bila je 20 μL, a njihova detekcija vršena je na 210 nm.

Priprema rastvora. Ispitivani halkoni i standardna jedinjenja pripremljeni su kao metanolni rastvori u koncentraciji od 0,1 mg/mL i injektovani u kondicioniran HPLC sistem u triplikatu.

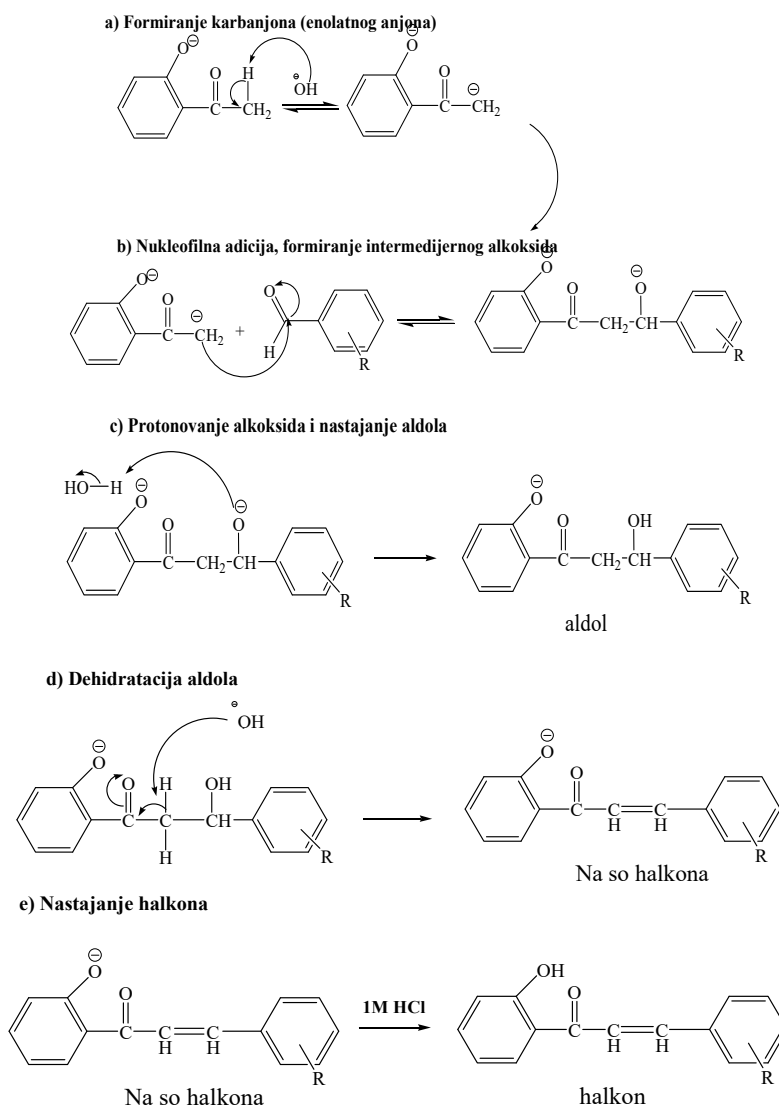
Za svako ispitivano jedinjenje zabeležena su retencionna vremena, t_R , kao i retencionno vreme rastvarača, t_0 , za svaki sastav mobilne faze, izračunati faktori kapa-

citeta i logaritamske vrednosti faktora kapaciteta, $\log k$, prema formulama 1a i 1b.

Obrada rezultata. Kompletna matematička i statistička obrada rezultata izvršena je uz pomoć softverskog alata Excel (Microsoft Office 2003, Cambridge Soft, SAD). U određivanju lipofilnosti halkona, odnosno u QSRR analizi ispitivanih halkona i standardnih jedinjenja, korišćena je linearna regresiona analiza. Za svaku regresionu jednačinu su determinisani sledeći statistički parametri: 95% nivo pouzdanosti (p vrednost), faktor korelacije (r) i Fišerov koeficijent (F).

REZULTATI I DISKUSIJA

Ispitivani halkoni (tabela 1) su sintetisani u reakciji Claisen–Schmidt kondenzacije koja se odvija na sobnoj temperaturi u prisustvu relativno jake baze (30% NaOH) iz 2-hidroksiacetofenona i 2-, 3- ili 4-monosupstituisanog benzaldehida. Uslov za reakciju kondenzacije je postojanje kiselog α -H atoma (H atom metil grupe 2-hidroksiacetofenona) koji odlazi u prisustvu baze. Tom prilikom nastaje karbanjon (enolatni anjon) (slika 2a), koji kao nukleofil reaguje sa elektropozitivnim ugljenikovim atomom karbonilne grupe monosupstituisanog benzaldehida (slika 2b) i gradi intermedijerni alkoksid. Protonovanjem alkoksida nastaje ketol (slika 2c) koji kao nečistoća u manjem procentu može da zaostane u reakcionoj smeši i uklanja se hromatografijom na koloni. Pošto je nastajanje ketola ravnotežna reakcija, sledećom fazom dehidracije ketola u



Slika 2. Mehanizam bazno katalizovane aldolne kondenzacije.
Figure 2. The mechanism of base-catalyzed aldol condensation.

baznoj sredini, koja je ireverzibilna, nastaje α,β -nezasićeni keton (halkon), slika 2d.

Elektron akceptorski supstituenti ($-F$, $-Cl$ i $-CF_3$) prisutni u molekulu benzaldehida olakšavaju ireverzibilnu dehidraciju ketola u baznoj sredini, što povećava prinos reakcije. Zbog prisutne kisele fenolne grupe nastali proizvod je u obliku natrijumove soli iz koje dodatkom 1 mol/L HCl nastaje fenol (slika 2e). Bazno katalizovana aldolna kondenzacija koja se odvija na sobnoj temperaturi (25 °C) u vodeno-etanolnom rastvoru kao proizvod daje samo *trans* izomer α,β -nezasićenog ketona, što je potvrđeno spektroskopskim metodama (1H -NMR, $J_{\text{vinil H}} = 15,2\text{--}15,6$ Hz) [6,11]. Enonska struktura u molekulu halkona (Slika 1) koja povezuje dva benzenova prstena predstavlja kombinovanu hromoforu koja uslovljava batohromno pomerenje apsorpcionih maksimuma benzena prema vidljivoj

oblasti spektra te su dobijeni halkonski proizvodi žuto obojeni.

Lipofilnost halkona određivana je primenom RP HPLC metode pri čemu stacionarnu fazu predstavlja silika gel modifikovan C18 ugljovodoničnim lancima. Međutim, kod C-18 stacionarne faze na površini postoje nemodifikovane silanolne grupe koje interaguju sa molekulima organskih modifikatora iz mobilne faze (vodonične veze, dipol-dipol interakcije). Mogućnost uspostavljanja ovih interakcija, kao i njihov stepen zavisice od elektronskih svojstava i mogućnosti građenja vodoničnih veza upotrebljenog organskog modifikatora [23]. U nizu organskih modifikatora koji se koriste u određivanju $\log k_w$ pokazalo se da metanol kao organski modifikator ima najmanju elucionu moć na oktadecil-modifikovanom silika-gelu, kao i najmanju moć sorpcije te je shodno tome i korišćen u radu.

Da bi ispitali uticaj sastava mobilne faze na retenciju jedinjenja variran je zapremski udeo metanola kao organskog modifikatora. Za svaki zapremski odnos metanol/voda (75:25, 70:30, 65:35, 60:40 i 55:45), HPLC sistem je prethodno kondicioniran u trajanju od 30 min, a zatim su injektovani pripremljeni metanolni rastvori ispitivanih halkona i standardnih jedinjenja. Za svako ispitivano jedinjenje zabeleženo je retenciono vreme (t_R), kao i retenciono vreme rastvarača, t_0 , za svaki sastav mobilne faze.

Dobijeni rezultati (tabela 2) pokazuju da retencija ispitivanih jedinjenja opada sa povećanjem udela organske komponente u mobilnoj fazi. Iz vrednosti t_R i t_0 izračunate su vrednosti faktora kapaciteta k , kao i $\log k$, prema jednačinama 1a i 1b.

Primenom linearne regresije ispitana je zavisnost dobijenih $\log k$ vrednosti od udela organskog rastvarača u mobilnoj fazi (ϕ). Parametar lipofilnosti $\log k_w$ određen je ekstrapolacijom dobijenih pravih na 0% zapremskog udela metanola, tj. dobijena je vrednost faktora kapaciteta za hromatografski sistem u kome bi mobilnu fazu predstavljala voda. U tabeli 3 prikazane su $\log k_w$ vrednosti ispitivanih halkona.

Vrednosti $\log k_w$ dobijene ekstrapolacijom ne zavise od prirode organske komponente, pošto one predstavljaju retenciju u čistoj vodi. Takođe, pored nespecifičnih interakcija ispitivanih supstanci sa funkcionalnim grupama na površini upotrebljene stacionarne faze, na retenciju u značajnoj meri utiču jake specifične interakcije između ispitivanih jedinjenja i komponenta mobilne faze (npr. mogućnost građenja vodoničnih veza povećava rastvorljivost jedinjenja u mobilnoj fazi i uslovljava slabiju retenciju). Različiti stepen interakcija ispitivanih jedinjenja sa stacionarnom, odnosno mobilnom fazom pri upotrebi različitih organskih rastvarača utiče na razlike u $\log k$ vrednostima, pa samim tim i na $\log k_w$ vrednosti. U nizu organskih modifikatora koji se koriste u određivanju $\log k_w$ pokazalo se da metanol kao organski modifikator ima najmanju elucionu moć

na oktadecil-modifikovanom silika-gelu, kao i najmanju moć sorpcije te je shodno tome i korišćen u radu.

Da bi se odredile $\log P$ vrednosti ispitivanih halkona pod istim hromatografskim uslovima određene su i $\log k_w$ vrednosti za pet halkonima hemijski sličnih standardnih supstanci (tabela 3). Određene $\log k_w$ vrednosti za standardne supstance su korelisane sa njihovim $\log P$ vrednostima koje iznose: za 4-hidroksibenzaldehid, $\log P = 0,94$, salicilaldehid, $\log P = 2,07$, 2-metoksi-4-aliilfenol (eugenol) $\log P = 2,99$, mentol, $\log P = 3,31$ i za 2,3,4,5,6 pentahlorofenol, $\log P = 5,01$ [24]. Linearom regresijom konstruisana je standardna kriva zavisnosti $\log P$ od $\log k_w$ vrednosti:

$$\log P = 0,839 \log k_w + 0,689; r^2 = 0,9923, S.E. = 0,154 \quad (3)$$

Na osnovu formirane linearne jednačine (3), iz određenih $\log k_w$ vrednosti za ispitivane halkone izračunate su njihove $\log P_{EXP}$ vrednosti (Tabela 4).

Eksperimentalno određene $\log P$ vrednosti ispitivanih halkona nalaze se u opsegu od 3,44 (halkon **4**) do 4,98 (halkon **11**). Halkon **11** u *orto* položaju prstena B ima trifluorometil grupu koja je u nizu uvedenih alkil, oksialkil i halo grupa, najlipofilnija i najvoluminoznija grupa ($\pi = 0,847$ i $V_V = 39,800 \text{ \AA}$) [25]. Supstitucijom vodonikovih atoma metil grupe atomima fluora voluminoznost pa time i sterni efekti metil grupe ($V_V = 21,300 \text{ \AA}$) se povećavaju, što utiče na geometriju molekula. Prisustvo hlora grupe u *orto* položaju prstena B ne menja geometriju molekula, ali utiče na lipofilnost i elektronsku gustinu. Doprinos hlora lipofilnosti halkona je manji u poređenju sa trifluorometil grupom, ali daleko veći u poređenju sa metil, metoksi i fluoro grupama [25], pa je halkon **12** lipofilniji od halkona **1–10**. Doprinos metil grupe lipofilnosti halkona zavisi od njenog položaja u prstenu B i najviše je izražena kada je metil grupa u *meta* položaju prstena B [25]. Supstitucija vodonika fluorom ($+\pi, +\sigma$), povećava lipofilnost [26,27]. S obzirom na elektronegativnost F, moglo bi se očekivati da je C–F fragment molekula, slične polarizabil-

Tabela 2. Retenciono vreme ispitivanih halkona (min)
Table 2. Retention time of studied chalcones (min)

ϕ	Jedinjenje												t_0
	1	2	3	4	5	6	7	8	9	10	11	12	
0,75	5,511	6,107	6,626	6,643	9,370	2,817	8,575	2,575	9,443	2,976	5,785	8,137	0,791
0,70	7,797	8,780	9,797	10,498	14,458	3,861	13,31	3,448	14,881	3,906	9,465	14,192	0,812
0,65	13,125	14,986	16,975	19,755	26,504	6,099	24,08	5,286	27,330	5,158	15,346	23,452	0,829
0,60	23,810	27,333	31,287	40,286	51,128	10,336	45,40	8,650	52,630	8,717	28,715	45,259	0,832
0,55	45,623	51,243	59,437	84,043	100,000	18,300	87,089	14,683	103,092	14,000	54,549	94,713	0,824

Tabela 3. Vrednosti $\log k_w$ standardnih jedinjenja i ispitivanih halkona
Table 3. Values $\log k_w$ of studied chalcones

Jedinjenje	1	2	3	4	5	6	7	8	9	10	11	12
$\log k_w$	4,365	4,427	4,455	5,127	4,963	3,849	4,849	3,628	4,999	3,281	4,565	4,976

Tabela 4. Vrednosti $\log P$ halkona dobijene eksperimentalnim putem i različitim računskim postupcima
 Table 4. Experimentally and theoretically obtained $\log P$ values of synthesized chalcones

Halkon	$\log P_{Exp}$	$Clog P$	$\log P_{Marvin}$	$Alog Ps$	$Aclog P$	$AB/\log P$	$milog P$	$Alog P$	$Mlog P$	$KOWWIN$	$Xlog P2$	$Xlog P3$
1	4,30	4,10	4,43	3,94	3,27	3,76	3,91	3,64	4,05	4,15	4,03	3,99
2	4,35	4,10	4,43	3,95	3,27	3,76	3,89	3,64	4,05	4,15	4,03	3,99
3	4,47	4,10	4,43	4,02	3,27	3,76	3,69	3,64	4,05	4,15	4,03	3,99
4	3,44	3,29	4,01	3,23	2,91	3,09	3,27	3,17	3,09	3,47	3,04	3,53
5	3,54	3,29	4,01	3,23	2,91	3,09	3,25	3,17	3,09	3,47	3,04	3,53
6	3,62	3,29	4,01	3,23	2,91	3,09	3,51	3,17	3,09	3,47	3,04	3,53
7	4,85	4,46	4,76	4,00	3,52	4,12	4,20	3,92	3,91	4,50	4,31	4,25
8	4,88	4,46	4,76	3,98	3,52	4,12	3,97	3,92	3,91	4,50	4,31	4,25
9	4,75	4,46	4,76	4,00	3,52	4,12	4,18	3,92	3,91	4,50	4,31	4,25
10	4,28	3,88	4,04	3,94	3,10	3,67	3,58	3,42	3,34	4,04	3,79	3,86
11	4,98	4,84	5,17	4,30	3,97	4,67	4,42	4,38	4,54	4,92	4,80	4,77
12	4,89	4,67	4,81	4,24	3,82	4,28	4,20	4,10	4,18	4,60	4,40	4,51

nosti kao C–O ili C–N fragmenti i da je dobar akceptor vodonika, što utiče na građenje intra- ili intermolekulskih vodoničnih veza, ali za razliku od C-heteroatom fragmenata C–F fragment je loš akceptor vodonika, pa je njegov doprinos lipofilnosti halkona (halkoni **1–3**) veći u poređenju sa metoksi grupom (halkon **10**) [26,27].

Halkoni sa dve fenolne grupe u strukturi imaju niže $\log P$ vrednosti jer prisustvo fenolne grupe nepovoljno utiče na lipofilnost halkona. Lipofilnost halkona se smanjuje u zavisnosti od položaja fenolne grupe u prstenu B. Najmanje lipofilan je halkon **4** sa fenolnom grupom u *para* položaju prstena B. Prisustvo fenolne grupe u *para* položaju omogućava nesmetanu konjugaciju elektronskog para fenolne grupe sa fenopropenonskim sistemom, što povećava kiselost vodonikovog atoma, on lako gradi vodonične veze i doprinosi povećanju hidrofilitnosti halkona **1**. Fenolne grupe u *orto* i *meta* položajima ne stupaju u konjugaciju pa je time kiselost njihovih H atoma manja.

Brojna istraživanja su pokazala statistički značajnu vezu između retencionih parametara ($\log k_w$) serije

srodnih supstanci dobijenih primenom reverzno-fazne hromatografije i kompjuterski izračunatih $\log P$ vrednosti [28,29]. Da bi se ustanovilo da li definisani hromatografski sistem može da se upotrebi za dobijanje parametara koji opisuju lipofilnosti, $\log P$ vrednosti dobijene eksperimentalnim putem su poređene sa izračunatim $\log P$ vrednostima, dobijenim primenom različitih teorijskih algoritama zasnovanih na različitim metodama fragmentacije, a koji su inkorporirani u komercijalne softvere ($C \log P$, $\log P_{Marvin}$, $Alog Ps$, $Aclog P$, $AB/\log P$, $milog P$, $Alog P$, $Mlog P$, $KOWWIN$, $Xlog P2$ i $Xlog P3$) [19,20] (tabela 4).

U tabeli 5 date su jednačine pravih i statistički parametri koji opisuju zavisnost između eksperimentalno određenih i izračunatih $\log P$ vrednosti.

Rezultati u tabeli 5 ukazuju na to da se $\log P$ vrednosti izračunate upotrebom različitih algoritama u različitim stepenu korelišu sa eksperimentalno dobijenim $\log P$ vrednostima.

Poređenjem $\log P_{Exp}$, dobijenih na RP-18 stacionarnoj fazi, i parametara lipofilnosti izračunatih pomoću

Tabela 5. Jednačine korelacije oblika $\log P_{exp} = a \log P_{theoretical} + b$ između eksperimentalne i teorijskih vrednosti za $\log P$ ispitivanih halkona
 Table 5. $\log P_{exp} = a \log P_{theoretical} + b$ equation correlation between experimental and theoretical $\log P$ values for studied chalcones

Parametar	a	b	r	r^2	F	p -value
$Clog P$	1.0060	0.2598	0.9845	0.9693	316.0742	0,2903
$\log P_{Marvin}$	1.3040	-1.5005	0.9151	0.8374	50.7576	0,0992
$Alog Ps$	1.3728	-0.9069	0.9463	0.8954	85.6300	0,1440
$aclog P$	1.4658	-0.5222	0.9217	0.8495	56.4512	0,4427
$AB/\log P$	1.0649	0.3222	0.9689	0.9387	153.1044	0,3508
$milog P$	1.3555	-0.8417	0.9298	0.8646	63.8428	0,2273
$Alog P$	1.3460	-0.5830	0.9471	0.8970	87.0991	0,2994
$Mlog P$	0.9984	0.6011	0.8755	0.7665	32.8181	0,3850
$KOWWIN$	1.1327	-0.3495	0.9807	0.9617	251.3155	0,2697
$Xlog P2$	0.9234	0.7358	0.9786	0.9576	225.9491	0,0129
$Xlog P3$	1.3322	-1.0161	0.9414	0.8863	77.9513	0,1278

različitih kompjuterskih programa (tabela 5), vidi se da je najbolja korelacija (r = korelacioni koeficijenti) postignut sa Clog P vrednostima izračunatim pomoću programa ChemOffice (r = 0,9845), dok je najmanja korelacija postignuta sa vrednostima log P dobijenim korišćenjem programa ChemAxon (r = 0,9151), što ukazuje da algoritam inkorporiran u program ChemOffice može da se primene za izračunavanje log P vrednosti 2-hidroksihalkona čiji je prsten B mono *orto*, *meta* ili *para* supstituisan.

ZAKLJUČAK

Primenom linearne regresione analize dobijena je jednačina zavisnosti log P vrednosti od hromatografski određenog parametra lipofilnosti (log k_w), koja se može koristiti za određivanje lipofilnosti novosintetisanih halkona i srodnih jedinjenja. Lipofilnost jedinjenja okarakterisana je i izračunatim log P vrednostima. Parametri lipofilnosti dobijeni primenom RP-HPLC metode pokazuju slaganje sa izračunatim vrednostima dobijenim primenom programa ChemOffice, što ukazuje na to da je ovaj program pogodan za određivanje log P vrednosti novosintetisanih halkona kao i jedinjenja, strukturno sličnih halkonima.

Zahvalnica

Ovaj rad je deo projekta OI 172041 koji je finansiran od strane Ministarstva prosvete, nauke i tehnološkog razvoja Republike Srbije.

LITERATURA

- [1] J.R. Dimmock, D.W. Elias, M.A. Beazely, N.M. Kandepu, Bioactivities of Chalcones, *Curr. Med. Chem.* **6** (1999) 1125–1149.
- [2] D.I. Batovska, T.I. Todorova, Trends in Utilization of the Pharmacological Potential of Chalcones, *Curr. Clin. Pharmacol.* **5** (2010) 1–29.
- [3] Z. Nowakowska, A review of anti-infective and anti-inflammatory chalcones, *Eur. J. Med. Chem.* **42** (2007) 125–137.
- [4] F.L. Ansari, S. Nazir, H. Noureen, B. Mirza, Combinatorial Synthesis and Antibacterial Evaluation of an Indexed Chalcone Library, *Chem. Biodivers.* **2** (2005) 1656–1663.
- [5] D.D. Bozic, M.T. Milenkovic, B.M. Ivkovic, I. Cirkovic, Newly-synthesized chalcones-inhibition of adherence and biofilm formation of methicillin-resistant *Staphylococcus aureus*, *Braz. J. Microb.* **45** (2014) 263–270.
- [6] B. Ivkovic, B.K. Nikolic, B. Ilic, Ž. Žižak, R. Novaković, O. Čudina, S. Vladimirov, Phenylpropiofenone derivatives as potential anticancer agents: Synthesis, biological evaluation and quantitative structure-activity relationship study, *Eur. J. Med. Chem.* **63** (2013) 239–255.
- [7] O. Sabzevari, Galati, M.Y. Moridani, A. Siraki, P.J. O'Brien, Molecular cytotoxic mechanisms of anticancer hydroxychalcones, *Chem-Bio. Interac.* **148** (2004) 57–67.
- [8] Y.M. Lin, Y. Zhoua, M.T. Flavina, L.M. Zhoua, W. Niea, F.C. Chen, Chalcones and Flavonoids as Anti-Tuberculosis Agents, *Bioorgan. Med. Chem.* **10** (2002) 2795–2802.
- [9] P.M. Sivakumar, S. Priya, M. Doble, Synthesis, Biological Evaluation, Mechanism of Action and Quantitative Structure–Activity Relationship Studies of Chalcones as Antibacterial Agents, *Chem. Biol. Drug. Des.* **73** (2009) 403–415.
- [10] P. Boeck, P.C. Leal, R.A. Yunes, V.C. Fiiho, S. Lopez, M. Sortino, A. Escalante, R.L.E. Furlan, S. Zacchino, Antifungal activity and studies on mode of action of novel xanthoxylone-derived chalcones, *Arch Pharm (Weinheim)* **338** (2005) 87–95.
- [11] J. Basic, M. Kalinic, B. Ivkovic, S. Eric, M. Milenkovic, S. Vladimirov, Z. Vujic, Synthesis, QSAR analysis and mechanism of antibacterial activity of simple 2-hydroxy chalcones, *Dig. J. Nanomater. Bios.* **9** (2014) 1537–1546.
- [12] K.L. Lahtchev, D.I. Batovska, S.P. Parushev, V.M. Ubiyovkov, A.A. Sibirny, Antifungal activity of chalcones: A mechanistic study using various yeast strains, *Eur. J. Med. Chem.* **43** (2008) 2220–2228.
- [13] D.N. Brooke, A.J. Dobbs, N. Williams, Octanol–Water Partition Coefficients (P)-Measurement, Estimation, and Interpretation, Particularly for Chemicals with P -Greater Than-10 (5), *Ecotoxicol. Environ. Safety* **11** (1986) 251–260.
- [14] S.K. Poole, C.F. Poole, Separation methods for estimating octanol–water partition coefficients, *J. Chromatogr., B* **797** (2003) 3–19.
- [15] P. Sciler, Simultaneous determination of partition coefficient and acidity constant of a substance, *Eur. J. Med. Chem.* **9** (1974) 663–665.
- [16] X. Liu, H. Tanaka, A. Yamauchi, B. Testa, H. Chuman, Determination of lipophilicity by reversed-phase high-performance liquid chromatography: Influence of 1-octanol in the mobile phase, *J. Chromatogr., A* **1091** (2005) 51–59.
- [17] T. Baczek, M. Markuszewski, R. Kalisz, M.A. Van Straten, H.A. Claessens, Linear and Quadratic Relationships between Retention and Organic Modifier Content in Eluent in Reversed Phase High-Performance Liquid Chromatography: A Systematic Comparative Statistical Study, *J. High Resol. Chromatogr.* **23** (2000) 667–676.
- [18] Clinical and Laboratory Standards Institute (CLSI): Performance standards for antimicrobial susceptibility testing 15th informational supplement. CLSI document M100-S15, Wayne, PA, USA, 2005.
- [19] ChemOffice Ultra 7.0, <http://www.cambridgesoft.com/>, (date accessed: 15.02.2015.)
- [20] ALOGPS2.1, <http://www.vclab.org> (date accessed: 15.02.2015.)
- [21] M. Liu, P. Wilairat, M.L. Go, Antimalarial alkoxyated and hydroxylated chalcones: structure activity relationship analysis, *J. Med. Chem.* **44** (2001) 4443–4452.
- [22] X. Wu, E.R.T. Tiekink, I. Kostetski, N. Kocherginsky, A.L.C. Tan, S.B. Khoo, P. Wilairat, M.L. Go, Anti-

- plasmodial activity of ferrocenyl chalcones: Investigations into the role of ferrocene, *Eur. J. Pharm. Sci.* **27** (2006) 175–187.
- [23] H. Lamparczyk, M. Atomura, K. Jinno, Qualitative description of dispersive and inductive electrostatic interactions in reversed-phase liquid chromatography, *Chromatographia* **23** (1987) 752–759.
- [24] A. Leo, C. Hanch, D. Elkins, Partition coefficients and their uses, *Chem. Rev.* **71** (1971) 525–616.
- [25] Substituent constants, <http://www.wiredchemist.com/chemistry/data> (date accessed: 23.02.2015.)
- [26] F. Leroux, Atropisomerism, biphenyls, and fluorine: A comparison of rotational barriers and twist angles, *Chembio. Chem.* **5** (2004) 644–649.
- [27] B.E. Smart, Fluorine substituent effects (on bioactivity). *J. Fluorine Chem.* **109** (2001) 3–11.
- [28] D. Dabić, M. Natić, Z. Džambaski, M. Stojanović, R. Marković, D. Milojković-Opsenica, Ž. Tešić, Estimation of lipophilicity of *N*-substituted 2-alkylidene-4-oxothiazolidines by means of reversed-phase thin-layer chromatography, *J. Liq. Chrom. Relat. Tech.* **34** (2011) 791–804.
- [29] J. Veličković, Ž. Tešić, D. Milojković-Opsenica, Evaluation of the lipophilicity of some 1-arylpiperazines by planar chromatography, *J. Planar. Chromatogr.* **17** (2004) 323–327.

SUMMARY

DETERMINATION OF THE LIPOFILICITY OF 2'-HYDROXYCHALCONES BY RP-HPLC METHOD

Jasmina V. Bašić¹, Branka M. Ivković², Slavica Stevanović³, Anđelka Lazarević¹, Zorica B. Vujić²

¹Highly-Health School of Professional Studies in Belgrade, Zemun, Serbia

²Department of Pharmaceutical Chemistry, Faculty of Pharmacy, University of Belgrade, Belgrade, Serbia

³Department of Analytical Chemistry and Quality Control, Faculty of Technology and Metallurgy, University of Belgrade, Belgrade, Serbia

(Scientific paper)

Lipophilicity of twelve synthesized chalcones, whose ring B is a ortho, meta or para monosubstituted with alkyl, oxyalkyl groups or halogens was determined by reverse phase liquid chromatography, using octadecyl-functionalized (RP-18) silica gel as a stationary phase and two-component mixture of methanol/water as a mobile phase. Linear dependence of $\log k'$ values of the volume fraction of methanol in the mobile phase was determined for all analyzed compounds, with high coefficient of correlation ($r > 0.99$). Extrapolation of the line to 0% methanol concentration resulted in the capacity factor of chromatographic system where water is the mobile phase ($\log k_w$). For five standard substances, chemically similar to chalcones, $\log k_w$ values were determined under experimental conditions and they were correlated with $\log P$ values of those compounds available in the literature. $\log P_{\text{EXP}}$ values of synthesized chalcones were calculated on the basis of the created standard curve. In order to estimate the relevance of the experimentally obtained $\log P$ values for chalcones, correlation of $\log P_{\text{EXP}}$ values with the $\log P$ values obtained through various computational procedures was performed using linear regression analysis. Statistical parameters of dependence showed that the best matching of the results had been achieved with ChemOffice program, suggesting that this program is suitable for calculating $\log P$ values of newly-synthesized chalcones, as well as of compounds structurally similar to chalcones.

Keywords: Chalcones • Lipophilicity • HPLC

Adsorpcija aflatoksina B₁ na prirodnim alumosilikatima – koncentratu montmorilonita i zeolitu

Marija A. Marković¹, Aleksandra S. Daković¹, George E. Rottinghaus², Mirjana D. Stojanović¹, Vera T. Dondur³, Milan M. Kragović¹, Zvonko P. Gulišija¹

¹Institut za tehnologiju nuklearnih i drugih mineralnih sirovina, Beograd, Srbija

²Veterinary Medical Diagnostic Laboratory, College of Veterinary Medicine, University of Missouri, Columbia, MO, USA

³Fakultet za fizičku hemiju, Univezitet u Beogradu, Beograd, Srbija

Izvod

Adsorpcija aflatoksina B₁ je ispitivana na koncentratu bentonita (montmorilonit) i prirodnom zeolitu – klinoptilolitu, pri polaznoj koncentraciji toksina 4 ppm, pri različitim količinama čvrste faze u suspenziji (1, 0,5, 0,22 i 0,1 g/L) i na različitim pH vrednostima (3, 7 i 9). Rezultati su pokazali da, smanjenje sadržaja čvrste faze u suspenziji dovodi do smanjenja broja aktivnih centara odgovornih za adsorpciju aflatoksina B₁, pa i do izraženijih razlika u adsorpciji ovog toksina na mineralima. Tako, na koncentratu montmorilonita, pri najnižem sadržaju čvrste faze u suspenziji od 0,1 g/L, indeks adsorpcije aflatoksina B₁ iznosi 97% na pH 3, 88% na pH 7 i 82% na pH 9, dok kod prirodnog zeolita adsorpcija aflatoksina B₁ iznosi 9% na pH 3 i 7% na pH 7 i 9. Rezultati prikazani u ovom radu su samo potvrdili činjenicu da upravo razlike u strukturama minerala uslovljavaju različitu efikasnost adsorpcije aflatoksina B₁.

Ključne reči: mikotoksini, aflatoksin B₁, adsorpcija, klinoptilolit, montmorilonit.

Dostupno na Internetu sa adrese časopisa: <http://www.ache.org.rs/HI/>

Mikotoksini su sekundarni metaboliti pojedinih vrsta plesni i obično se nalaze na zrnastim hranivima. U organizam životinja dospavaju putem kontaminirane hrane. Oboljenja koja izazivaju mikotoksini nisu kontagiozna, vezana su za hranu i/ili specifična hraniva i ne leče se antibioticima i drugim lekovima [1,2]. Konzumiranje kontaminirane hrane sa niskim sadržajem mikotoksina tokom dužeg vremenskog perioda ima sličan efekat kao i korišćenje hrane sa povećanim sadržajem mikotoksina kraće vreme. Mikotoksini, najčešće prisutni u stočnoj hrani su: aflatoksini, ohratoksini, zearalenon, trihoteceni i fumonizini. Aflatoksinima je ranijih godina uglavnom bila zaražena ljudska i stočna hrana u tropskim i subtropskim područjima. Međutim, poslednjih godina situacija se značajno menja, pa se ovi toksini sve češće nalaze u hrani i hranivima u zemljama Evrope, pa i u Srbiji [3–5].

Aflatoksini su sekundarni metaboliti plesni *Aspergillus flavus* i *Aspergillus parasiticus* [6]. Pogodni substrati na kojima se obično nalaze aflatoksini su kukuruz, pšenica, grašak, suncokret, soja, kikiriki i dr. Nastanku aflatoksina pogoduje relativna vlažnost sredine preko 85%, kao i sadržaj vlage u podlozi od 30%. Optimalna temperatura za proizvodnju aflatoksina je 30–35 °C, dok se pri temperaturama nižim od 13 °C i višim od 42 °C toksini ne stvaraju [7].

Prepiska: A. Daković, Institut za tehnologiju nuklearnih i drugih mineralnih sirovina, Franše đ' Eperea 86, 11000 Beograd, Srbija.

E-pošta: a.dakovic@itnms.ac.rs

Rad primljen: 15. maj, 2015

Rad prihvaćen: 14. oktobar, 2015

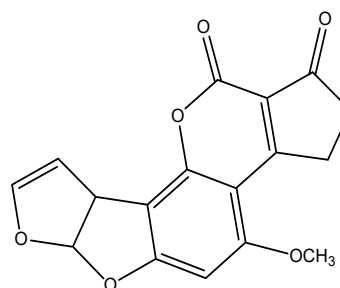
NAUČNI RAD

UDK 66.081.3:582.28:549.67

Hem. Ind. 70 (5) 519–524 (2016)

doi: 10.2298/HEMIND150515058M

Po strukturi aflatoksini su grupa srodnih jedinjenja difurano kumarinskog tipa. Aflatoksini B serije sadrže β-keto laktonske, a aflatoksini G serije, α-bis laktonske funkcionalne grupe. Dobili su naziv prema boji kojom fluoresciraju pod dejstvom UV svetlosti; plava fluorescentna svetlost (blue), odnosno zelena fluorescentna svetlost (green) [8,9]. Od svih do sada poznatih aflatoksina, u pogledu zastupljenosti i toksičnosti, je najvažniji aflatoksin B₁. Toksičnost aflatoksina opada u sledećem nizu: B₁>G₁>B₂>G₂. Strukturna formula molekula aflatoksina B₁ ((6aR,9aS)-2,3,6a,9a-tetrahidro-4-metoksi-1H,11H-cyclopenta[c]furo[3',2':4,5]furo[2,3-h][1]benzopiran-1,11-dion) prikazana je na slici 1.



Slika 1. Strukturna formula aflatoksina B₁.
Figure 1. Structural formulae of aflatoxin B₁.

Aflatoksin B₁ je otkriven pedesetih godina prošlog veka kao izazivač masovnog uginuća ćuraka u Velikoj Britaniji koje su konzumirale kikirikijevu sačmu kontaminiranu ovim toksinom [10]. Od tada, pa do danas ne prestaje interesovanje za ispitivanje uticaja aflatoksina

B₁ na ljude i životinje, tim pre što je aflatoksin prema klasifikaciji Američkog nacionalnog instituta za ispitivanje karcinoma (NRC) svrstan u grupu 1B u koju spadaju dokazani kancerogeni [8,9].

Danas je sasvim sigurno da je i hrana ljudi kontaminirana mikotoksinima, pa odatle i rizik za zdravlje ljudi. Mikotoksikoze se dovode u vezu sa mnogim bolestima: karcinom jetre i aflatoksin B₁, endemska nefropatija i ohratoksin A, karcinom uterusa i zearalenon, itd. [11].

Problem uklanjanja mikotoksina je veoma aktuelan kada je u pitanju ljudska hrana i zdravlje. Dugi niz godina, najekonomičniji pristup u sprečavanju dejstva mikotoksina, odnosno detoksikaciji hrane zagađene mikotoksinima, je baziran na osvajanju novih efikasnih mineralnih adsorbentata koji se dodaju kao aditivi stočnoj hrani u određenoj koncentraciji. Njihova uloga je da adsorbuju mikotoksine u digestivnom traktu životinja i na taj način smanje njihovu biodostupnost, a samim tim i njihovu toksičnost.

Najčešće korišćeni mineralni adsorbenti su prirodni aluminosilikati: prirodni zeoliti (klinoptilolit, mordenit, itd.) i prirodni bentonit (montmorilonit) [12,13]. Zbog razlika u strukturi, različiti minerali imaju različitu efikasnost adsorpcije aflatoksina B₁. Od bentonitskih gline, najčešće korišćen mineralni adsorbent, koji se pokazao efikasan, u *in vitro* i *in vivo* uslovima, za adsorpciju aflatoksina B₁, je hidratisan natrijum-kalcijum-alumosilikat (hydrated sodium-calcium aluminosilicate – HSCAS – NovaSil™). Bentonitske gline su prirodne mineralne sirovine često mogu da sadrže nepoželjne prateće minerale, često su promenljivog hemijskog i mineraloškog sastava i osobina. To znači da gline različitog kvaliteta mogu da imaju različit afinitet prema aflatoksinu B₁. Na primer, analizom velikog broja (39) komercijalnih proizvoda aditiva stočnoj hrani iz SAD i Meksika, ustanovljeno je kod dvadeset proizvoda dominantno prisustvo smektitskih gline. Određene su značajne razlike u kvalitetu ovih sirovina, a posredno i značajne razlike u kapacitetu adsorpcije aflatoksina B₁ (i do deset puta). Ispitivanje adsorpcije aflatoksina B₁ na dvadeset smektitskih gline je pokazalo da samo tri proizvoda imaju visok kapacitet adsorpcije kao – NovaSil™ [14]. Takođe, u radovima u kojima je opisana adsorpcija aflatoksina B₁ na prirodnim zeolitima [15,16], veoma često nema dovoljno podataka o vrsti prirodnog zeolita sa kojim su rađena ispitivanja, kao i o njegovom mineraloškom sastavu. Prirodni zeoliti, kao prirodne nemetalične sirovine su veoma često promenljivog mineraloškog i hemijskog sastava.

Da bi se obezbedila visoka efikasnost adsorpcije aflatoksina B₁, jedan od uslova je i visok sadržaj osnovnog minerala u proizvodu, pa je u ovim ispitivanjima iz bentonitske gline izdvojen koncentrat montmorilonita i određena je efikasnost adsorpcije aflatoksina B₁. Rezul-

tati su upoređeni da rezultatima adsorpcije aflatoksina B₁ na prirodnom zeolitu, kod kojeg je dominantan mineral klinoptilolit.

EKSPERIMENTALNI DEO

Kao polazni materijal u eksperimentima adsorpcije aflatoksina B₁ korišćeni su bentonitska glina (ležište Šipovo, Republika Srpska), čiji je osnovni mineral montmorilonit (oko 90%), dok su prateće komponente kvarc i kalcit [17], kao i prirodni zeolit (ležište Zlatokop iz okoline Vranjske banje), čiji je osnovni mineral klinoptilolit (oko 70%), a kao nečistoće su prisutni kvarc i feldspat [18]. Iz rovne sirovine – bentonita, koncentracijom na centrifugi, izdvojen je koncentrat montmorilonita (klasa < 10 μm), dok je kod prirodnog zeolita višestepenim usitnjavanjem i klasiranjem polaznog materijala izdvojena klasa < 63 μm.

Ukupan sadržaj izmenljivih katjona, kako u koncentratu montmorilonita, tako i u prirodnom zeolitu je određen metodom sa 1 M NH₄Cl. Određena količina uzorka (1 g) se ostavi da stoji 24 h u 100 ml rastvora amonijum-hlorida, na pH 7, uz povremeno mućkanje. Posle toga rastvori se centrifugiraju i u filtratima su određeni sadržaji izmenljivih neorganskih katjona (Ca²⁺ i Mg²⁺, Na⁺ i K⁺) na atomskom apsorpcionog spektrofotometru Analytic Jena Spekol 1300.

U eksperimentima adsorpcije je korišćen aflatoksin B₁, analitičke čistoće (proizvođač Sigma–Aldrich). Aflatoksin B₁ je najpre rastvoren u acetonitrilu tako da je dobijen osnovni rastvor koncentracije 1000 ppm. Zatim su iz osnovnog rastvora pripremljeni radni rastvori u odgovarajućem elektrolitu (0.1 M K₂HPO₄; pH elektrolita je podešavan sa HNO₃ ili KOH) koji su korišćeni u eksperimentima adsorpcije.

Preliminarni eksperimenti adsorpcije aflatoksina B₁ su izvođeni tako što je u 10 mL elektrolita koji sadrži tačno određenu koncentraciju toksina (2 ppm), dodavano 100 mg svakog mineralnog adsorbenta. Naredni eksperimenti adsorpcije aflatoksina B₁ na adsorbentima su rađeni tako što su menjane količine čvrste faze u suspenzijama (1, 0,5, 0,2 i 0,1 g/L) na tri različite pH vrednosti rastvora 3, 7 i 9, pri koncentraciji aflatoksina B₁ u rastvoru od 4 ppm. Istovremeno je, za određivanje polazne količine toksina (C₀) pripremana i nulta proba, koja sadrži tačno određenu količinu toksina u elektrolitu bez adsorbenta. Suspenzije su mešane na magnetnoj mešalici određeno vreme (30 min) [12,19] na sobnoj temperaturi. Nakon isteka reakcionog vremena, suspenzije su centrifugirane i u filtratima su određivane koncentracije neadsorbovanog aflatoksina B₁ (C). Polazne, kao i neadsorbovane koncentracije toksina su određivane tečnom hromatografijom viskih performansi (HPLC). HPLC analiza je izvođena na Hitachi L-7100 pump sa Hitachi L-7200 autosampler i fluorescentnim detektorom Hitachi L-7480 (λ_{ex} = 365 nm i

$\lambda_{em} = 430$ nm). Brzina protoka mobilne faze (acetoni-tril: voda – 30:70) iznosila je 1 mL/min. Adsorbirana količina toksina je određivana kao razlika između polazne i neadsorbirane koncentracije toksina u rastvoru [12,17].

REZULTATI I DISKUSIJA

Mineraloški i hemijski sastav, kapacitet katjonske izmene, kao i efikasnost adsorpcije aflatoksina B₁ su važni parametri koji određuju da li alumosilikatni minerali mogu da se potencijalno koriste kao aditiv stočnog hrani za adsorpciju mikotoksina [14].

Poznato je da se neorganske forme alumosilikata (klinoptilolit i montmorilonit) najčešće koriste kao adsorbenti aflatoksina B₁, u *in vitro* uslovima. Međutim, zbog razlika u strukturi, očekivano je da ovi minerali imaju različitu efikasnost adsorpcije aflatoksina B₁. Ukratko, prirodni zeoliti su kristalni hidratirani alumosilikati, koji poseduju beskonačnu trodimenzionu strukturu sa kanalima i šupljinama. Sa druge strane, montmorilonit, pripada grupi slojevitih alumosilikata. Montmorilonit i klinoptilolit imaju sposobnost jonske izmene katjona, s tim da su izmenljivi katjoni smešteni kod montmorilonita u međuslojnom prostoru, dok se kod klinoptilolita nalaze u kanalima i šupljinama, kao i na spoljašnjoj površini. Očekivano je i da se adsorpcija aflatoksina kod bentonitskih glina može povećati izdvajanjem koncentrata montmorilonita, odnosno povećanjem sadržaja osnovnog minerala. Dostupnost i količina izmenljivih katjona minerala značajno utiču na indeks adsorpcije različitih mikotoksina.

U uzorcima prirodnog zeolita i koncentrata montmorilonita, metodom sa 1 M NH₄Cl je određena vrsta, kao i sadržaj osnovnih izmenljivih katjona, dok je ukupan kapacitet katjonske izmene uzoraka određen kao suma sadržaja izmenljivih katjona (Σ). Dobijeni rezultati su prikazani u tabeli 1.

Tabela 1. Sadržaj izmenljivih katjona (meq/100 g) u koncentratu montmorilonita i prirodnom zeolitu [14]
Table 1. Content of exchangeable cations (meq/100 g) in concentrate of montmorillonite and the natural zeolite [14]

Materijal	Ca ²⁺	Mg ²⁺	Na ⁺	K ⁺	Σ
Koncentrat montmorilonita	65,0	29,2	1,00	1,40	96,6
Prirodni zeolit	85,0	22,5	23,5	15,5	146,5

Tabela 2. Hemijski sastav (%) koncentrata montmorilonita i prirodnog zeolita [14]
Table 2. Chemical composition (%) of concentrate of montmorillonite and the natural zeolite [14]

Materijal	SiO ₂	Al ₂ O ₃	Fe ₂ O ₃	CaO	MgO	Na ₂ O	K ₂ O	Gubitak žarenjem
Koncentrovani montmorilonit	49,3	25,9	5,76	2,59	1,70	0,04	0,33	13,1
Prirodni zeolit	66,6	13,1	2,30	3,85	0,56	1,27	1,17	11,0

Kao što se iz tabele 1 može videti ukupan kapacitet katjonske izmene (KKI) koncentrata montmorilonita je 96,6 meq/100 g, a kao dominantan jon u izmenjivom položaju je prisutan jon kalcijuma. Ukupan kapacitet katjonske izmene uzorka zeolita iznosi 146,5 meq/100 g, pri čemu je dominantan jon u izmenjivom položaju jon kalcijuma [18], dok su natrijum, kalijum i magnezijum prisutni u znatno manjim količinama.

Kvantitativnom hemijskom analizom određen je hemijski sastav uzoraka koncentrata montmorilonita i prirodnog zeolita, kao i gubitak mase žarenjem do 900 °C, i dobijeni rezultati su dati u tabeli 2.

Da bi se odredilo da li uopšte alumosilikatni minerali pokazuju afinitet prema aflatoksinu B₁, u preliminarnim eksperimentima, adsorpcija toksina je ispitana na koncentratu montmorilonita, kao i na prirodnom zeolitu – klinoptilolitu, i pri sledećim uslovima: polazna koncentracija aflatoksina B₁ – 2 ppm, količina čvrste faze u suspenziji – 100 mg/10 mL, pH 3. Indeks adsorpcije toksina u procentima (%) je izračunat po sledećoj formuli:

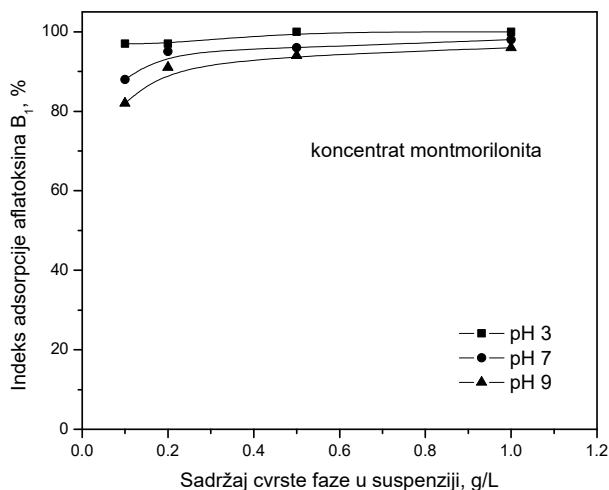
$$\text{Indeks adsorpcije} = 100 \frac{c_0 - c}{c_0} \quad (1)$$

gde je c_0 – polazna koncentracija aflatoksina B₁, a c – ravnotežna koncentracija aflatoksina B₁ u elektrolitu, nakon adsorpcije. Dobijeni rezultati su pokazali da je pri ovim eksperimentalnim uslovima adsorpcija aflatoksina na prirodnom zeolitu, kao i na koncentratu montmorilonita visoka i iznosi 100%.

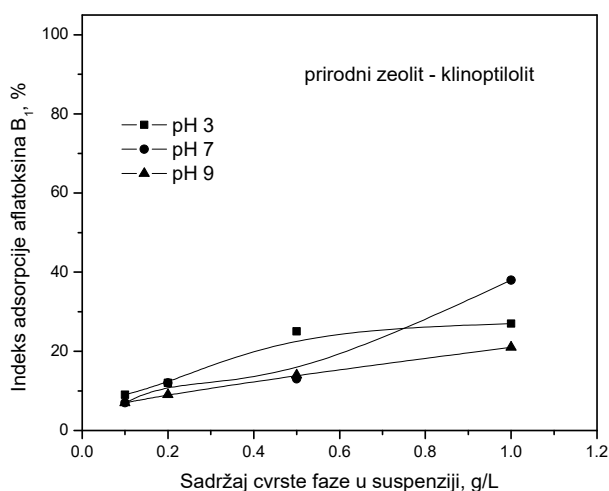
Kod proizvoda koji se nalaze na tržištu, za uklanjanje mikotoksina, kao dokaz visoke adsorpcije mikotoksina, u *in vitro* uslovima, je najčešće prikazan procenat (indeks) adsorpcije (%), tako da je prema deklaraciji, proizvod efikasan ukoliko je indeks adsorpcije 100%. Međutim, kod ovih proizvoda obično nisu definisani uslovi pod kojima je dobijen visok indeks adsorpcije. Na primer, nije definisana početna koncentracija toksina u rastvoru, kao i količina čvrste faze u suspenziji (odnosno odnos toksin:adsorbent) [4], na osnovu kojih bi se procenila efikasnost adsorpcije. Rezultati adsorpcije aflatoksina B₁ na prirodnom zeolitu i koncentratu montmorilonita, pri različitim sadržajima čvrste faze u suspenziji i različitim pH vrednostima, a pri početnoj koncentraciji toksina od 4 ppm, su prikazani na slikama 2 i 3.

Na osnovu dobijenih rezultata prikazanih na slikama 2 i 3 mogu se videti jasne razlike u adsorpciji aflatoksina B₁ na mineralima klinoptilolitu i montmorilonitu. Tako,

pri sadržaju čvrste faze u suspenziji od 1 g/L, adsorpcija aflatoksina B₁ na koncentratu montmorilonita iznosi 100% na pH 3, 98% na pH 7 i 96% na pH 9. Na prirodnom zeolitu, pri istom sadržaju čvrste faze u suspenziji, dobijene su znatno niže vrednosti indeksa adsorpcije aflatoksina B₁: 27% na pH 3, 38% na pH 7 i 21% na pH 9.



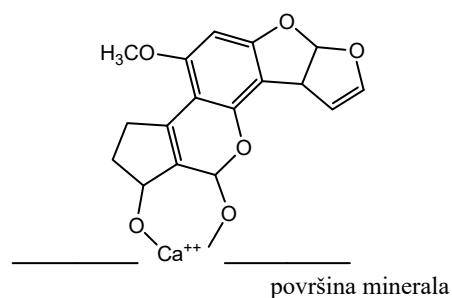
Slika 1. Strukturna formula aflatoksina B₁.
Figure 1. Structural formulae of aflatoxin B₁.



Slika 3. Adsorpcija aflatoksina B₁ na prirodnom zeolitu – klinoptilolitu.
Figure 3. Adsorption of aflatoxin B₁ by the natural zeolite – clinoptilolite.

Smanjenje sadržaja čvrste faze u suspenziji dovodi do smanjenja broja aktivnih centara odgovornih za adsorpciju aflatoksina B₁, pa i do izraženijih razlika u adsorpciji ovog toksina na mineralima. Tako, na koncentratu montmorilonita, pri sadržaju čvrste faze u suspenziji 0,1 g/L, indeks adsorpcije aflatoksina B₁ iznosi 97% na pH 3, 88% na pH 7 i 82% na pH 9, dok kod prirodnog zeolita adsorpcija aflatoksina B₁ iznosi 9% na pH 3 i 7% na pH 7 i 9. Iz dobijenih rezultata, prikazanih na slikama 2 i 3, se takođe primećuje i da adsorpcija aflatoksina B₁

na koncentratu montmorilonita praktično ne zavisi od pH sredine, dok se kod prirodnog zeolita uočavaju male razlike u adsorpciji ovog toksina na različitim pH vrednostima. U literaturi je poznato da su za adsorpciju aflatoksina B₁ odgovorni neorganski katjoni u alumosilikatnim mineralima. Predhodno je pomenuto, da najčešće korišćen mineralni adsorbent, koji se pokazao efikasan, u *in vitro* i *in vivo* uslovima, za adsorpciju aflatoksina B₁, je hidratisan natrijum kalcijum alumosilikat (hydrated sodium-calcium aluminosilicate – HSCAS – NovaSil™), koji je u suštini mineral montmorilonit. Phillips i saradnici [20] su prvi predložili mehanizam vezivanja i strukturu mogućeg HSCAS/aflatoxin B₁ helatnog kompleksa (slika 4) na osnovu pretpostavke da metalni joni u HSCAS (na prvom mestu Al³⁺ na ivicama minerala), reaguju sa dikarbonilnim funkcionalnim grupama aflatoksina B₁, obrazujući metalne helate. Dikarbonilni sistem aflatoksina B₁ se sastoji od karbonilnih grupa laktonskog i ciklopentanskog prstena koji može da gradi helatne komplekse sa jonima u mineralima [20,21].



Slika 4. Model kompleksa kation (mineral)/aflatoxin B₁.
Figure 4. Schematic representation of complex cation (mineral)/aflatoxin B₁.

Grant i saradnici [22,23] su ispitivali adsorpciju aflatoksina B₁ na HSCAS i na uzorku, koji je dobijen termičkim tretiranjem HSCAS, označenom kao Col-HSCAS. Col-HSCAS je dobijen zagrevanjem HSCAS na 200 °C 30 min, a zatim je uzorak žaren na 800 °C 1 h. Rezultati su pokazali da rušenjem alumosilikatne strukture dolazi do značajnog smanjenja adsorpcije aflatoksina B₁, što je ukazalo da je interakcija aflatoksina B₁ sa jonima u međuslojnom prostoru montmorilonita, odlučujuća za njegovu adsorpciju na HSCAS. Kannewischer i saradnici [14] su uradili XRD analizu uzorka smektitске gline pre i nakon adsorpcije aflatoksina B₁ i povrdili da se aflatoxin B₁ adsorbuje uglavnom u međuslojnom prostoru minerala montmorilonita.

I pored toga što prirodni zeolit – klinoptilolit poseduje znatno viši KKI, odnosno viši sadržaj neorganskih katjona (na prvom mestu kalcijum) na kojima bi aflatoxin B₁ mogao da se adsorbuje, u odnosu na koncentrat montmorilonita (tabela 2), adsorpcija aflatoksina B₁ na klinoptilolitu je značajno niža. Dobijeni rezultati

potvrđuju rezultate Lemke i saradnika [4] i Marroquin-Cardona i saradnika [24] koji su takođe zapazili znatno nižu adsorpciju aflatoksina B₁ na klinoptilolitu u odnosu na glinu iz grupe smektita – montmorilonit. Na osnovu struktura minerala klinoptilolita i montmorilonita, kao i dimenzija samog molekula aflatoksina B₁, [20] u slučaju prirodnog zeolita očigledno je da aflatoksin B₁ može da se adsorbuje samo na spoljašnjim površinama minerala dok su neorganski katjoni u kanalima nedostupni za adsorpciju. Sa druge strane, u slučaju minerala montmorilonita svi aktivni centri – neorganski katjoni u međuslojnom prostoru su jednako dostupni za adsorpciju ovog toksina, zbog čega ovaj mineral poseduje znatno viši afinitet prema aflatoksinu B₁. Takođe, mineraloška analiza, određivanje hemijskog sastava, kao i kapaciteta katjonske izmene su važni parametri koji definišu kvalitet minerala, pa pre eventualne primene proizvoda kao aditiva stočnoj hrani, neophodno je ispitati njegov kvalitet, odnosno odrediti sadržaj osnovnog minerala i ispitati adsorpciju aflatoksina B₁ u *in vitro* uslovima.

ZAKLJUČAK

U radu su prikazani rezultati adsorpcije aflatoksina B₁ na bentonitskoj glini iz koje je izdvojen koncentrat montmorilonita i prirodnom zeolitu kod kojeg je dominantan mineral klinoptilolit. Rezultati su pokazali da sa smanjenjem sadržaja čvrste faze u suspenziji, razlike u adsorpciji aflatoksina B₁ na ovim mineralima postaju sve izraženije, i da mineral montmorilonit pokazuje značajno višu efikasnost adsorpcije aflatoksina B₁. Adsorpcija aflatoksina B₁ na koncentratu montmorilonita, praktično ne zavisi od pH sredine, dok se kod prirodnog zeolita uočavaju manje razlike u adsorpciji na različitim pH vrednostima. Potvrđeno je da se adsorpcija aflatoksina B₁ na prirodnom zeolitu dešava samo na spoljašnjoj površini minerala, dok su kod koncentrata montmorilonita neorganski katjoni u međuslojnom prostoru odgovorni za adsorpciju, zbog čega koncentrat montmorilonita pokazuje značajno viši afinitet prema aflatoksinu B₁. Za eventualnu primenu alumosilikatnih minerala kao aditiva stočnoj hrani za adsorpciju aflatoksina B₁, neophodno je ispitati kvalitet minerala, odnosno odrediti mineraloški i hemijski sastav (sadržaj osnovnog minerala), kapacitet katjonske izmene, kao i odrediti afinitet minerala prema aflatoksinu B₁.

Zahvalnica

Rad je rezultat istraživanja na projektima 451-03-2802-IP Tip1/142, 172018 i 34013, koji se finansiraju sredstvima Ministarstva prosvete, nauke i tehnološkog razvoja Republike Srbije. Eksperimenti adsorpcije aflatoksina B₁ su urađeni u Veterinary Medical Diagnostic Laboratory, University of Missouri, Columbia, USA.

LITERATURA

- [1] S. Döll, S. Dänicke, The Fusarium toxins deoxynivalenol (DON) and zearalenone (ZON) in animal feeding, *Prev. Vet. Med.* **102** (2011) 132–145.
- [2] E.M. Binder, Managing the risk of mycotoxins in modern feed production, *Anim. Feed Sci. Tech.* **133** (2007) 149–166.
- [3] A.C. Pappas, E. Tsiplakou, M. Georgiadou, C. Anagnostopoulos, A.N. Markoglou, K. Liapis, G. Zervas, Bentonite binders in the presence of mycotoxins: Results of *in vitro* preliminary tests and an *in vivo* broiler trial, *Appl. Clay Sci.* **99** (2014) 48–53.
- [4] [4] S.L. Lemke, S.E. Ottinger, K. Mayura, C.L. Ake, K. Pimpkdee, N. Wang, T.D. Phillips, Development of a multi-tiered approach to the *in vitro* prescreening of clay-based enterosorbents, *Anim. Feed Sci. Tech.* **93** (2001) 17–29.
- [5] M. Miraglia, H.J.P. Marvin, G.A. Kleter, P. Battilani, C. Brera, E. Coni, F. Cubadda, L. Croci, B. De Santis, S. Dekkers, L. Filippi, R.W.A. Hutjes, M.Y. Noordam, M. Pisante, G. Piva, A. Prandini, L. Toti, G.J. van den Born, A. Vespermann, Climate change and food safety: An emerging issue with special focus on Europe, *Food Chem. Toxicol.* **47** (2009) 1009–1021.
- [6] Y.H. Shi, Z.R. Xu, J.L. Feng, C.Z. Wang, Efficacy of modified montmorillonite nanocomposite to reduce the toxicity of aflatoxin in broiler chicks, *Anim. Feed Sci. Tech.* **129** (2006) 138–148.
- [7] J.F. Robens, J.L. Richard, Aflatoxins in animal and human health, *Rev. Environ. Contam. Toxicol.* **127** (1992) 69–94.
- [8] IARC Monographs On Evaluation Of Carcinogenic Risks To Humans, Vol. 56, Some naturally occurring substances: Food items and constituents, heterocyclic aromatic amines and mycotoxins, IARC, Lyon, 1993.
- [9] S. Rawal, J.E. Kim, R. Coulombe Jr., Aflatoxin B₁ in poultry: Toxicology, metabolism and prevention, *Res. Vet. Sci.* **89** (2010) 325–311.
- [10] M.G. Tenorio Arvide, I. Mulder, A.L. Barrientos Velazquez, J.B. Dixon, Smectite clay adsorption of aflatoxin vs. octahedral composition as indicated by FTIR, *Clays Clay Miner.* **56** (2008) 571–578.
- [11] M.E. Zain, Impact of mycotoxins on humans and animals, *J. Saudi Chem. Soc.* **15** (2011) 129–144.
- [12] A. Daković, M. Tomašević-Čanović, V. Dondur, G.E. Rottinghaus, V. Medaković, S. Zarić, Adsorption of mycotoxins by organozeolites, *Colloids Surfaces, B* **46** (2005) 20–25.
- [13] Y. Deng, M. Szczerba, Computational evaluation of bonding between aflatoxin B₁ and smectite, *Appl. Clay Sci.* **54** (2011) 26–33.
- [14] I. Kannewischer, M.G. Tenorio Arvide, G.N. White, J.B. Dixon, Smectite clays as adsorbents of aflatoxin B₁: Initial steps, [https://soilcrop.tamu.edu/personnel/dixon/Kannewischer et al 2006.pdf](https://soilcrop.tamu.edu/personnel/dixon/Kannewischer%20et%20al%202006.pdf) (2006).
- [15] N.Q. Thieu, H. Pettersson, *In vitro* evaluation of the capacity of zeolite and bentonite to adsorb aflatoxin B₁ in simulated gastrointestinal fluids, *Mycotoxin Res.* **24** (2008), 124–129.

- [16] M. Nuryono, A. Agus, S. Wedhastri, Y.M.S. Maryudhani, D. Pranowo, Yunianto, E. Razzazi-Fazeli, Adsorption of aflatoxin B₁ in corn on natural zeolite and bentonite, *Indo. J. Chem.* **12** (2012) 279–286.
- [17] A. Daković, S. Matijašević, G.E. Rottinghaus, D.R. Ledoux, P. Butkeraitis, Ž. Sekulić, Aflatoxin B₁ adsorption by natural and copper modified montmorillonite, *Colloids Surfaces, B* **66** (2008) 20–25.
- [18] M. Kragović, A. Daković, Ž. Sekulić, M. Trgo, M. Ugrina, J. Perić, G. D. Gatta, Removal of lead from aqueous solutions by using the natural and Fe(III)-modified zeolite, *Appl. Surface Sci.* **258** (2012) 3667–3673.
- [19] D.R. Ledoux, G.E. Rottinghaus, *In vitro* and *in vivo* testing of adsorbents for detoxifying mycotoxins in contaminated feedstuffs, in: *Biotechnology in the Feed Industry, Proceedings of Alltech's 15th Annual Symposium* Nottingham University Press, 1999, pp. 369–379.
- [20] T.D. Phillips, B.A. Sarr, P.G. Grant, Selective chemisorption and detoxification of aflatoxins by phyllosilicate clay, *Nat. Toxins* **3** (1995) 204–213.
- [21] Y. Deng, A.L. Barrientos Velázquez, F. Billes, J.B. Dixon, Bonding mechanisms between aflatoxin B₁ and smectite, *Appl. Clay Sci.* **50** (2010) 92–98.
- [22] P.G. Grant, T.D. Phillips, Isothermal adsorption of aflatoxin B₁ on HSCAS clay, *J. Agric. Food Chem.* **46** (1998) 599–605.
- [23] P.G. Grant, S.L. Lemke, M.R. Dwyer, T.D. Phillips, Modified Langmuir equation for S-shaped and multiseite isotherm plots, *Langmuir* **14** (1998) 4292–4299.
- [24] A. Marroquin-Cardona, Y. Deng, J.F. Taylor, C.T. Hallmark, N.M. Johnson, T.D. Phillips, *In vitro* and *in vivo* characterization of mycotoxin-binding additives used for animal feeds in Mexico, *Feed Addit. Contam.* **26** (2009) 733–743.

SUMMARY

AFLATOXIN B₁ ADSORPTION BY THE NATURAL ALUMINOSILICATES – CONCENTRATE OF MONTMORILLONITE AND ZEOLITE

Marija A. Marković¹, Aleksandra S. Daković¹, George E. Rottinghaus², Mirjana D. Stojanović¹, Vera T. Dondur³, Milan M. Kragović¹, Zvonko P. Gulišija¹

¹*Institute for Technology of Nuclear and Other Mineral Raw Materials, Franjevačka 86, 11000 Belgrade, Serbia*

²*Veterinary Medical Diagnostic Laboratory, College of Veterinary Medicine, University of Missouri, Columbia, MO 65211, USA*

³*University of Belgrade, Faculty of Physical Chemistry, Studentski trg 12-16, 11000 Belgrade, Serbia*

(Scientific paper)

Aflatoxin B₁ adsorption by the concentrate of bentonite clay – montmorillonite and the natural zeolite – clinoptilolite and was investigated at the initial toxin concentration of 4 ppm, with different amounts of solid phase in suspension (1, 0.5, 0.2 and 0.1 g/L) and different pH values – 3, 7 and 9. Results indicated that for both minerals, decreasing the amount of solid phase in suspension, decrease the amount of active sites relevant for adsorption of aflatoxin B₁. Thus, for concentrate of montmorillonite, at the lowest level of solid phase in suspension (0.1 g/L), aflatoxin B₁ adsorption indexes were 97% at pH 3, 88% at pH 7 and 82% at pH 9, while for the natural zeolite, adsorption of toxin was 9% at pH 3 and 7% at pH 7 and 9. Since inorganic cations in minerals are mainly responsible for aflatoxin B₁ adsorption, even the natural zeolite – clinoptilolite has much higher cation exchange capacity (the content of inorganic exchangeable cations) compared to the concentrate of montmorillonite, adsorption of aflatoxin B₁ by this mineral is much lower. Comparing the molecular dimensions of aflatoxin B₁ molecule with the dimension of channels of clinoptilolite and interlamellar space of montmorillonite it is obvious that this toxin is adsorbed only at the external surface of clinoptilolite while in the montmorillonite all active sites are equally available for its adsorption. Thus, the concentrate of montmorillonite possesses higher adsorption capacity for aflatoxin B₁. Results presented in this paper confirmed the fact that the differences in the structure of minerals led to their different efficiency for adsorption of aflatoxin B₁. Mineralogical and chemical composition, determination of cation exchange capacity, etc., are very important parameters influencing the effectiveness of minerals as aflatoxin B₁ adsorbents.

Keywords: Mycotoxins • Aflatoxin B₁ • Adsorption • Clinoptilolite • Montmorillonite

Primena dizajna smeše u formulaciji i karakterizaciji čvrstih samo-nanoemulgujućih terapijskih sistema sa karbamazepinom

Marko Z. Krstić, Svetlana R. Ibrić

Univerzitet u Beogradu – Farmaceutski fakultet, Katedra za farmaceutsku tehnologiju i kozmetologiju, Beograd, Srbija

Izvod

U radu je prikazana priprema i karakterizacija formulacija čvrstih samo-nanoemulgujućih terapijskih sistema sa slabo rastvorljivom, visokodoziranom lekovitom supstancom, karbamazepinom. U prvoj fazi je primenom dizajna smeše odabran tečni samo-nanoemulgujući terapijski sistem (SNEDDS) koji se sastojao iz triglicerida srednje dužine lanca, Polisorbata 80, Labrasol®-a i Transcutol®-a HP. Odabran tečni SNEDDS je adsorbovan na 4 porozna nosača: Neusilin® UFL2, Neusilin® FL2, Sylsya® 320 i dijatomit. Udeo karbamazepina je bio stalan (20%), a manji je odnos adsorpcioni nosač:SNEDDS, 1:1 i 1:2. Iz izrađenih formulacija je ispitana brzina rastvaranja karbamazepina i izvršena je karakterizacija primenom termogravimetrijske analize, diferencijalno skenirajuće kalorimetrije, infracrvene spektroskopije sa Furijeovom transformacijom, difrakcije X-zraka na uzorcima u prahu i skenirajuće elektronske mikroskopije. Dizajn smeše se pokazao kao korisna tehnika za optimizaciju SNEDDS. Formulacijom čvrstih SNEDDS je postignuto značajno povećanje brzine rastvaranja karbamazepina u odnosu na čist karbamazepin i komercijalne tablete karbamazepina sa trenutnim oslobađanjem.

Ključne reči: brzina rastvaranja, dizajn smeše, Polisorbat 80, Transcutol® HP, Labrasol®, Neusilin® UFL2, Neusilin® FL2, Sylsya® 320, dijatomiti, karbamazepin.

Dostupno na Internetu sa adrese časopisa: <http://www.ache.org.rs/HI/>

NAUČNI RAD

UDK 615:615.03:66

Hem. Ind. 70 (5) 525–537 (2016)

doi: 10.2298/HEMIND150623059K

Veliki broj farmakološki aktivnih supstanci koje su već u upotrebi, kao i one čija se potencijalna primena u farmakoterapiji istražuje, ima ograničenu rastvorljivost u vodi, odnosno, biološkim tečnostima. S obzirom na to da većinu karakteriše dobra permeabilnost (klasa II prema biofarmaceutskom sistemu klasifikacije [1]), brzina rastvaranja lekovite supstance predstavlja ograničavajući faktor za njihovu resorpciju i biološku raspoloživost [2]. Jedan od pristupa za prevazilaženje ovog problema jeste primena formulacija čvrstih samo-emulgujućih terapijskih sistema (engl. *solid self-emulsifying drug delivery system* – SSEDSS). SSEDSS imaju niz prednosti u odnosu na tečne samo-emulgujući terapijski sistem (engl. *self-emulsifying drug delivery system* – SEDDS), kao što su poboljšanje i smanjenje varijabilnosti resorpcije lekovite supstance, poboljšanje permeabilnosti, lakša procesna kontrola i niži troškovi proizvodnje i transporta, veća stabilnost proizvoda i bolja prihvatljivost od strane pacijenta [3,4]. Tehnika prevođenja tečnih SEDDS u čvrste koja se poslednjih godina u velikoj meri koristi jeste adsorpcija na hidrofobni nosač. Ovakvom formulacijom SSEDSS se postiže povećanje brzine rastvaranja i potencijalno biološke raspoloživosti, usled solubilizacije lekovite supstance od strane

komponenti SEDDS i boljeg kvašenja usled velike specifične površine poroznih adsorpcionih nosača [5,6]. Kao porozni adsorbensi poslednjih godina se istražuju sintetski i prirodni adsorbensi na bazi magnezijum-aluminometasilikata i slijicijum-dioksida [5–7]. Usled kompleksnosti formulacije SSEDSS i velikog broja pomoćnih supstanci koje ulaze u njen sastav, veliki izazov za istraživače predstavlja formulacija ovih sistema sa visokodoziranom lekovitom supstancama, kako bi dobijeni farmaceutski oblik imao prihvatljivu masu za pacijenta [5]. Tečni SEDDS su izotropna mešavina ulja, surfaktanta i/ili korastvarača/kosurfaktanta koja emulgovanjem, odnosno nakon razblaživanja vodom (u kontaktu sa vodom u gastro-intestinalnom traktu (GIT)) i blagom mešanju pod uticajem motiliteta želuca i tankog creva [8,9] formira finu ulje-u-vodi emulziju. Time solubilizovana lekovita supstanca postaje dostupna za resorpciju. U zavisnosti od sastava formulacije i veličine kapi unutrašnje faze emulzije koja nastaje nakon razblaživanja vodom, samo-emulgujući terapijskog sistemi se dele na: samo-mikroemulgujuće (engl. *self-microemulsifying drug delivery system* – SMEDDS, veličina kapi do 100 nm), samo-nanoemulgujuće (engl. *self-nanoemulsifying drug delivery system* – SNEDDS, veličina kapi od 100 do 300 nm) i samo-emulgujuće (veličina kapi preko 300 nm) (SEDDS) [9–13]. Prilikom odabira tečnog samo-emulgujućeg terapijskog sistema do sada je najčešće korišćena tehnika konstruisanja pseudo-ternernih faznih dijagrama, gde je smeši ulja, surfaktanta i kosurfaktanta dodavana vodena faza u kapima [5]. Ovu metodu

Prepiska: M.Z. Krstić, Univerzitet u Beogradu – Farmaceutski fakultet, Katedra za farmaceutsku tehnologiju i kozmetologiju, Vojvode Stepe 450, Beograd, Srbija.

E-pošta: mkrstic109@gmail.com

Rad primljen: 23. jun, 2015

Rad prihvaćen: 6. oktobar, 2015

karakteriše veliki broj eksperimenata i dugotrajnost, uz vizuelno praćenje promena u sistemu, što sa sobom nosi određeni stepen subjektivnosti. Iz tog razloga, u radu je ispitana mogućnost primene eksperimentalnog dizajna, tipa smeše (engl. *mixture design*), kao alternativa konstruisanju pseudo-ternernih faznih dijagrama, u odabiru tečnog SNEDDS. Dizajn smeše predstavlja vrstu eksperimentalnog dizajna koja se koristi kada se ispituje formulacija koju čine više različitih sastojaka, čiji je zbir udela stalan. Postoje različiti tipovi dizajna smeše, ali D-optimalni eksperimentalni dizajn se najčešće koristi jer se može prilagoditi svakom eksperimentalnom planu. Omogućava da se na osnovu najmanjeg broja eksperimenata pouzdano može doći do određenih zaključaka. D-optimalnim dizajnom (D od determinanta–determinanta matrice koja se koristi za određivanje koeficijenata jednačine tj. modela) moguće je lako i efikasno pronaći najbolji podskup eksperimenata iz seta eksperimenata, na osnovu zadatog kriterijuma, tj. postavljenih ograničenja. Za svaki od ulaznih parametara postavljaju se granične vrednosti (donja i gornja) u okviru kojih se oni mogu varirati, s tim što donja vrednost ne sme biti jednaka nuli [14].

Kao model supstanca, korišćen je karbamazepin, antiepileptik, koji prema Biofarmaceutskom sistemu klasifikacije spada u klasu II. Odlikuje se visokom permeabilnošću i niskom rastvorljivošću u vodi (0,271 mg/mL, 37 °C) koja je uzrok ograničene resorpcije i niske bioraspoloživosti pri oralnoj primeni [15,16]. Kako bi se ispitali uticaji razlike u specifičnoj strukturi i površini adsorpcionih nosača, u radu su korišćeni tri sintetska adsorbensa, na bazi magnezijum-aluminometasilikata (Neusilin® UFL2 i Neusilin® FL2) i slijum-dioksida (Sylsya® 320), i jedan prirodni adsorpcioni nosač (dijatomit).

Cilj ovog rada je formulacija čvrstih samo-nanoemulgujućih terapijskih sistema (SSNEDDS) sa visokim udelom lekovite supstance, karbamazepina, radi povećanja njegove brzine rastvaranja. Dodatni ciljevi su bili da se proceni mogućnost primene dizajna smeše u odabiru tečnog samo-nanoemulgujućeg terapijskog sistema sa odgovarajućim odnosom lipid/surfaktant/kosurfaktant, kao i da se ispita uticaj vrste i udela adsorpcionog nosača na brzinu oslobađanja i promenu polimorfnog oblika karbamazepina.

EKSPERIMENTALNI DEO

Materijal

Korišćena model supstanca karbamazepin (KBZ), odgovara specifikacijama navedenim u monografiji Ph. Eur. 8.0. Trigliceridi srednje dužine lanca, kaprilno-kaprilski trigliceridi (Mygliol® 812, Sasol GmbH, Nemačka) kao masna faza, Polisorbat 80 (Tween® 80, Sigma-Aldrich Chemie GmbH, Nemačka) i PEG-8 kaprilno/kaprin-

ski gliceridi (Labrasol®, Gattefosse Batch, Francuska) kao surfaktanti, a kao kosurfaktant korišćen je dietilenglikolmonooletar (Transcutol® HP, Gattefosse Batch, Francuska). Kao adsorpcioni nosači korišćeni su Neusilin® UFL2 (Fuji Chemical Industry, Japan), Neusilin® FL2 (Fuji Chemical Industry, Japan), Sylsya® 320 (Fuji Sylsya Chemical, Japan) i dijatomit (Mount Sylvania, Pty. Ltd, Australija). Kao referentni preparat ispitivan je registrovani proizvod na teritoriji Republike Srbije tablete karbamazepina sa trenutnim oslobađanjem.

Metode

Odabir tečnog samo-nanoemulgujućeg terapijskog sistema primenom dizajna smeše

Formulacija tečnog samo-nanoemulgujućeg terapijskog sistema. Primenom optimizacione tehnike, dizajna smeše, uz pomoć kompjuterskog programa *Design Expert®* (version 8.0.7.1, Stat-Ease, Inc, Minneapolis, MN, USA), definisan je D-optimalni eksperimentalni dizajn smeše koju čine tri komponente, sastojci SEDDS: lipidna faza (A – kaprilno-kaprilski trigliceridi), surfaktant (B – smeša Polisorbat 80 i Labrasol® u odnosu 1:1) i kosurfaktant (C – Transcutol® HP). Ove tri komponente predstavljaju ulazne parametre i njihov ukupan zbir udela je 100%. Granične vrednosti (opsezi) udela ovih komponenti postavljene su na osnovu literaturnih podataka i prethodnih *screening* studija i bile su sledeće: $10\% \leq A \leq 30\%$, $40\% \leq B \leq 60\%$ i $30\% \leq C \leq 50\%$.

Primenom D-optimalnog eksperimentalnog dizajna dobijen je eksperimentalni plan (prikazan u delu Rezultati i diskusija – tabela 2) koji se sastojao od 16 formulacija SEDDS.

Merenje veličine kapi i indeksa polidisperziteta primenom fotonske korelacione spektroskopije

Nakon razblaživanja svih izrađenih SEDDS sa visoko prečišćenom vodom u odnosu SEDDS:voda 10:90 i mešanja na vorteksu (Vortex mixer V1 plus, Boeco, Nemačka) određena je veličina kapi i indeks polidisperziteta dobijenih emulzija (izlazni parametri, Y_1 i Y_2).

Veličina kapi i indeks polidisperziteta određivani su tehnikom fotonske korelacione spektroskopije pri čemu je korišćen uređaj Zetasizer Nano ZS90 (Malvern Instruments, Velika Britanija), na temperaturi od $20 \pm 0,1$ °C. Uređaj je opremljen He–Ne laserom koji generiše upadnu koherentnu monohromatsku svetlost talasne dužine 633 nm. Svetlost rasuta nakon prolaska kroz kivetu sa uzorkom detektuje se pod uglom od 90°. Rad uređaja je integrisan sa softverom (*Dispersion Technology Software*, DTS). Dobijeni rezultati prikazani su kao prosečna veličina kapi (Z-ave) i indeks polidisperziteta (*Pdl*), za tri uzastopna merenja.

Modelovanje uticaja ulaznih na izlazne parametre primenom dizajna smeše

D-optimalnim eksperimentalnim dizajnom smeše moguće je dobiti odgovarajući matematički model (jednačine (1)–(4)), koji opisuje uticaj udela komponenta SEDDS kao nezavisno promenljivih na veličinu kapi i *Pdl* kao zavisno promenljive. Modeli, koje je moguće dobiti su:

$$\text{linearni: } Y = b_1A + b_2B + b_3C \quad (1)$$

$$\text{kvadratni: } Y = b_1A + b_2B + b_3C + b_{12}AB + b_{13}AC + b_{23}BC \quad (2)$$

$$\text{specijalni kubni: } Y = b_1A + b_2B + b_3C + b_{12}AB + b_{13}AC + b_{23}BC + b_{123}ABC \quad (3)$$

$$\text{kubni: } Y = b_1A + b_2B + b_3C + b_{12}AB + b_{13}AC + b_{23}BC + b_{123}ABC + \gamma_{12}AB(A-B) + \gamma_{13}AC(A-C) + \gamma_{23}BC(B-C) \quad (4)$$

gde su b_1 – b_{123} i γ_{12} – γ_{23} koeficijenti koji pokazuju uticaj nezavisno promenljivih, kao i njihovih međusobnih interakcija na vrednost zavisno promenljive. Vrednosti koeficijenata izračunavane su višestrukom linearnom regresionom analizom, korišćenjem softvera *Design Expert*® (version 8.0.7.1, Stat-Ease, Inc, Minneapolis, MN, USA).

Matematički model koji najbolje opisuje vezu između ulaznih i izlaznih parametara bira se na osnovu poređenja nekoliko statističkih parametara, uključujući standardnu devijaciju (*Sd*), koeficijent višestruke korelacije (R^2), prilagođen koeficijent višestruke korelacije (prilagođeni R^2) i predvidiv ostatak zbira kvadrata (*PRESS*). *PRESS* pokazuje koliko dobro model fituje podatke i za izabrani model njegova vrednost treba da bude manja u poređenju sa drugim modelima. Za razliku od vrednosti *PRESS*, vrednosti za R^2 i prilagođeni R^2 treba da budu veće u odnosu na druge modele, dok vrednost standardne devijacije treba da bude manja. Kompromisom između postavljenih zahteva vrši se odabir pogodnog matematičkog modela. Nakon odabira matematičkog modela regresionom analizom određene su vrednosti koeficijenta u modelu i posle eliminacije članova, koji nisu statistički značajni ($p > 0,05$) dobijeni su finalni matematički modeli.

Matematički model, tj. finalna jednačina, razmatra L-pseudo vrednosti ulaznih parametara (*A*, *B* i *C*), koje se kreću od 0 do 1. Vrednost 0 se dodeljuje donjoj granici, a vrednost 1 gornjoj granici ulaznih parametara, dok se sve ostale vrednosti izračunavaju iz sledećih jednačina:

Kaprilno–kaprinski trigliceridi (*A*):

$$A_{1(L-Pseudo)} = (A_1 - 10)/20 \quad (5)$$

Polisorbat 80:Labrasol® (1:1, smeša surfaktantna (*B*):

$$B_{1(L-Pseudo)} = (B_1 - 40)/20 \quad (6)$$

Transcutol® HP (kosurfaktant) (*C*):

$$C_{1(L-Pseudo)} = (C_1 - 30)/20 \quad (7)$$

gde su A_1 , B_1 i C_1 bilo koje vrednosti udela lipida, surfaktanta i kosurfaktanta, redom, u okviru postavljenih granica.

Optimizacija formulacije tečnog samo-nanoemulgujućeg terapijskog sistema

Nakon uspostavljanje korelacije između ispitivanih parametara i dobijanja modela izvršena je optimizacija sa zahtevima da veličina kapi bude od 100 do 200 nm, a *Pdl* od 0,1 do 0,2. Pod ovim uslovima, dva odgovora su kombinovana tako da se odredi optimizaciona oblast i dobije SNEDDS visoke stabilnosti, na šta nam ukazuje zadata vrednost *Pdl*. Iz različitih delova optimizacione oblasti odabrane su 3 formulacije SNEDDS kojima je nakon razblaživanja vodom (10:90) određena veličina kapi i *Pdl*, primenom fotonske korelacione spektroskopije, radi procene uspešnosti predviđanja. Od te tri formulacije odabrana je jedna formulacija sa najmanjim udelom surfaktanata i kosurfaktanata, koja je korišćena za izradu čvrstih samo-nanoemulgujućih terapijskih sistema.

Formulacija čvrstih samo-nanoemulgujućih terapijskih sistema

Odabrani tečni SNEDDS je nanet na četiri različita adsorpciona nosača (Neusilin® UFL2, Neusilin® FL2, Sylvania® 320 i dijatomit). Udeo KBZ bio je konstantan (20%), a odnos tečnog SNEDDS i adsorpcionog nosača iznosio je 1:1 i 2:1. SSNEDDS su izrađeni tako što je prethodno izrađenoj homogenoj smeši adsorpcionog nosača i KBZ postepeno u malim količinama uz mešanje dodavan tečni SNEDDS do dobijanja uniformne smeše, koja je nakon toga prosejana kroz sito od nerđajućeg čelika, veličine promera 300 μm. Izrađeno je 8 formulacija prikazanih u tabeli 1.

Tabela 1. Formulacije čvrstih samo-nanoemulgujućih terapijskih sistema sa KBZ-om

Table 1. Formulation of solid self-nanoemulsifying drug delivery systems containing carbamazepine

Broj formulacije	Vrsta nosača i odnos nosač:SNEDDS	Oznaka formulacije
F1	Neusilin FL2:SNEDDS 1:1	NFL2_SNEDDS_1_1
F2	Neusilin FL2:SNEDDS 1:2	NFL2_SNEDDS_1_2
F3	Neusilin UFL2:SNEDDS 1:1	NUFL2_SNEDDS_1_1
F4	Neusilin UFL2:SNEDDS 1:2	NUFL2_SNEDDS_1_2
F5	Sylvania 320:SNEDDS 1:1	Syl_SNEDDS_1_1
F6	Sylvania 320:SNEDDS 1:2	Syl_SNEDDS_1_2
F7	Dijatomiti:SNEDDS 1:1	Dij_SNEDDS_1_1
F8	Dijatomiti:SNEDDS 1:2	Dij_SNEDDS_1_2

Karakterizacija čvrstih samo-nanoemulgujućih terapijskih sistema sa KBZ-om

In vitro procena brzine rastvaranja KBZ-a

Ispitivanje brzine rastvaranja KBZ-a iz izrađenih SSNEDDS i komercijalno dostupnih tableta KBZ-a sa trenutnim oslobađanjem izvedeno je u aparaturi sa rotirajućom lopaticom (Erweka DT70, Nemačka) pod sledećim eksperimentalnim uslovima: medijum – prečišćena voda, zapremina medijuma – 900 ml, temperatura medijuma – 37 °C i brzina obrtanja rotirajuće lopatice – 50 rpm. Po 4 ml uzorka je uzimano nakon 10, 20, 30, 60, 90 i 120 min uz nadoknađivanje medijuma posle uzorkovanja. U uzorcima je, nakon filtriranja, količina rastvorenog KBZ-a određivana spektrofotometrijski (Evolution 300, Termo Fisher Scientific, Engleska) na 287 nm. Za svaki od izrađenih SSNEDDS izvedeno je po tri ispitivanja i procenat rastvorenog KBZ-a izražen je kao srednja vrednost.

Termogravimetrijska analiza (TGA)

TGA merenja su izvršena na TGA Q5000 termalnom analizatoru (TA Instruments, SAD) sa dvadesetpetopozicionim autosamplerom. Tokom analize su korišćene aluminijumske posude, u koje su stavljani uzorci u količini od 3 do 5 mg, analizirani u temperaturnom opsegu od 20 do 320 °C pri brzini zagrevanja od 10 °C/min, u struji azota, sa protokom od 25 ml/min.

Diferencijalna skenirajuća kalorimetrija (DSC)

DSC merenja izvršena su na DSC Q2000 termalnom analizatoru (TA Instruments, Nemačka). Precizno odmerene mase uzoraka (1–2 mg) stavljane su u T-Zero® aluminijumske posude, koji su potom hermetički zatvarane, i analizirani u temperaturnom opsegu od 20 do 200 °C pri brzini zagrevanja od 10 °C/min, u struji azota, sa protokom od 50 ml/min. Instrument je kalibrisan korišćenjem indijum standarda. Entalpija, početne temperature i temperature topljenja su automatski izračunavane korišćenjem originalnog softvera (TA Instruments, Nemačka).

Mikroskopija na vrućoj ploči (engl. Hot stage microscopy – HSM)

HSM snimanja izvršena su korišćenjem Mettler Toledo Hot Stage mikroskopa (Hot-Stage FP82HT, Controller/processor FP 90, Microscope DME Model 13595, Camera PL-A622 firewire camera, Mettler Toledo, Nemačka) i softvera Studio Capture 3.1, u temperaturnom opsegu od 20 do 250 °C.

Difrakcija X-zracima na uzorcima u prahu (PXRD)

PXRD analiza je izvršena na difraktometru Bruker D8 Advance (Bruker, Nemačka), na sobnoj temperaturi, opremljenog bakarnom anodom ($\lambda = 0,15418$ nm, 40 kV, 40 mA). Uzorci, prethodno po potrebi usitnjeni, stavljani su na kvarcnu ploču sa aluminijumskim drža-

čem. Reflektovana svetlost je detektovana na Lynx-eye PSD detektoru.

Infracrvena spektrofotometrija sa Furijeovom transformacijom (FTIR)

FTIR spektri su dobijeni korišćenjem Perkin Elmer Spectrum One FTIR spektrometra (Perkin Elmer, Walham, SAD) spojenog sa horizontalnim Golden Gate MKII jedno-reflektivnim ATR sistemom (Specac, 214 Kent, Velika Britanija), opremljenog sa Zn–Se sočivom i povezanog sa odgovarajućim softverom.

Skenirajuća elektronska mikroskopija (SEM)

Praškasti uzorci su fiksirani na odgovarajuće nosače za uzorke pomoću trake koja je lepljiva sa obe strane, zatim su sušeni na vazduhu, a nakon toga obloženi ultra tankim slojem zlata (10 nm). SEM snimanja su izvršena na uređaju HITACHI SU 8000 (Hitachi, Japan), pri naponu od 2000 V.

REZULTATI I DISKUSIJA

Optimizacija formulacije tečnog samo-nanoemulgujućeg terapijskog sistema

U Tabeli 2 prikazani su ulazni i izlazni parametri koji odgovaraju eksperimentalnom planu dobijenom korišćenjem softvera *Design Expert*® (version 8.0.7.1, Stat-Ease, Inc, Minneapolis, MN, USA). Jasno se vidi da se sa malim variranjem udela lipida, surfaktanta i kosurfaktanta dobijaju velike razlike u veličini kapi i vrednosti *Pdl*. Tako se veličina kapi kreće u rasponu od 118,7 nm u formulaciji 4 (20,64% lipida, 40,00% smeše surfaktanta i 39,36% kosurfaktanta) do 513,1 nm u formulaciji 3 (10,01% lipida, 40,00% smeše surfaktanta i 49,99% kosurfaktanta). Na osnovu vrednosti *Pdl* uočena je velika razlika u stabilnosti dobijenih emulzija. Neočekivano formulacija 3 sa najmanjim udelom lipida, a najvećim udelom kosurfaktanta, ima vrednost *Pdl* 1 i najveću veličinu kapi, što ukazuje na nestabilnost ove formulacije. Ova formulacija potencijalno ukazuje da kosurfaktant (Transcutol® HP), čiji je udeo u ovoj formulaciji na najvišem nivou, ima najmanji pozitivni uticaj na stabilnost sistema. Sa druge strane formulacija 15 (13,64% lipida, 42,85% smeše surfaktanta i 43,51% kosurfaktanta) ima vrednost *Pdl* 0,076, što ukazuje na to da ova formulacija ima najveću stabilnost.

Uzimajući u obzir pomenute statističke parametre (*Sd*, R^2 , prilagođeni R^2 i *PRESS* vrednost) izabrani matematički model koji najbolje opisuje odnos između ulaznih i izlaznog parametara, veličine kapi, je specijalni kubni. Nakon isključivanja parametara koji nemaju statistički značaj ($p > 0,05$) dobijena je finalna jednačina (tabela 3). Vrednosti koeficijenata uz *A*, *B* i *C* ukazuju na efekat ovih promenljivih na odgovor sistema. Pozitivan znak koeficijenta ukazuje na sinergistički efekat, dok negativan označava antagonistički efekat na odgovor.

Tabela 2. Eksperimentalni plan dobijen primenom dizajna smeše (ulazni i izlazni parametri)

Table 2. Experimental matrix obtained by applying mixture design (input and output parameters)

Broj formulacije	Ulazni parametri			Izlazni parametri	
	A: kaprilno–kaprinski trigliceridi,%	B: Polisorbat 80:Labrasol® (1:1), %	C: Transcutol® HP, %	Y ₁ : Veličina kapi nm	Y ₂ : Pdl
1	15,05	42,07	42,88	232,6±28,85	0,151±0,041
2	13,70	52,86	33,44	162,7±3,52	0,291±0,019
3	10,01	40,00	49,99	513,1±5,25	1,000±0,009
4	20,64	40,00	39,36	118,7±5,29	0,213±0,025
5	15,05	42,07	42,88	232,6±28,85	0,151±0,041
6	10,01	59,99	30,00	193,0±2,29	0,205±0,006
7	20,70	49,30	30,00	150,0±5,11	0,226±0,010
8	10,00	49,08	40,92	188,7±7,21	0,283±0,014
9	20,64	40,00	39,36	118,7±5,29	0,213±0,025
10	23,81	43,04	33,15	189,8±6,07	0,300±0,020
11	29,99	40,01	30,00	202,1±6,52	0,387±0,010
12	10,01	59,99	30,00	193,0±2,29	0,205±0,006
13	16,57	46,42	37,01	318,7±6,60	0,459±0,008
14	29,99	40,01	30,00	202,1±6,52	0,387±0,010
15	13,64	42,85	43,51	233,6±8,56	0,076±0,013
16	20,70	49,30	30,00	150,0±5,11	0,226±0,010

Takođe, veći koeficijent uz nezavisnu promenljivu ima veći uticaj na promenu odgovora.

Na isti način je izvršena statistička obrada za drugi izlazni parametar, *Pdl*, pri čemu je odabran kubni model i na osnovu njega formirana finalna matematička jednačina (tabela 3).

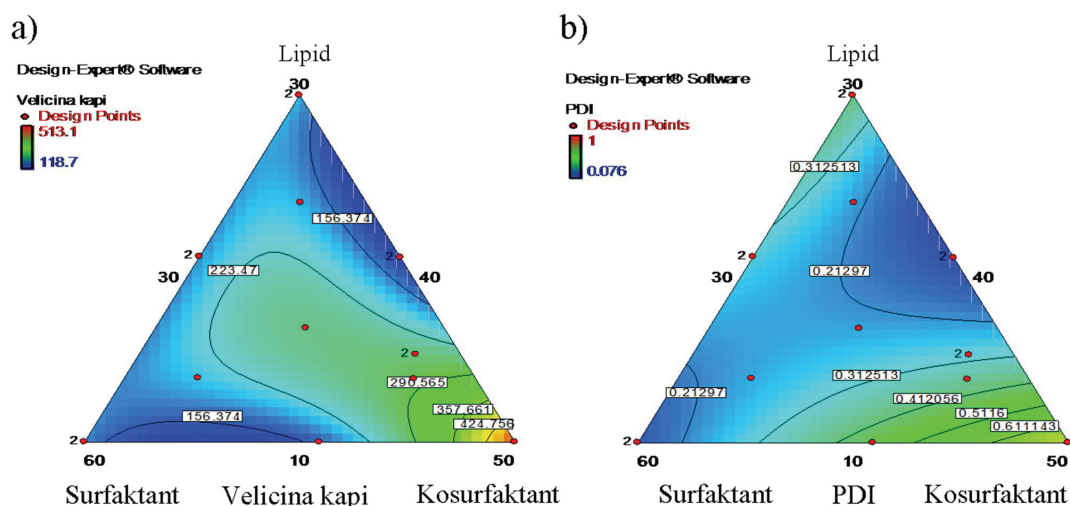
Na slici 1 dati su konturni dijagrami koji pokazuju promene vrednosti veličine kapi i *Pdl* u zavisnosti od udela komponenata SEDDS. U uglovima dijagrama su smešteni maksimalni udeli kaprilno–kaprinskih triglicerida, Polisorbat® 80:Labrasol® (1:1) i Transcutol® HP, dok se njihovi minimalni udeli nalaze na stranama dijagrama nasuprot uglovima, redom. Između uglova i sup-

rotnih strana dijagrama vrednosti komponenata smeše se postepeno smanjuju. Crvene tačke na konturnom dijagramu predstavljaju izrađene i ispitane formulacije SEDDS. Generalno su konturni dijagrami predstavljeni rasponom boja od najtamnije plave, do najintenzivnije crvene, gde najtamnijoj plavoj boji odgovaraju najniže vrednosti za veličinu kapi i *Pdl*, dok najintenzivnijoj crvenoj odgovaraju najviše vrednosti za veličinu kapi i *Pdl* u formulacijama.

Sa slike 1 jasno se vidi da se sa povećanjem udela surfaktanta, a smanjenjem udela lidipa i kosurfaktanta dobijaju SEDDS koji nakon razblaživanja vodom, imaju manju veličinu kapi i manji *Pdl*, što je značajno sa

Tabela 3. Faktori modela, njegovog redukovano oblika i dobijeni matematički model za veličinu kapi i *Pdl*; matematički model redukovano specijalnog kubnog modela za veličinu kapi: $189,93A + 173,72B + 491,85C - 906,92AC - 720,63BC + 4027,17ABC$;matematički model redukovano kubnog modela za *Pdl*: $0,41A + 0,16B + 0,71C - 1,73AC$ Table 3. The factors of the model, its reduced form, and the resulting mathematical model for droplet size and *Pdl*

Faktori i njihova značajnost pre redukovanja modela		Faktori i njihova značajnost nakon redukovanja modela	
Veličina kapi			
Faktori	<i>p</i> vrednost	Faktori	<i>p</i> vrednost
AB	0,1310	Nije značajan	–
AC	< 0,0001	AC	<0,0001
BC	0,0012	BC	0,0020
ABC	0,0011	ABC	0,0023
<i>Pdl</i>			
AB	0,6966		
AC	0,0086	AC	0,0093
BC	0,1180		
ABC	0,3892		

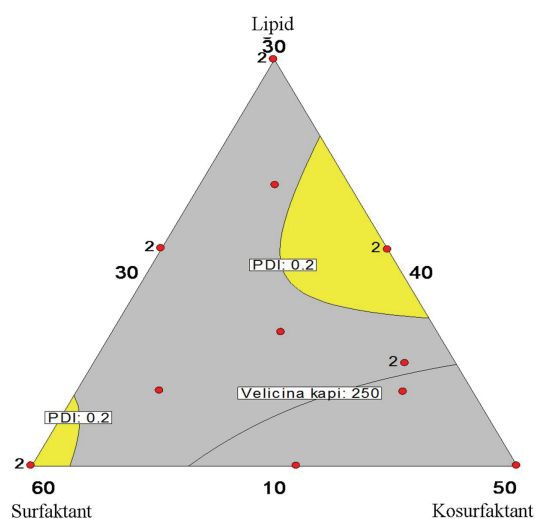


Slika 1. 2D konturni dijagram zavisnosti izlaznih od ulaznih parametara za a) veličinu kapi i b) *Pdl*.
Figure 1. 2D contour plots for the effect of input parameters on the outputs for a) droplet size and b) *Pdl*.

aspekta stabilnosti dobijenih sistema. Takođe se uočava da se pri srednjim vrednostima udela svih komponenti sistema dobija formulacija koja ima zadovoljavajuću stabilnost na šta ukazuje vrednost *Pdl* koja je manja od 0,3 i veličina kapi od oko 250 nm.

Na slici 2 je prikazan prihvatljiv region u kom se ukrštaju zadate vrednosti odgovora (veličina kapi od 100 do 200 nm i *Pdl* od 0,1 do 0,2).

Radi procene sposobnosti dizajna smeše da predvidi odgovore sistema, iz različitih delova optimizacione regije konturnog dijagrama odabrane su tri formulacije koje zadovoljavaju postavljene kriterijume za veličinu kapi i *Pdl*. Rezultati dobijeni merenjem veličine kapi i *Pdl* izrađenih SNEDDS nakon razblaženja vodom (u odnosu 10:90) pomoću fotonske korelacione spektroskopije upoređeni su sa predviđenim vrednostima kako bi se proverilo da li odabrani matematički modeli daju dobru korelaciju (tabela 4). Poređenjem dobijenih i predviđenih vrednosti uočava se da se primenom dizajna smeše može pouzdano predvideti veličina kapi i *Pdl* izrađenih SEDDS, jer je razlika između predviđenih i eksperimentalno dobijenih vrednosti za veličinu kapi i *Pdl* u okviru standardne devijacije izmerenih odgovora.



Slika 2. 2D konturni dijagram sa regionima u okviru kojih se nalaze optimalne formulacije.
Figure 2. 2D contour plots with areas having the optimal formulation.

Formulacija broj O₂ je odabrana za izradu SSNEDDS, jer pored toga što zadovoljava zadate opsege za veličinu kapi i *Pdl*, ima i visok udeo triglicerida (21,12%), a manji udeo surfaktanta (42,24%), što je značajno sa aspekta bezbednosti primene, jer visok udeo surfak-

Tabela 4. Udeli komponenta tri odabrane test optimalne formulacije, predviđene i dobijene vrednosti veličine kapi i *Pdl*
Table 4. Ratios of components for the three selected test optimal formulations, predicted and obtained values of droplet size and *Pdl*

Formulacija	Lipid, %		Surfaktant, %		Kosurfaktant, %		Predviđene vrednosti		Eksperimentalno dobijene vrednosti	
	Kaprilno–kapriliški trigliceridi	Polisorbat 80/Labrasol® (1:1)	Transcutol® HP	Veličina kapi nm	<i>Pdl</i>	Veličina kapi nm	<i>Pdl</i>			
O ₁	22,27	43,06	34,67	150,96	0,192	153,2±3,56	0,194±0,023			
O ₂	21,12	42,24	36,64	147,94	0,161	157,02±9,21	0,184±0,036			
O ₃	11,14	58,15	30,71	171,07	0,187	160,80±10,84	0,176±0,012			

tanata može dovesti do iritacije na nivo gastrointestinalnog trakta [17,18].

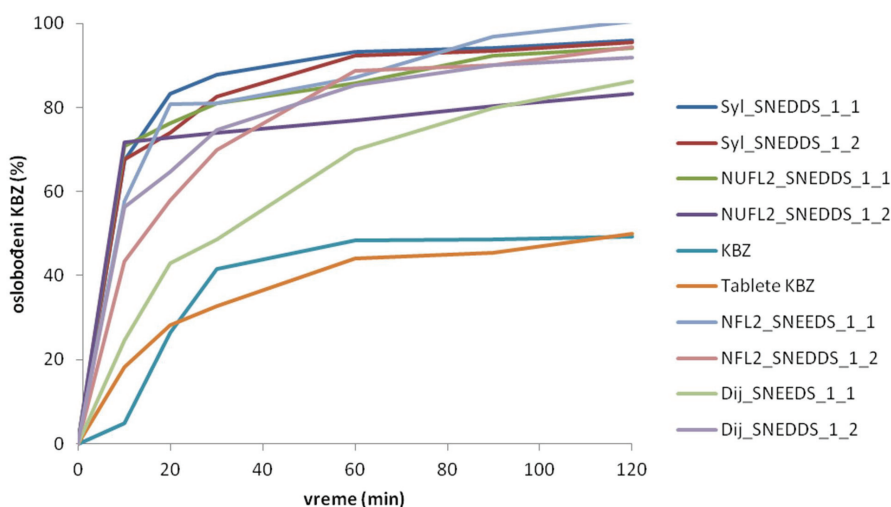
In vitro profili brzine rastvaranja KBZ-a iz SSNEDDS

Profili brzine rastvaranja KBZ iz izrađenih SSNEDDS, kao i profil brzine rastvaranja čistog KBZ i KBZ iz komercijalnih tableta sa trenutnim oslobađanjem prikazani su na slici 3. Sa grafika se može videti da se formulisanjem SSNEDDS povećava brzina rastvaranja KBZ. Povećanje brzine rastvaranja jeste posledica sinergizma između komponenti SNEDDS i adsorpcionog nosača. SNEDDS dovodi do povećanja brzine rastvaranja prvenstveno usled solubilizacije KBZ, a adsorpcioni nosači dovode do povećanja brzine rastvaranja usled boljeg kvašenja zahvaljujući velikoj specifičnoj površini. Formulacijom SSNEDDS sa KBZ postiže se povećanje njegove brzine rastvaranja u odnosu na čist KBZ i komercijalne tablete sa trenutnim oslobađanjem KBZ-a. U prvih 10 min se iz svih 8 formulacija SSNEDDS postiže visok procenat oslobođenog KBZ, koji se kreće u rasponu od 40–80% KBZ, a čistog KBZ svega 4,91%, odnosno 18,19% KBZ iz tableta sa trenutnim oslobađanjem. Najverovatnije u tih prvih 10 min dolazi do oslobađanja KBZ sa površine adsorpcionih nosača. Razlike koje postoje su verovatno posledica u razlikama u specifičnoj površini adsorpcionih nosača. Najveće povećanje brzine rastvaranja KBZ u početnom trenutku, ali i kasnije postignuto je korišćenjem nosača Sylysia® 320, zatim Neusilin® UFL2, pa Neusilin® FL2 i najmanje povećanje korišćenjem dijatomita. Ovakvi rezultati su očekivani imajući u vidu specifičnu površinu datih nosača. Sylysia® 320 i Neusilin® UFL2 imaju specifičnu površinu od 300 m²/g [19–22], Neusilin® FL2 150 m²/g [19–21], dok je specifična površina dijatomita daleko manja i iznosi 30,92 m²/g [23,24]. Formulacija koja je pokazala najveći procenat oslobođenog KBZ jeste formulacija F5 koja sadrži jed-

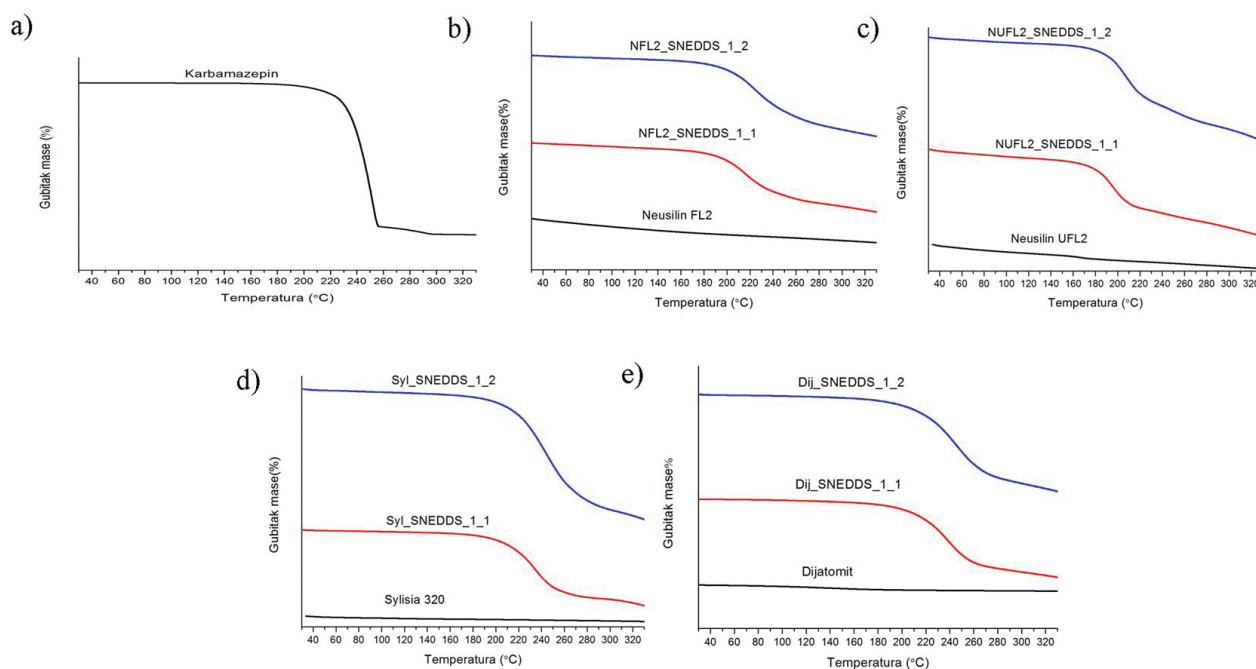
nak udeo SNEDDS i adsorpcionog nosača (Sylysia® 320), iz ove formulacije je za 30 minuta oslobođeno oko 90% karbamazepina. Nakon 30 min kod obe formulacije sa Sylysia® 320 uočeno je oslobađanje više od 80% KBZ, što ogovara farmakopejskom zahtevu za preparate sa trenutnim oslobađanjem. Razlike koje se javljaju nakon 10 min u brzini oslobađanja KBZ-a iz formulacija u kojima su kao nosači korišćeni Sylysia® 320, zatim Neusilin® UFL2 su posledice specifične strukture ova dva nosača. Poznato je da Neusilin® UFL2 ima malu veličinu čestica (2–8 μm) i da poseduje uske i duge pore [25] u koje tečni SNEDDS može da uđe nakon adsorbovanja i „zarobi” određenu količinu KBZ, pa je to možda razlog za nešto niži procenat oslobođenog KBZ u odnosu na sisteme sa Sylysia® 320. Sa profila brzina oslobađanja KBZ iz formulacija sa različitim odnosima SNEDDS i adsorpcionog nosača, uočava se veće povećanje brzine oslobađanja iz formulacijama kod kojih je jednak odnos SNEDDS-a i adsorpcionog nosača, u odnosu na formulacije gde je odnos SNEDDS:nosač 2:1. Ovaj uticaj smanjenja brzine rastvaranja KBZ sa povećanjem udela SNEDDS je u suprotnosti sa rezultatima koje su dobili Milović i saradnici [19], a može se objasniti time da se povećanjem udela SNEDDS-a zatvara određeni broj pora na samom nosaču, pa se time „zarobljava” dodatna količina KBZ i na taj način usporava njegovo rastvaranje. Pri primeni dijatomita, u prvih 10 min dolazi do oslobađanja velikog procenta KBZ (oko 50%), jer se oslobađa KBZ adsorbovan na površinu nosača. Nakon toga dolazi do postepenog oslobađanja KBZ iz šupljina nosača zbog njegove specifične strukture [7,24].

Karakterizacija SSNEDDS

Termogravimetrijska analiza (TGA). Na slici 4 prikazane su TGA krive čistog KBZ i formulacija SSNEDDS sa različitim čvrstim nosačima: Neusilin® FL2, Neusilin®



Slika 3. In vitro profili brzine rastvaranja KBZ-a iz izrađenih čvrstih samo-nanoemulgujućih terapijskih sistema.
Figure 3. In vitro profiles of CBZ dissolution rate from solid self-nanoemulsifying drug delivery systems.



Slika 4. TGA krive; a) KBZ i formulacije sa: b) Neusilin® FL2, c) Neusilin® UFL2, d) Sylysia® 320 i e) dijatomitima.
 Figure 4. The TGA curves; a) pure carbamazepine and formulations with: b) Neusilin® FL2, c) Neusilin® UFL2 d) Sylysia® 320 and e) diatomites.

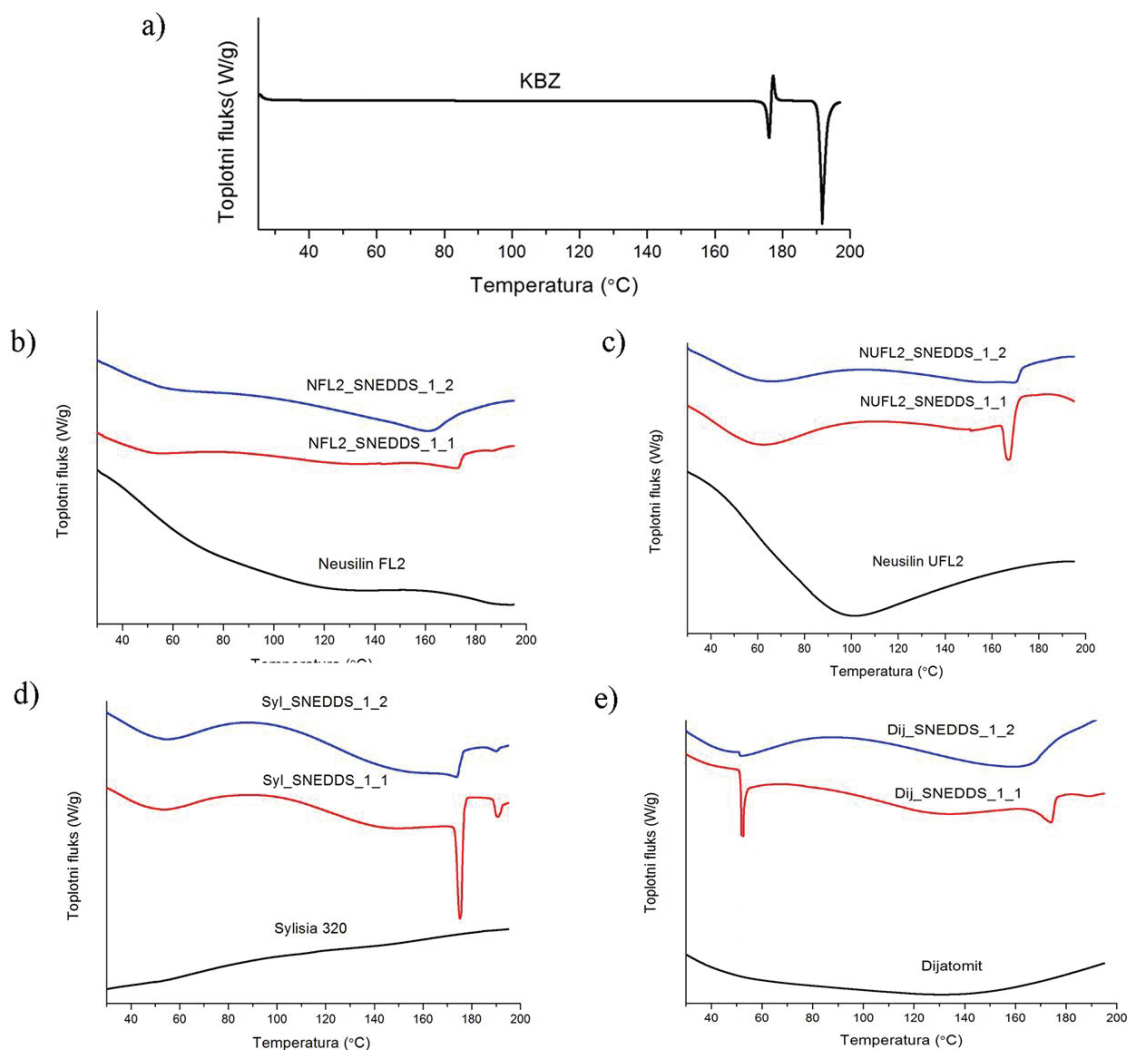
UFL2, Sylysia® 320 i dijatomitima. Kod čistog KBZ se u opsegu od 20 do 200 °C uočava gubitak mase od 0,769%, a nakon toga u temperaturnom opsegu od 200 do 250 °C nagli gubitak mase od oko 75%. Ovakav nagli gubitak mase predstavlja početak degradacije čistog KBZ i opisan je u literaturi [5,7,26]. Svi adsorpcioni nosači su se pokazali stabilnim, i tokom zagrevanja nije uočen veći gubitak mase. Kod formulacija SSNEDDS sa KBZ uočen je mali gubitak mase do 200 °C, čime je pokazana njihova stabilnost na povišenim temperaturama. Međutim, daljim zagrevanjem ispitivanih formulacija uočava se nagla promena mase, kao posledica degradaciji KBZ.

Diferencijalna skenirajuća kalorimetrija (DSC). Na slici 5 su prikazani DSC termogrami KBZ i formulacija SSNEDDS sa Neusilin® FL2, Neusilin® UFL2, Sylysia® 320 i dijatomitima kao čvrstim nosačima. Na slici 5a uočava se niz termalnih događaja, koji su zabeleženi tokom zagrevanja uzoraka. Uočljivo je da se tokom zagrevanja, uzorak čistog KBZ topi, što odgovara prvom endotermnom piknu na 175,08 °C koji se pripisuje topljenju polimorfnog oblika III, nakon toga uočava se egzotermni pik na 176,63 °C, koji potiče od rekristalizacije polimorfnog oblika III u polimorfni oblik I. Na 190,95 °C uočava se još jedan endotermni pik koji potiče od topljenja polimorfnog oblika I KBZ. Ovi rezultati za čist KBZ su u saglasnosti sa rezultatima predstavljenim u literaturi [5,7,17,27–29]. Na DSC krivama za čiste nosače (Neusilin® FL2, Neusilin® UFL2, Sylysia® 320 i dijatomit) uočavaju se širi ne tako izraženi endotermni pikovi, što verovatno predstavlja posledicu inicijalnog gubitka vlage.

Na DSC krivama izrađenih SSNEDDS formulacija sa Neusilin® FL2 uočavaju se endotermni pikovi topljenja. Kod formulacije NFL2_SNEEDS_1_1 uočavamo dve tačke topljenja na 158,60 (slabije izraženi pik) i na 183 °C. Prvi pik je verovatno posledica topljenja polimorfne forme III, a drugi pik topljenja polimorfne forme I. Ovi pikovi se javljaju na nešto nižim temperaturama u odnosu na čist KBZ i literaturne podatke, što je verovatno posledica međusobne interakcije KBZ sa pomoćnim supstancama [7]. Kod formulacije NUFL2_SNEEDS_1_2 prilikom zagrevanja dolazi do inicijalnog gubitka vlage, a nakon toga se uočava pik slabog intenziteta na 130,31 °C i široki endotermni pik topljenja na 160 °C, koji takođe ukazuju na to da se radi o polimorfnom obliku III KBZ [27]. Jasni egzotermni rekristalizacioni pikovi prelaska KBZ iz polimorfnog oblika III u polimorfni oblik I, nisu uočeni kod svih uzoraka.

Kod formulacija sa Neusilin® UFL2 uočavamo slične promene kao kod formulacija sa Neusilin® FL2 samo se temperature razlikuju za par stepeni. Na DSC krivoj za formulaciju NUFL2_SNEEDS_1_1 endotermni pik topljenja KBZ je na 164 °C. Slične promene uočene su i kod formulacija sa Sylysia® 320 i dijatomitima. Na osnovu DSC krivih može se pretpostaviti da je KBZ u svim formulacijama SSNEDDS ostao u polimorfnom obliku III [27].

Mikroskopija na vrućoj ploči (HSM). Na mikrofografiji čistog KBZ (nije prikazano) do temperature od oko 160 °C se ne uočavaju nikakve promene. Na temperaturi od 170,4 °C dolazi do topljenja prizmatičnih kristala KBZ (polimorfni oblik III, što odgovara prvom endotermnom piknu na DSC termogramu). Nakon toga na temperaturi



Slika 5. DSC termogrami; a) KBZ i formulacije sa: b) Neusilin® FL2, c) Neusilin® UFL2, d) Sylysia® 320 i e) dijatomitima.

Figure 5. The DSC thermograms; a) pure carbamazepine and formulations with: b) Neusilin® FL2, c) Neusilin® UFL2 d) Sylysia® 320 and e) diatomites.

od oko 177,9 °C dolazi do naknadne rekristalizacije i pojave igličastih kristala, što odgovara rekristalizacionom piknu na DSC krivoj KBZ (prelazak KBZ iz polimorfnog oblika III u polimorfni oblik I). Na temperaturi od 190,4 °C dolazi do topljenja kristalne forme I, što odgovara drugom endotermnom piknu na DSC krivoj KBZ.

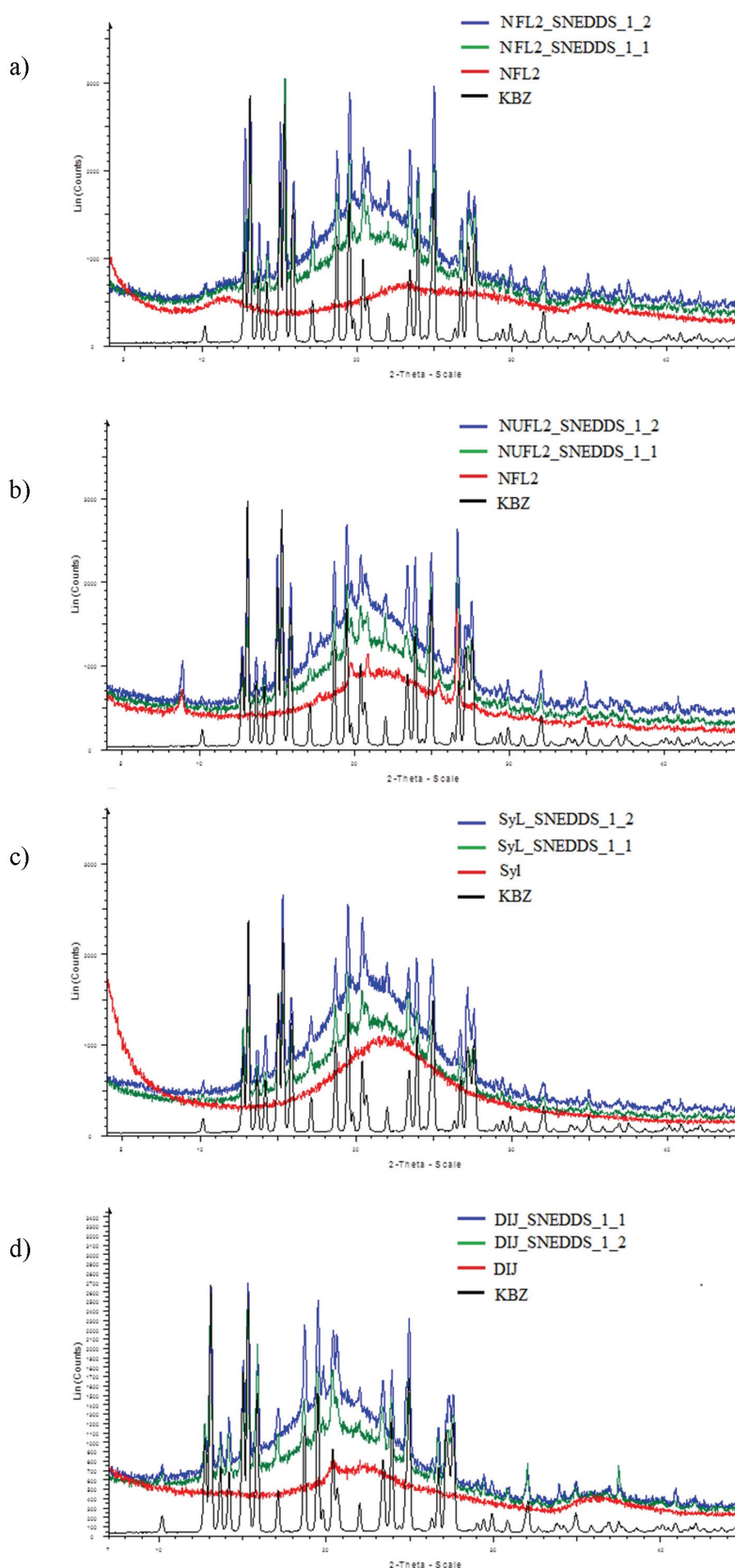
Zbog male količine KBZ (20%) u formulaciji SSNEDDS se teško uočavaju jasne promene kao kod čistog KBZ, tokom analize formulacija primenom HSM.

Difrakcija X-zracima na uzorcima u prahu (PXRD). Da bi se potvrdile pretpostavke dobijene HSM, DSC i TGA analizom da se KBZ nalazi u svim formulacijama SSNEDDS u kristalnoj formi i da verovatno tokom zagrevanja u nekim formulacijama dolazi do prelaska KBZ-a u amorfnu formu izvršena je PXRD analiza. Ova tehnika osim što predstavlja zlatni standard i tehniku izbora u utvrđivanju polimorfnih oblika KBZ, izvodi se na sobnoj temperaturi, pa je uticaj zagrevanja uzorka tokom analize isključen.

Slika 6 ilustruje PXRD difraktograme KBZ i odgovarajućih SSNEDDS. Na difraktogramu čistog KBZ uočavaju se visokointenzivni difrakcioni pikovi za sledeće 2θ uglove: 13,02, 15,22, 15,78, 19,40, 24,92, 27,50 i 31,86°, koji su u skladu sa literaturnim rezultatima karakterističnim za kristalni oblik III KBZ [7,27,28]. Očekivano je da se na difraktogramu nosača ne uočavaju nikakvi pikovi jer je sam nosač u amorfnom stanju.

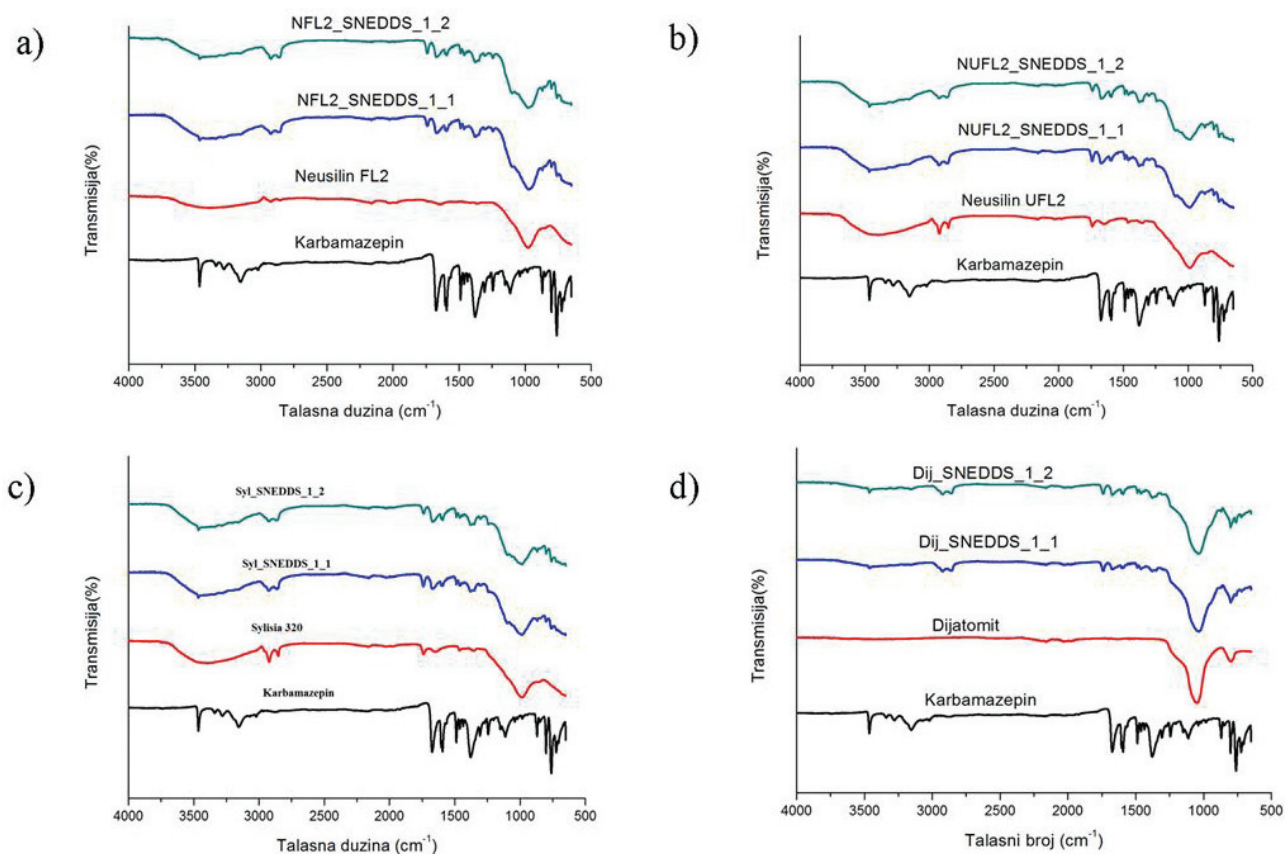
Svi karakteristični pikovi za polimorfni oblik III KBZ nalaze se i na difraktogramima svih izrađenih formulacija SSNEDDS, što ukazuje i potvrđuje pretpostavku da je KBZ u svim formulacijama ostao u polimorfnom obliku III.

Infracrvena spektrofotometrija sa Furijevom transformacijom (FTIR). Na slici 7 su prikazani spektri KBZ, adsorpcionih nosača i formulacija SSNEDDS. Spektar KBZ-a ukazuje da je on u polimorfnom obliku III. Na taj zaključak ukazuju karakteristične trake na 3462 (–NH valenciona vibracija), 1674 (–CO–R vibracija), 1593 i



Slika 6. PXR D difraktogrami KBZ i i formulacija sa: a) Neusilin® FL2, b) Neusilin® UFL2, c) Sylsya® 320 i d) diatomitima.

Figure 6. PXR D diffractograms of pure carbamazepine and formulations with: a) Neusilin® FL2, b) Neusilin® UFL2 c) Sylsya® 320 and d) diatomites.



Slika 7. FTIR spektri KBZ i i formulacija sa: a) Neusilin® FL2, b) Neusilin® UFL2, c) Sylysia® 320 i d) dijamitima.
Figure 7. FTIR spectra of pure carbamazepine and formulations with: a) Neusilin® FL2, b) Neusilin® UFL2 c) Sylysia® 320 and d) diatomites.

1605 cm^{-1} (opseg za $-\text{C}=\text{C}-$ i $-\text{C}=\text{O}$ vibraciju i $-\text{NH}$ deformaciju) [7,27]. U svim formulacijama izrađenih SSNEDDS uočavaju se ove trake, što ukazuje da nije došlo do značajne interakcije između KBZ i nosača i da je KBZ ostao u polimorfnoj formi III.

Skenirajuća elektronska mikroskopija (SEM). Na slici 8 prikazane su SEM mikrofografije izrađenih formulacija pod različitim uveličanjem. Na svim mikrofografijama uočavaju se neravnine koje potiču od kristala samog KBZ.

ZAKLJUČAK

U ovom radu je pokazano da se tehnika eksperimentalnog dizajna, dizajna smeše, može koristiti sa velikom uspešnošću u odabiru tečnog samo-nanoemulgujućeg terapijskog sistema. Ova tehnika, u odnosu na standardnu korišćenu tehniku konstruisanja pseudo-ternernih faznih dijagrama u odabiru tečnog samo-emulgujućeg terapijskog sistema, daje niz prednosti u pogledu šireg opsega i odnosa komponenti sistema koje se ispituju, preciznijih i objektivnijih parametara koji se prate u odnosu na vizuelno praćenje promene sistema. Takođe, broj eksperimenata i utrošak korišćenih ekscipijenasa je daleko manji, pa je samim tim ušteda u vremenu i novcu velika.

Formulacijom čvrstih samo-nanoemulgujućih terapijskih sistema sa KBZ postignuto je značajno povećanje brzine rastvaranja KBZ u odnosu na čist KBZ i tablete KBZ sa trenutnim oslobađanjem. Najveća brzina rastvaranja KBZ postignuta je iz formulacije sa Sylysia® 320 i pri odnosu, adsorpcioni nosač:SNEDDS od 1:1. Iz ove formulacije je za 30 min oslobođeno oko 90% KBZ, dok je čistog KBZ za isto vreme oslobođeno svega 41%. Osim iz formulacija sa Sylysia® 320, značajno povećanje brzine oslobađanja KBZ je postignuto i iz formulacija u kojima je kao adsorbens korišćen Neusilin® UFL2, dok je nešto sporije oslobađanje KBZ postignuto korišćenjem Neusilin® FL2, ali ipak brže u odnosu na čist karbamazepin. U formulacijama SSNEDDS, iz kojih je postignuto najsporije oslobađanje karbamazeipina, kao adsorpcioni nosač korišćeni su dijamiti. Primenom analitičkih tehnika je utvrđeno da je KBZ u svim formulacijama SSNEDDS ostao u farmakološki najaktivnijem polimorfnom obliku III.

Dalja istraživanja bi treba da idu u formulaciji finalnog farmaceutskog oblika, tableta ili kapsula, kao i u proceni *in vivo* ponašanja formulisanog sistema.

Zahvalnica

Istraživanje je realizovano u okviru projekata TR 34007, koje finansira Ministarstvo prosvete, nauke i tehnološkog razvoja Republike Srbije. Zahvalnost dugujemo i studentkinjama Ani Vuletić i Tijani Antić koje su nam pomogle u izvođenju dela eksperimenata.

LITERATURA

- [1] A.V. Kyatanwar, K. R. Jadhav, V. J. Kadam, Self Micro-Emulsifying Drug Delivery System (SMEDDS): Review, *Int. J. Pharm.* **3(1)** (2010) 75–83.
- [2] L.X. Yu, G.L. Amidon, J.E. Polli, H. Zhao, M.U. Mehta, D.P. Conner, V.P. Shah, L.J. Lesko, M.L. Chen, V.H. Lee, A.S. Hussain, Biopharmaceutics classification system: the scientific basis for biowaiver extensions, *Pharm. Res.* **19** (2002) 921–925.
- [3] P. Sudheer, N. Kumar, S. Puttachari, U. Shankar, R.S. Thakur, Approaches Development of Solid – Self Micron Emulsifying Drug Delivery System: Formulation Techniques and Dosage Forms – a review, *Asian J. Pharm. Life Sci.* **2** (2010) 214–225.
- [4] H. Ma, M. Chu, K. Itagaki, P. Xin, X. Zhou, D. Zhang, Y. Wang, J. Fu, S. Sun, Formulation and *in vitro* Characterization of a novel Solid lipid-based drug delivery system, *Chem. Pharm. Bull.* **62** (2014) 1173–1179.
- [5] M. Krstic, S. Razic, Lj. Djekić, V. Dobricic, M. Momcilovic, D. Vasiljevic, S. Ibric, Application of a Mixture Experimental Design in the Optimization of the Formulation of Solid Self-Emulsifying Drug Delivery Systems Containing Carbamazepine, *Lat. Am. J. Pharm.* **34** (2015) 885–894.
- [6] M. Milović, J. Đuriš, D. Vasiljević, Z. Đurić, S. Ibrić, Potencijalna primena surfaktantnih sistema u formulaciji farmaceutskih oblika sa teško rastvorljivim lekovitim supstancama, *Hem. Ind.* **66** (2012) 667–676.
- [7] M. Krstic, S. Razic, D. Vasiljevic, Dj. Spasojevic, S. Ibric, Application of experimental design in examination of the dissolution rate of carbamazepine from formulations. Characterization of the optimal formulation by DSC, TGA, FT-IR and PXRD analysis, *J. Serb. Chem. Soc.* **80** (2015) 209–222.
- [8] K. Kawakami, Modification of physicochemical characteristics of active pharmaceutical ingredients and application of supersaturatable dosage forms for improving bioavailability of poorly absorbed drugs, *Adv. Drug Delivery Rev.* **64** (2012) 480–495.
- [9] C.W. Pouton, Formulation of poorly water-soluble drugs for oral administration: physicochemical and physiological issues and the lipid formulation classification system, *Eur. J. Pharm. Sci.* **29** (2006) 278–287.
- [10] E.J. Acosta, T. Nguyen, A. Witthayapanyanon, J.H. Harwell, D.A. Sabatini, Linker-Based Bio-Compatible Microemulsions, *Enviro. Sci. Tech.* **39** (2004) 1275–1282.
- [11] F. Kesisoglou, S. Panmai, Y.H. Wu, Application of nanoparticles in oral delivery of immediate release formulations, *Curr. Nanosci.* **3** (2007) 183–190.
- [12] M. Rosen, *Surfactants and Interfacial Phenomena*. 3rd ed., John Wiley & Sons. Hoboken, NJ, 2004.
- [13] Lj. Djekic, M. Primorac, Formulacija i karakterizacija samo-mikroemulgujućih nosača lekovitih supstanci na bazi biokompatibilnih nejonskih surfaktanata, *Hem. Ind.* **68** (2014) 565–573.
- [14] L. Eriksson, N. Johansson, C. Kettaneh-Wold, S. Wikström, S. Wold, *Design of Experiments: Principles and Applications*, 3rd ed., MKS Umetrics AB, Umea, 2008.
- [15] S. Mitchell, T. Reynolds, T. Dasbach, A compaction process to enhance dissolution of poorly water-soluble drugs using hydroxypropyl methylcellulose, *Int. J. Pharm.* **250** (2003) 3–11.
- [16] R. Talukder, C. Reed, T. Dürig, M. Hussain, Dissolution and Solid-State Characterization of Poorly Water-Soluble Drugs in the Presence of a Hydrophilic Carrier, *AAPS Pharm. Sci. Tech.* **12** (2011) 1227–1233.
- [17] A.P. Rogerio, C.L. Dora, E.L. Andrade, J.S. Chaves, L. Silva, E. Lemos-Senna, J.B. Calixto, Anti-inflammatory effect of quercetin-loaded microemulsion in the airways allergic inflammatory model in mice, *Pharm. Res.* **61** (2010) 288–297.
- [18] J.S. Yuan, M. Ansari, M. Samaan, E. Acosta, Linker-based lecithin microemulsions for transdermal delivery of lidocaine, *Int. J. Pharm.* **349** (2008) 130–143.
- [19] M. Milovic, J. Djuris, Lj. Djekic, D. Vasiljevic, S. Ibric, Characterization and evaluation of solid self-microemulsifying drug delivery systems with porous carriers as systems for improved carbamazepine release, *Int. J. Pharm.* **436** (2012) 58–65.
- [20] S. Hailu, R. Bogner, Complex Effects of Drug/Silicate Ratio, Solid-State Equivalent pH, and Moisture on Chemical Stability of Amorphous Quinapril Hydrochloride Coground with Silicates, *J. Pharm. Sci.* **100** (2011) 1503–1515.
- [21] Fuji Chemical Industry Co., Ltd. (2009). The Specialty Excipinet Neusilin®, dostupno na linku http://www.harke.com/fileadmin/images/pharma/Broschueren/Fuji_Neusilin.pdf (poslednji pristup 30.06.2015.).
- [22] <http://www.fujisilysia.com/products/sylysia/> (poslednji pristup 01.07.2015.).
- [23] M.S. Aw, S. Simović, Y. Yu, J. Addai-Mensah, D. Losic, Porous silica microshells from diatoms as biocarrier for drug delivery applications, *Powder. Technol.* **223** (2012) 52–58.
- [24] M.S. Aw, S. Simovic, J. Addai-Mensah, D. Losic, Silica microcapsules from diatoms as new carrier for delivery of therapeutics, *Nanomedicine* **6** (2011) 159–173.
- [25] V. Agarwal, A. Siddiqui, H. Ali, S. Nazzal, Dissolution and powder flow characterization of solid self-emulsified drug delivery system (SEDDS), *Int. J. Pharm.* **366** (2009) 44–52.
- [26] Z. Qi, D. Zhang, F. Chen, J. Miao, B. Ren, Thermal decomposition and non-isothermal decomposition kinetics of carbamazepine, *Russ. J. Phys. Chem., A* **88** (2014) 2308–2313.
- [27] A.L. Grzesiak, M. Lang, K. Kim, A.J. Matzger, Comparison of the Four Anhydrous Polymorphs of Carbamazepine and the Crystal Structure of Form, *Int. J. Pharm. Sci.* **92** (2003) 2260–2271.

- [28] C. Rustichelli, G. Gamberini, V. Ferioli, M.C. Gamberini, R. Ficarra, S. Tommasini, Solid-state study of polymorphic drugs: Carbamazepine, *J. Pharm. Biomed. Anal.* **23** (2000) 41–54.
- [29] Y. Kobayashi, S. Itai, K. Yamamoto, Physicochemical properties and bioavailability of carbamazepine polymorphs and dehydrate, *Int. J. Pharm.* **193** (2000) 137–146.

SUMMARY

APPLICATION OF MIXTURE EXPERIMENTAL DESIGN IN FORMULATION AND CHARACTERIZATION OF SOLID SELF-NANOEMULSIFYING DRUG DELIVERY SYSTEMS CONTAINING CARBAMAZEPINE

Marko Z. Krstić, Svetlana R. Ibrić

University of Belgrade – Faculty of Pharmacy, Department of Pharmaceutical Technology and Cosmetology, Belgrade, Serbia

(Scientific paper)

One of the problems with orally used drugs is their poor solubility, which can be overcome by creating solid self-nanoemulsifying drug delivery systems (SNEDDS). The aim is to choose the appropriate SNEDDS using mixture design and adsorption of SNEDDS on a solid carrier to improve the dissolution rate of carbamazepine. Self-emulsifying drug delivery systems (SEDDS) consisting of oil phase (caprylic-capric triglycerides), a surfactant (Polisorbat 80 and Labrasol® (1:1)) and cosurfactant (Transcutol® HP) are formed by applying mixture design. 16 formulations were formulated, where the proportion of lipids, surfactant and cosurfactant were varied (input parameters) in the following ranges: 10–30%, 40–60%, 30–50%, respectively. After dilution of SEDDS with water (90% water), the droplet size and polydispersity index (Pdl) of the obtained emulsions (output parameters) were measured using photon correlation spectroscopy. After processing data, appropriate mathematical models that describe the dependence of input and output parameters were selected. The optimized SNEDDS was adsorbed on the carbamazepine and solid carrier physical mixture, containing 20% carbamazepine. Neusilin® UF12, Neusilin® FL2, Sylysia® 320 and diatomite were used as the carriers. The ratio of SNEDDS:carrier was 1:1 or 2:1. Dissolution testing was carried out in the rotation paddles apparatus. Characterization of solid SNEDDS was performed using the hot stage microscopy (HSM), thermogravimetric analysis (TGA), differential scanning calorimetry (DSC), infrared spectrophotometry with Fourier transformation (FT-IR), scanning electron microscopy (SEM) and X-ray diffraction (PXRD). Selected SNEDDS consisting of lipids (21.12%), surfactant (42.24%) and cosurfactant (36.64%) had a droplet size 157.02 ± 34.09 nm and *Pdl* 0.184 ± 0.021 . Drug release profiles showed that in all formulations dissolution rate increased (the fastest drug release was observed in formulations with Sylysia® 320). It can be concluded that in all formulations carbamazepine is present in the thermodynamically most stable polymorphic form III. Formulation of solid SNEDDS can significantly increase dissolution rate of carbamazepine, with conservation of the polymorphic form III CBZ and potentially increased bioavailability.

Keywords: Dissolution rate • Mixture design • Polisorbat 80 • Labrasol® • Transcutol® HP • Neusilin® UF12 • Neusilin® FL2 • Sylysia® 320 • Diatomite • Carbamazepine

Granular flow in static mixers by coupled DEM/CFD approach

Lato Pezo¹, Milada Pezo², Aca Jovanović¹, Nenad Kosanić³, Aleksandar Petrović³, Ljubinko Lević⁴

¹University of Belgrade, Institute of General and Physical Chemistry, Belgrade, Serbia

²University of Belgrade, Laboratory for Thermal Engineering and Energy, Institute of Nuclear Sciences "Vinča", Belgrade, Serbia

³University of Belgrade, Faculty of Mechanical Engineering, Belgrade, Serbia

⁴University of Novi Sad, Faculty of Technology, Novi Sad, Serbia

Abstract

The mixing process greatly influences the mixing efficiency, as well as the quality and the price of the intermediate and/or the final product. Static mixer is used for premixing action before the main mixing process, for significant reduction of mixing time and energy consumption. This type of premixing action is not investigated in detail in the open literature. In this article, the novel numerical approach called Discrete Element Method is used for modelling of granular flow in multiple static mixer applications (1–3 Komax or Ross mixing elements were utilized), while the Computational Fluid Dynamic Method was chosen for fluid flow modelling, using the Eulerian multiphase model. The main aim of this article is to predict the behavior of granules being gravitationally transported in different mixer configuration and to choose the best configuration of the mixer taking into account the total particle path, the number of mixing elements and the quality of the obtained mixture. The results of the numerical simulations in the static mixers were compared to experimental results, the mixing quality is examined by *RSD* (relative standard deviation) criterion, and the effects on the mixer type and the number of mixing elements on mixing process were studied. The effects of the mixer type and the number of mixing elements on mixing process were studied using analysis of variance (ANOVA). Mathematical modelling is used for optimization of number of Ross and Komax segments in mixer in order to gain desirable mixing results.

Keywords: DEM/CFD, prediction, static mixer, Komax, Ross, particle tracking.

Available online at the Journal website: <http://www.ache.org.rs/HI/>

Static mixers are low energy consuming equipment (due to the gravitational flow of the material) and efficiently mixing devices, that can handle a wide range of applications. Detailed review on static mixers, concerning the mechanisms, applications, classification and characterization methods focusing on mixing process and mass transfer performance is given by various researchers [1–3]. The mixing process is very complex and sensitive, and it must be optimally configured. Too long mixing process may cause deformation of the particles that are mixed, to reduce the quality of the mixture and may also cause the increase in the price of technological process and the final product. The mixing process is a result of diffusion, convection and shear, which are the main mechanisms of the homogenization [3–6].

The problems related to the optimization of the mixing processes can be overcome by using a mathematical modelling. Experiments are usually complex and require more financial resources. The models can

drastically reduce the empirical work necessary for predicting parameters of the mixing process.

Models based on Discrete Element Method (DEM) have been developed in the past and shown to be reliable and efficient in catching particle interactions and predicting mixing process for investigation of particle mixing. The soft-sphere method originally developed by Cundall and Strack [7], was the first granular dynamics simulation technique published in the open literature. They developed the linear spring and the dashpot model whereby the magnitude of the normal force between two particles was the sum of spring force and damping force. Lagrangian tracking techniques have been used in many studies in order to characterize the mixing performance in different systems [8–11]. A detailed review and definitions of the quality of a mixture, the mixing mechanisms, the possibilities for the choice of solid mixer, the experimental assessment of homogeneity and mixing indexes are presented in Poux *et al.* [12].

The computational expense of the DEM is very high owing to the extensive contact detection algorithm, and solid time step limitations to resolve particle interactions *via* collisions. Numerical simulations and mathematical modelling are very powerful tools for optimization.

SCIENTIFIC PAPER

UDC 544:66:62

Hem. Ind. 70 (5) 539–546 (2016)

doi: 10.2298/HEMIND151013060P

Correspondence: L. Pezo, University of Belgrade, Institute of General and Physical Chemistry, Studentski trg 12/V, 11000 Beograd, Serbia.

E-mail: latopezo@yahoo.co.uk

Paper received: 13 October, 2015

Paper accepted: 27 October, 2015

The focus of this paper was to optimize the geometry and to compare different static mixer devices. Komax and Ross are commercial products, with known geometry, used widely in various branches of industry.

In this paper, experimental and numerical comparison between various multiple Komax and Ross mixing configurations has been performed. The fluid is treated as a continuum while the solid phase is modelled using the DEM. The fluid (air) velocity and pressure field are computed by using the Computational Fluid Dynamic (CFD) approach. In the DEM, particle–particle and the particle–wall interactions are resolved and the time integration is performed using Newton’s second law of motion. DEM modelling gives information about particle–particle interactions, particle–wall interactions, position, velocity and acceleration of particle and forces acting on the particle. This information can be useful for construction and design of the mixing devices. Appropriate modelling can contribute better mixing quality and overcome defects and problems that can occur during the mixing process. The quality of the mixing process is analysed using relative standard deviation (RSD) criteria [13]. The effects of the mixer type and the number of mixing elements on mixing process were studied using analysis of variance (ANOVA). The main aim of this study was to demonstrate the use of DEM/CFD simulation coupling in planning the number of Komax or Ross elements in order to gain desirable mixing results.

MATERIALS AND METHODS

Mathematical model

This paper studies the flow in two types of twisted-blade static mixers (Komax or Ross mixing elements, linked in a series of 1–3 pieces). It evaluates the mixing performance by calculating the trajectory of suspended particles through the mixer. The mathematical model is solved in two stages, first the fluid velocity and pressure field are determined by CFD, and then, using a separate study, the particle trajectories of the granular materials are computed by DEM. The conservations of mass and momentum in terms of the local mean variables over a computational cell are given by Navier–Stocks equations [14]:

$$\frac{\partial(\rho_f \varepsilon)}{\partial t} + \nabla(\rho_f \varepsilon u) = 0$$

and

$$\frac{\partial(\rho_f \varepsilon u)}{\partial t} + \nabla(\rho_f \varepsilon u \cdot u) = -\nabla p - F_{p-f} + \nabla(\varepsilon \tau) + \rho_f \varepsilon g$$

(1)

where ε , u , t , ρ_f , p , F_{p-f} , τ and g are: porosity, mean fluid velocity, time, fluid density, pressure, volumetric fluid–particle interaction force, fluid viscous stress tensor, and acceleration due to gravity. Fluid particle interaction force is defined by:

$$F_{p-f} = \frac{1}{V_{\text{cell}}} \sum_{i=1}^{k_i} \rho_{p-f,i} \tag{2}$$

where $F_{p-f,i}$ is the total fluid force on particle i and k_i is the number of particles in a CFD cell. The solid phase is treated as a discrete phase and described by the so-called DEM [13]. According to this model, the translational and rotational motions of a particle at any time t , can be described by Newton’s law of motion:

$$m_i \frac{dv_i}{dt} = f_{p-f,i} + \sum_{j=1}^{k_j} (f_{c,jj} + f_{d,jj}) + m_i g$$

and

$$I_i \frac{d\omega_i}{dt} = \sum_{j=1}^{k_j} (T_{ij} + M_{ij}) \tag{3}$$

where m_i , I_i , v_i and ω_i are: the mass, moment of inertia, translational and rotational velocities of particle i , respectively. The fluid flow field can be obtained by solving Eqs. (1) by use of a standard CFD method. The particle behaviour can be obtained by solving Eq. (3) by an explicit time integration method.

The modelling technique is based on the assumption that the particle is soft (soft particle method), and that particles are allowed to overlap [7]. The amount of overlap is labelled as Δx , and the normal and tangential relative velocities determine the collision forces (F_n and F_t), based on the Kelvin–Voigt model [10,15]. Figure 1 illustrates the collision force as the result of normal and tangential forces. The normal force F_n is considered as the repulsive force that pushes the particles apart (or particle from bounding geometry), depicted as the action of the spring, and also dissipation action, resulting in an effective coefficient of restitution, shown as dashpot action. Tangential component is considered as an incrementing spring action and dashpot action that is subject to frictional limits.

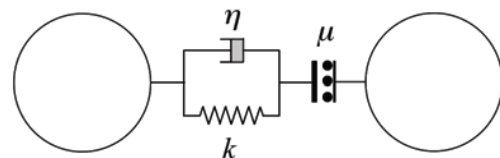


Figure 1. Kelvin–Voigt contact model.

The contact forces in normal and tangential direction are defined as:

$$F_{ij}^n = (-k_n \delta_{ij}^n - \eta_n v_{ij}^n) \quad \text{and} \quad F_{ij}^t = (-k_n \delta_{ij}^t - \eta_n v_{ij}^t) \quad (4)$$

The modelling of the fluid flow by CFD is performed at the computational cell level, whilst the modelling of the solids flow by DEM is accomplished at the individual particle level. Coupling DEM and CFD is achieved as follows: DEM gives information about positions and velocities of individual particles at each time step, for the evaluation of porosity and volumetric fluid–particles interaction force in a computational cell. Incorporation of the resulting forces into DEM will produce information about the motion of individual particle for the next time step [15].

Experimental method

The experimental apparatus was specially designed for this study, using transparent Plexiglass consisted of three segments (Ross and Komax configurations), Fig. 2a. The upper segment of the mixer (marked with 0) is divided into the two compartments with a barrier and a mobile panel. Spherical painted synthetic zeolite 4A granules (approx. 2.5 mm) are placed in both compartments, red granules in the first compartment and blue granules in the second compartment. The characteristics of the zeolite granules are given in the literature [16]. This compartment is used only for the initial separation of the granules before the premixing. The first and last compartments are used to collect the granules before and after the premixing is done. These compartments are also made of transparent plexiglass with a

height of 60 mm. The second compartment is a premixing device, with 3 segments (marked as 1, 2 and 3), each with a height of 60 mm, and the outlet diameter of 60 mm. The segments are connected in the way that the outlet of the first right-handed segment is connected with second, left-handed segment, at an angle of 90 degrees relative to the vertical axis, Fig. 2b–d. Figure 2b shows the computer model of Ross mixer.

Fig. 2c presents the special design of the Komax static mixer used for this experiment. It consists of three mixing elements, two right-handed Komax segments and one left-handed Komax segment. The elements are made of white plastic (ABS), in thickness of 1.5 mm, by using a 3D printing device (CubePro Trio, used for rapid prototyping). The tube in which the segments are placed is made of 3 mm transparent plexiglass. After passing through three segments of the static mixer, granules fall at the bottom of the lower compartment of the premixer.

Fig. 2d presents the computer model of Komax mixer. Fig. 2e shows Komax mixing element and Fig. 2f presents Ross mixing element computer model. These computer models were used in numerical simulation.

The conditions under which the experiments were conducted are the same as in the numerical simulation conditions.

Numerical model

Numerical evaluations were performed for observed Ross and Komax static mixer configurations. The

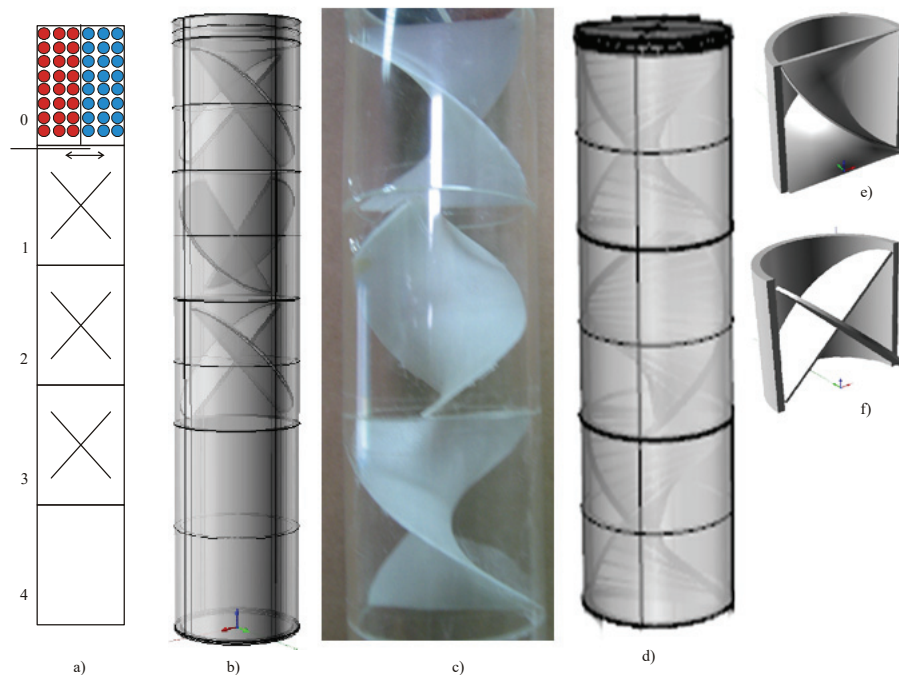


Figure 2. a) Scheme of the static mixer used in the experiment, b) static mixer, type Ross with three elements (3d computer model), c) Komax mixer with three elements used in the experiment, d) static mixer type Komax with three elements (3d computer model), e) mixing element type Komax (3d computer model) and f) mixing element type Ross (3d computer model).

first segment of the mixer is filled with 30,000 spherical particles, diameter 2.5 mm. The inlet compartment filled with 15,000 red particles and a second compartment filled with 15,000 blue particles, outlet-pressure outlet (atmospheric pressure) and wall – the other side of the mixer and the blades of the mixer (Fig. 2a). No slip condition is adopted at the wall. The adiabatic conditions at the walls are applied. It is assumed that the surface roughness is ideal with fresh surface. The influence of the gravity is taken into account and it represents the force which leads the particles to the bottom. The density of the particles released is normalized to the magnitude of the fluid velocity at the inlet. This means that there are more particles released where the inlet velocity is highest. It is assumed that the gas (air) velocity is close to zero, and the impact of fluid on particle movement is minimal. Particle density was 650 kg/m^3 , fluid density was 1.2 kg/m^3 , viscosity $1.8 \times 10^{-5} \text{ kg/ms}$, particle friction coefficient was 0.3, Young's modulus was 10^7 , Poisson's ratio of particles was 0.25, while CFD time step was $5 \times 10^{-5} \text{ s}$ and DEM time step was $5 \times 10^{-6} \text{ s}$.

The set of balance equations (Eq. (1)–(3)) is solved by using the control volume based finite difference method. Semi Implicit Method for Pressure-Linked Equations (SIMPLE) numerical method is used for solving pressure-correction equation from the momentum and mass balance equations [14]. The elements used in numerical mesh are tetrahedral and size of an element is less than 10^{-8} m^3 . A discretization of partial differential equations is carried out by their integration over control volumes of basic and staggered grids. The convection terms are approximated with upwind finite differences, while diffusion and source terms are approximated with central differences [14]. The calculation error for every balance equation and every control volume is kept within limits of 10^{-5} by iterative solution of sets of linear algebraic equations. CFD time step is ten times larger than the DEM time step. The DEM time step is limited by the natural oscillation period of spring-mass system used to model contacting particles. It should satisfy the following equation (m is particle mass and k is stiffness coefficient):

$$\Delta t_{\text{DEM}} \leq \frac{1}{10} 2\pi \sqrt{\frac{m}{k}} \quad (5)$$

Colour image analysis

In order to check the quality of the mixing process, using *RSD* criteria, colour image analysis is performed. Colour images of experimental and computer simulation results were captured by a Sony PowerShot A550, which is a common digital camera for home use. The macro function of the digital camera has been used, to cover a scene area of approximately $\varnothing 60 \text{ mm}$. Samples were placed on a white paper napkin set on a flat white

painted surface, inside the closed chamber, 15 cm below the digital camera. Paper napkins were used in order to avoid undesired reflection effects from chamber's walls. With this setup, it was possible to capture images with negligible shadows and without specular reflections.

Response surface methodology

The RSM method was selected to estimate the main effect of the process variables on the mixing process. The independent variables were the type of the mixing element (Ross or Komax) and the number of elements (1–3), and the dependent variable observed was *RSD* criteria. A model was fitted to the response surface generated by the experiment. The model used was a function of the variables:

$$Y = \beta_0 + \sum_{i=1}^2 \beta_i X_i + \sum_{i=1}^2 \beta_{ii} X_i^2 + \beta_{12} X_1 X_2, \quad k = 1, 2, \dots, 8 \quad (6)$$

where: β are constant regression coefficients.

Analysis of variance (ANOVA) and response surface regression method (RSM) were performed using StatSoft Statistica, for Windows, ver. 10, program.

RESULTS AND DISCUSSIONS

The results of the DEM/CFD simulation are compared with experimental results. The mechanical properties of zeolite granules are taken from [16]. CFD modelling is used to determine the fluid velocity field and the pressure field, and DEM is used for determining the particle behaviour and particle trajectories during the mixing process. In the following, we consider two different representative cases (1, 2 and 3-segment Ross element configuration and 1, 2 and 3-segment Komax elements configuration). The velocity and the pressure field of the fluid phase were obtained *via* CFD calculations, as well as particle trajectories, Fig. 3a–f presents the mixing results, performed with three-segmented Ross and Komax configuration. Fig. 3a–d refer to the fluid phase. The influence of fluid phase on particle behaviour can be significant, especially in the case of forced or turbulent flow. Fluid phase can influence the velocity and acceleration of the particles and that can affect on the trajectory of the particles and forces acting on the particles.

Fig. 3e and f show the trajectory of 8,000 particles through one pass of the mixer. Particle trajectory has influence on the mixing quality. Optimal prolonging of the trajectory contributes better homogeneity of the mixture [3].

DEM analysis is the most reliable and most convincing method to optimize the mixing process according to mixing quality. The results of the numerical simulations of the movement of one representative par-

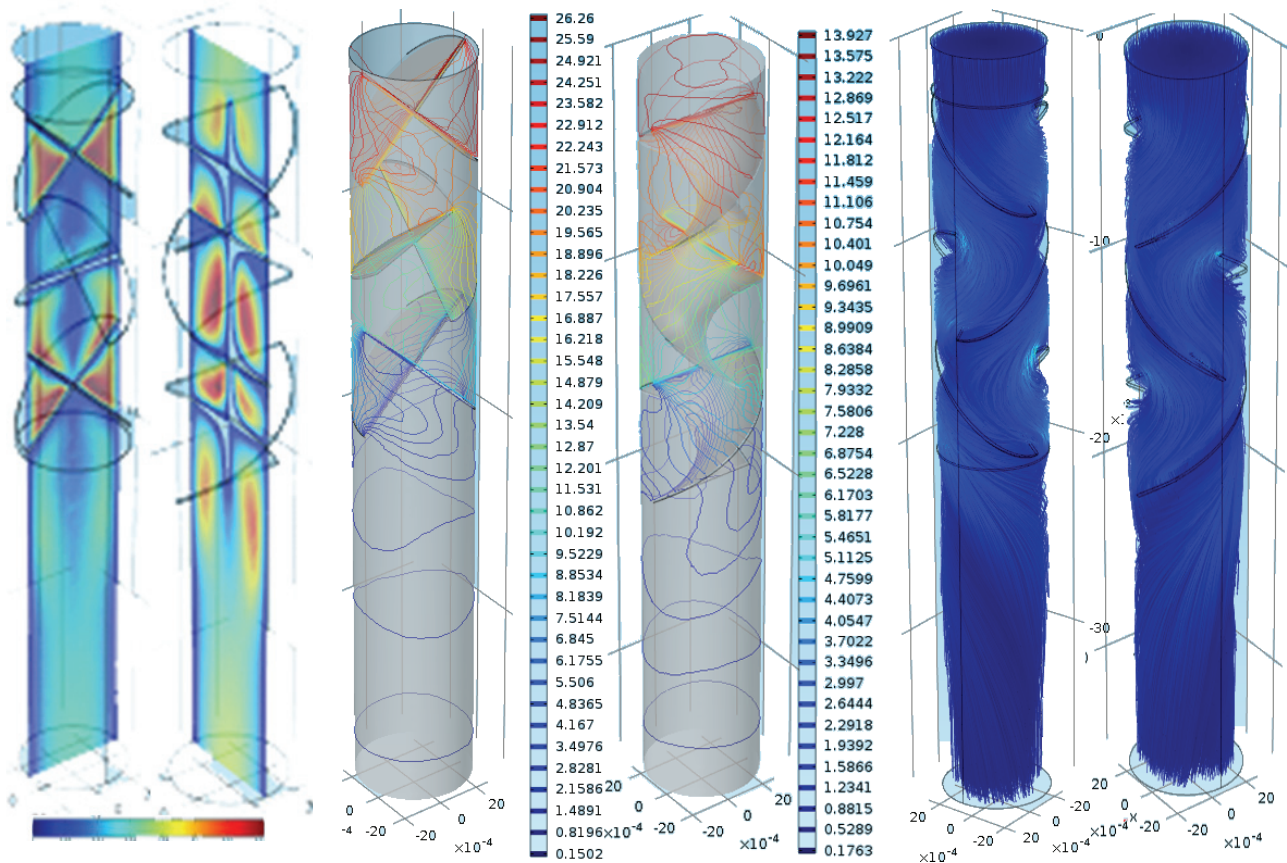


Figure 3. Velocity field of fluid phase, axial direction section (Pa) for: a) Ross and b) Komax mixers configuration; pressure fields in static mixer for: c) Ross and d) Komax mixers; particle trajectories for: e) Ross and f) Komax mixers.

title are shown on Fig. 4 – trajectory, velocity and acceleration in x , y and z direction of one particle during the mixing process (inside the Komax mixer). The position of the representative particle is dramatically changed within the mixer, with significant turn-overs in particle velocity and acceleration, which greatly contributes to the possibility of increased mixing quality [3].

Overall particle trajectory for three-segmented Komax and Ross configurations, gained by numerical simulations were: 436 and 430 mm, respectively.

In this work, RSD was used to follow the evolution of mixing uniformity for the static mixers with different configurations, explained above, [12]:

$$RSD = 100 \frac{\sigma}{\bar{x}}, \quad \sigma = \sqrt{\sum_{i=1}^M (\bar{x} - x_i)^2 (M - 1)^{-1}} \quad (7)$$

where M is the number of samples, x_i the concentration of sample i , and \bar{x} the average concentration of all samples. For instance, concentration of red particles in a sample is calculated as the ratio of the number of red particles and the total number of particles.

The results of numerical simulations of mixing processes in Ross and Komax mixers are presented on Fig.

5. The mixing process begins after particles leave the upper segment (marked as 0, Fig. 2a, as soon as the mobile panel is removed, enabling the granules to fall toward the static mixer). The particles are rapidly blended in the first section, as seen from the figure, reaching the mixing degree of 20–27% at the outlet. Because of the twisted surface geometry, Komax mixing element shows better mixing results in this section (20–22%) compared to Ross (24–27%). Particle velocities are greater in Komax mixer, especially between segment 1 and 2, as seen from Fig. 5. Both mixers shows more effective mixing after second and third section. Komax mixing elements reaches the mixing degree of 6–8% and 4–5% at the outlets, while the mixing quality of 11–13% and 5–6% were obtained at the outlets of section 2 and 3, using Ross elements. This is expected, because of the higher particle velocities in the Komax mixer. The small, but steady decrease in the mixing degree was observed for both Komax and Ross blending elements during DEM/CFD simulation, Fig. 5 (after segment 4). This is due to centrifugal force affecting the motion of granules that exit the mixing compartment. The use of the quadratic grid divider could enable the mixing degree to remain constant after granules left the third mixing element.

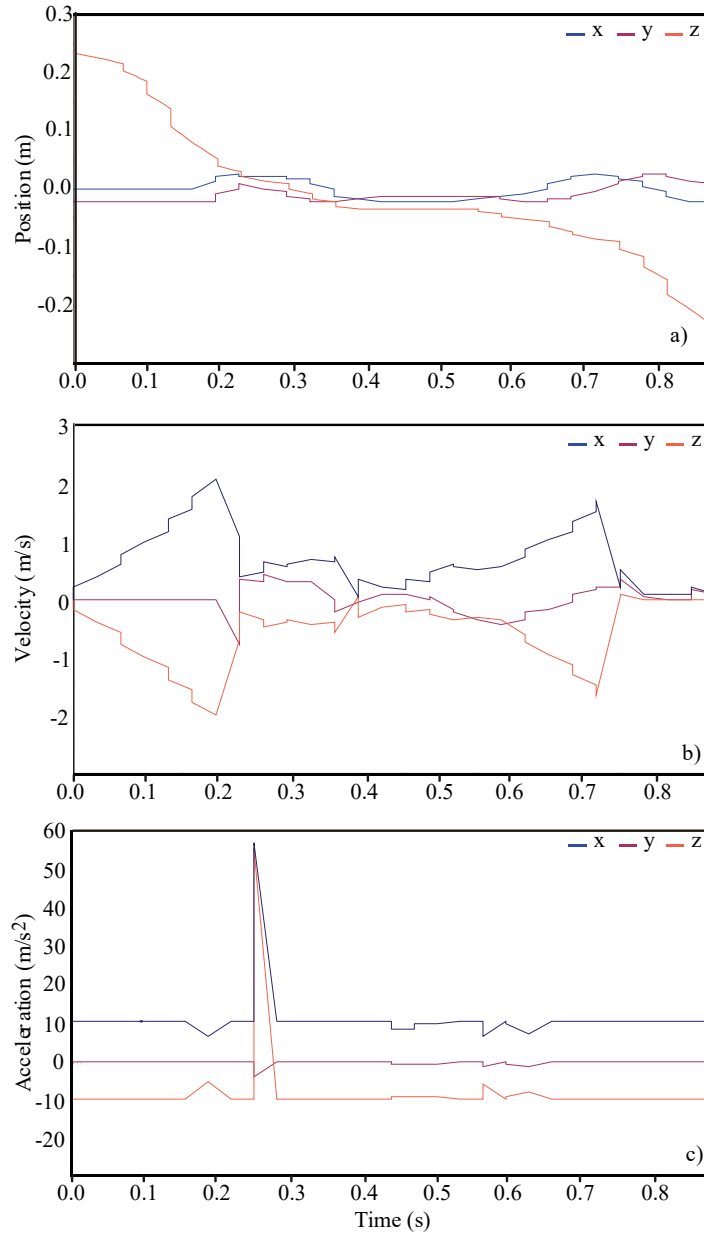


Figure 4. Trajectory, velocity and acceleration in x, y and z direction of one particle during mixing process in Komax mixer.

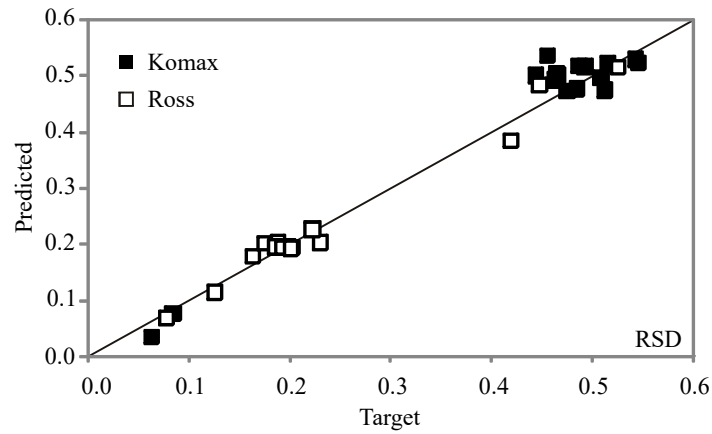


Figure 5. RSD criteria for experimental and numerical results in Ross and Komax mixers.

Table 1 shows the influences of process variables on observed response, for numerical simulation of mixing in Ross and Komax mixers. The analysis revealed that the linear terms of both variables contributed substantially to generate a significant SOP model. The influence of mixing element type (MET) was significant in SOP model, statistically significant at $p < 0.10$ level, while the influence of the number of elements (NE) was the most important in the SOP model calculation ($p < 0.01$). The quadratic term of NE was also very influential (statistically significant at $p < 0.01$ level), as well as the interchange term MET \times NE ($p < 0.10$).

Table 1. Analysis of variance (ANOVA) for experimental and numerical results in Ross and Komax mixers; ⁺significant at $p < 0.01$ level, ^{**}significant at $p < 0.10$ level, MET – mixing element type, NE – number of mixing elements, df – degrees of freedom, SoS – sum of squares, F – F test

	df	SoS	F	p
MET	1	0.002 ^{**}	3.41	0.08
NE	1	0.397 ⁺	646.70	<0.01
NE ²	1	0.107 ⁺	174.49	<0.01
MET \times NE	1	0.002 ^{**}	3.79	0.06
Error	27	0.017		
r^2		0.968		

A high r^2 is indicative that the variation was accounted and that the data fitted satisfactorily to the proposed model. The r^2 value was found very satisfactory and showed the good fit of the model to experimental results.

CONCLUSION

Coupled DEM/CFD approach was used to investigate mechanisms of fluid flow and particle tracking for granular flow. In the DEM, particle–particle and the particle–wall interactions are resolved and the time integration is carried out using Newton's second law of motion. Mixture model was used in CFD analysis for the determination of the characteristics of the fluid phase. DEM analysis was used to determine the particle trajectories and the history of particle positions in order to determine the quality of the mixture. The mixing quality was estimated by a mixing criterion, named RSD (relative standard deviation). The effects of the mixer type and the number of mixing elements on mixing process were studied using analysis of variance (ANOVA). The aim of this study is to predict the behaviour of granules in different mixer configuration and to optimize the number of mixing elements taking into account the price of the final product, the duration of the mixing process and the quality of the mixture. It is obvious that the mixer based on Komax elements enables better mixing quality, compared to Ross, espe-

cially when the height of installation is low. However, the use of Ross is more financially acceptable, due to its simpler geometry. According to the results, the number of mixing elements is more influential parameter than the type of mixing elements. It seems that this type of device can be used only as premixing device and additional mixer is necessary to gain the good quality of the mixture. However, the premixing process can contribute better quality of the mixture and can significantly reduce the mixing time and the cost of the mixing process.

Acknowledgements

This work was supported by the Ministry of Education, Science and Technological Development of the Republic of Serbia, grant No. TR31055.

REFERENCES

- [1] J. Bridgwater, Mixing of powders and granular materials by mechanical means-A perspective, *Particuology* **10** (2012) 397–427.
- [2] A. Ghanem, T. Lemenand, D. Della Valle, H. Peerhosaini, Static mixers: Mechanisms, applications and characterization methods – A review, *Chem. Eng. Res. Des.* **92** (2014) 205–228.
- [3] A. Jovanović, M. Pezo, L. Pezo, Lj. Lević, DEM/CFD analysis of granular flow in static mixers, *Powder Technol.* **266** (2014) 240–248.
- [4] R.K. Thakur, Ch. Vial, K.D.P. Nigam, E.B. Nauman, G. Djelveh, Static Mixers in the Process Industries – A Review, *Trans IChemE* **1** (2003) 787–826.
- [5] M. Rafiee, M. J.H. Simmons, A. Ingram, E. Hugh Stitt, Development of positron emission particle tracking for studying laminar mixing in Kenics static mixer, *Chem. Eng. Res. Des.* **91** (2013) 2106–2113.
- [6] H.E.H. Meijer, M.K. Singh, P.D. Anderson, On the performance of static mixers: A quantitative comparison, *Prog. Polym. Sci.* **37** (2012) 1333–1349.
- [7] P.A. Cundall, O.D. L. Strack, A discrete numerical model for granular assemblies. *Géotechnique* **29** (1979) 47–65.
- [8] M.E. Pierce, PFC3D Modeling of Inter-Particle Percolation in Caved Rock Under Draw, Numerical Modeling in Micromechanics Via Particle Methods, in Proceedings of the 2nd International PFC Symposium, Kyoto, Japan, October 2004, Leiden: Balkema, 2004, pp. 149–156.
- [9] J. Neuwirth, S. Antonyuk, S. Heinrich, M. Jacob, CFD–DEM study and direct measurement of the granular flow in a rotor granulator, *Chem. Eng. Sci.* **86** (2013) 151–163.
- [10] Y. Tsuju, T. Kawaguchi, T. Tanaka, Discrete particle simulation of two-dimensional fluidized bed, *Powder Technol.* **77** (1993) 79–87.
- [11] V. Kumar, V. Shirke, K.D.P. Nigam, Performance of Kenics static mixer over a wide range of Reynolds number. *Chem. Eng. J.* **139** (2008) 284–295.

- [12] M. Poux, P. Fayolle, J. Bertrand, Powder mixing: some practical rules applied to agitated systems, *Powder Technol.* **68** (1991) 213–234.
- [13] A. Lemieux, G. Leonard, J. Doucet, L.A. Leclaire, F. Viens, J. Chaouki, Large-scale numerical investigation of solids mixing in a V-blender using the discrete element method, *Powder Technol.* **181** (2008).205–216.
- [14] S.V. Patankar, *Numerical Heat Transfer and Fluid Flow*, 1st ed., Hemisphere Publishing Corporation, Washington DC, 1980.
- [15] K.W. Chu, B. Wang, D.L. Xu, Y.X. Chen, A.B. Yu, CFD–DEM simulation of the gas–solid flow in a cyclone separator, *Chem. Eng. Sci.* **66** (2011) 834–847.
- [16] J. Lin, X.F. Shu, J.X. Dong, The experimental determination of mechanical properties of zeolite ferrierite crystal, *Mater. Lett.* **59** (2005) 1595–1597.

IZVOD

PROTOK GRANULISANOG MATERIJALA U STATIČKOJ MEŠALICI – DEM/CFD PRISTUP

Lato Pezo¹, Milada Pezo², Aca Jovanović¹, Nenad Kosanić³, Aleksandar Petrović³, Ljubinko Lević⁴

¹Univerzitet u Beogradu, Institut za opštu i fizičku hemiju, Studentski trg 12/V, 11000 Beograd, Srbija

²Univerzitet u Beogradu, Institut za nuklearne nauke Vinča, Laboratorija za termotehniku i energetiku, p. pr. 522, 11001 Beograd, Srbija

³Univerzitet u Beogradu, Mašinski fakultet, Kraljice Marije 16, 11000 Beograd, Srbija

⁴Univerzitet u Novom Sadu, Tehnološki fakultet, Bulevar Cara Lazara 1, 21000 Novi Sad, Srbija

(Naučni rad)

Proces mešanja veoma utiče na kvalitet krajnjeg poluproizvoda i/ili krajnjeg proizvoda, a parametri procesa mešanja i dizajn opreme veoma utiču na efikasnost mešanja, kvalitet proizvoda i cenu proizvoda. U ovom radu, prikazana je upotreba metode diskretnih elemenata (engl. Discrete Element Method – DEM) na modelovanje mešanja granula u različitim konfiguracijama statičkih mešača (korišćene su različite Komax i Ross konfiguracije za mešanje). Za modelovanje protoka fluida primenjena je metoda numeričke mehanike fluida (engl. Computational Fluid Dynamic – CFD), korišćenjem Ojlerovog dvofaznog modela. Povezivanjem rezultata ove dve metode dobijaju se pouzdan, dovoljno tačan i adekvatan model koji daje rezultate koji odgovaraju eksperimentalnim merenjima. Statičke mešalice se široko koriste u industiji prerade hrane, farmaceutskoj ili hemijskoj industriji. Ovaj tip mešalice se koristi uglavnom kao predmešač, pre glavnog mešanja, pri čemu se značajno smanjuje vreme mešanja i štedi energija. Ova vrsta mešanja nije dovoljno ispitivana u literaturi. Kvalitet mešanja granula zeolita u ovom radu je ispitivan dobro poznatim kriterijumom za kvalitet mešanja, pod nazivom relativna standardna devijacija. Uticaj tipa mešalice i broja elemenata za mešanje ispitivani su analizom varijanse (ANOVA). Cilj ovog rada je bio da se predvidi ponašanje granulisanog materijala u različitim konfiguracijama mešalice i da se optimizuju parametri procesa uzimajući u obzir trajanje procesa mešanja, kvalitet mešavine i cenu finalnog proizvoda. Za potrebe ovog rada, napravljene su statičke mešalice tipa Ross i Komax od providnog pleksiglasa, dizajnirane u CAD paketu, napravljene korišćenjem CNC glodalice. Pošto su napravljene elementi bili prozirni, praćenje procesa mešanja granula je bilo i vizuelno. Praćene su i analizirane trajektorije, brzine i ubrzanja čestica, u cilju procene kvaliteta procesa mešanja. Dobro poznati kriterijum za kvalitet mešanja, pod nazivom relativna standardna devijacija (RSD) je korišćen za ovu svrhu. Optimizacija dimenzija i parametara mešanja u statičkoj mešalici je izvedena korišćenjem matematičkog modeliranja. Cilj ovog rada je bio da se predvidi ponašanje granuliranog materijala u različitim konfiguracijama mešalice i da optimizuje parametre procesa uzimajući u obzir trajanje procesa mešanja, kvalitet mešavine i cenu finalnog proizvoda mešanja. U istraživanju je primećeno da su Komax elementi primenljiviji, u poređenju sa Ross elementima, posebno kada je visina instalacije mala. Međutim, upotreba Ross je finansijski prihvatljivija, zbog njegove jednostavnije geometrije. Dodatni pregrada sa kvadratnim otvorima, koja se postavlja na izlazu iz statičke mešalice, koristi se da bi se umirilo kretanje granula na obodu cevi, kao i da smanji segregacija granula.

Ključne reči: DEM/CFD • Statički mikser • Komax • Ross • Trajektorije čestica

Viscoelastic behaviour of carboxyl-terminated (butadiene-co-acrylonitrile)-based composite propellant binder containing polyglycidyl-type bonding agent

Saša J. Brzić¹, Gordana S. Uščumlić², Mirjana V. Dimić¹, Miloš Tomić², Vesna Ž. Rodić¹,
Bojana Z. Fidanovski¹

¹Military Technical Institute, Belgrade, Serbia

²Faculty of Technology and Metallurgy, University of Belgrade, Belgrade, Serbia

Abstract

The influence of tris(2,3-epoxypropyl) isocyanurate as bonding agent on the physicochemical, viscoelastic and uniaxial tensile mechanical properties of carboxyl-terminated (butadiene-co-acrylonitrile) cured with the polyglycidyl ether of glycerol and epichlorhydrin was investigated. Cross-link density values were estimated by swelling measurement. Temperature and frequency dependencies of rheological behaviour parameters (storage modulus, loss modulus, loss factor and glass-rubber transition temperature) were also analyzed. Based on the frequency dependencies of storage modulus, put in the range of temperature from -50 to 20 °C by the experiment, master curves ($\log G'$ vs. $\log \omega$) were generated, reaching broader frequency interval in comparison to that used in the measurements. By choosing the glass-rubber transition temperature to be the reference one, Williams-Landel-Ferry equation constants were determined. Further, material constants, fractional free volume at the glass-rubber transition temperature and thermal coefficient of free volume expansion were calculated. Although small quantity of tris(2,3-epoxypropyl) affects the network density, the dynamic mechanical analysis showed that the bonding agent content did not affect the glass-rubber transition temperature of the tested materials.

Keywords: carboxyl-terminated (butadiene-co-acrylonitrile), viscoelastic properties, glass-rubber transition temperature.

Available online at the Journal website: <http://www.ache.org.rs/HI/>

The essential ingredients of a composite propellant are a crosslinked binder (an organic polymer) and an oxidizer (usually ammonium perchlorate). The binder, as the name implies, holds the composition together and acts as an auxiliary fuel. The use of hydroxyl-terminated (HTPB) and carboxyl-terminated (CTPB) poly(butadienes) as prepolymers for composite propellants is the most common choice of polymeric materials to achieve the desired mechanical properties of the propellant in rocket motors [1–3]. In order to improve uniaxial tensile characteristics, an interaction between the ammonium perchlorate (AP) particles and the polymeric binder is necessary, which is achieved by bonding agents added to composite propellant composition. Bonding agents are typically used in HTPB-based composite propellants since these polymers are weakly polar [4]. Due to the highly polar carboxyl (-COOH) group, carboxyl-terminated prepolymers (CTPB) do not require the use of bonding agents. If for composite propellant production, carboxyl-terminated (butadi-

ene-co-acrylonitrile) (CTBN) based propellant binder is taken, experiments have shown that tris(2,3-epoxypropyl) isocyanurate (TEIC) as bonding agent significantly improves uniaxial tensile characteristics [5]. The molecular structure of the polymer based composite propellant binder is the largest factor in determining the mechanical properties of the mixed and cured propellant. The mechanical properties of composite propellants depend strongly on the time, temperature, loading procedure and loading history [6]. Since the bonding agent is ingredient that is added to modify the mechanical properties of the propellant, precise knowledge of the dynamic mechanical behaviour is extremely important.

The main objective of this paper is to broaden our knowledge of applying dynamic mechanical analysis to the study of CTBN-based propellant binder. As far as we are aware, there are no publications in the extensive literature, except our previous investigation, that have surveyed not only the viscoelastic properties of CTBN-based composite propellant binder but also the effect of this type of bonding agent on the CTBN-based composite propellant binder behavior.

SCIENTIFIC PAPER

UDC 678-13:678.7:544

Hem. Ind. 70 (5) 547-556 (2016)

doi: 10.2298/HEMIND150918062B

Correspondence: S.J. Brzić, Military Technical Institute, Ratka Resanovića 1, 11000 Belgrade, Serbia.

E-mail: sasabrzc@gmail.com

Paper received: 18 September, 2015

Paper accepted: 3 November, 2015

EXPERIMENTAL

Materials

Four CTBN-based composite propellant binder compositions (Table 1) selected for this study consisted of 100 phr of CTBN (1300×15, BF Goodrich, viscosity at 25 °C: 66.2 Pa s, carboxyl functionality: 1.9, number-average molecular weight: 3800 g/mol, specific gravity at 23 °C: 0.931 g/cm³, glass-liquid transition temperature, T_g : -63.3 °C), 1.7 phr of antioxidant (2,2'-methylene-bis(4-methyl-6-tertbutyl phenol), commercially available as a product called AO 2246 and under a lot of other brand names (Fluka AG, Switzerland) and 0.44 phr of cure catalyst (iron(III)-acetylacetonate, (Fe(acac)₃, Merck-Schuchardt, Germany). Mix ratio of propellant binder ingredients is expressed in phr, this means parts per hundred of resin based on 100 parts of CTBN.

Preferred curing agents for carboxyl functional prepolymers are multifunctional epoxides. When epoxy curing agents are used to cure a carboxy functional prepolymer in composite propellant formulation, the E/COOH ratio between the two components is preferably in the range of from 1.05 to about 1.2. Presence of ammonium perchlorate as oxidizer, causes side reactions including the curing agent. As a result, less complete polymer network is formed. The E/COOH ratio between the epoxy groups E of the curing agent to the carboxyl groups COOH of the CTBN was 1.20. The curing of CTBN was achieved by an epoxid curing using LX 112 (polyglycidyl ether of glycerol and epichlorhydrin, EW: 145, Ladd Research Industries, USA).

The chemical structures of the propellant ingredients are shown in Figure 1.

Tris(2,3-epoxypropyl) isocyanurate was prepared by the reaction of cyanuric acid and epichlorhydrin in

accordance with a modified literature method [7]. Investigated composite propellant binder samples differ from each other in bonding agent content. Composition CPB00 is a baseline propellant binder composition containing no bonding agent. TEIC content (ξ) varied from 0.1 to 0.3 wt.% of the total mass of the investigated propellant binder.

Methods

Mixing of propellant binder formulations was conducted in a 1.5 l DRAIS FH planetary mixer at a temperature of 60 °C. CTBN, AO 2246 and TEIC were blended thoroughly for 15 min at ambient pressure and then vacuum mixed for another 15 min. LX 112 was then added to the mixture, mixed for 10 minutes at ambient pressure and then vacuum mixed for another 10 min. Then, Fe(acac)₃ was added to the mixture and the same procedure was repeated. Finally, the prepared mixture was cast and cured in teflon-coated metal plates to form 3 mm thick slabs. The curing was performed for 5 days at 70 °C.

The network density of a cured propellant binder samples was estimated by the degree of swelling by an appropriate solvent at equilibrium [8]. As solvent, toluen was used. The gravimetric technique was applied for measuring the swell ratio of crosslinked propellant binder networks. Swelling test was carried out on rectangular specimens with length of 20 mm, width of 20 mm and thickness of 3 mm at the $T = 25$ °C. In preliminary experiments, the sample was allowed to swell for 4 days, but mass became constant after two days, indicating that equilibrium was reached. Therefore tested binder samples were swelled for two days.

Swell ratio is computed as:

Table 1. Investigated propellant binder compositions, phr (wt.% of the total mass of the tested propellant binder)

Sample	Propellant binder				
	CTBN 1300x15	LX 112	TEIC	AO 2246	Fe(acac) ₃
CPB00	100 (90.22)	8.70 (7.85)	(0)	1.70(1.53)	0.44 (0.40)
CPB01	100 (90.13)	8.70 (7.84)	(0.1)	1.70(1.53)	0.44 (0.40)
CPB02	100 (90.04)	8.70 (7.83)	(0.2)	1.70(1.53)	0.44 (0.40)
CPB03	100 (89.95)	8.70 (7.83)	(0.3)	1.70(1.53)	0.44 (0.40)

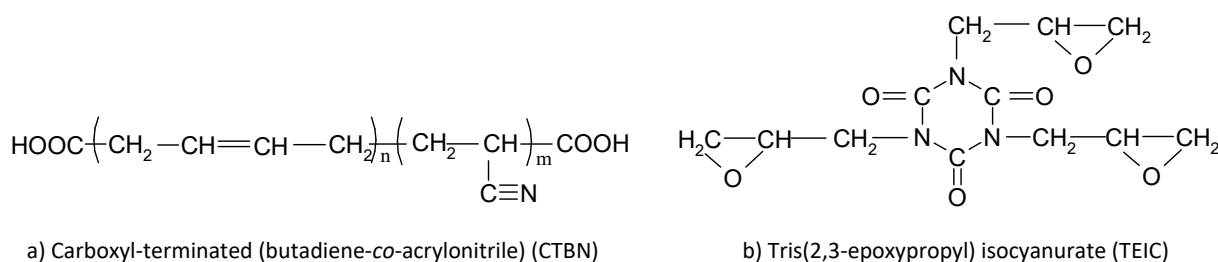


Figure 1. The chemical structures of the ingredients of the investigated propellant binders.

$$q = \frac{W_d + W_g - W_d K}{W_d} \quad (1)$$

where: W_d – sample weight before immersed in toluen, W_g – sample weight after two days in toluen and K – ratio of the densities of the solvent to the polymer.

The density of toluene is 0.86 g/cm^3 , and those of cured propellant binder samples were in the range from 0.953 to 0.956 g/cm^3 , measured following Archimedes principle [9].

The value of network density, N , of the binder samples was estimated by the value of v_r using the Flory–Rehner equation, Eq.(2):

$$\ln(1 - v_r) + v_r + \chi v_r^2 = -N V_1 \left(v_r^{\frac{1}{3}} - \frac{v_r}{2} \right) \quad (2)$$

where: v_r – volume fraction of the binder in the swollen gel, χ – Flory–Huggins polymer–solvent interaction parameter, V_1 – molar volume of the solvent, N – network density of the tested binder sample. The value of Flory–Huggins polymer–solvent interaction parameter (χ) taken for polybutadiene–toluene system and the value of molar volume V_1 of swelling solvent are: 0.35 and $106 \text{ cm}^3 \cdot \text{mol}^{-1}$, respectively [8].

The DMA measurements were carried out in the torsion deformation mode by using a mechanical spectrometer model “RMS-605” manufactured by the former Rheology Business Unit of company Rheometric Scientific Inc., Piscataway, NJ, USA. The temperature range applied was from -90 to $80 \text{ }^\circ\text{C}$, the heating rate was $5 \text{ }^\circ\text{C min}^{-1}$ and the single frequency point of 1 Hz was chosen. Strain amplitude was 0.1% . The samples for DMA tests were of rectangular bar shape ($63 \text{ mm} \times 12 \text{ mm} \times 3\text{--}4 \text{ mm}$). Complex shear modulus was determined, $G^*(\omega) = G'(\omega) + iG''(\omega)$. Extracted data were the shear storage and loss moduli, G' and G'' , respectively, and the loss factor $\tan \delta = G''/G'$. Each binder sample was first tested at a constant frequency and temperature over above mentioned range.

The temperature corresponding to the maximum of the loss factor is taken as the nominal glass transition temperature, correctly named as glass–rubber transition temperature (T_g) [10]. Finally, the viscoelastic properties were measured over three decades of frequency in the temperature range from -50 to $20 \text{ }^\circ\text{C}$, scanned with a heating rate of $5 \text{ }^\circ\text{C min}^{-1}$.

Frequency was varied from 0.1 to 100 rad/s , with 16 equidistant values on a logarithmic scale. The measurement reproducibility is very high so only one sample per each testing condition was tested [11].

DSC analyses, in order to investigate the thermally based glass–rubber transition temperature of the samples, were carried out using the DSC Q20 manufactured by TA Instruments with liquid nitrogen cooling for low temperatures. The temperature scale was calibrated

using the melting temperature of high purity indium. The small amount of the sample ($\sim 5 \text{ mg}$) was scanned with a heating rate of $10 \text{ }^\circ\text{C min}^{-1}$, starting from $-90 \text{ }^\circ\text{C}$ and ending at $50 \text{ }^\circ\text{C}$. The glass–rubber transition temperature of the sample was determined from the midpoint of the transition.

The uniaxial tensile mechanical properties of the investigated samples were evaluated at $20 \text{ }^\circ\text{C}$ using INSTRON 1122 uniaxial tensile test machine fitted with a 500 N load cell. Small dog bone samples (115 mm length, 25 mm width and 3 mm thickness) were used. Crosshead speed of tensile machine was 50 mm/min , while the effective gauge length of the test samples was 46.5 mm .

RESULTS AND DISCUSSION

Network density of propellant binder samples

Since the swollen binder sample is very touch-sensitive and prone to cracking, the gravimetric technique is used for measuring the swell ratio of cross-linked propellant binder network. Results of the analysis (Table 2) show that with the increase of TEIC content, the cross-link density of the investigated binder samples increase also. The highest N value is observed for CPB02 (0.2 mass\% of TEIC) binder sample. We conclude that the cross-link density of a polymer network cannot be determined definitely using this method alone. Gel fraction, as a result of sol–gel analysis could be important additional molecular parameter when prediction of cross-link density of a polymer network is contemplated. However, the increase in N value suggests that the degree of cross-linking should increase.

Table 2. Values for network density N and volume fraction of binder in swollen gel v_r of propellant binder samples determined by swelling tests.

Parameter	Sample			
	CPB00	CPB01	CPB02	CPB03
$\xi / \text{mass\%}$	0	0.1	0.2	0.3
v_r	0.102	0.108	0.112	0.110
$N \times 10^{-5} / \text{mol} \cdot \text{cm}^{-3}$	4.37	4.90	5.26	5.10

The increase of the network density value points to the fact that the functional epoxy groups of TEIC are involved in the propellant binder network formation.

Dynamic mechanical analysis of composite propellant binder samples

Based on a weakly cross-linked polymeric matrix, composite rocket propellants show very large changes in mechanical properties with temperature [12]. Figure 2 shows the viscoelastic response of baseline composite propellant binder sample CPB00 in terms of G' , G'' and $\tan \delta$ as a function of temperature.

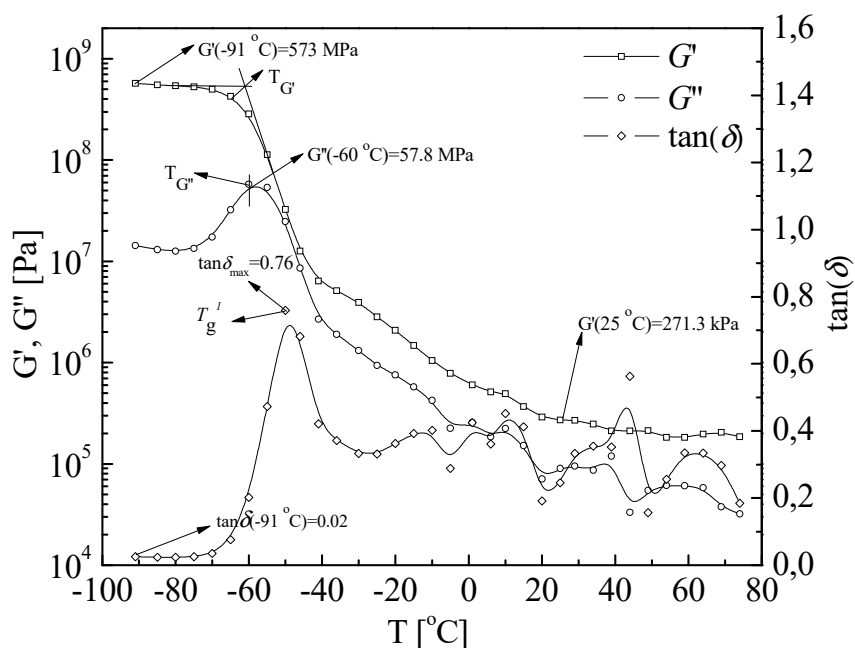


Figure 2. Characteristic values of the CPB00 baseline composition shown by the DMA thermogram of $\omega = 6.28 \text{ rad s}^{-1} = 1 \text{ Hz}$.

It follows from Figure 2 that the G' is almost constant at low temperatures and it reaches the maximum value in the region below the glass transition (-70 to -40 °C). The transition from the glassy to the rubbery state (the onset point on the G' - T curve at $T = -65$ °C) has as consequence a drop in the G' value by a factor of about 90 (from 573 MPa at -91 °C to 6.4 MPa at -40 °C). With increasing temperature (between $T = -40$ °C and $T = 20$ °C) the G' curve exhibits a two-step character, indicative of two separate relaxation processes. Similar temperature dependence of G' curve was observed in the CTBN-based composite propellant composition having AP [5]. Thus, the existence of two relaxation process observed in the composite propellant composition could not be attributed only to the influence of AP solid particles on the polymer network mobility. Copolymers often show a broadening of the transition region with a decrease in the slope of the modulus curve. Part of broadening of the transition region could be due to the heterogeneity in the molecular weight between cross-links. Also, the reason for slow decrease of the storage modulus could be crystallinity within a polymer structure of tested propellant binder samples [13].

The glass–rubber transition temperature (T_g) of elastomer bonded composite propellant is one of the most important property determining their in-service application [14]. This means that the T_g value of the composite propellant binder must be lower than the minimum service temperature (usually -40 to -54 °C depending on application).

A molecular interpretation of the viscoelastic behavior can be given considering the $\tan \delta$, which describes molecular rearrangement regions, corresponding to the binder fractions with different mobility. Poly(butadiene)-based elastomers contain soft and rigid segments [6]. The soft segments consist of large flexible non-crystalline polymer chains, in this case, poly(butadiene), while rigid (hard) segments consist of cross-linking units.

The peak of $\tan \delta$ positioned between $T = -50$ °C and $T = -45$ °C (its temperature location is designated as T_g), is attributed to the glass–rubber transition temperature (Table 3). This relaxation process involves reorientational motions of prepolymer (CTBN) main chains between the crosslinks within the soft segment regions. These polymer network segments have very low density of ester groups and are the polybutadiene

Table 3. $\tan \delta_{(\max)1}$ values and T_g (°C) values determined by G'' , G' , $\tan \delta$ and from DSC curves

Sample	T_g / °C				Maximum value of $\tan \delta_{(\max)1}$
	T in max of G''	Tangens method with G'	T in max. of $\tan \delta$	DSC at 10 °C/min	
CPB00	-57.9	-64.3	-48.7	-62.4	0.76
CPB01	-59.8	-66.3	-47.5	-62.0	0.57
CPB02	-57.9	-64.2	-48.5	-60.5	0.83
CPB03	-56.5	-62.2	-47.9	-62.8	0.85

part of binder which reorient at very low temperatures. The T_g value for the baseline composition, CPB00, is -48.7°C .

The peaks, that appear at higher temperatures, between -30 and 60°C , correspond to the relaxation process related to the motions within hard segment units. Hard segments could also contain polymeric chains formed by the reaction of secondary hydroxyl groups and epoxy groups [15] (Figure 3). However, the parts of $\tan \delta$ above seem somewhat scattered in data, so interpretation is difficult to give.

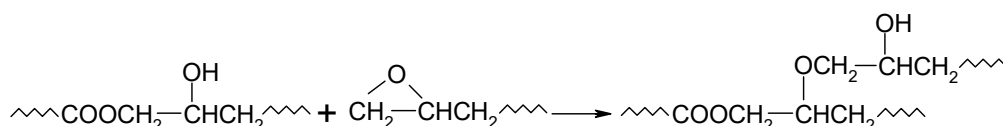


Figure 3. The reaction of the epoxy group of bonding agent TEIC and the secondary hydroxyl group of the binder system formed by the curing reaction between CTBN and the epoxy-based curing agent.

The Figure 4 shows temperature dependencies of the storage modulus, G' , loss modulus, G'' and the loss factor, $\tan \delta$ of the composite propellant binder samples. CPB01 binder sample (0.1% TEIC) has the low-

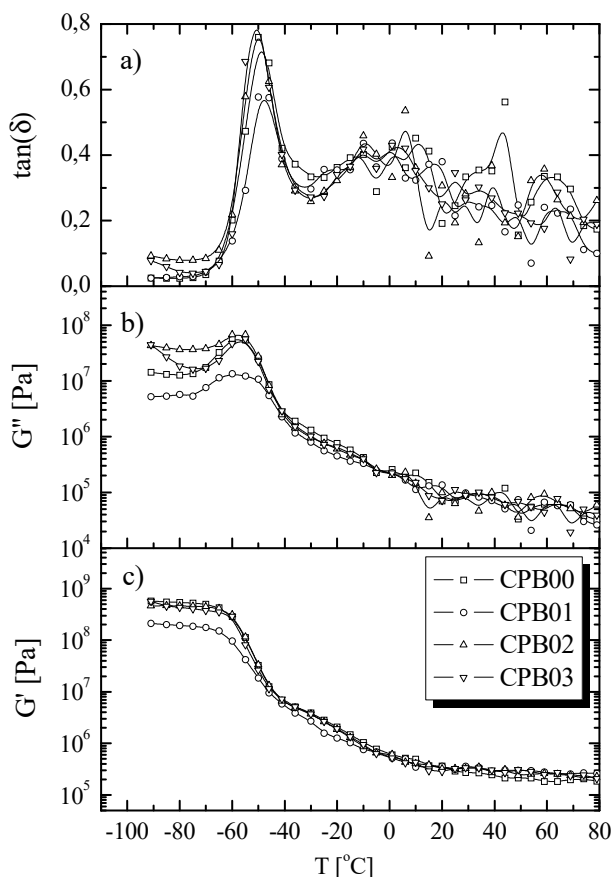


Figure 4. Temperature dependencies of: a) loss factor ($\tan \delta$), b) loss modulus (G'') and c) storage modulus (G') for the investigated propellant binder samples.

est values of G' in the plateau of glassy state. Modulus in the glassy state is determined primarily by the strength of the intermolecular forces and the way the polymer chains is packed [16]. The increase in storage modulus values with increasing TEIC content suggests that a tougher, more rigid network is obtained at higher TEIC concentrations. The results are consistent with swelling measurements which indicate an increase in the crosslink density with introduction TEIC in binder samples.

For the propellant binder samples only quite small variations in T_g were observed, despite the changes in effective crosslink density as evident in the storage modulus values. The reason is the concentration of cross-link points apart from the polybutadiene parts, which are responsible for the main glass-rubber transition at low temperatures.

For all binder samples, regardless the TEIC content, T_g values are located in the narrow temperature range ($T_g \approx -50^\circ\text{C}$).

Numerous studies indicate that the restricted mobility and the heterogeneity of the polymer system arise from the presence of cross-link within the polymer network [17]. Crosslinks are leading towards the decrease in number of possible conformational motions, *i.e.*, conformational freedom of polymer chain segments, resulting in limited mobility regions around the crosslink points. It is also significant to consider the influence of crosslink density on the glass-rubber transition temperature position.

Extremely high crosslink density values shift the glass-rubber transition toward higher temperatures. Glass-rubber transition temperatures, determined by DSC (Figure 5 and Table 3), are lower than the ones determined by DMA. The reason is the “static” determination, which means no mechanical deformation causing strain hardening is applied, neglecting the volume change by thermal expansion [18].

The invariance in T_g values, regardless of the method of determining, indicates that distances between the crosslink points within the polymer network of tested binder samples are such that the restrictions affected by the presence of the bonding agent during the crosslink process do not contribute to differences in T_g value. In other words, cooperative reorientational motions of polymer network segments, related to main

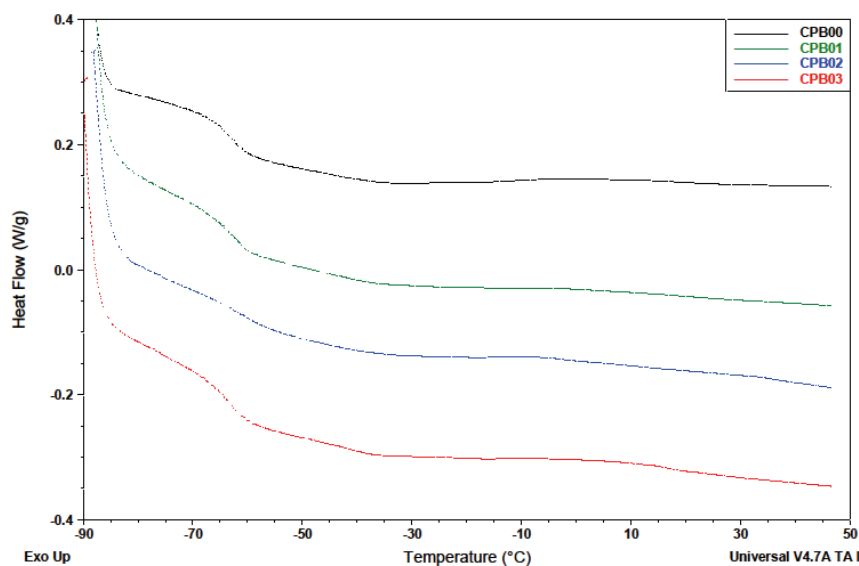


Figure 5. DSC curves of tested binder samples.

relaxation transition are not influenced. The corresponding relaxation time is only changed minor by the structural changes in binder cross-link structure due to TEIC addition.

In Table 3 are shown the intensity of T_g , $\tan \delta_{(\max)1}$, values on the loss factor curve for the tested propellant binders. The $\tan \delta_{(\max)1}$ value is influenced by the segmental motion of the polymer chains. The lower the mobility restrictions on the polymer chains are, the higher the $\tan \delta_{(\max)1}$ values. Although the $\tan \delta_{(\max)1}$ decrease with addition of 0.1 wt.% of TEIC, further increase bonding agent content significantly increase this value. The maximum was recorded for the CPB03 propellant binder sample. This can be explained by inhibition of the chain segment relaxation processes or by an increase in the rigidity of the chain segments, increasing the propellant polymer network heterogeneity.

Frequency dependence of composite propellant binder samples

Figure 6 shows the frequency dependences of G' of propellant binder samples. Storage modulus increases in a regular fashion with increasing frequency or decreasing temperature, suggesting that time-temperature superposition of the data is possible. Similar results were obtained for each of the four propellant binder samples.

The storage modulus *versus* temperature curves at various frequencies were shifted using the time-temperature superposition principle (tTSP), based on the assumption of the equivalence loading in temperature and time [19]. The amount of shifting along the horizontal (x -axis) of each curve to align with the reference temperature curve is generally described by the Wil-

liams-Landel-Ferry (WLF) equation [20], which defines the shift factor a_T , in dependence of the temperature change:

$$\log(a_T(T)) = \frac{-C_1(T-T_0)}{C_2 + T - T_0} \quad (3)$$

The symbols are: a_T – shift factor (representing the ratio between the time needed for some phenomenon to be developed at certain temperature T and the time for the same phenomenon at reference temperature, T – test temperature, T_0 – reference temperature, C_1 , C_2 – WLF constants, which depend on the reference temperature. The authors of the WLF equation found that for many amorphous polymers, independent of chemical structure and with the glass transition temperature as reference temperature, the two constants C_1 and C_2 have universal values of 17.44 and 51.6 °C, respectively. But surely this is a rough approximation. For more accurate calculations it is necessary to determine the values of a shift factor a_T , and constants C_1 and C_2 for each material in consideration.

The master curve reference temperature was $T_0 = -20$ °C. In practice, it is best to choose a reference temperature at the midpoint of the data and superpose the data to this temperature [13]. Figure 5 shows several important features concerning the viscoelastic response of the propellant binder samples. G' reaches the maximum at low temperatures (high frequencies). At higher temperatures (lower frequencies) G' curves enter the rubbery plateau. Master curves of the binder samples show a gradual slope in transition region. Storage modulus change along with the strain rate change is small, indicating these materials are almost insensitive to the strain rate, *i.e.*, temperature. The influence of

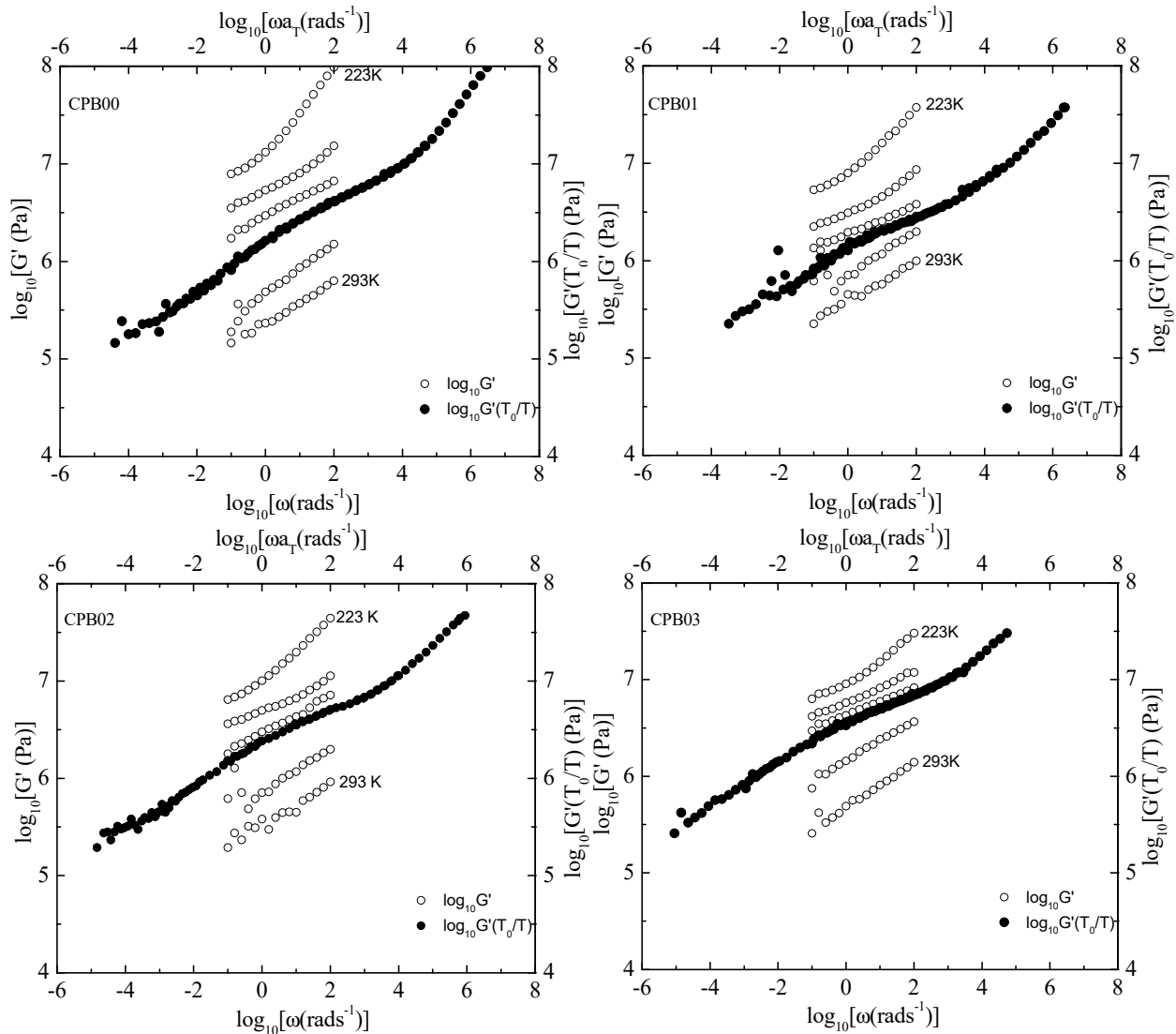


Figure 6. Storage modulus (G') as a function of frequency for tested binder samples and corresponding master curves established with the reference curve obtained at $T_o = -20$ °C.

reference temperature's choice on master curve's position and shape of storage modulus frequency dependence for a binder sample CPB00 is shown in Figure 7.

It is notified that, regardless of the reference temperature, master curves are of the same shape, but the curve representing higher reference temperature is shifted to the higher frequency. The temperature dependency of shift factor a_T values for all binder samples is shown in Table 4.

From the relation between WLF equation constants obtained with two reference temperatures the relation given in Eqs. (4) and (5) can be obtained. In one case, the glass–rubber transition temperature T_g is reference, and in the other case the reference temperature is named T_o .

$$C_{1,g} = \frac{C_1 C_2}{C_2 + T_g - T_o} \quad (4)$$

$$C_{2,g} = C_2 + T_g - T_o \quad (5)$$

Further on, between the two sets of constants the Eq.(6) is valid and Eq.(7) results from above:

$$C_1 C_2 = C_{1,g} C_{2,g} \quad (6)$$

$$T_g - C_{2,g} = T_o - C_2 = T_{inf} \quad (7)$$

T_{inf} is the temperature at which, regardless the way T_o is selected, the $\log(a_T(T))$ value becomes infinite according to WLF equation, see Eq. (8). Physically, it is the temperature at which cooperative motions of polymer network segments appear at infinitely small deformation frequencies, being previously restricted at glass–rubber transition temperature. The WLF equation formulated with T_g as reference is given in Eq.(8):

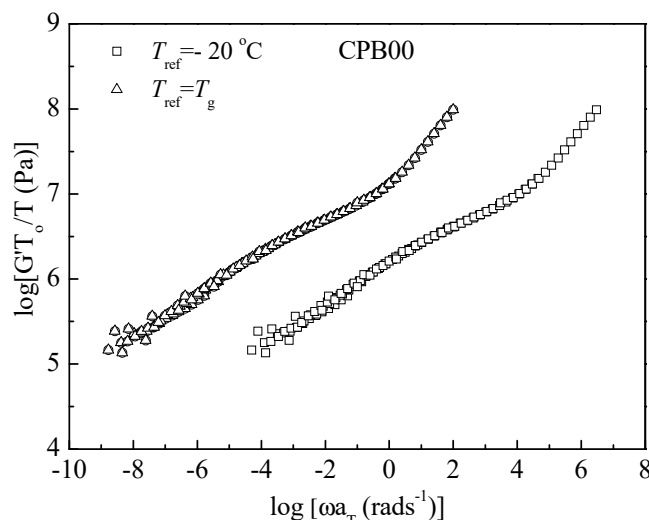


Figure 7. Master curves of storage modulus (G') for the sample CPB00 shown for two referent temperatures, $T_{ref} = T_g$ and $T_{ref} = T_0 = -20$ °C.

$$\log(a_T(T)) = \frac{-C_{1,g}(T - T_g)}{C_{2,g} + T - T_g} \quad (8)$$

Since the WLF equation is based on the free volume concept, the following relations can be derived [21]:

$$C_{1,g} = \frac{B}{2.303f_g} \quad (9)$$

$$C_{2,g} = \frac{f_g}{\alpha_f} \quad (10)$$

where: B is a constant in the Doolittle equation, which is assumed equal to unity, f_g is the fractional free volume of the elastomer at the T_g and α_f is the thermal coefficient of expansion of the free volume above T_g .

Table 5 presents the WLF and free volume constants for the investigated binder samples.

Obtained results confirm that WLF equation constants $C_{1,g}$ and $C_{2,g}$, are not “universal”, but roughly approximated by the universal values. If “universal” constants are used, significant mistakes would be made for estimating how composite propellant behaves at different temperatures and strain rates. According to literature data, there are moderate deviations from the given $C_{1,g}$ value depending on the polymer type, while

with constant $C_{2,g}$ deviations are larger [22]. This also applies to our binder samples. α_f/B values are lower than the one derived from WLF equation. Obtained f_g/B values are within the boundaries found in literature for most of polymer systems.

Uniaxial tensile properties of propellant binder samples

The average and standard deviation (SD) values of uniaxial tensile mechanical properties, *i.e.*, the tensile strength (σ_m), the strain at maximum load (ϵ_m) and Young's modulus (E) for the investigated binder samples are listed in Table 6.

All of the values listed in Table 6 were obtained as an average of five specimens. The uniaxial tensile properties of composite propellant depend on tensile properties of propellant binder, which in turn determines the strain capability of the propellant. High strain capability of binder network is favourable considering long shelf life of propellant system [23]. The value of the strain at maximum load of the baseline composition, primarily caused by the prepolymer (CTBN) molecular weight, is 464.34%, which is quite acceptable value compare to that of other materials used for composite propellant manufacture. CTBN-based composite propellant binder gives much higher value of the strain at

Table 5. Experimental values of WLF equation and free volume constants

Sample	C_1	$C_2 / ^\circ\text{C}$	$C_{1,g}$	$C_{2,g} / ^\circ\text{C}$	$T_{inf} / ^\circ\text{C}$	$(f_g/B) \times 10^{-2}$	$(\alpha_f/B) \times 10^{-4} / \text{K}^{-1}$
Universal ^a	–	–	17.40	51.60	–	2.5	4.80
CPB00	13.37	120.29	17.62	91.29	–141.3	2.46	2.70
CPB01	16.23	133.45	20.74	104.45	–154.5	2.09	2.00
CPB02	14.97	120.36	19.88	90.61	–140.6	2.18	2.41
CPB03	10.64	88.71	15.92	59.27	–109.3	2.73	4.60

^aThese values were determined by averaging the values of a wide variety of polymers [20]

Table 6: Values of tensile strength (σ_m), strain at maximum load (ε_m) and Young's modulus (E) on uniaxial tensile test of CTBN based propellant binder samples at $T = 20$ °C. SD: standard deviation, ξ : TEIC content of the total mass of the investigated propellant binder

Sample	ξ / wt.%	σ_m (SD) / MPa	ε_m (SD) / %	E (SD) / MPa
CPB00	0	0.275 (0.33)	464.34 (38.40)	0.179 (0.43)
CPB01	0.1	0.287 (0.19)	529.42 (56.41)	0.188 (0.23)
CPB02	0.2	0.250 (0.37)	473.03 (40.94)	0.165 (0.21)
CPB03	0.3	0.219 (0.10)	369.98 (25.36)	0.182 (0.14)

maximum load compare to the HTPB-based one, which can have the value which does not exceed 275%. Addition of 0.1 wt.% TEIC in CTBN based propellant binder increases all uniaxial tensile properties. On one hand, increasing the tensile strength and Young's modulus is caused by larger amount of hard segments. On the other hand, the incorporation of TEIC into the propellant binder formulation increases the value of strain at maximum load as a consequence of the increased molecular weight of the polymer chains between the crosslink points. TEIC at 0.1 wt.% causes an increase in tensile strength of 4.62% with a simultaneous increase in the strain at maximum load value of 14.02%. Further increase of TEIC content resulted in a slight decrease of values of all uniaxial tensile characteristics.

CONCLUSIONS

Samples of composite propellant binder based on carboxyl-terminated (butadiene-co-acrylonitrile) cured with polyglycidyl ether of glycerol and epichlorhydrin (LX-112) containing the bonding agent tris(2,3-epoxypropyl) isocyanurate (TEIC) were investigated with DSC, DMA and uniaxial tensile testing. Although the network density increased with addition of TEIC, the temperature dependences of rheological parameters reveal that the glass-rubber transition temperature of the investigated propellant binders does not change by the addition of tris(2,3-epoxypropyl) isocyanurate. The glass-rubber transition temperature, T_g , of all propellant binders was about -48 °C determined as maximum temperature of $\tan \delta$ with DMA at 1 Hz deformation frequency. Considering the temperature dependencies of $\tan \delta$ the fluctuation behavior around a storage temperature is observed.

Time-temperature superposition was used to construct modulus-frequency master curves that have been generated for the temperature range from -50 to 20 °C considering the curve at -20 °C as reference. The experimental frequency range of three logarithmic decades measured between -50 to 20 °C, is extended to ten logarithmic decades. By choosing the glass-rubber transition temperature of tested binder samples to be the reference temperature in WLF equation and based on C_1 and C_2 constants values at reference temperature of -20 °C of the same equation, not only the values of

“universal” constants $C_{1,g}$ and $C_{2,g}$ have been calculated, but also the fractional free volume at the glass-rubber transition temperature and the thermal coefficient of free volume expansion. The former is in agreement, while the latter is lower than the literature data. Due to the requirements during in-service applications, composite propellant binders with low glass-rubber transition and certain stress-strain capabilities are desired. Of the various composite propellant binder properties, none has been more difficult to achieve than the low temperature requirements. It has been so difficult to find composite propellant binder that meet the -54 °C goal. Based on shown test results, considering the fact that this type of prepolymer is commercially available, it can be stated that CTBN could be successfully used as composite propellant prepolymer. More specific, T_g values (about -48 °C), considered together with favorable values of the strain at maximum load, quite justify the use of the CTBN as prepolymer for case-bonded composite propellant grain production.

In order to achieve higher values of uniaxial tensile characteristics, it is acceptable to introduce TEIC as bonding agent within the binder composition in amounts not higher than 0.1%.

REFERENCES

- [1] J.P. Agrawal, High Energy Materials: Propellants, Explosives and Pyrotechnics, Wiley, Weinheim, 2010.
- [2] W. Arendale, in: C. Boyars, K. Klager (Eds.), Propellants, Manufacture, Hazards and Testing, American Chemical Society, Washington, DC, 1969, Vol. 88, pp. 67–83.
- [3] B.K. Bihari, W.S. Wani, N.P.N. Rao, P.P. Singh, B. Bhat-tacharya, Determination of Activation Energy of Relaxation Events in Composite Solid Propellants by Dynamic Mechanical Analysis, Def. Sci. J. **64** (2014) 173–178.
- [4] J.P. Consaga, US patent 4944815 (1990).
- [5] S. Brzić, M. Dimić, Lj. Jelisavac, J. Djonlagić, G. Ušćumlić, J. Bogdanov, Influence of polyglycidyl-type bonding agents on the viscoelastic properties of a carboxyl-terminated poly(butadiene-co-acrylonitrile)-based composite rocket propellant, Cent. Eur. J. Energ. Mater. **12** (2015) 307–321.
- [6] J.L. de la Fuente, M.F. Garcia, M.L. Cerrada, Viscoelastic Behavior in a Hydroxyl-Terminated Polybutadiene Gum and Its Highly Filled Composites: Effects of the Type of

- Filler on the Relaxation Processes, *J. Appl. Polym. Sci.* **88** (2003) 1705–1712.
- [7] H. Price, US patent 3910908 (1975).
- [8] M. Kohga, Viscoelastic Behavior of Hydroxyl Terminated Polybutadiene Containing Glycerin, *J. Appl. Polym. Sci.* **122** (2011) 706–713.
- [9] MIL-STD 286 B: Propellants, Solid: Sampling, Examination and Testing, 1991.
- [10] S. Cerri, M.A. Bohn, K. Menke, L. Galfeti, Aging of HTPB/Al/AP Rocket Propellant Formulations Investigated by DMA Measurements, *Propellants Explos. Pyrotech.* **38** (2013) 190–198.
- [11] S. Cerri, M. Bohn, K. Menke, L. Galfetti, Ageing Behaviour of HTPB Based Rocket Propellant Formulation, *Cent. Eur. J. Energ. Mater.* **6** (2009) 149–165.
- [12] H. Shekhar, Effect of Temperature on Mechanical Properties of Solid Rocket Propellants, *Def. Sci. J.* **61** (2011) 529–533.
- [13] L.E. Nielsen, R.F. Landel, *Mechanical Properties of Polymers and Composites*, 2nd ed., Marcel Dekker, New York, 1994, pp. 1–557.
- [14] M. Bohn, in: R. Armstrong, J. Short, D.K. Anand (Eds.), *Impacts on the Loss Factor Curve and Quantification of Molecular Rearrangement Regions from it in Elastomer Bonded Energetic Formulations*, CALCE EPSC Press, University of Maryland, 2012, pp. 195–235.
- [15] J.W. Blank, Z.A. He, M. Picci, Catalysis of the Epoxy–Carboxy Reaction, in *Proceedings of Int. Waterborne High-Solids, Powder Coat. Symp.*, New Orleans, LA, 2003, pp. 23.1–23.18.
- [16] H.L. Ornaghi, A.S. Bolner, R. Fiorio, A.J. Zattera, S.C. Amico, Mechanical and Dynamic Mechanical Analysis of Hybrid Composites Molded by Resin Transfer Molding, *J. App. Polym. Sci.* **118** (2010) 887–896.
- [17] M.J. Schroeder, C.M. Roland, Segmental Relaxation in End-Linked Poly(dimethylsiloxane) Networks, *Macromolecules* **35** (2002) 2676–2681.
- [18] M. Bohn, Modelling of loss factor of elastomer binders of high explosive charges and composite rocket propellants to separate binder fractions with different molecular mobility used to follow ageing, in *Proceedings of the 18th International Seminar on New Trends in Research of Energetic Materials*, Pardubice, Czech Republic, 2015, pp. 490–521.
- [19] K.P. Menard, *Dynamic Mechanical Analysis: A Practical Introduction*, CRC Press LLC, Boca Raton, New York, 1999, pp. 1–205.
- [20] J.D. Ferry, *Viscoelastic properties of polymers*, 3rd ed., John Wiley & Sons, New York, 1980, pp. 1–641.
- [21] I. Emre, *Rheology of Solid Polymers*, The British Society of Rheology, Glasgow, 2005, pp. 49–100.
- [22] S. Brzić, Lj. Jelisavac, J. Galović, D. Simić, J. Petković, Viscoelastic Properties of Hydroxyl-terminated Polybutadiene-based Composite Rocket Propellants, *Hem. Ind.* **68** (2014) 435–443.
- [23] T. Seyidoglu, M.A. Bohn, Effect of curing agents and plasticizers on the loss factor curves of HTPB-binders quantified by modelling, in *Proceedings of the 18th International Seminar on New Trends in Research of Energetic Materials*, Pardubice, Czech Republic, 2015, pp. 794–815.

IZVOD

VISKOELASTIČNO PONAŠANJE VEZIVA KOMPOZITNOG RAKETNOG GORIVA NA BAZI KARBOKSI-TERMINIRANOG (BUTADIEN-CO-AKRILONITRIL) KOPOLIMERA SA VEZUJUĆIM AGENSOM POLIGLICIDILNOG TIPA

Saša Brzić¹, Gordana Ušćumlić², Mirjana Dimić¹, Miloš Tomić², Vesna Ž. Rodić¹, Bojana Z. Fidanovski¹

¹*Vojnotehnički Institut, Ratka Resanovića 1, 11030 Beograd, Srbija*

²*Tehnološko-metalurški fakultet, Univerzitet u Beogradu, Karnegijeva 4, 11120 Beograd, Srbija*

(Naučni rad)

U radu je ispitan uticaj tris(2,3-epoksiopropil)-izocijanurata kao vezujućeg agensa na fizičko-hemijske, viskoelastične i jednoosne mehaničke karakteristike karboksi-terminiranog kopolimera (butadien-co-akrilonitril) umreženog sa poliglicidil etrom glicerola i epihlorhidrina. Vrednosti gustine umreženosti određene su metodom bubrenja. Analizirane su temperaturne i frekvencione zavisnosti parametara reološkog ponašanja (modula sačuvane (G') i izgubljene energije (G''), tangensa ugla gubitaka, $\tan \delta$, kao i temperature ostakljivanja, T_g). Na osnovu vrednosti frekvencionih zavisnosti modula sačuvane energije, eksperimentalno određenih u temperaturnom opsegu od -50 do 20 °C, konstruisane su zbirne (master) krive, koje prekrivaju znatno širi interval frekvencija (11 logaritamskih dekada) u odnosu na onaj u kome je vršeno merenje. Odabirom temperature ostakljivanja kao referentne temperature, određene su "univerzalne" konstante WLF jednačine, na osnovu kojih su izračunate vrednosti parcijalne slobodne zapremine na temperaturi ostakljivanja, f_g/B , i koeficijent toplotnog širenja slobodne zapremine, α_f/B . Iako male količine tris(2,3-epoksiopropil)-izocijanurata utiču na gustinu umreženosti, rezultati dinamičke mehaničke analize pokazuju da sadržaj ovog vezujućeg agensa ne utiče na temperaturu ostakljivanja ispitivanih sastava veziva.

Ključne reči: Karboksi-terminirani kopolimer (butadien-co-akrilonitril) • Viskoelastična svojstva • Temperatura ostakljivanja

Meat quality of Swallow-Belly Mangulica pigs reared under intensive production system and slaughtered at 100 kg live weight

Vladimir M. Tomović¹, Nikola Z. Stanišić², Marija R. Jokanović¹, Žarko S. Kevrešan³, Branislav V. Šojić¹, Snežana B. Škaljac¹, Igor B. Tomašević⁴, Aleksandra B. Martinović⁵, Aleksandra R. Despotović⁶, Danijela Z. Šuput¹

¹University of Novi Sad, Faculty of Technology Novi Sad, Novi Sad, Serbia

²Institute for Animal Husbandry, Zemun, Serbia

³University of Novi Sad, Institute for Food Technology, Novi Sad, Serbia

⁴University of Belgrade, Faculty of Agriculture, Belgrade, Serbia

⁵University of Donja Gorica, Faculty for Food Technology, Food Safety and Ecology, Donja Gorica, Podgorica, Montenegro

⁶University of Montenegro, Biotechnical Faculty Podgorica, Podgorica, Montenegro

Abstract

Quality parameters including sensory and physical characteristics and proximate and mineral composition in *M. psoas major*, *M. semimembranosus*, *M. longissimus thoracis et lumborum* and *M. triceps brachii* of Swallow-Belly Mangulica pigs were determined. Type of muscles had no significant effect ($P > 0.05$) on water-holding capacity, protein, total fat and K, P and Ca content. The *M. psoas major* was the highest in pH_{24h}, water-holding capacity, CIEa* and CIEb* values, moisture, K, P and Cu content, and the lowest in visual marbling score and total fat content. The *M. semimembranosus* was the highest in Mg and Ca content, and the lowest in CIEl* value (darkest muscle) and K content. The lightest colour (CIEl* value), the highest content of protein, total fat and total ash, and the lowest visual colour score, pH_{24h}, CIEa* and CIEb* values, content of moisture, Na, Ca, Zn, Fe and Cu were found in *M. longissimus thoracis et lumborum*. The highest visual colour and marbling score, the highest content of Na, Zn and Fe, and the lowest water-holding capacity, content of protein, total ash, P and Mg were found in *M. triceps brachii*.

Keywords: pigs, Swallow-Belly Mangulica, intensive production system, meat quality.

Available online at the Journal website: <http://www.ache.org.rs/HI/>

The major sources of variability in food (pork) quality are the wide diversity of soils and climatic conditions (geographical origin), seasonal variations, physiological state and maturity, as well as cultivar and breed [1]. The continuous innovations in the breeding systems, rearing practices, feeds composition, pre-slaughter handling, slaughtering methods, chilling and storage conditions largely contribute to induced changes in pork quality [2-4].

In recent years, demand for meat and meat products from southern European indigenous pig breeds has increased [5]. The most representative Serbian indigenous pig breed is the Mangulica, which is primarily bred in the Northern part of the country (Autonomous Province of Vojvodina, located in the Pannonian Plain). In Serbia, there are three varieties: White (Blond), Swallow-Belly and Red Mangulica [6-13]. This indigenous pig is mainly kept under free-range (outdoor) systems till live weight about 150 kg – approximately 2

years [11]. The free-range system increases the value of animal products due to the influence of outdoor rearing on the sensory, chemical and physical characteristics [5]. Traditionally, meat from indigenous, as well as Mangulica, pigs has been processed into unique highly-priced dry-cured meat products: dry-hams, loins, and sausages [14,15]. Most of these products still rely primarily on local, traditional manufacturing processes. However, there is a lack of information about characteristics of meat from Swallow-Belly Mangulica pigs, reared under intensive production system, for fresh consumption.

Having in mind that, the objective of this paper was to investigate the sensory (colour and marbling), physical (pH value, colour and water-holding capacity) and chemical (proximate and mineral composition) characteristics of *M. psoas major*, *M. semimembranosus*, *M. longissimus thoracis et lumborum* and *M. triceps brachii* of intensively reared Swallow-Belly Mangulica pigs. This study represents the continuation of the research on the meat quality of Swallow-Belly Mangulica pigs reared under different conditions.

SCIENTIFIC PAPER

UDC 636.4:637.5'64:66

Hem. Ind. 70 (5) 557-564 (2016)

doi: 10.2298/HEMIND150613063T

Correspondence: V.M. Tomović, University of Novi Sad, Faculty of Technology Novi Sad, Bulevar cara Lazara 1, 21000 Novi Sad, Serbia.
E-mail: tomovic@uns.ac.rs

Paper received: 13 June, 2015

Paper accepted: 3 November, 2015

EXPERIMENTAL

Meat samples collection and preparing

This study included 15 Swallow-Belly Mangulica pigs. The composition of the intensive pig diet is presented in Table 1. The finishers were housed in pens with fully slatted floor and 0.80 m² space allocation per pig. Each pen contained 10 animals. The environmental temperature in the building was 22 °C. All pigs had ad libitum access to diet and water [16]. Carcasses were conventionally chilled for 24 h in a chiller at 2–4 °C. After chilling, *M. psoas major* (PM), *M. semimembranosus* (SM), *M. longissimus thoracis et lumborum* (LTL) and *M. triceps brachii* (TB) were removed from the right side of each carcass. The meat samples for measurements of sensory and physical characteristics and determination of proximate and mineral composition were prepared as described in detail by Tomović *et al.* [11].

Meat quality measurements

Sensory analysis (colour and marbling), physical measurements (pH value, water-holding capacity and colour), proximate composition (moisture, protein, total fat and total ash), mineral composition (phosphorous, potassium, sodium, magnesium, calcium, zinc, iron and copper), quality control programme and statistical analysis were performed as described in detail by Tomović *et al.* [11].

RESULTS

Scores for sensory evaluated colour ranged from 3.2 (LTL) to 5.1 (TB), while scores for sensory evaluated marbling ranged from 1.0 (PM) to 2.3 (TB), Table 2. The LTL muscles showed significantly ($P < 0.001$) the lightest visual colour and PM muscles showed significantly ($P < 0.001$) the lowest marbling score, comparing to other three muscles.

Table 2. Sensory characteristics of meat from Swallow-belly Mangulica pigs reared under intensive production system; PM – *M. psoas major*; SM – *M. semimembranosus*; LTL – *M. longissimus thoracis et lumborum*; TB – *M. triceps brachii*; ab, pq and wx indicate significant difference within column at $P < 0.05$, < 0.01 and < 0.001 , respectively

Muscle	Value	Colour	Marbling
PM	$X \pm SD$	4.9±0.6 ^{a,p,w}	1.0±0.0 ^{b,q,x}
	Range	(4.0–5.8)	(1.0–1.0)
SM	$X \pm SD$	4.9±0.4 ^{a,p,w}	1.8±0.5 ^{a,p,w}
	Range	(4.5–5.4)	(1.0–2.4)
LTL	$X \pm SD$	3.2±0.8 ^{b,q,x}	2.1±0.5 ^{a,p,w}
	Range	(1.9–3.8)	(1.6–2.9)
TB	$X \pm SD$	5.1±0.5 ^{a,p,w}	2.3±0.3 ^{a,p,w}
	Range	(4.3–5.8)	(1.9–2.8)
<i>P</i> value		< 0.001	< 0.001
All muscles	$X \pm SD$	4.5±1.0	1.8±0.6
	Range	(1.9–5.8)	(1.0–2.9)

Table 1. The composition of pig diet

Ingredient	Starter (from 10 days to 8–9 kg body weight (approximately from 10 to 50 days))	Grover (from 8–9 to 25 kg body weight (approximately from 50 to 120 days))	Finisher 1 (from 25 to 60 kg body weight (approximately from 120 to 200 days))	Finisher 2 (from 60 to 100 kg body weight (approximately from 200 to 300 days))
Corn (dry)	56.57	58.76	–	–
Corn (silage)	–	–	62.93	68.76
Wheat meal	6.0	9.0	15.0	15.0
Soybean meal	17.1	15.7	14.0	9.1
Sunflower meal	2.5	3.5	5.0	4.0
Soy grits	10.0	5.0	–	–
Ekofish meal	–	4.0	–	–
Fish meal	4.5	–	–	–
Limestone	1.4	1.5	1.4	1.4
Monocalcium phosphate	0.5	1.0	0.6	0.7
Salt	0.18	0.32	0.40	0.45
Mineral premix	1.0	1.0	0.5	0.5
Synthetic lysine	0.05	0.02	0.07	0.09
Minazel plus	0.2	0.2	0.1	–
Calculated composition				
Crude protein	20	18	15	13

The pH value was significantly ($P < 0.001$) the lowest in LTL muscles (5.56) than in PM (6.07), TB (6.05) and SM muscles (6.02). Water-holding capacity (RZ, M/T and M/RZ values) did not differ significantly ($P > 0.05$) among four muscles. Values for RZ, M/T and M/RZ varied between 5.06 (PM) and 6.66 (TB), 0.41 (TB) and 0.51 (PM), and between 0.74 (TB) and 1.11 (PM), respectively (Table 3). Significantly ($P < 0.001$) the lightest colour (highest CIEL* value) was obtained for LTL muscles (48.39), comparing to other three muscles. CIEL* values for other three muscles were: 38.56 (PM), 38.26 (TB) and 37.46 (SM). The PM muscles were the highest in redness (CIEa* value, 21.03), followed by TB (17.69), SM (14.72) and LTL (10.13) muscles, with significant ($P < 0.001$) differences among all four muscles. Also, PM muscles were significantly ($P < 0.001$) the highest in yellowness (CIEb* value, 6.98), comparing to other three muscles. CIEb* values for other three mus-

cles were: 4.98 (TB), 4.72 (SM) and 4.14 (LTL), Table 4.

Moisture content in the LTL muscles (72.03 g/100 g) was significantly lower comparing with PM muscles (74.22 g/100 g, $P < 0.01$) and TB muscles (73.20 mg/100 g, $P < 0.05$). The SM muscles exhibited intermediate level of moisture content (73.06 g/100 g). The TB muscles were significantly ($P < 0.05$) the lowest in total ash content (0.99 g/100 g), comparing to other three muscles. The LTL muscles showed numerically the highest total ash content (1.10 g/100 g). Protein content varied between 21.44 (TB) and 22.25 g/100 g (LTL), while total fat content was between 3.16 (PM) and 4.47 g/100 g (LTL), with no significant ($P > 0.05$) difference among all four muscles (Table 5).

Potassium content varied between 279 (SM) and 303 mg/100 g (PM), phosphorus content varied between 218 (TB) and 228 mg/100 g (PM), while calcium content was between 5.46 (LTL) and 7.68 mg/100 g (SM), with

Table 3. Physical characteristics of meat from Swallow-belly Mangulica pigs reared under intensive production system; PM – *M. psoas major*; SM – *M. semimembranosus*; LTL – *M. longissimus thoracis et lumborum*; SM – *M. semimembranosus*; TB – *M. triceps brachii*. WHC – water-holding capacity; M = surface of the pressed meat film; T = surface of the wet area on the filter paper; RZ = T – M; ab, pq and wx indicate significant difference within column at $P < 0.05$, < 0.01 and < 0.001 , respectively

Muscle	Value	pH _{24h}	WHC		
			RZ / cm ²	M/T	M/RZ
PM	X±SD	6.07±0.23 ^{a,p,w}	5.06±1.22	0.51±0.09	1.11±0.46
	Range	(5.83–6.38)	(3.30–6.30)	(0.43–0.65)	(0.76–1.87)
SM	X±SD	6.02±0.07 ^{a,p,w}	5.75±0.47	0.45±0.02	0.86±0.10
	Range	(5.93–6.09)	(5.30–6.50)	(0.42–0.48)	(0.73–0.96)
LTL	X±SD	5.56±0.05 ^{b,q,x}	5.71±0.82	0.42±0.05	0.75±0.15
	Range	(5.49–5.62)	(4.70–6.40)	(0.37–0.48)	(0.60–0.92)
TB	X±SD	6.05±0.21 ^{a,p,w}	6.66±1.19	0.41±0.07	0.74±0.22
	Range	(5.79–6.27)	(5.15–8.40)	(0.31–0.51)	(0.45–1.06)
P value		<0.001	0.118	0.135	0.164
All muscles	X±SD	5.92±0.26	5.80±1.07	0.45±0.07	0.87±0.29
	Range	(5.49–6.38)	(3.30–8.40)	(0.31–0.65)	(0.45–1.87)

Table 4. Physical characteristics of meat from Swallow-belly Mangulica pigs reared under intensive production system; PM – *M. psoas major*; SM – *M. semimembranosus*; LTL – *M. longissimus thoracis et lumborum*; SM – *M. semimembranosus*; TB – *M. triceps brachii*; abcd, pqrs and wxyz indicate significant difference within column at $P < 0.05$, < 0.01 and < 0.001 , respectively

Muscle	Value	Colour		
		CIEL* (lightness)	CIEa* (redness)	CIEb* (yellowness)
PM	X±SD	38.56±2.32 ^{b,q,x}	21.03±2.19 ^{a,p,w}	6.98±1.01 ^{a,p,w}
	Range	(35.77–40.99)	(17.77–23.30)	(6.05–8.23)
SM	X±SD	37.46±1.42 ^{b,q,x}	14.72±1.39 ^{c,r,y}	4.72±0.51 ^{b,q,x}
	Range	(35.81–39.58)	(13.42–16.74)	(4.26–5.42)
LTL	X±SD	48.39±1.77 ^{a,p,w}	10.13±0.98 ^{d,s,z}	4.14±0.48 ^{b,q,x}
	Range	(47.13–51.42)	(8.93–11.24)	(3.71–4.87)
TB	X±SD	38.26±2.59 ^{b,q,x}	17.69±1.35 ^{b,q,x}	4.98±0.41 ^{b,q,x}
	Range	(35.15–41.33)	(15.44–18.94)	(4.55–5.41)
P value		<0.001	<0.001	<0.001
All muscles	X±SD	40.67±4.97	15.89±4.35	5.20±1.25
	Range	(35.15–51.42)	(8.93–23.30)	(3.71–8.23)

Table 5. Proximate composition (g/100 g) of meat from Swallow-belly Mangulica pigs reared under intensive production system; PM – *M. psoas major*; SM – *M. semimembranosus*; LTL – *M. longissimus thoracis et lumborum*; TB – *M. triceps brachii*; ab and pq indicate significant difference within column at $P < 0.05$, < 0.01 and < 0.001 , respectively

Muscle	Value	Moisture	Protein	Total fat	Total ash
PM	$X \pm SD$	74.22±0.82 ^{a,p}	21.46±0.80	3.16±0.25	1.06±0.07 ^a
	Range	(73.03–75.32)	(20.13–22.27)	(2.86–3.46)	(0.97–1.13)
SM	$X \pm SD$	73.06±0.74 ^{ab,pq}	22.16±0.39	3.58±0.94	1.08±0.05 ^a
	Range	(71.94–73.77)	(21.81–22.64)	(2.45–4.82)	(1.00–1.14)
LTL	$X \pm SD$	72.03±1.09 ^{b,q}	22.25±0.41	4.47±1.13	1.10±0.01 ^a
	Range	(70.44–73.03)	(21.70–22.80)	(3.35–6.08)	(1.09–1.11)
TB	$X \pm SD$	73.20±0.60 ^{a,pq}	21.44±0.53	4.22±0.44	0.99±0.05 ^b
	Range	(72.49–73.99)	(20.74–21.97)	(3.47–4.60)	(0.93–1.06)
<i>P</i> value		0.007	0.058	0.064	0.023
All muscles	$X \pm SD$	73.13±1.10	21.82±0.64	3.86±0.89	1.06±0.06
	Range	(70.44–75.32)	(20.13–22.80)	(2.45–6.08)	(0.93–1.14)

no significant ($P > 0.05$) difference among all four muscles. Sodium content in the LTL muscles (50.3 mg/100 g) was significantly ($P < 0.05$) lower comparing with TB muscles (59.2 mg/100 g) and PM muscles (58.4 mg/100 g). The SM muscles exhibited intermediate level of sodium content (53.1 mg/100 g). The magnesium content was significantly higher in SM muscles (24.7 mg/100 g) than in LTL (23.5 mg/100 g, $P < 0.05$), PM (22.8 mg/100 g, $P < 0.01$) and TB muscles (22.6 mg/100 g, $P < 0.01$). The zinc content was significantly lower in LTL muscles (2.35 mg/100 g) than in PM (3.25 mg/100 g, $P < 0.01$), SM (3.47 mg/100 g, $P < 0.001$) and TB muscles (3.90 mg/100 g, $P < 0.001$). Also, zinc content was significantly ($P < 0.05$) lower in PM muscles than in TB muscles. The TB muscles were the highest in iron content (3.26 mg/100 g), followed by PM (2.74 mg/100 g), SM (1.85 mg/100 g) and LTL muscles (1.08 mg/100 g), with significant ($P < 0.01$ or < 0.001) differences among all four muscles. The content of copper was significantly ($P < 0.01$ or < 0.001) higher in PM (0.15 mg/100 g) and TB muscles (0.14 mg/100 g) than in SM

(0.11 mg/100 g) and LTL muscles (0.10 mg/100 g), (Table 6).

DISCUSSION

Meat quality has five dimensions: sensory quality, technological quality, nutritional quality, hygienic and toxicological quality and immaterial quality (the last dimension has environmental, ethical, ethnical and religious aspects). The sensory factors of meat quality include colour, marbling, odour, taste, juiciness, consistency and tenderness, while technological factors of meat quality include pH value, colour, water-holding capacity, tenderness, protein content and its status, fat content and its status and connective tissue content [17,18].

The most important parameters, which enable identification of sensory and technological meat quality, include the pH value, measured in the muscle tissue 30–60 min (*pre-rigor* state) and 24 hours *post-mortem* (*post-rigor* state), meat colour and water-holding cap-

Table 6. Mineral composition (mg/100 g) of meat from Swallow-belly Mangulica pigs reared under intensive production system; PM – *M. psoas major*; SM – *M. semimembranosus*; LTL – *M. longissimus thoracis et lumborum*; TB – *M. triceps brachii*; abcd, pqrs and wxy indicate significant difference within column at $P < 0.05$, < 0.01 and < 0.001 , respectively

Muscle	Value	K	P	Na	Mg	Ca	Zn	Fe	Cu
PM	$X \pm SD$	303±17	228±21	58.4±6.1 ^a	22.8±0.6 ^{b,q}	7.38±1.40	3.25±0.56 ^{b,p,wx}	2.74±0.30 ^{b,q,w}	0.15±0.02 ^{a,p,w}
	Range	(285–327)	(196–247)	(52.6–65.1)	(22.1–23.6)	(5.34–8.92)	(2.78–3.95)	(2.36–3.20)	(0.14–0.19)
SM	$X \pm SD$	279±9	224±13	53.1±1.9 ^{ab}	24.7±0.6 ^{a,p}	7.68±1.26	3.47±0.33 ^{ab,p,w}	1.85±0.05 ^{c,r,x}	0.11±0.01 ^{b,q,wx}
	Range	(267–292)	(204–241)	(50.9–56.0)	(24.0–25.4)	(5.59–8.89)	(3.11–3.85)	(1.80–1.91)	(0.09–0.12)
LTL	$X \pm SD$	296±22	224±4	50.3±5.3 ^b	23.5±1.0 ^{b,pq}	5.46±1.08	2.35±0.26 ^{c,q,x}	1.08±0.19 ^{d,s,y}	0.10±0.02 ^{b,q,x}
	Range	(279–333)	(219–229)	(44.3–58.9)	(22.5–24.9)	(4.18–6.56)	(2.12–2.67)	(0.88–1.35)	(0.08–0.13)
TB	$X \pm SD$	286±28	218±12	59.2±5.8 ^a	22.6±0.9 ^{b,q}	6.22±1.63	3.90±0.29 ^{a,p,w}	3.26±0.41 ^{a,p,w}	0.14±0.02 ^{a,p,wx}
	Range	(271–335)	(198–230)	(54.3–67.7)	(21.3–23.6)	(4.86–8.10)	(3.64–4.40)	(2.79–3.77)	(0.12–0.17)
<i>P</i> value		0.296	0.690	0.038	0.004	0.677	<0.001	<0.001	<0.001
All muscles	$X \pm SD$	291±21	223±14	55.3±6.0	23.4±1.1	6.69±1.55	3.25±0.68	2.23±0.89	0.13±0.03
	Range	(267–335)	(196–247)	(44.3–67.7)	(21.3–25.4)	(4.18–8.92)	(2.12–4.40)	(0.88–3.77)	(0.08–0.19)

acidity measured 24 h *post-mortem* [18,19].

The rate of *post-mortem* pH value decline affects some other meat quality parameters (colour, water holding capacity) [20]. In this study PM, SM and TB muscles had significantly ($P < 0.001$) higher ultimate pH value than LTL muscles. Also, almost all individual ultimate pH values, except for LTL muscles, were over the characteristic range for pork (5.3–5.8 [18,21]) (Table 3). Ultimate pH of meat from Swallow-Belly Mangulica pigs reared under intensive production system were higher, especially in PM, SM and TB muscle, comparing with results previously published by Tomović *et al.* [11] for free-range reared Swallow-Belly Mangulica pigs slaughtered at 150 kg body weight. Similar results for ultimate pH in LTL muscles from other southern European indigenous pig breeds (Chato Murciano and Cinta Senese) were reported by Peinado *et al.* [22], Pugliese *et al.* [23] and Galián *et al.* [24].

Colour is one of the most important quality characteristic of fresh pork [3,19,25,26]. According to sensory analysis, colour of LTL muscles was evaluated as reddish pink (score 3.2), while other three muscles (PM, SM and TB) had significantly ($P < 0.001$) darker colour than reddish pink (higher than score 3), Table 2. Results of instrumental colour (CIEL* value) measurement shown same trend, *i.e.*, LTL muscles were significantly ($P < 0.001$) the lightest (Table 4). Thus, regarding all individual values for lightness (CIEL* value, Table 4) three groups of muscles (PM, SM and TB) had dark colour (dark colour: CIEL* < 42 [27–29]). Also, the LTL muscles had all individual CIEL* values lower than 53 (Table 4), what is the highest acceptable CIEL* values for LTL muscle of normal quality [18,27–29]. Good relationship between visual evaluations of colour and instrumental colour measurements ($r = -0.91$, $P < 0.001$) was also determined. All this indicate that meat from Swallow-Belly Mangulica has from reddish-pink to purplish–red colour. Results for colour obtained in this study could be explained with previously elaborated effects of ultimate pH on colour and with calculated correlation coefficient between colour and ultimate pH ($r = 0.78$ and $r = -0.88$, $P < 0.001$). Colour of meat from Swallow-Belly Mangulica pigs reared under intensive production system parallel that reported by Tomović *et al.* [11], as well as results reported for LTL muscles from other southern European indigenous pig breeds by Cava *et al.* [14] and Estévez *et al.* [30] for Iberian pigs, Galián *et al.* [15,24], Poto *et al.* [31] and Peinado *et al.* [22] for Chuto Murciano pigs, and Pugliese *et al.* [23,32] for Nero Siciliano and Cinta Senese pigs.

Beside the colour, water-holding capacity is also one of the most important quality characteristic of fresh pork [3,16,20,25]. In this study water-holding capacity (RZ, M/T and M/RZ values) was not significantly ($P > 0.05$) affected by the type of muscle (Table 3),

being in agreement with results previously published by Tomović *et al.* [11]. Obtained results indicated good water-holding capacity of meat from Swallow-Belly Mangulica (a bigger M/T ratio indicating a better water-holding capacity; exudative meat: $M/T < 0.35$, non-exudative meat: $M/T = 0.35–0.45$, dry meat: $M/T > 0.45$ [33]). As for colour, results for water-holding capacity obtained in this study could be explained with previously elaborated effects of ultimate pH on water-holding capacity, as well as with calculated correlation coefficient between water-holding capacity and ultimate pH ($r = 0.52$, $P < 0.05$ and $r = 0.57$, $P < 0.01$).

The nutritive factors of meat include proteins and their composition, fats and their composition, vitamins, minerals, utilization, digestibility, and biological value [17,18].

In this study protein and total fat contents were not significantly ($P > 0.05$) affected by the type of muscle. The protein level in all individual muscle was higher than 20 g/100 g (Table 5). Results for protein content are in agreement with results previously published by Tomović *et al.* [11] for Swallow-Belly Mangulica and for modern (Large White and Landrace) pigs [34], as well as with results reported for LTL muscles from southern European indigenous pig breeds by Cava *et al.* [14], Pugliese *et al.* [23,32] and Parunović *et al.* [9] for Iberian, Cinta Senese, Nero Siciliano and Mangulica pigs. Among the qualitative traits of meat, evaluating intramuscular fat content seems to be the best way to separate indigenous pigs from modern ones [5]. Considering that the sensory traits of raw meat are linked to intramuscular fat content it is believed that 2–2.5 g/100 g of intramuscular fat content is the minimum acceptable level [35]. Meat from Swallow-Belly Mangulica pigs reared under intensive production system had total fat content higher than 2.45 g/100 g (up to 6.08 g/100 g), Table 5. The corresponding value in modern (Large White and Landrace) pigs was less than 1.5 g/100 g [34]. Comparing with the data reported by Lawrie and Ledward [25] for lean pigs at the age of 6 months, another prominent characteristic of Swallow-Belly Mangulica muscles is almost twice higher total fat content. Total fat content determined in this study in PM, SM and TB muscles were at the similar level as previously reported results for Swallow-Belly Mangulica pigs, while the total fat content in LTL muscles was almost two times less [11]. Regarding fat content in LTL muscles from southern European indigenous pigs, results reported by other authors were in the wide range: 12.87–27.93 g/100 g for Iberian pigs [36], 2.26–4.79 for Iberian pigs [14], 2.51–3.34 g/100 g for Iberian pigs [30], 6.39 g/100 g for Chato Murciano pigs [22], 3.32–4.27 g/100 g for Nero Siciliano pigs [32], 3.29–4.04 g/100 g for Cinta Senese pigs [23], 10.21 g/100 g for Chato Murciano pigs [15], 10.47 g/100 g for Chato

Murciano pigs [31], <2 g/100 g for Casertana pigs [37], 6.1–7.9 g/100 g for Chato Murciano pigs [24] and 13.52 g/100 g for Swallow-belly Mangulica pigs and 17.54 g/100 g for White Mangulica pigs [9]. As expected, in this study, the inverse relationship of moisture content with protein ($r = -0.75$, $P < 0.001$) and with total fat content ($r = -0.69$, $P < 0.01$) was determined. In addition, correlation coefficient for the relationship between marbling and total fat content was good ($r = 0.65$, $P < 0.01$).

In scientific literature there is a lack of information about mineral content in meat from indigenous pigs. In this study, Na, Mg, Zn, Fe and Cu content was significantly ($P < 0.05$) affected by the type of muscle. The content of the minerals in decreasing order in all four muscles was: K, P, Na, Mg, Ca, Zn, Fe and Cu (Table 6). Only two minerals (sodium and iron) were present in different amount than in meat from free-range reared Swallow-Belly Mangulica pigs slaughtered at 150 kg body weight. Sodium was lower for all four muscles, while iron was higher only in TB muscles [11]. Considering all investigated minerals, iron and copper content obtained in this study for LTL muscles from Swallow-Belly Mangulica pigs were noticeably lower than in Chato Murciano pigs [15,31]. Meat exhibits natural variations in the amounts of nutrients contained and the limits of the natural nutrient variations are not defined. Major sources of variation in meat are the proportion of lean to fat tissue, and the proportion of edible to inedible materials (bone and gristle). Variations in the lean-fat ratio affect the levels of most other nutrients, which are distributed differently in the two fractions [1].

CONCLUSION

Comparing obtained results of meat quality of Swallow-Belly Mangulica pigs reared under intensive production system and slaughtered at 100 kg live weight with previously determined meat quality of free-range reared Swallow-Belly Mangulica pigs and slaughtered at 150 kg body weight, it can be concluded that Swallow-Belly Mangulica pigs can be reared indoor with remained typical and good sensory, technological and nutritive quality.

Acknowledgements

Research was financially supported by the Ministry of Education, Science and Technological Development, Republic of Serbia, project TR31032. These results are also part of the project No 114-451-809/2015 (Improvement of meat quality from indigenous and modern pig breeds produced in Vojvodina for the production of traditional dry fermented sausages and dry cured meat products), which is financially supported by the Provincial Secretariat for Science and Technological Dev-

elopment, Autonomous Province of Vojvodina, Republic of Serbia.

REFERENCES

- [1] H. Greenfield, D.A.T. Southgate, Food composition data: Production, management and use, 2nd ed., Food and Agriculture Organisation of the United Nations, Rome, 2003.
- [2] K. Rosenvold, H.J. Andersen, Factors of significance for pork quality – A review, *Meat Sci.* **64** (2003) 219–237.
- [3] V. Olsson, J. Pickova, The influence of production systems on meat quality, with emphasis on pork, *Ambio* **34** (2005) 338–343.
- [4] H. Greenfield, J. Arcot, J.A. Barnes, J. Cunningham, P. Adorno, T. Stobaus, R.K. Tume, S.L. Beilken, W.J. Muller, Nutrient composition of Australian retail pork cuts 2005/2006, *Food Chem.* **117** (2009) 721–730.
- [5] C. Pugliese, F. Sirtori, Quality of meat and meat products produced from southern European pig breeds, *Meat Sci.* **90** (2012) 511–518.
- [6] B.D. Scherf, World watch list for domestic animal diversity, 3rd ed., Food and Agriculture Organisation of the United Nations, Rome, 2000.
- [7] DAD-IS (Domestic animal diversity information system), <http://dad.fao.org/>
- [8] I. Egerszegi, J. Rátky, L. Solti, K.-P. Brüssow, Mangalica – an indigenous swine breed from Hungary (Review), *Arch. Tierz. Dummerstorf* **46** (2003) 245–256.
- [9] N. Parunović, M. Petrović, V. Matekalo-Sverak, D. Radojković, D. Vranić, Č. Radović, Cholesterol and total fatty acid content in *M. longissimus dorsi* of Mangalitsa and Swedish landrace, *Acta Aliment.* **41** (2012) 161–171.
- [10] M.R. Jokanović, V.M. Tomović, B.V. Šojić, S.B. Škaljac, T.A. Tasić, P.M. Ikonić, Ž.S. Kevrešan, Cadmium in meat and edible offal of free-range reared Swallow-belly Mangulica pigs from Vojvodina (northern Serbia), *Food Addit. Contam., B Surveill.* **6** (2013) 98–102.
- [11] V.M. Tomović, B.A. Žlender, M.R. Jokanović, M.S. Tomović, B.V. Šojić, S.B. Škaljac, Ž.S. Kevrešan, T.A. Tasić, P.M. Ikonić, M.M. Šošo, Sensory, physical and chemical characteristics of meat from free-range reared Swallow-Belly Mangulica pigs, *J. Anim. Plant Sci.* **24** (2014) 704–713.
- [12] R.J. Šević, D.R. Lukač, V.S. Vidović, N.M. Puvača, B.M. Savić, D.B. Ljubojević, V.M. Tomović, N.R. Džinić, Some parameters of nutritional quality of meat obtained from Mangalitsa and Landrace pig breeds, *Chem. Ind.*, 2016, in press, DOI:10.2298/HEMIND140604071S.
- [13] V. Tomović, B. Žlender, M. Jokanović, M. Tomović, B. Šojić, S. Škaljac, Ž. Kevrešan, T. Tasić, P. Ikonić, Đ. Okanović, Physical and chemical characteristics of edible offal from free-range reared Swallow-Belly Mangalica pigs, *Acta Aliment.* **45** (2016) 190–197.
- [14] R. Cava, M. Estévez, J. Ruiz, D. Morcuende, Physico-chemical characteristics of three muscles from free-range reared Iberian slaughter at 90 kg live weight, *Meat Sci.* **63** (2003) 533–541.
- [15] M. Galián, B. Peinado, C. Martínez, M.J. Periago, G. Ros, A. Poto, Comparative study of the characteristics of the

- carcass and the meat of the Chato Murciano pig and its cross with Iberian pig, reared indoors, *Anim. Sci. J.* **78** (2007) 659–667.
- [16] V.M. Tomović, Lj.S. Petrović, M.S. Tomović, Ž.S. Kevrešan, N.R. Džinić, Determination of mineral contents of semimembranosus muscle and liver from pure and crossbred pigs in Vojvodina (northern Serbia), *Food Chem.* **124** (2011) 342–348.
- [17] K. Hofmann, Definition and measurements of meat quality, in: *Proceedings of the 36th international congress of meat science and technology*, Havana, Vol. III, 1990, pp. 941–954.
- [18] K.O. Honikel, Biochemical and physico-chemical characteristics of meat quality, *Meat Technol.* **40** (1999) 105–123.
- [19] J.R. Bendall, H.J. Swatland, A review of the relationships of pH with physical aspects of pork quality, *Meat Sci.* **24** (1988) 85–126.
- [20] E. Huff-Lonergan, S.M. Lonergan, Mechanisms of water-holding capacity of meat: The role of postmortem biochemical and structural changes, *Meat Sci.* **71** (2005) 194–204.
- [21] F.J.M. Smulders, F. Toldra, J. Flores, M. Prieto, *New technologies for meat and meat products*, Audet Tijdschriften, Utrecht, 1992.
- [22] B. Peinado, A. Poto, F. Gil, G. López, Characteristics of the carcass and meat of the Chato Murciano pig, *Livest. Prod. Sci.* **90** (2004) 285–292.
- [23] C. Pugliese, R. Bozzi, G. Campodoni, A. Acciaioli, O. Franci, G. Gandini, Performance of Cinta Senese pigs reared outdoors and indoors. 1. Meat and subcutaneous fat characteristics, *Meat Sci.* **69** (2005) 459–464.
- [24] M. Galián, A. Poto, B. Peinado, Carcass and meat quality traits of the Chato Murciano pig slaughtered at different weights, *Livest. Sci.* **124** (2009) 314–320.
- [25] R.A. Lawrie, D.A. Ledward, *Lawrie's meat science*, 7th ed., Woodhead Publishing Ltd. and CRC Press LLC, Cambridge, 2006.
- [26] R.A. Mancini, M.C. Hunt, Current research in meat color, *Meat Sci.* **71** (2005) 100–121.
- [27] S.T. Joo, R.G. Kauffman, B.C. Kim, G.B. Park, The relationship of sarcoplasmic and myofibrillar protein solubility to colour and water-holding capacity in porcine longissimus muscle, *Meat Sci.* **52** (1999) 291–297.
- [28] V.M. Tomović, M.R. Jokanović, Lj.S. Petrović, M.S. Tomović, T.A. Tasić, P.M. Ikonić, Z.M. Šumić, B.V. Šojić, S.B. Škaljac, M.M. Šoško, Sensory, physical and chemical characteristics of cooked ham manufactured from rapidly chilled and earlier deboned *M. semimembranosus*, *Meat Sci.* **93** (2013) 46–52.
- [29] V.M. Tomović, Lj.S. Petrović, N.R. Džinić, Effects of rapid chilling of carcasses and time of deboning on weight loss and technological quality of pork semimembranosus muscle, *Meat Sci.* **80** (2008) 1188–1193.
- [30] M. Estévez, D. Morcuende, R. Cava López, Physico-chemical characteristics of *M. longissimus dorsi* from three lines of free-range reared Iberian pigs slaughtered at 90 kg liveweight and commercial pigs: a comparative study, *Meat Sci.* **64** (2003) 499–506.
- [31] A. Poto, M. Galián, B. Peinado, Chato Murciano pig and its crosses with Iberian and Large White pigs, reared outdoors, Comparative study of the carcass and meat characteristics, *Livest. Sci.* **111** (2007) 96–103.
- [32] C. Pugliese, G. Calagna, V. Chiofalo, V. Moretti, S. Margiotta, O. Franci, G. Gandini, Comparison of the performances of Nero Siciliano pigs reared indoors and outdoors. 2. Joints composition, meat and fat traits, *Meat Sci.* **68** (2004) 523–528.
- [33] K. Hofmann, R. Hamm, E. Blüchel, Neues über die Bestimmung der Wasserbindung des Fleisches mit Hilfe der Filterpapierpressmethode, *Die Fleischwirtsch.* **62** (1982) 87–92.
- [34] V.M. Tomović, B.A. Žlender, M.R. Jokanović, M.S. Tomović, B.V. Šojić, S.B. Škaljac, T.A. Tasić, P.M. Ikonić, M.M. Šoško, N.M. Hromiš, Technological quality and composition of the *M. semimembranosus* and *M. longissimus dorsi* from Large White and Landrace Pigs, *Agric. Food Sci.* **23** (2014) 9–18.
- [35] P. Affentranger, C. Gerwig, G.J.F. Seewer, D. Schwörer, N. Künzi, Growth and carcass characteristics as well as meat and fat quality of three types of pigs under different feeding regimens, *Livest. Sci.* **45** (1996) 187–196.
- [36] A.I. Mayoral, M. Dorado, M.T. Guillén, A. Robina, J.M. Vivo, C. Vazquez, J. Ruiz, Development of meat and carcass quality characteristics in Iberian pigs reared outdoors, *Meat Sci.* **52** (1999) 315–324.
- [37] G. Salvatori, F. Filetti, C. Di Cesare, G. Maiorano, F. Pilla, G. Oriani, Lipid composition of meat and backfat from Casertana purebred and crossbred pigs reared outdoors, *Meat Sci.* **80** (2008) 623–631.

IZVOD

KVALITET MESA SVINJA LASASTE MANGULICE ODGAJANIH U INTENZIVNOM PROIZVODNOM SISTEMU I ŽRTVOVANIH SA TELESNOM MASOM OD 100 kg

Vladimir M. Tomović¹, Nikola Z. Stanišić², Marija R. Jokanović¹, Žarko S. Kevrešan³, Branislav V. Šojić¹, Snežana B. Škaljac¹, Igor B. Tomašević⁴, Aleksandra B. Martinović⁵, Aleksandra R. Despotović⁶, Danijela Z. Šuput¹

¹Univerzitet u Novom Sadu, Tehnološki fakultet Novi Sad, Bulevar cara Lazara 1, 21000 Novi Sad, Srbija

²Institut za stočarstvo, Autoput 16, 11080 Zemun, Srbija

³Univerzitet u Novom Sadu, Naučni institut za prehrambene tehnologije, Bulevar cara Lazara 1, 21000 Novi Sad, Srbija

⁴Univerzitet u Beogradu, Poljoprivredni fakultet, Nemanjina 6, 11080 Belgrade, Srbija

⁵Univerzitet Donja Gorica, Fakultet za prehrambenu tehnologiju, bezbjednost hrane i ekologiju, Donja Gorica, 81000 Podgorica, Crna Gora

⁶Univerzitet Crne Gore, Biotehnički fakultet Podgorica, Mihaila Lalića 1, 81000 Podgorica, Crna Gora

(Naučni rad)

Lasasta Mangulica je primitivna rasa svinja koja se najčešće uzgaja u ekstenzivnim uslovima. Cilj ovog rada bio je da se ispita kvalitet mesa svinja Lasaste Mangulice odgajanih u intenzivnom proizvodnom sistemu. Senzorna (boja i mramoriranost) i fizička (pH vrednost, sposobnost vezivanja vode i instrumentalno određena boja – CIEL*a*b*) svojstva, kao i osnovni hemijski sastav (vlaga, proteini, ukupna mast i ukupni pepeo) i sadržaj minerala (K, P, Na, Mg, Ca, Zn, Fe i Cu) određeni su u četiri mišića (*M. psoas major* – PM, *M. semimembranosus* – SM, *M. longissimus thoracis et lumborum* – LTL i *M. triceps brachii* – TB). Tip mišića ne utiče značajno ($P > 0,05$) na sposobnost vezivanja vode i sadržaj proteina, ukupne masti, K, P i Ca. Kod mišića PM utvrđena je statistički ili numerički najviša vrednost pH_{24h} (6,07), najbolja sposobnost vezivanja vode, najveći udeo crvene (CIEa* = 21,03) i žute (CIEb* = 6,98) boje i najveći sadržaj vlage (74,22 g/100 g), K (303 mg/100 g), P (228 mg/100 g) i Cu (0,15 mg/100 g), kao i najmanja mramoriranost i najmanji sadržaj ukupne masti (3,16 g/100 g). Kod mišića SM utvrđen je statistički ili numerički najveći sadržaj Mg (24,7 mg/100 g) i Ca (7,68 mg/100 g), kao i najtamnija instrumentalno određena boja (CIEL* = 37,46) i najmanji sadržaj K (279 mg/100 g). Najsvetlija instrumentalno određena boja (CIEL* = 48,39), najveći sadržaj proteina (22,25 g/100 g), ukupne masti (4,47 g/100 g) i ukupnog pepela (1,10 g/100 g), kao i najsvetlija senzorski ocenjena boja, najniža vrednost pH_{24h} (5,56), najslabija sposobnost vezivanja vode, najmanji udeo crvene (CIEa* = 10,12) i žute (CIEb* = 4,14) boje, najmanji sadržaj vlage (72,03 g/100 g), Na (50,3 mg/100 g), Ca (5,46 mg/100 g), Zn (2,35 mg/100 g), Fe (1,08 mg/100 g) i Cu (0,10 mg/100 g) utvrđeni su u LTL mišićima, sa numeričkim ili značajnim razlikama. Najtamnija senzorski ocenjena boja, najveći sadržaj Na (59,2 mg/100 g), Zn (3,90 mg/100 g) i Fe (3,26 mg/100 g), kao i najslabija sposobnost vezivanja vode, najmanji sadržaj proteina (21,44 g/100 g), ukupnog pepela (0,99 g/100 g), P (218 mg/100 g) i Mg (22,6 mg/100 g) utvrđeni su u TB mišićima, takođe sa numeričkim ili značajnim razlikama.

Ključne reči: Svinje • Lasasta Mangulica • Intenzivni proizvodni sistem • Kvalitet mesa

Morphology and adsorption of chromium ion on uranium 1,2,4,5-benzenetetracarboxylic acid metal organic framework (MOF)

Remy M.K. Vala, Donbebe Wankasi, Ezekiel D. Dikio

Applied Chemistry and Nanoscience Laboratory, Department of Chemistry, Vaal University of Technology, Vanderbijlpark, South Africa

Abstract

In this paper, we report the synthesis of metal organic framework of uranium 1,2,4,5-benzenetetracarboxylic acid (U-H₄btec MOF) by solvothermal method. The obtained MOF was characterized by Fourier transform infrared spectroscopy (FTIR), scanning electron microscopy (SEM), transmission electron microscopy (TEM), X-ray diffraction spectroscopy (XRD), energy dispersive spectroscopy (EDS), thermogravimetric and differential thermogravimetric analysis (TGA/DTA). The morphology of the uranium 1,2,4,5-benzenetetracarboxylic acid MOF observed by SEM, revealed the presence of flaky porous structure. Adsorption of Cr³⁺ from aqueous solution onto the uranium 1,2,4,5-benzenetetracarboxylic acid MOF was systematically studied. Langmuir and Freundlich adsorption isotherms were applied to determine the adsorption capacity of the MOF to form a monolayer. Kinetic determination of the adsorption of Cr³⁺ suggested both chemisorption and physisorption probably due to the presence of carbonyl groups within the MOF and its porous structure.

Keywords: adsorption, physisorption, metal organic frameworks; 1,2,4,5-benzenetetracarboxylic acid, uranyl acetate dehydrate, SEM.

Available online at the Journal website: <http://www.ache.org.rs/HI/>

SCIENTIFIC PAPER

UDC 66.081.3:547:543.42

Hem. Ind. 70 (5) 565–572 (2016)

doi: 10.2298/HEMIND150609065V

Metal organic frameworks (MOFs) are two or three-dimensional (3-D) coordination (polymers) of metal ions and organic ligands [1]. The design and synthesis of MOFs are receiving great attention because of their architecture, topology, and potential applications [2]. MOFs are potential adsorbents due to their porous structure with high specific surface area; they can also play an important role in the area of catalysis and separation [3]. As adsorbents, metal-organic frameworks have been used for hydrogen storage [4–8], gas separation and purification [9], and adsorption of volatile organic compounds [10].

Different approaches are used to synthesize MOFs, such as under solvothermal conditions, employing multidentate ligands capable of binding to a metal ion to form porous complexes of supramolecular structures [3,11]. Thus, a variety of organic ligands, metal ions, and solvent systems is explored for the preparation of numerous MOFs of exotic architectures as reported in the literature [12]. The supermolecular structure is maintained together by different interactions, such as metal-to-ligand π bonding, π - π interactions or others.

Researchers have used 1,2,4,5-benzenetetracarboxylate anion as a ligand in different study. For instance, thin films of organic-inorganic hybrid materials have

been grown by the atomic layer deposition technique [13]. Lanthanide ions were used to prepare lanthanide-containing coordination polymers with 1,2,4,5-benzenetetracarboxylate acid (=H₄btec); the compounds showed 3-D and their potential porosities were estimated by a computational method to be in the range of 1281 to 836 m² g⁻¹ [14]. Several metals have been used to prepare MOFs, such as Mn, La, Ag, Co, Cu, Cr, Fe and Zn for instance. Liu *et al.* [15] prepared 3-D material of H₄btec anion with magnesium.

However, as far as we know, uranium 1,2,4,5-benzenetetracarboxylic acid has not been synthesised for adsorption of chromium. Therefore, in this work, we report the synthesis of uranium 1,2,4,5-benzenetetracarboxylic acid (U-H₄btec), MOF from uranyl acetate and its characterization by scanning electron microscope, transmission electron microscope, x-ray diffraction spectroscopy, Fourier transform infrared spectroscopy and thermogravimetric analysis. The uranium MOF was used as a substrate for the adsorption of chromium ions in aqueous solution.

EXPERIMENTAL

Materials

1,2,4,5-benzenetetracarboxylate acid, uranyl acetate dihydrate, and *N,N*-dimethylformamide (DMF) were purchased from Merck. All were used as-received without further purification.

Correspondence: E.D. Dikio, Applied Chemistry and Nanoscience Laboratory, Department of Chemistry, Vaal University of Technology, P. O. Box X021, Vanderbijlpark 1900, Republic of South Africa
E-mail: ezekield@vut.ac.za

Paper received: 9 June, 2015

Paper accepted: 26 October, 2015

Preparation

The metal ion and H₄btec were dissolved in DMF and transferred to a round bottom flask. The mixture was then refluxed at 70 °C for 2 h. The resulting solution was cooled at room temperature. The solution was then centrifuged for 30 min at 3000 rpm, and decanted. The solid residue was washed with 20 mL DMF and centrifuged again for 30 min and decanted. After centrifugation, the residue was oven dried for 4 h at 100 °C.

Characterization

The metal organic framework was characterized by FT-IR, TGA, FE-SEM, HR-TEM, EDS and XRD. IR spectra were recorded using Perkin–Elmer Spectrum 400 FT-IR/FT-NIR spectrometer in the range of 400–4000 cm⁻¹. TGA was carried out with a heating rate of 10 °C/min using STA 6000 thermal analyser Perkin–Elmer. The surface morphology measurement was recorded with a JEOL 7500F field emission scanning electron microscope (SEM) and was coupled to an EDS analyser. The HR-TEM image was obtained by CM 200 electron microscope operated at 100 kV. Powder X-ray diffraction (PXRD) patterns were collected with Bruker Kα1 radiation of wavelength λ = 1.540598 Å and Kα2 radiation of wavelength λ = 1.544426 Å. Scan speed of 1 s/step and step size of 0.03°.

Determination of Cr³⁺

The concentrations of chromium ions in solutions before and after equilibrium were determined by AA-7000 atomic absorption spectrometer-auto sampler. The absorption parameters are given in the Table 1.

Adsorption experiment of Cr³⁺ by U-H₄btec MOF

Batch adsorption experiments were performed by contacting 0.01 g of Uranium H₄btec (U-H₄btec) MOF powder with 15 mL of the aqueous solution of different initial concentrations of CrCl₃·6H₂O at pH 7.2. The experiments were performed on an orbital shaker for a period of 10, 20, 30, 40, 50, and 60 min at 150 rpm in sealed 50 mL vessels. The remaining concentration of Cr³⁺ in each sample after adsorption at different time intervals was determined by atomic absorption spectroscopy after centrifugation. The Cr³⁺ concentration retained in the adsorbent phase was calculated according to:

$$q_e = \frac{V(C_i - C_e)}{W} \quad (1)$$

where C_i and C_e are the initial and equilibrium concentrations (mg/L) of Cr³⁺ solution, respectively; V is the volume (L); and W is the mass (g) of the adsorbent.

RESULTS AND DISCUSSION

The MOF of the prepared material is built on uranium cations and 1,2,4,5-benzenetetracarboxylate anions. In addition to the cation-anion interactions, the MOF structure is probably stabilized by π–π stacking interactions within the U-H₄btec system. The cation–anion and π–π interactions network lead to 3-D channels. The channels are an important honeycomb-like (zeolite-like) which can house different kind of matters.

FT-IR analysis

The FT-IR spectrum of U-H₄btec is shown in Fig. 1. The broad band that appeared around 3402 cm⁻¹ can be assigned to be the O–H vibration due to the presence of humidity and the unreacted carboxylic acid groups. The C–H bond vibration of aromatic ring appeared at 2999 cm⁻¹ and the C=O at 1746 cm⁻¹. The absorption band between 1589 and 1366 cm⁻¹ can be assigned to carbon-carbon stretching vibrations in the aromatic ring of H₄btec. FT-IR spectra of the compounds feature absorptions of the MOF below 920 cm⁻¹ may be attributed to the bond between uranium and oxygen, as observed by Kim *et al.* [16].

TGA analysis

The TGA and DTG plots of U-H₄btec MOF are presented in Fig. 2. From the DTG plot, the thermal decomposition of U-H₄btec appeared to be a complex process involving a large number of chemical reactions with three main steps of mass loss. The first mass loss around 70 °C can be most probably related to the release of moisture (12.3%). The next two main steps are probably related to organic volatiles, they occurred around 130 and 440 °C. The other small steps occurred in between 130 and 440 °C and after. The observation of the TGA plot permit to envisage a possible U-H₄btec MOF decomposition beyond the setting. Unfortunately, the TGA instrument used could not allow temperature above 900 °C.

XRD analysis

The XRD pattern of U-H₄btec MOF is presented in Fig. 3. The pattern showed three prominent peaks at 2θ 6.20, 8.09 and 10.34°. Similar pattern has been reported by Kazy *et al.* [17]. The fourth peak, with low intensity appeared at 2θ 18.59°.

Table 1. Absorption parameters for the adsorption of chromium ions unto uranium MOF

Parameter	Lamp current mA	λ nm	Slit width nm	Lamp mode	Fuel gas flow rate, L/min	Support gas flow rate, L/min	Flame type	Burner height mm
Value	10	357.9	0.7	BGC-D2	2.8	15.0	Air-C ₂ H ₂	9.0

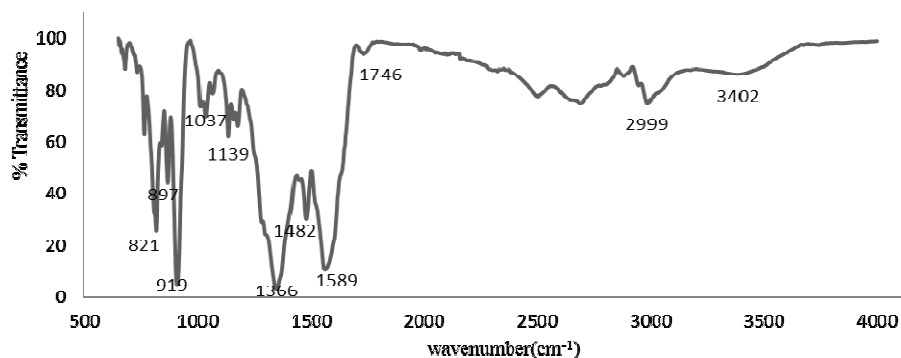


Fig. 1. FTIR spectrum for U- H_4btcc .

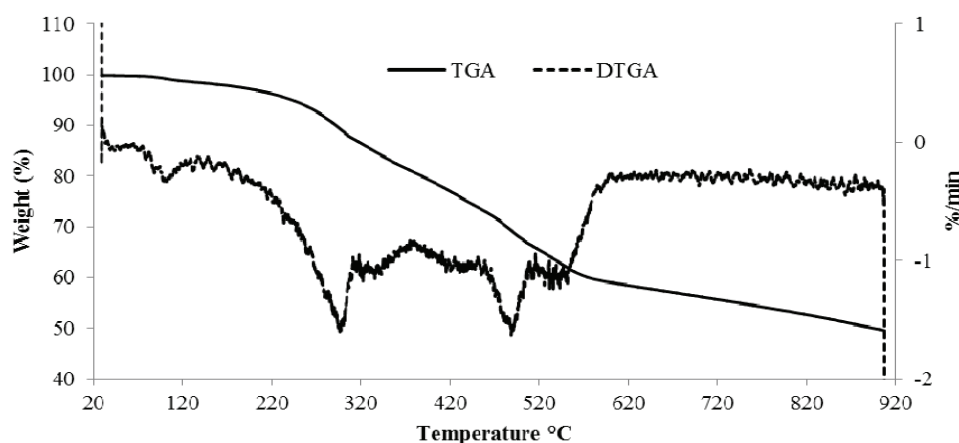


Fig. 2. TGA and DTG of U- H_4btcc MOF.

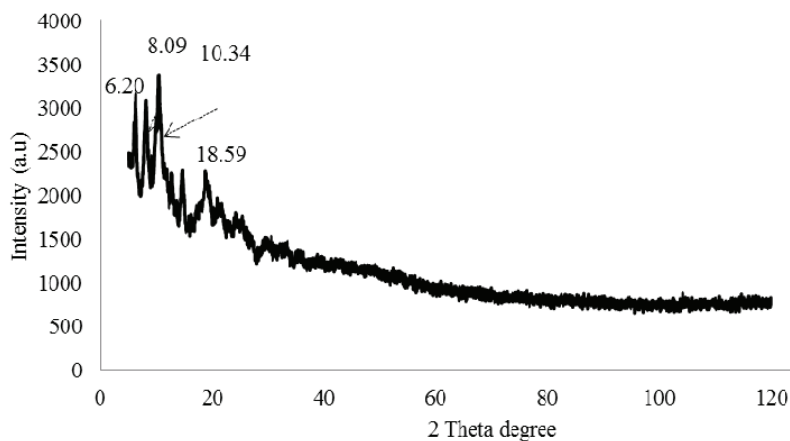


Fig. 3. XRD spectrum for Uranium pyromellitic at room temperature.

SEM and EDS analysis

The scanning electron microscopy (SEM) image of U- H_4btcc MOF is shown in Fig. 4. The visual observation of the SEM image did not reveal specific shapes, such as rod or stick but, showed the morphology of a porous and flaky material. The flaky structure resembling to a bunch of petals is likely to play an important role if the MOF has to be used as adsorbent. It is possible that the flaky structure of this MOF was strongly influenced by the properties of uranium. The EDS spectrum (Fig. 5)

showed clearly the presence of uranium in the structure of the MOF.

TEM Analysis

Transmission electron microscopy (TEM) analysis was conducted to study the internal morphology of synthesized U- H_4btcc MOF. The TEM image of uranium 1,2,4,5-benzene tetracarboxylic acid MOF obtained is presented in Fig. 6. TEM result suggested the existence of U- H_4btcc MOF in the form of pellets with particles

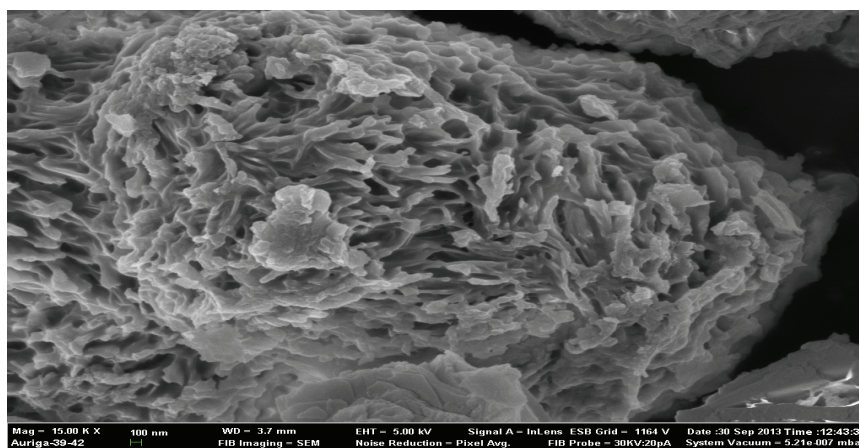


Fig. 4. SEM image for U-H₄btec MOF.

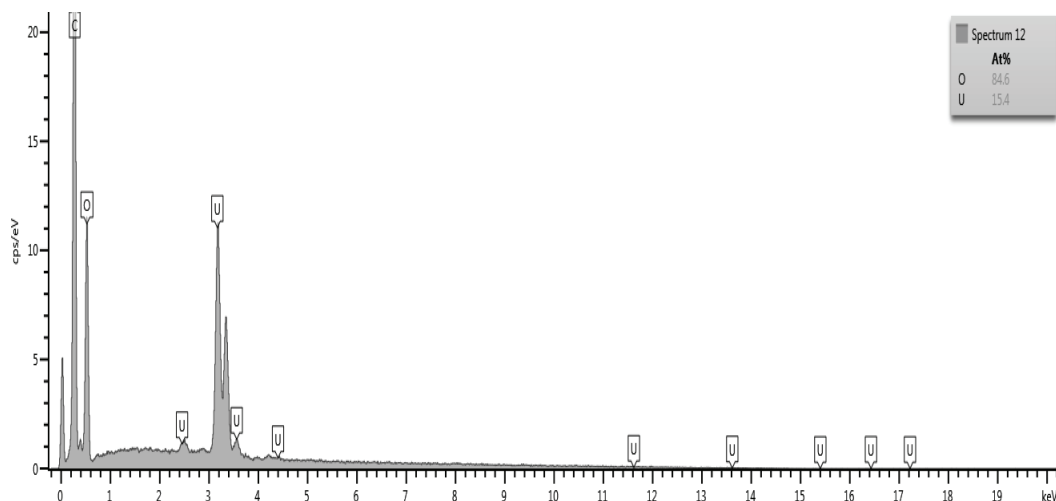


Fig. 5. EDS analysis.

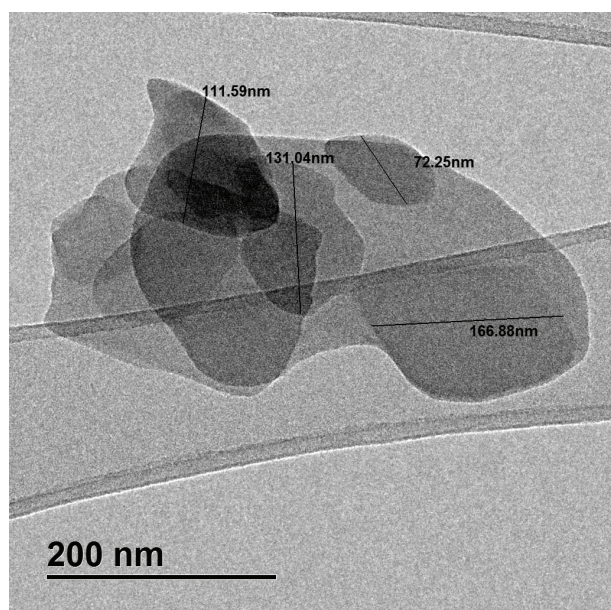


Fig. 6. TEM image for U-H₄btec MOF.

diameter varying between 72.25 and 166.88 nm. The typical TEM image clearly confirmed the flaky and porous structure of the U-H₄btec framework which is in accordance with the SEM result.

Adsorption results

Adsorption was conducted using a batch setup and chromium ions were determined using atomic absorption spectroscopy (with $r^2 = 0.9999$). The Langmuir and Freundlich isotherms were used to assess the adsorption behaviour of U-H₄btec MOF. The kinetics of adsorption was investigated by means of contact time, pseudo-first, and pseudo-second order reaction, in order to possibly explain the sorption mechanism, such as mass transfer and/or chemical reaction.

Effect of contact time

Time is one of the prime factors determining the adsorption behaviour of a system. Contact time was used in order to understanding the amount of Cr³⁺ adsorbed at various time intervals by a fixed amount of

the adsorbent and to monitor the equilibrium. Results (Fig. 7) showed that for the five different concentrations, equilibrium was achieved after about 30 min. The general adsorption trend could be described as: sharp increase of U-H₄btec uptake during the first 30 min and then equilibrium. All the plots, however, have features that suggest a cover up step before equilibrium.

Effect of concentration

The effect of initial concentration in the range of 20 to 100 mg/L on adsorption is presented in Fig. 8. Result showed that with the same amount of adsorbent, the concentration of Cr³⁺ adsorbed increased with the concentration of the initial solution. This fact can be explained by the mass transfer of Cr³⁺ and pressure onto the inner adsorption sites of the adsorbent.

Pseudo first and pseudo second order reaction

Plots of pseudo first and pseudo second order are shown in Figs. 9 and 10. They had high r^2 (from 0.8743 to 0.997) meaning that adsorption probably underwent physisorption and chemisorption processes [18]. This can be explain by the lone pair electron on oxygen

atoms (of the carboxylic moiety, behaving like a ligand) that could be responsible of a bond between the adsorbent and Cr³⁺, possible π - π electron donor-acceptor interactions between the aromatic rings moiety of the adsorbent (H₄btec) and Cr³⁺, and the presence of pores in the 3-D structure the MOF which could have trapped the adsorbate.

Adsorption isotherms

Langmuir and Freundlich isotherms (linear plots) were used to study the adsorption of Cr³⁺ by U-H₄btec MOF and results are presented in Figs. 11 and 12. The Langmuir model advocate for equality of affinity between adsorption sites-adsorbate and that adsorption at one site does not affect adsorption at an adjacent site on monolayer surfaces [19,20]. The Freundlich model, however, describes the equilibrium on heterogeneous systems and does not assume monolayer capacity [19,21]. Correlation coefficients (r^2) were used to estimate the best fit isotherm model for the adsorption of Cr³⁺. r^2 values of the two models (Langmuir and Freundlich) are almost in the same range (similar), suggesting that Cr³⁺ were adsorbed on

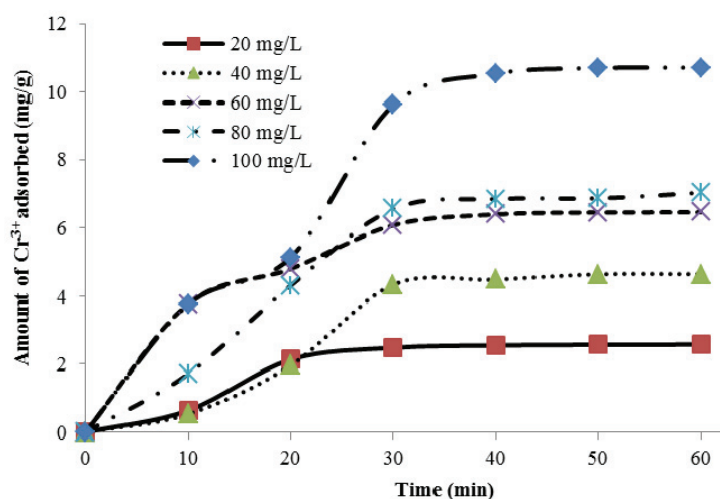


Fig. 7. Effect of time on adsorption.

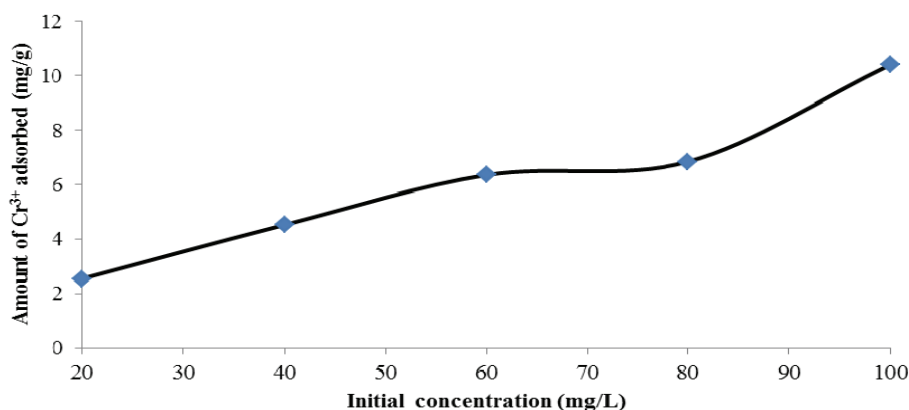


Fig. 8. Effect of Initial concentration of chromium ions.

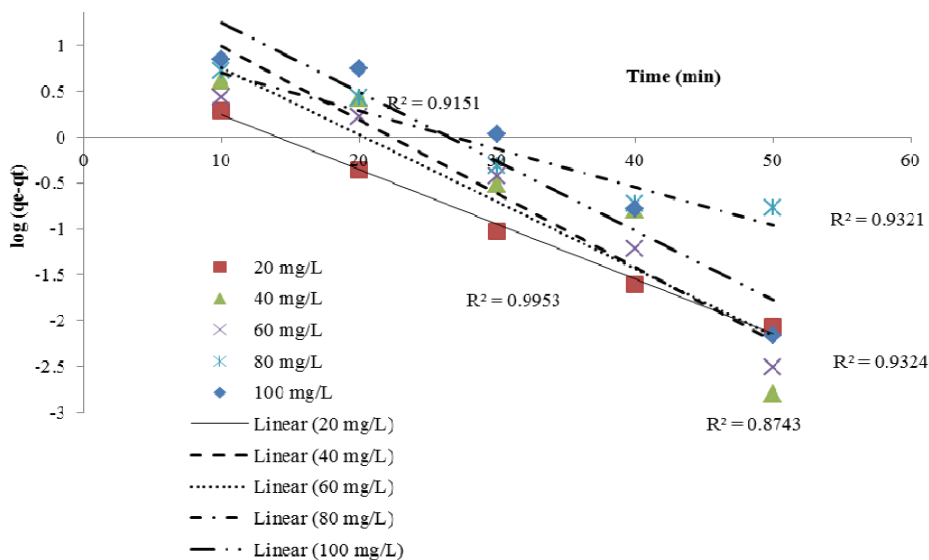


Fig. 9. Pseudo first order plot of adsorption of chromium ion.

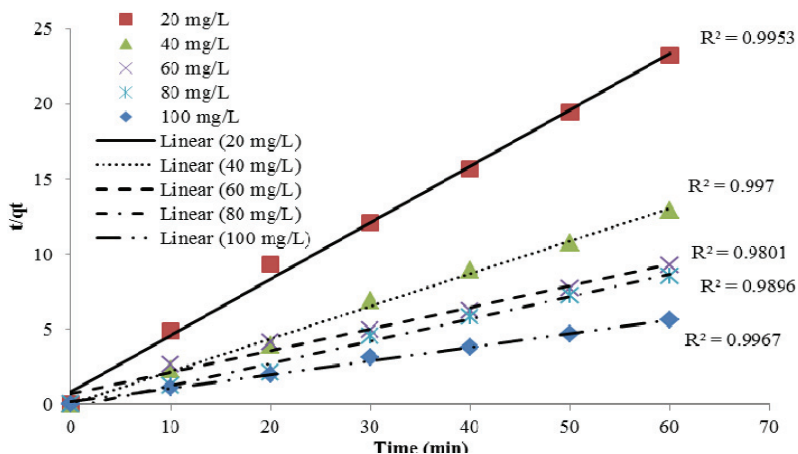


Fig. 10. Pseudo second order plot for the adsorption of chromium ions.

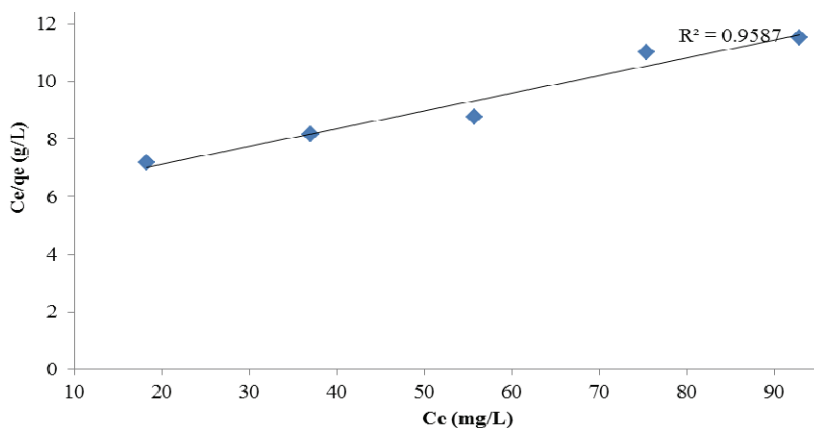


Fig. 11. Langmuir isotherm for the adsorption of chromium ions.

the surface (monolayer) and the inner sites (multilayer system) of the adsorbent. This implication should not surprise since the adsorbent (MOF) is assumed to be a three-dimensional system. Therefore, Cr^{3+} with its 75.5

pm radius size could have penetrated the $U-H_4btec$ pores and be adsorbed by the inner adsorption sites.

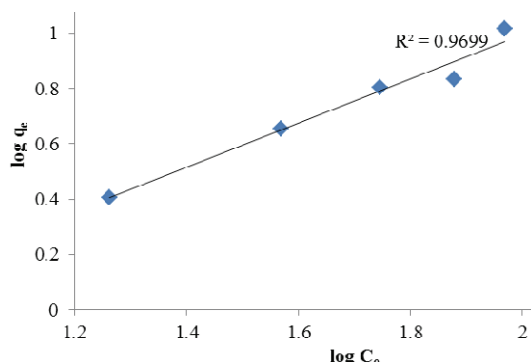


Fig. 12. Freundlich Isotherm for the adsorption of chromium ions on uranium MOF.

CONCLUSION

This work presented the synthesis of uranium 1,2,4,5-benzene tetracarboxylic acid metal organic framework by solvothermal method. Unlike many other results (rod and stick shapes), the SEM characterization of U-H₄btec MOF showed a flaky and porous morphology of the material. Used as adsorbent, the U-H₄btec MOF showed promising adsorption properties with equilibrium reached during the first 30 min. It was observed that the Cr³⁺ uptake increased with the concentration of the initial solution and adsorption could have followed chemisorption and physisorption. Also, isotherms (Langmuir and Freundlich) suggested monolayer and multilayer systems.

Acknowledgement

This work was supported by a research grant from the Faculty of Applied and Computer Science Research and Publications Committee of Vaal University of Technology, Vanderbijlpark, Republic of South Africa.

REFERENCES

- [1] Q. Li, W. Zhang, O.Š. Miljanić, C.H. Sue, Y.L. Zhao, L. Liu, C.B. Knobler, J.F. Stoddart, O.M. Yaghi, Docking in Metal-Organic Frameworks, *Science* **325** (2009) 855–859.
- [2] G. Férey, Hybrid porous solids: past, present, future, *Chem. Soc. Rev.* **37** (2008) 191–214.
- [3] S. Natarajan, P. Mahata, Non-carboxylate based metal-organic frameworks (MOFs) and related aspects, *Curr. Opin. Solid State Mater. Sci.* **13** (2009) 46–53.
- [4] S. Proch, J. Herrmannsdörfer, R. Kempe, C. Kern, A. Jess, L. Seyfarth, J. Senker, Pt@MOF-177: synthesis, room-temperature hydrogen storage and oxidation catalysis, *Chem. Eur. J.* **14** (2008) 8204–8212.
- [5] R. Zacharia, D. Cossement, L. Lafi, Volumetric hydrogen sorption capacity of monoliths prepared by mechanical densification of MOF-177, *J. Mater. Chem.* **20** (2008) 2145–2151.
- [6] S.S. Han, W.A. Goddard, High H₂ storage of hexagonal metal-organic frameworks from first-principles-based grand canonical Monte Carlo simulations, *J. Phys. Chem.* **112** (2008) 13431–13436.
- [7] D. Saha, S. Deng, Synthesis, characterization and hydrogen adsorption in mixed crystals of MOF-5 and MOF-177, *Int. J. Hydrogen Energy* **34** (2009) 2670–2678.
- [8] E. Poirier, A. Dailly, Thermodynamics of hydrogen adsorption in MOF-177 at low temperatures: measurements and modelling, *Nanotechnology* **20** (2009) 1–6.
- [9] M. Gallo, D. Glossman-Mitnik, Fuel gas storage and separations by metal–organic frameworks: Simulated adsorption isotherms for H₂ and CH₄ and their equimolar mixture, *J. Phys. Chem., C* **113** (2009) 6634–6642.
- [10] K. Yang, F. Xue, Q. Sun, R. Yue, D. Lin, Adsorption of volatile organic compounds by metal–organic frameworks MOF-177, *J. Environ. Chem. Eng.* **1** (2013) 713–718.
- [11] E.D. Dikio, A.M. Farah, Synthesis, characterization and comparative study of copper and zinc metal organic frameworks, *Chem. Sci. Trans.* **2** (2013) 1386–1394.
- [12] G. Kumar, R. Gupta, Molecularly designed architectures – the metal-organic way, *Chem. Soc. Rev.* **42** (2013) 9403–9453.
- [13] K.B. Klepper, O. Nilsen, H. Fjellervåg, Deposition of thin films of organic–inorganic hybrid materials based on aromatic carboxylic acids by atomic layer deposition, *Dalton Trans.* **39** (2010) 11628–11635.
- [14] Y. Luo, K. Bernot, G. Calvez, S. Freslon, C. Daiguebonne, O. Guillou, N. Kerbellec, T. Roisnel, 1,2,4,5-Benzene-tetracarboxylic acid: a versatile ligand for high dimensional lanthanide–based coordination polymers, *Cryst. Eng. Comm.* **15** (2013) 1882–1896.
- [15] Y.Y. Liu, Z.F. Ng, E.A. Khan, H.K. Jeong, C.B. Ching, Z.P. Lai, Synthesis of continuous MOF-5 membranes on porous-alumina substrates, *Microp. Mesop. Mater.* **118** (2009) 296–301.
- [16] J.G. Kim, Y.S. Park, Y.K. Ha, K. Song, Infrared Spectra of Uranium Oxides Measured by ATR–FTIR, *J. Nucl. Sci. Technol.* **46** (2009) 1188–1192.
- [17] S.K. Kazy, S.F. D’Souza, P. Sar, Uranium and thorium sequestration by a *Pseudomonas* sp.: Mechanism and chemical characterization, *J. Hazard. Mater.* **163** (2009) 65–72.
- [18] Y.S. Ho, G. McKay, Pseudo-second order model for sorption processes, *Process Biochem.* **34** (1999) 451–465.
- [19] V. Vadivelan, K.V. Kumar, Equilibrium, kinetics, mechanism, and process design for the sorption of methylene blue onto rice husk, *J. Colloid Interface Sci.* **286** (2005) 90–100.
- [20] D. Mohan, C.U. Pittman Jr., M. Bricka, F. Smith, B. Yancey, J. Mohammad, P.H. Steele, M.F. Alexandre-Franco, V. Gómez-Serrano, H. Gong, Sorption of arsenic, cadmium, and lead by chars produced from fast pyrolysis of wood and bark during bio–oil production, *J. Colloid Interface Sci.* **310** (2007) 57–73.
- [21] S. Chatterjee, S. Chatterjee, B.P. Chatterjee, A.K. Guha, Adsorptive Removal of Congo Red, a Carcinogenic Textile Dye by Chitosan Hydrobeads: Binding Mechanism, Equilibrium and Kinetics, *Colloids Surfaces, A* **299** (2007) 146–152.

IZVOD**MORFOLOGIJA I ADSORPCIJA JONA HROMA NA METAL–ORGANSKOM OKVIRU (MOF) URAN–1,2,4,5-BENZEN-TETRAKARBOKSILNA KISELINA**

Remy M.K. Vala, Donbebe Wankasi, Ezekiel D. Dikio

Applied Chemistry and Nanoscience Laboratory, Department of Chemistry, Vaal University of Technology, Vanderbijlpark, South Africa

(Naučni rad)

U ovom radu pokazana je sinteza metalnog organskog okvira (MOF) uranijum 1,2,4,5-benzentetrakarboksilne kiseline (U-H4bttec MOF) primenom metode termalnog rastvaranja. Izvršena je karakterizacija dobijenog MOF primenom infracrvene spektroskopije sa Furijeovom transformacijom (FTIR), skenirajuće elektronske mikroskopije (SEM), transmisione elektronske mikroskopije (TEM), difrakcije X-zraka (XRD), spektroskopije dispergovane energije (EDS) i termogravimetrijske i diferencijalne termogravimetrijske analize (TGA/DTA). Morfologija MOF uranijum 1,2,4,5-benzentetrakarboksilne kiseline analizirana pomoću SEM pokazuje prisustvo lisnate porozne strukture. Adsorpcija Cr^{3+} iz vodenog rastvora na MOF uranijum 1,2,4,5-benzentetrakarboksilnu kiselinu je sistematski ispitana. Langmuir i Freundlich adsorpcione izoterme su primenjene za određivanje adsorpcionog kapaciteta MOF za formiranje monosloja. Kinetičko određivanje adsorpcije Cr^{3+} ukazuje kako na proces hemisorpcije tako i fizioadsorpcije, verovatno zbog prisustva karbonilne grupe u okviru MOF i njegove porozne strukture.

Ključne reči: Adsorpcija • Fizioadsorpcija • Metalni organski okvir • 1,2,4,5-Benzentetrakarboksilna kiselina • Uranil acetat dehidrat • SEM

Testing of the functional garments with microencapsulated phase-change material in simulated high temperature conditions

Dalibor B. Jovanović¹, Predrag N. Stojisavljević¹, Sveta G. Cvetanović², Dušan S. Rajić³, Radovan M. Karkalić⁴, Negovan D. Ivanković⁴, Željko B. Senić⁵

¹Technical Test Center, General staff of the SAF, Belgrade, Serbia

²University of Niš, Faculty of Occupational Safety, Niš, Serbia

³University of Belgrade, Innovation Center, Faculty of Technology and Metallurgy, Belgrade, Serbia

⁴University of Defense, Military Academy, Belgrade, Serbia

⁵Military Technical Institute, Belgrade, Serbia

Abstract

An organic phase change material (PCM) possesses the ability to absorb and release large quantity of latent heat during a phase change process over a certain temperature range. This paper presents results related to thermo-physiological efficiency of special underwear with organic PCM integrated in textile through microencapsulation process. The efficiency of PCM underwear was tested through physiological examinations in simulated high-temperature conditions, where test-subjects were voluntarily exposed to heat stress tests wearing NBC protective suit with PCM underwear (option "THERM") and without it (option "NoTHERM"). It can be concluded that wearing a PCM textile clothes under NBC protective suit, during physical activity in high-temperature conditions, reduces sweating and alleviates heat stress manifested by increased core and skin temperature and heart rate values.

Keywords: phase change, microencapsulation, protective suit, underwear, physiological measurements.

Available online at the Journal website: <http://www.ache.org.rs/HI/>

PROFESSIONAL PAPER

UDC 67/68:614:62

Hem. Ind. 70 (5) 573–579 (2016)

doi: 10.2298/HEMIND150716064J

Phase change materials possess the ability to change their state with a certain temperature range. These materials absorb energy during the heating process as phase change takes place, otherwise this energy can be transferred to the environment in the phase change range during a reverse cooling process [1]. The insulation effect reached by the PCM is dependent on temperature and time; it takes place only during the phase change (in the temperature range of the phase change) and terminates when the phase change in all of the PCMs would complete. Since, this type of thermal insulation is temporary, it can be referred to as dynamic thermal insulation. Numerous engineering applications have made the topic of melting of phase change material in enclosures one of the most active fields in heat transfer research today [2].

During the complete melting process, the temperature of the PCM as well as its surrounding area remains nearly constant. The same is true for the crystallization process; during the entire crystallization process the temperature of the PCM does not change significantly either. Phase change process of PCM from solid to liquid and vice versa is schematically shown in Figure 1 [3].

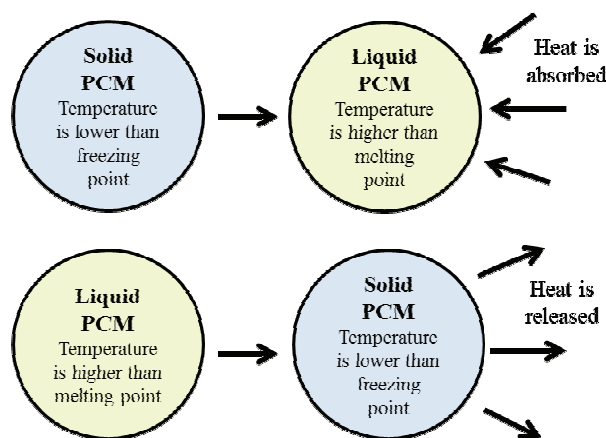


Figure 1. Phase change process.

The large heat transfer during the melting process as well as the crystallization process without significant temperature change makes PCM interesting as a source of heat storage material in practical applications. When temperature increases, the PCM microcapsules absorb heat and storing this energy in the liquefied phase change materials. When the temperature falls, the PCM microcapsules release this stored heat energy and consequently PCM solidify [4]. For substances that are solid, conduction is the predominate mode of heat transfer. For liquids, convection heat transfer predo-

Correspondence: D.B. Jovanović, Technical Test Center, Belgrade, Serbia.

E-mail: jovcadach@hotmail.com

Paper received: 16 July, 2015

Paper accepted: 3 November, 2015

minates, and for vapors convection and radiation are the primary mode of heat transfer. When the melting temperature of a PCM is reached during heating process, the phase change from the solid to the liquid occurs. During this phase change, the PCM absorbs large quantities of latent heat from the surrounding area. PCM may repeatedly converted between solid and liquid phases to utilize their latent heat of fusion to absorb, store and release heat or cold during such phase conversions.

Phase change materials are able theoretically to change state at nearly constant temperature and therefore to store large quantity of energy [5]. Using the thermal energy storage (TES) of phase change material (PCM) which has a melting point from 15 to 35 °C is one of the most effective ideas for effective utilization of this kind of materials in the field of personal body cooling.

Currently, more than 500 natural and synthetic PCMs are known [6]. These materials differ from one another in their phase change temperature ranges and their heat storage capacities.

Classification and properties of organic PCMs

In 1971, Hale *et al.* published “Phase Change Materials Handbook” in which they provided data related with the material properties of more than 500 promising PCMs needed by the thermal design engineers to bridge the gap between research achievements and actual systems [7]. Since then numerous studies have focused on organic PCMs. The well-known and extensively studied organic PCMs, which undergo solid–liquid phase transition during heating and subsequent cooling, have been paraffin waxes, poly(ethylene glycol)s, fatty acids and their derivatives. In addition, a group of organic PCMs, such as polyalcohols and polyethylenes, which undergo solid–solid phase transition at a fixed temperature by absorbing and releasing large amount of the latent heat, have been paid attention as the promising organic PCMs.

Comprehensive lists of the most possible candidates as organic PCMs have been reported in the literature by Lane *et al.* [8], Lorsch *et al.* [9], Abhat [10], Humphries and Griggs [11], Farid and Khudhair [12], Zalba *et al.* [13], Farid *et al.* [14] and Cabeza *et al.* [15]. In all these studies, a number of criteria to be fulfilled by an ideal organic PCM candidate have been listed as:

- exhibiting high latent heat capacity to provide a high thermal storage density,
- small volume change during phase transition,
- repeatability of phase change,
- thermal stability in the course of numerous heating and cooling cycles,
- high density to allow a small size of storage container, as well as being (vi) chemically stable,
- non-corrosive, non-toxic, nonflammable,

–low-cost and easily available.

The limitations reported by many researchers are the low thermal conductivity possessed by many organic PCMs leading to low charging and discharging rates, supercooling effect in cooling cycles, and need for containers for preventing the leakage of PCMs [16–18].

One of the most important groups of organic PCMs is paraffin waxes (Table 1). They consist of a mixture of mostly straight-chain *n*-alkanes, $\text{CH}_3(\text{CH}_2)_n\text{CH}_3$. The melting point of a paraffin wax increase with increasing chain length as seen in Table 1, which can be attributed to the increase in the induced dipole attractions between *n*-alkane chains, *e.g.*, the melting point of *n*-tetradecane (14 C atoms) is 5.9 °C, while that of *n*-octacosane (28 C atoms) is around 62 °C [7,19].

Table 1. Thermal properties of paraffin waxes with the number of carbon atoms ranging from 12 to 28

Paraffin wax	Number of C atoms	Melting point °C	Latent heat of fusion, kJ/kg
<i>n</i> -Octacosane	28	61.4	253
<i>n</i> -Heptacosane	27	59	236
<i>n</i> -Hexacosane	26	56.4	256
<i>n</i> -Pentacosane	25	53.7	238
<i>n</i> -Tetracosane	24	50.9	255
<i>n</i> -Tricosane	23	47.6	232
<i>n</i> -Docosane	22	44.4	249
<i>n</i> -Heneicosane	21	40.5	200
<i>n</i> -Eicosane	20	36.8	246
<i>n</i> -Nonadecane	19	32.1	222
<i>n</i> -Octadecane	18	28.2	244
<i>n</i> -Heptadecane	17	22	213
<i>n</i> -Hexadecane	16	18.2	237
<i>n</i> -Pentadecane	15	10	205
<i>n</i> -Tetradecane	14	5.9	228

Microencapsulation of PCMs

Microencapsulation is a process by which solid particles, liquid droplets, or gas bubbles, named as the core material, are coated with polymer or co-polymer materials, named as the shell material. The term microcapsule is generally used to describe particles with diameters between 1 and 1000 μm. Particles smaller than 1 μm are called nanoparticles, whereas particles greater than 1000 μm are named microgranules or macrocapsules [20]. The shell material of capsules can be formulated by using a wide variety of materials including natural and synthetic polymers, depending on the chemical characteristics and intended use of the core, the conditions under which the product is stored, the processing conditions to which the microcapsules are exposed as well as the cost and availability [21]. The morphology of microcapsules depends mainly on

the core material and the deposition process of the shell. Microcapsules may have regular or irregular shapes, and they can be classified as mononuclear type, polynuclear type and matrix type on the basis of their morphology. Mononuclear microcapsules contain the shell around the core, while polynuclear capsules have many cores enclosed within the shell. In matrix type capsules, the core material is distributed homogeneously into the shell material. In addition to these three basic morphologies, microcapsules can also be mononuclear with multiple shells, or they may form clusters of microcapsules [22]. The main advantages of microencapsulation can be summarized as: *i*) protection of unstable, sensitive materials from their environments prior to use, *ii*) better processing by improving solubility and dispersibility of core and shell materials, *iii*) employment of a variety of core materials, *iv*) production with a high concentration and high yield, *v*) shelf-life enhancement by preventing degradative reactions and evaporation, *vi*) safe and convenient handling of core materials and *vii*) masking of odor or taste [23].

The impact of phase-change materials (PCM) on intelligent thermal-protective clothing has been investigated by many researchers [24]. In the heating process, when the PCM layer's temperature increases above the PCM's melting point, the PCM melts and becomes liquid. During this process, thermal energy is absorbed and stored. After all the PCM becomes liquid, the temperature continually increases. When the PCM layer's temperature reaches over melting point, the conductive fabrics were powered off. The temperature of the PCM layer then decreases after a short time. When the temperature of the PCM layer decreases below melting point, the liquid PCM becomes solid and releases heat energy. In this process, the PCM acts as a thermal buffer material by releasing stored heat.

Study methods

The PCMs efficiency was tested through physiological examinations of special underwear (model Outlast®, Outlast Europe GmbH, 100% polyester fabric, weight of 177,6 g/m²). With this type of underwear, organic PCM (*n*-octadecane, melting point 28 °C) through microencapsulation was incorporated into the textile material.

Ten male soldiers were voluntarily subjected to exertional heat stress tests (EHST) consisted of walking on treadmill (5.5 km/h) in hot conditions (40 °C) in climatic chamber, wearing chemical protective suits. The efficiency of PCM underwear was tested through physiological examinations in simulated hot conditions, where test-subjects voluntarily exposed to heat stress tests wearing nuclear-biological-chemical (NBC) protective suit with PCM underwear (option "THERM") and without it (option "NoTHERM"). Physiological strain was determined by mean skin temperature (*T_{sk}*), body

core temperature (*T_{ty}*) and heart rate values (*HR*), while sweat rates (*SwR*) indicated changes in hydration status.

The procedures performed in the present study corresponded to the standards or thermal strain evaluation by physiological measurements [25,26]. Skin temperatures were measured continuously using contact probes with transducers TSD202E and TSD202F (precision ±0.2 °C, range 0–60 °C, response time 0.9 s; BIOPAC Systems Inc., USA). The thermistors were set at 4 locations (neck, right scapula, left hand and right shin). Mean skin temperatures (*T_{sk}*) were calculated every 5 min from values obtained and weighted. Core (tympanic) temperatures (*T_{ty}*) were continuously measured using contact probe TSD202A (precision ±0.1 °C, range 20–50 °C, response time 0.6 s) with transducer introduced into the auditory canal and placed toward the eardrum [10,11]. Data are presented as mean ± *SD*. The significance of differences between parameters obtained during EHSTs was tested by Student's *t*-test, with significance level *p* < 0.05.

EXPERIMENTAL RESULTS

Body core temperature

Changes in test subject's tympanic temperature (*T_{ty}*), while performing EHST in chemical protective suit, with body thermoregulating underwear („THERM“) and without it („NoTHERM“), are shown in Figure 2.

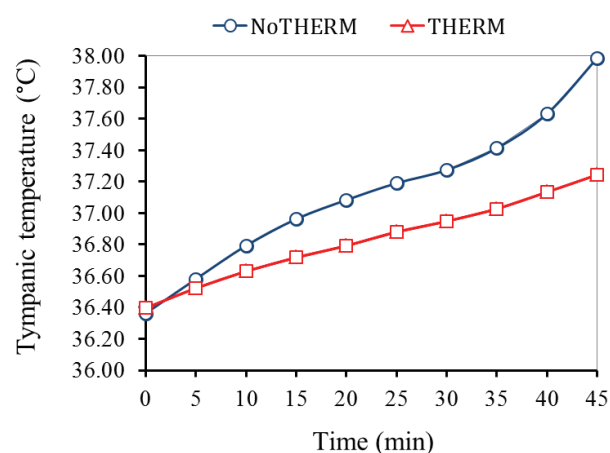


Figure 2. The mean tympanic temperature during EHSTs.

The increase of tympanic temperature in all test subjects, in the cases with thermoregulation and without it, are shown graphically in Figure 3.

In NoTHERM group changes in temperature values over time are characterized by similar dynamics: rapid growth in the first 15 and last 10 min, a little slower in the middle part of the EHST. In the THERM group better temperature stability was noted, without any significant changes in growth increase during the EHST.

In the 45th min of the test, compared to the NoTHERM option, significantly lower values of the *T_{ty}* ($p < 0.05$) in the THERM group were observed (0.74 ± 0.08 °C). The total temperature increase of 1.67 ± 0.15 °C was recorded in NoTHERM group, while in THERM group the increase was much lower (0.84 ± 0.05 °C) [3].

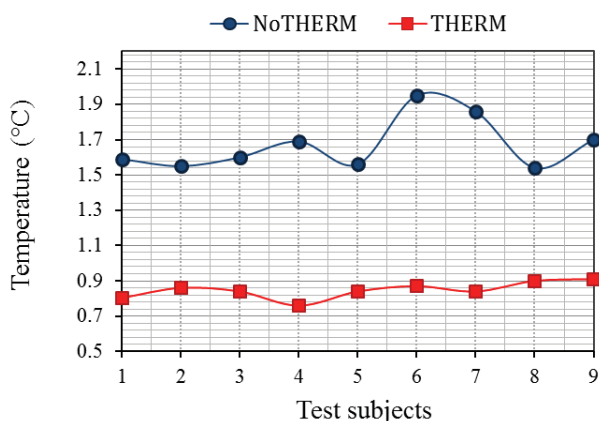


Figure 3. The increase of *T_{ty}* during EHSTs.

Skin temperature

Graphical reviews of mean skin temperature (*T_{sk}*) values during EHST are displayed in Figure 4 [3].

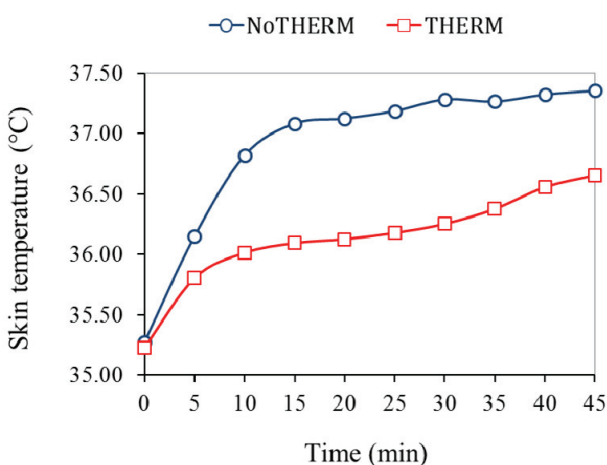


Figure 4. The mean skin temperature during EHSTs.

In both cases, during the first part of the EHST (up to 15th min), mean skin temperature rapidly increased until sweating occurred, then slowed towards the end of test. Minimum oscillation in *T_{sk}* changes was recorded in the group THERM, which is characterized by a significantly lower ($p < 0.05$) increase of temperature from the start to the end of the EHST (1.43 ± 0.22 °C), compared to group NoTHERM.

Mean skin temperature on four local skin points (neck, scapula, arm, leg), in both groups (NoTHERM, THERM), in 45th min of the EHST, are shown in Table 2.

Table 2. Mean *T_{sk}* values (°C) measured on four local skin points in 45th min EHST

<i>T_{sk}</i>	NoTHERM	THERM
<i>T_{sk}₁</i> (neck)	37.27±0.58	36.34±0.42
<i>T_{sk}₂</i> (scapula)	37.43±1.22	35.7±0.82
<i>T_{sk}₃</i> (arm)	37.57±0.53	37.52±0.73
<i>T_{sk}₄</i> (leg)	37.14±1.03	37.02±1.14

In experimental group THERM in the end of EHST significantly lower values of skin temperature were observed in relation to the option NoTHERM (an average of 0.66 ± 0.12 °C, $p < 0.05$).

Heart rate

The dynamics of the average heart rates in both groups are displayed in Figure 5.

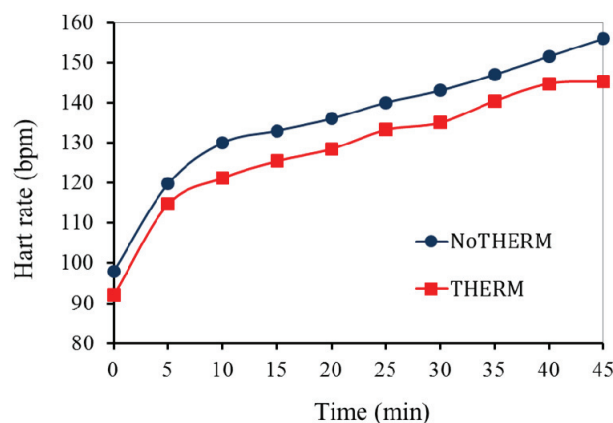


Figure 5. The mean heart rates during EHSTs.

The mean values of the hart rate and total increase (Δ HR) in both groups (NoTHERM, THERM) are displayed in Table 3.

Table 3. Mean values of HR and total growth (Δ HR) while using NBC suit without thermoregulation (NoTHERM) and with functional underwear (THERM)

Time min	NoTHERM (bpm)		THERM (bpm)	
	$X \pm SD$	Δ HR	$X \pm SD$	Δ HR
0	98±12	58	92±33	53
5	120±13		115±10	
10	130±14		121±12	
15	133±13		125±14	
20	136±13		128±15	
25	140±10		133±15	
30	143±7		135±8	
35	147±10		140±8	
40	152±8		145±11	
45	156±8		145±19	

Mean values of HR ($\pm SD$) noticed on every 5 min of the EHST are shown, as well as total increase of heart rate (ΔHR), calculated as difference between values recorded in the first and last minute of EHST ($\Delta HR = HR_{45} - HR_0$).

In both groups rapid increase of HR was recorded in the first 10 min, and then it slowed significantly.

This trend is particularly specific in NoTHERM group, where the heart rate increased in the first 10 min for 32 ± 9 bpm, and within the next 35 min only for 26 ± 7 bpm. The maximum value of HR was observed in NoTHERM group at the end of the EHST (156 ± 8 bpm), while at the same time in THERM group was lower for 11 bpm (145 ± 19 bpm). When comparing the mean values of HR between the two tested groups, a significant difference ($p < 0.05$) can be observed (in the THERM group mean HR was 128 ± 16 bpm, in the NoTHERM group 135 ± 17 bpm).

In order to minimize the differences regarding EHST durations, sweat rate (SwR) was expressed per hour (Figure 6). The average rate of sweating, as expected, was higher in NoTHERM group (0.56 ± 0.09 l/(m² h)). Statistically significant lower sweating was observed in THERM group in relation to the NoTHERM (0.42 ± 0.06 L/(m² h)); $p < 0.05$.

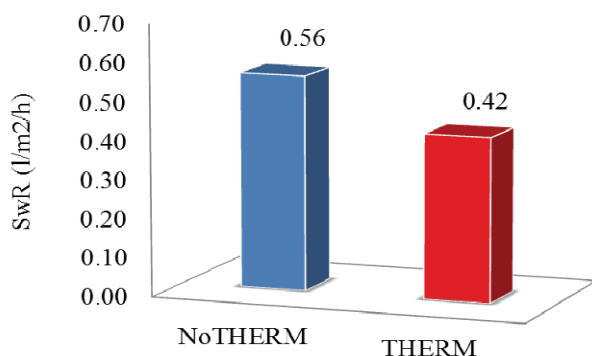


Figure 6. The mean sweat rates during EHSTs.

DISCUSSION

In our experimental conditions (40 °C), *n*-octadecane microencapsulated inside underwear, showed significant stability during the most of exercises, despite high ambient temperatures. Rapid activation caused by the adequate melting point of 28.2 °C (Table 1), while a relatively long and stable thermoregulating effect is a consequence of the high latent heat of fusion (244 kJ/kg).

The choice of organic PCM with 18 C atoms in this case had a direct influence on a clothes thermoregulation efficiency, observed through T_{ty} and T_{sk} parameters. Activation point (which is practically equal to the compound melting point) of the *n*-octadecane allows activation of microcapsules and absorption of

the excess heat from the body that occurs during physical exercises in a climate chamber. Better thermoregulation while using underwear has been proven by lower values of T_{ty} and T_{sk} measured during EHST, lower cardiovascular load as well as lower intensity of perspiration.

Experimental group THERM is characterized by the smallest fluctuations in temperature as a function of time during EHST, which additionally indicates the stability of the thermoregulation process.

Perspiration as a mechanism of revealing excess heat has special significance in heat stress due to physical activity, when it occurs not only as a consequence of thermal factors (increasing T_{ty} and T_{sk}), but also „non-thermal“ indicators such as central activation, activation of muscle mechano-metabo receptors activity and baroreflex activation due to physical activity [27]. According to our study results, the intensity of respiration when using PCM underwear has a lower value of 25% compared to the option without thermoregulation. This may contribute to the prevention of dehydration while working in complex conditions that require wearing NBC protective equipment.

Many other studies also confirmed that cooling efficiency depends on the selected type of PCM and its thermal properties. Our results are consistent with the study of Fok and coworkers [28] who carried out the investigation of the same PCM – paraffin *n*-octadecane, to cool a motorcycle helmet. Paper presents the experimental investigations on the influence of the simulated solar radiation, wind speed and heat generation rate on the cooling system. The results show that helmet cooled with the phase change material provide prolonged thermal comfort period compared to a normal helmet. Their findings also indicate that the heat generation from the head is the predominant factor affecting the PCM's melting time.

Study results confirmed that usage a textile thermoregulating clothes with integrated organic PCM, have direct influence on improving thermophysiological properties of NBC protective suit.

CONCLUSION

Study results confirmed that usage of the PCM with high latent heat of fusion (from 200 to 250 kJ/kg) and a melting point around 30 °C results in a very efficient body thermoregulation in hot conditions. Our study also confirmed opinions from other studies that application of PCM with a higher melting point ensures stable and permanent cooling for a longer period of time [28,29]. Based on physiological parameters measured during EHSTs (groups NoTHERM and THERM), it can be concluded that a decisive influence on the thermoregulation efficiency has melting point and latent

heat of fusion of the used compound for textile application.

Our study results open possibility for developing own phase-change material for textile application, with appropriate thermal, physical and chemical properties, suitable for use under the nuclear-biological–chemical protective suits, combat vests or uniforms, in different missions and under extreme temperature conditions.

Acknowledgements

Ministry of Education, Science and Technological Development of the Republic of Serbia supported this work, Grant No. TR34034 (2011–2015).

REFERENCES

- [1] K.K. Pillai, B.J. Brinkwarth, The storage of low grade thermal energy using phase change materials, *Appl. Energy* **2** (1976) 205–216.
- [2] A. Abhat, Low temperature latent heat thermal energy storage, *Thermal energy storage*, D. Reidel Publication, Dordrecht, 1981.
- [3] D. Jovanović, Examination of means for improving physiological suitability under highly toxic contamination and high ambient temperatures, dissertation, University of Defense, Belgrade, 2013.
- [4] D.V. Hale, M.J. Hoover, M.J. O'Neill, *Phase change materials handbook*, Marshal Space Flight Center, Huntsville, AL, 1971.
- [5] R. Biswas, Thermal storage using sodium sulfate decahydrate and water, *Sol. Energy* **99** (1977) 99–100.
- [6] B. Charlsson, H. Stymme, G. Wattermark, An incongruent heat of fusion system $\text{CaCl}_2 \cdot 6\text{H}_2\text{O}$ made congruent through modification of chemical composition of the system, *Sol. Energy* **23** (1979) 333–350.
- [7] N. Sarier, E. Onder, Organic phase change materials and their textile applications: An overview, *Thermochim. Acta* **540** (2012) 8–9.
- [8] G.A. Lane, D.N. Glew, E.C. Clark, H.E. Rossow, S.W. Quigley, S.S. Drake, J.S. Best, Heat of fusion systems for solar energy storage subsystems for the heating and cooling of building, in: L.U. Lilleleht (Ed.), *Proceedings of the workshop on Solar Energy Storage Subsystems for the Heating and Coolings of Buildings*, The University Press of Virginia, Charlottesville, VA, 1975, pp. 43–45.
- [9] H.G. Lorsch, K.W. Kauffman, J.C. Denton, Thermal energy storage for heating and air conditioning, future energy production system, *Heat Mass Transf.* **1** (1976) 69–85.
- [10] A. Abhat, Low temperature latent heat thermal energy storage: heat storage materials, *Sol. Energy* **30** (1983) 313–332.
- [11] W.R. Humphries, E.I. Griggs, *A designing handbook for phase change thermal control and energy storage devices*, NASA Technical Paper, 1977, p. 1074.
- [12] M.M. Farid, A.M. Khudhair, Effect of Natural convection on the process of melting and solidification of paraffin wax, *Chem. Eng. Commn.* **57** (1987) 297–316.
- [13] B. Zalba, J. MaMarin, L.F. Cabeza, H. Mehling, Review on thermal energy storage with phase change: materials, heat transfer analysis and applications, *Appl. Therm. Eng.* **23** (2003) 251–283.
- [14] M.M. Farid, A.M. Khudhair, S.A.K. Razack, S. Al-Hallaj, A review on phasechange energy storage: materials and applications, *Energ. Convers. Manage.* **45** (2004) 1597–1615.
- [15] L.F. Cabeza, A. Castell, C. Barreneche, A. de Gracia, A.I. Fernandez, Materials used as PCM in thermal energy storage in buildings: a review, *Renew. Sust. Energ. Rev.* **15** (2011) 1675–1695.
- [16] F. Agyenim, N. Hewitt, P. Eames, M. Smyth, A review of materials heat transfer and phase change problem formulation for latent heat thermal energy storage systems (LHTESS), *Renew. Sust. Energ. Rev.* **14** (2010) 615–628.
- [17] J.K. Choi, J.G. Lee, J.H. Kim, H.S. Yang, Preparation of microcapsules containing phase change materials as heat transfer media by in-situ polymerization, *J. Ind. Eng. Chem.* **7** (2001) 358–362.
- [18] C. Alkan, Enthalpy of melting and solidification of sulfonated paraffins as phase change materials for thermal energy storage, *Thermochim. Acta* **451** (2006) 126–130.
- [19] N. Sarier, E. Onder, The manufacture of microencapsulated phase change materials suitable for the design ofthermally enhanced fabrics, *Thermochim. Acta* **452** (2007) 149–160.
- [20] C. Thies, Microencapsulation, in: A. Seidel (Ed.), *Kirk–Othmer Encyclopedia of Chemical Technology*, 5th ed., John Wiley & Sons Inc., Hoboken, NJ, 2006, pp. 438–463.
- [21] P.L. Foris, R.W. Brown, P.S. Phillips, Capsule manufacture, US Patent 4,100,103 (1978).
- [22] S.K. Ghosh, Functional coatings and microencapsulation: a general perspective, in: S.K. Ghosh (Ed.), *Functional Coatings: By Polymer Microencapsulation*, Wiley-VCH Verlag GmbH & Co. KGaA, Weinheim, 2006, pp. 1–28.
- [23] S. Gschwander, P. Schossig, H.M. Henning, Micro-encapsulated paraffin in phase-change slurries, *Sol. Energ. Mater. Sol., C* **89** (2005) 307–315.
- [24] S.X. Wang, Y. Li, J.Y. Hu, H. Tokura, Q.W. Song, Effect of phasechange material on energy consumption of intelligent thermalprotective clothing, *Polym. Test.* **25** (2006) 580–587.
- [25] ISO 9886: Ergonomics – evaluation of thermal strain by psychological measurements, 2008.
- [26] ISO 12894 (E): Ergonomics of the thermal environment – Medical supervision of individuals exposed to extreme hot or cold environment, 2008.
- [27] S.S. Radaković, J. Marić, M. Surbatović, S. Radjen, Effects of acclimation on water and electrolitic disbalance in soldiers during exertional heat stress, *Vojnosanitarni Pregled* **64** (2007) 199-204 (in Serbian).
- [28] S.C. Fok, F.L. Tan, C.C. Sua, Experimental Investigations on the Cooling of a Motorcycle Helmet with Phase Change Material, *Thermal Sci.* **3** (2001) 807–816.
- [29] D. Jovanović, R. Karkalić, Lj. Tomić, Z. Veličković, S.S. Radaković, Efficacy of a novel phase change material for microclimate body cooling, *Thermal Sci.* **18** (2014) 697-705.

IZVOD**ISPITIVANJE FUNKCIONALNE ODEĆE SA MIKROENKAPSULIRANIM FAZNO-PROMENLJIVIM MATERIJALOM U SIMULIRANIH USLOVIMA TOPLE SREDINE**

Dalibor B. Jovanović¹, Predrag N. Stojisavljević¹, Sveta G. Cvetanović², Radovan M. Karkalić³, Negovan D. Ivanković³, Željko B. Senić⁴, Dušan S. Rajić⁵

¹*Tehnički opitni centar Vojske Srbije, Beograd, Srbija*

²*Univerzitet u Nišu, Fakultet zaštite na radu, Niš, Srbija*

³*Univerzitet odbrane, Vojna akademija, Beograd, Srbija*

⁴*Vojnotehnički institut, Beograd, Srbija*

⁵*Univerzitet u Beogradu, Inovacioni centar Tehnološko-metalurškog fakulteta, Beograd, Srbija*

(Stručni rad)

Materijali koji menjaju fazno stanje (PCM) organskog tipa imaju sposobnost apsorpcije i emisije velikih količina toplotne energije tokom procesa faznih promena (prelaza iz jednog agregatnog stanja u drugo). Upotreba PCM u svrhe namenskog skladištenja energije ili stvaranja efekta toplotne izolacije je naučno potvrđena i industrijski testirana. U novije vreme naročito raste interes istraživača za nanošenje PCM na tekstilne materijale metodama premazivanja ili mikroenkapsulacije. U radu su prikazani rezultati ispitivanja termofiziološke efikasnosti specijalnog rublja sa organskim PCM integrisanim u tekstilni materijal kroz proces mikroenkapsulacije. Efikasnost PCM rublja je testirana kroz proveru termofizioloških parametara u veštački simuliranim uslovima tople sredine (klima komora), gde su ispitanici izloženi testovima toplotnog opterećenja pri nošenju ABH zaštitne odeće bez specijalnog rublja (opcija "NoTHERM") i sa PCM rubljem (opcija "THERM"). Može se zaključiti da nošenje odeće za termoregulaciju bazirane na integraciji organskih PCM, ispod ABH zaštitnog odela, tokom fizičke aktivnosti u toplim uslovima, umanjuje intenzitet znojenja i ublažava termalno opterećenje korisnika.

Ključne reči: Fazna promena • Mikroenkapsulacija • Zaštitna odeća • Rublje • Termofiziološka merenja

Mechanical characterization of composite solid rocket propellant based on hydroxy-terminated polybutadiene

Nikola I. Gligorijević, Vesna Ž. Rodić, Saša Ž. Živković, Bojan M. Pavković, Momčilo M. Nikolić, Stevan M. Kozomara, Sredoje D. Subotić

Military Technical Institute, Belgrade, Serbia

Abstract

This paper presents the procedure of uniaxial mechanical characterization of composite solid rocket propellant based on hydroxy-terminated polybutadiene (HTPB), whose mechanical properties strongly depend on temperature, strain rate, natural aging and accumulated damage. A method of processing data is presented in order to determine time-temperature shift factor and master curves for tensile strength, ultimate strain and relaxation modulus, depending on reduced time. Functional dependences of these features represent an input for structural analysis of a rocket motor propellant grain. The effects of natural aging on the mechanical properties are also considered.

Keywords: composite propellant, viscoelasticity, mechanical characterization, tensile strength, ultimate strain, time-temperature shift factor, relaxation modulus, safety factor, reduced time.

Available online at the Journal website: <http://www.ache.org.rs/HI/>

SCIENTIFIC PAPER

UDC 662.1/.4:62:547

Hem. Ind. 70 (5) 581–594 (2016)

doi: 10.2298/HEMIND150217067G

Elastomeric materials have been incorporated as structural elements in many engineering applications. One of their important applications is for design of solid propellant grains in rocket motors.

There are two main types of solid rocket propellants, double-base and composite. Double-base propellant is composed as approximately equal-part mixture of nitrocellulose gelled by a nitrate ester such as nitroglycerin, which depends upon the nitro chemical groups in the nitrocellulose and nitrate ester for oxygen. Composite propellant is composed as a mixture of approximately 75–85% of fine oxidizer powder embedded into the remaining 15–25% of polymer matrix [1–3]. In both cases the elastomeric content is sufficiently large to cause the mixture to exhibit strong strain rate- and temperature-dependent mechanical properties [4].

For elastic materials, in the field of small strains and one-dimensional tension, there is a linear relation between stress (σ) and strain (ε), which can be compared to behavior of a spring:

$$\sigma = E\varepsilon \quad (1)$$

E – Young's modulus of elasticity.

Viscoelastic mechanical behavior is something between the behavior of elastic spring and viscous fluid. For viscoelastic materials, this relationship is not linear. It depends on strain rate and temperature [5–7].

The relation between the two usually can be presented by a complex differential equation. Under certain assumptions, the viscoelastic material may be treated as linear-viscoelastic material [1,8,9], which is represented by following expression:

$$\left[P_n \frac{d^n}{dt^n} + \dots + P_1 \frac{d}{dt} + P_0 \right] \sigma(t) = \left[Q_m \frac{d^m}{dt^m} + \dots + Q_1 \frac{d}{dt} + Q_0 \right] \varepsilon(t) \quad (2)$$

or more compactly:

$$[O_1] \sigma(t) = [O_2] \varepsilon(t) \quad (3)$$

where O_1 and O_2 are differential operators. Linear operator d^i/dt^i represents the i -th derivative with respect to time; P_i and Q_i are material constants which may be obtained by uniaxial tension tests. Although the Eq. (2) is complex, if the mechanical properties of material are known, depending on temperature and time, it is theoretically possible to conduct structural analysis by means of mathematical transformations and principles of elastic analysis [1,4,6,7].

Mechanical behavior of any material depends on temperature range in which it is going to be used. All materials behave as elastic below their glass transition temperatures (T_g). For instance, if we introduce an analogy between T_g for elastomers and the high temperature above which the metals become plastic, we can explain the elastic metals behavior at ambient temperature. For their structural analysis the expression (1) is widely used in the theory of elasticity.

Correspondence: N.I. Gligorijević, Military Technical Institute, Ratka Resanovića 1, 11000 Belgrade, Serbia.
E-mail: nikola.gligorijevic@gmail.com
Paper received: 17 February, 2015
Paper accepted: 13 November, 2015

The value of T_g is the first feature that should be determined in the process of mechanical characterization of a composite propellant composition based on a certain type of polymer (such as HTPB). The glass transition temperature T_g of the composite solid propellant composition, based on HTPB, which is discussed in this paper is approximately equal to -70°C [10,11].

The composite rocket propellant, based on HTPB, is viscoelastic over its glass transition temperature T_g in its operational temperature range between -40 and 50°C .

All of its mechanical properties vary with temperature, real time due to aging, and significantly with strain rate which is also a kind of a time dependence.

For this reason, it is necessary to conduct mechanical characterization of viscoelastic material in order to get all the dependences, necessary to improve a reliable structural analysis which substantially differs from the analysis for elastic materials. Usually, the structural analysis is based on uniaxial mechanical characterization.

The purpose of mechanical characterization of the viscoelastic rocket propellant is to conduct the structural analysis for a rocket propellant grain as viscoelastic body and to assess the time-distribution of the safety factor, or more generally, to determine the reliability of the rocket motor. The safety factor is the ratio between tensile strength and real stress that acts on a body, or between ultimate and real strain:

$$v_\sigma(t) = \frac{\sigma_m(t)}{\sigma(t)}; v_\varepsilon(t) = \frac{\varepsilon_m(t)}{\varepsilon(t)} \quad (4)$$

Real stresses and strains depend on the loads that act on the body, but also on environmental temperature and relaxation modulus [1,5–7] of the material.

$$\sigma, \varepsilon = f(T, E_{\text{rel}}(t)) \quad (5)$$

From the Eqs. (4) and (5) it can be seen that it is necessary to determine the three main dependencies: $\sigma_m(T, t)$, $\varepsilon_m(T, t)$ and $E_{\text{rel}}(T, t)$. The first two, tensile strength and ultimate strain are required for failure analysis, and the third, relaxation modulus, for the real stress and strain calculations.

According to Heller's model [10,12,13], each of these features is a combination of basic values in the very beginning of the propellant service life ($\sigma_{m0}, \varepsilon_{m0}, E_{m0}$), aging factors ($\eta_\sigma, \eta_\varepsilon, \eta_E$) and cumulative damage (D) due to load effects during storage.

$$\sigma_m(t) = \sigma_{m0} \eta_\sigma(t) [1 - D(t)] \quad (6)$$

$$\varepsilon_m(t) = \varepsilon_{m0} \eta_\varepsilon(t) [1 - D(t)] \quad (7)$$

$$E_{\text{rel}}(t) = E_{\text{rel}0} \eta_E(t) [1 - D(t)] \quad (8)$$

There are different opinions on how to describe the changes of the mechanical properties of viscoelastic

materials during time. Sutton [14], for instance, suggests that changes occur only due to the effects of load and he doesn't consider the effects of natural aging ($\eta_\sigma, \eta_\varepsilon, \eta_E$). He finds that changes in mechanical properties are primarily due to cumulative damage (D) [11,14–17]. Sometimes, propellant aging is considered as a unique result of simultaneous action of chemical, physical and aging due to the effects of mechanical loads [18]. However, all authors agree that it is necessary to determine the basic initial values of the mechanical properties ($\sigma_{m0}, \varepsilon_{m0}, E_{m0}$), immediately after propellant production. Sometimes for the structural analysis only these values are used, such as there are no further changes due to aging.

The basic values of mechanical properties ($\sigma_{m0}, \varepsilon_{m0}, E_{m0}$) are formally represented in Eqs. (6–8) as constants. Really, these features are variables, that depend on temperature and strain rate, usually presented in the form of master curves [1,5–7,19]. There are several convenient tests for the mechanical characterization of viscoelastic material. It is customary to test uniaxial specimens in tension. Four tests are commonly used [1,6,19]:

1. Step-strain input, measure stress-relaxation output,
2. Step-stress input, measure creep-strain output,
3. Constant strain-rate input, measure stress output and
4. Sinusoidal stress (strain) input, measure strain (stress) output.

In practice, the most commonly used test is constant strain-rate test (No. 3) because data processing is similar to the processing the test results made by elastic materials. For a discussion of cyclic loads, the test No. 4 is also very useful.

Usually, in the literature, only the principles for determination of viscoelastic mechanical properties can be found. The main goal of this paper is to present the complete procedure of the composite solid propellant characterization and determination of the master curves for tensile strength, allowable strain and relaxation modulus. These features are used as an input in the process of structural analysis of the propellant grain in rocket motor and its reliability estimation. Moreover, the possibility of application these results after a certain period of propellant storage was analysed [10,19].

EXPERIMENTS

Composite propellant composition and preparation of test samples

A composite solid propellant composition based on hydroxy-terminated polybutadiene (HTPB) has been tested [20], composed by 23,4% HTPB based binder,

75% crystalline oxidizer (ammonium perchlorate, AP), 1% Al metal powder, 0,5% lithium fluoride as burning rate depressant and 0,1% carbon black powder (C) as burning stabilizer. Within the HTPB based binder, isophorone diisocyanate (IPDI) as curing agent (cross-linker) was used, as well as dioctyl adipate (DOA) as plasticizer, 2,2-methylene-bis(4-methyl-6-tertiary-butyl phenol) (AO22) as antioxidant and triethylene-tetra-mine (TET), as bonding agent.

The NCO/OH ratio between the isocyanate groups of IPDI to the hydroxy groups was 0.86.

During propellant grain manufacturing, propellant blocks were also cast and placed into a dry environment at 20 °C. The specimens were cut from the blocks immediately before daily series testing. The remaining blocks were returned to thermally controlled dry stock. Thus, external loads or other forms of damage didn't affect the propellant blocks.

For uniaxial constant strain-rate tests and stress–strain curves measuring, tensile tester “Instron-1122” was used.

Propellant specimens are usually tempered in small separated thermal chambers with constant temperatures for at least two hours before tension test. The same temperature is also prepared in the main chamber on the Instron tester (Fig. 1). When the test temperature has to be low, the main chamber is cooled by liquid CO₂. Before test, each individual specimen is transferred into a chamber on the testing machine, with further tempering until the desired temperature is stabilized.

In Fig. 1 it can be seen that the height of the chamber is large enough to enable movement of the tensile tester cross-head, which is higher than the maximum strain of the specimen.



Figure 1. Tensile tester „Instron-1122“.

When the temperature chamber is not mounted on the tester, the values of real strain on standard (room) temperature can be measured by extension-meter.

When the tests have to be performed at other temperatures, using temperature chamber, it is not possible to mount extension-meter. However, for JANNAF-C specimen the effective gauge length of $l_0 = 68.4$ mm has been widely adopted in the literature [1,6,7,16]. Our tests on standard temperature have shown strong agreement between strain measured by extension-meters and strain based on the displacement of the tester cross-head and effective gauge length.

Two sets of tension tests have been made. At first, fresh, virgin propellant was tested, immediately after curing, in order to make master curves for the characteristic mechanical properties. Propellant specimens of the “JANNAF-C” type [6,8] were tested in 96 different modes, under various temperature and strain rate conditions (Table 1), with 7–9 replicates in each mode. Twelve different temperatures and twelve different strain rates were used (ten degree steps in the range –60 to 50 °C), constant crosshead speeds between 0.2 and 1000 mm/min. The influence of time as a result of strain rate was analyzed.

In contrast to the first, in the second group of tests the impact of real-time on the mechanical properties was analyzed, having regard to the natural aging. The propellant was tested in two different periods. For the first time, 15 days after production, and for the second time, about three months later. The tests were carried out only at standard temperature (20 °C), at several different cross-head speeds.

The procedure in the first set of tests [1,4–7,11] was as follows: at the initial, constant temperature (*i.e.*, –60 °C in the left column in Table 1), uniaxial tension tests were performed at several different tester cross-head speeds (*i.e.*, 5, 10, 20, 50, 100, 200, 500 and 1000 mm/min). Then, the procedure has been continued at the next temperature –50 °C. And so on, until the testing has been completed at the upper limit temperature, 50 °C.

Table 1. Test modes of uni-axial tension; R – crosshead speed

R mm/min	T / °C												
	–60	–50	–40	–30	–20	–10	0	10	20	30	40	50	
1000	*	*	*	*									
500	*	*	*	*	*	*	*	*					
200	*	*	*	*	*	*	*	*	*	*	*	*	*
100	*	*	*	*	*	*	*	*	*	*	*	*	*
50	*	*	*	*	*	*	*	*	*	*	*	*	*
20	*	*	*	*	*	*	*	*	*	*	*	*	*
10	*	*		*	*	*	*	*	*	*	*	*	*
5	*	*				*	*	*	*	*	*	*	*
2							*	*	*	*	*	*	*
1								*	*	*	*	*	*
0.5									*	*	*	*	*
0.2											*	*	*

Three characteristic mechanical properties (Fig. 2) were determined in each single test: the initial modulus (E), the maximum allowable stress, termed tensile strength (σ_m) and the strain at maximum stress (ε_m). At some temperatures there was no need to carry out tests at all different cross-head speeds. The number of test modes for each test temperature was less or equal to the number of possible tester speeds (strain rates). Each individual stress-strain test, as a combination of strain rate and test temperature, have given only three values, one point for each of the three summary property plots: initial modulus, tensile strength and strain at maximum stress (ultimate strain).

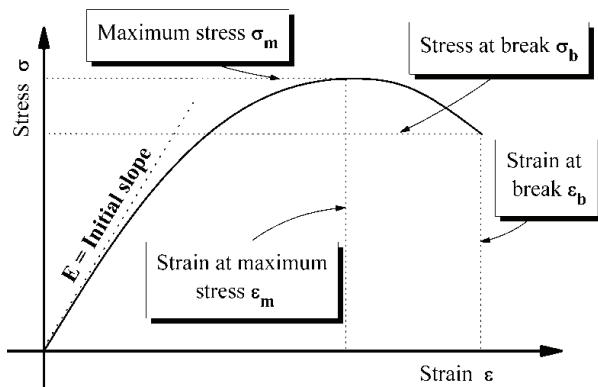


Figure 2. Typical stress-strain curve in the constant strain-rate test.

In the second group of tests, uniaxial tension tests were carried out, not in the very beginning of the service life, like the first series of tests, but still in the initial period after production, the first time after 15 days and the second time 105 days after curing. Both times, the second group of tests was performed only at standard temperature (20 °C), at nine different cross-head speeds: 0.5, 1, 2, 5, 10, 20, 50, 100 and 200 mm/min. The measured values for all three characteristic mechanical properties (σ_m , ε_m and E) are shown in Table 2.

Table 2. Coefficients that define regression for relaxation modulus master curve

i	1	2	3	4	5	6	7
τ_i / s	10^{-7}	10^{-6}	10^{-5}	10^{-4}	10^{-3}	10^{-2}	10^{-1}
E_i daN cm ⁻²	10.50	40.82	149.61	108.65	139.54	55.56	65.97
i	8	9	10	11	12	13	
τ_i / s	10^0	10^1	10^2	10^3	10^4	10^5	
E_i daN cm ⁻²	35.31	40.12	14.29	17.90	4.24	1.14	
E_e daN cm ⁻²	36.31						

Test method

The JANNAF specimen, conditioned at a constant temperature, is extended at a constant cross-head speed (V) until it breaks. The strain rate ($\dot{\varepsilon}$) is also a constant value, commonly denoted as R . For this type of specimen the value of $l_0 = 68.4$ mm is used as effective specimen length [6]. The value of force at the extended length is measured as time progresses.

The following values for analysis are defined.

Strain at time t :

$$\varepsilon = \frac{V}{l_0} t = \dot{\varepsilon} t \tag{9}$$

True stress:

$$\sigma = \frac{F(1+\varepsilon)}{A_0} = \frac{F}{A_0} \left(1 + \frac{V}{l_0} t\right) \left(\frac{\text{daN}}{\text{cm}^2}\right) \tag{10}$$

Strain rate:

$$\frac{d\varepsilon}{dt} = \dot{\varepsilon} (s^{-1}) = R = \frac{V(\text{mm/min})}{60l_0(\text{mm})} \tag{11}$$

Processing of measurement results

Each test mode in this type of test gives three values, one for all of the three summary plots. The all three plots (σ_m , ε_m , E) should have the same abscissa, which represents reciprocal of the propellant specimen strain rate, $\log(\dot{\varepsilon}^{-1}) = \log(1/R)$, and have time dimension. The range from the maximum cross-head speed (1000 mm/min) to minimum value (0,2 mm/min) is high, so the logarithmic scale of the abscissa is suitable for further analysis.

For the first series of tests the further procedure was as follows: when all the points were plotted, 96 of them, the regression lines were created for each temperature in all the three material property plots. The procedure was repeated for the entire temperature range from -60 to 50 °C, at ten-degree increments.

Whenever it is necessary to make a plot of a feature that depends on temperature, the reference temperature, denoted as T_R or T_0 has to be arbitrarily chosen. Standard value ($T_0 = 20$ °C) is usually recommended [6,7,21,22], although there are cases where it is better to adopt a value about 50 °C over the glass-transition temperature [5]. Since the elastic forces in polymers are proportional to absolute temperature [1,5,6], tensile strength and initial modulus have to be normalized by factor (T_0 / T). The initial modulus dependence on temperature and strain rate is shown in Fig. 3.

Similarly, the regression lines for tensile strength vs. strain rate were formed for different test temperatures in the summary plot (Fig. 4). As in the previous plot for the modulus, each temperature dependence was fitted by linear function.

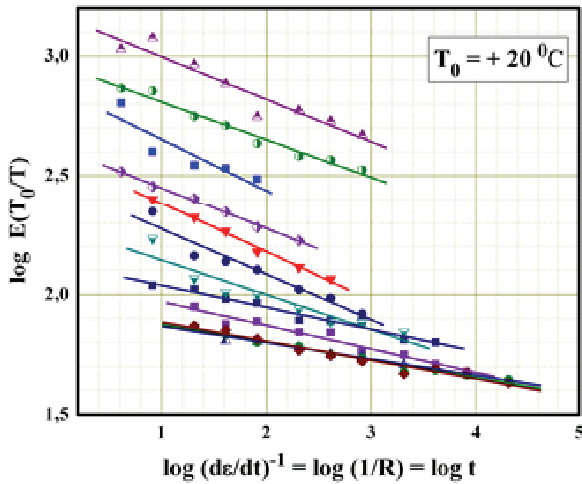


Figure 3. Initial modulus vs. temperature and strain rate.

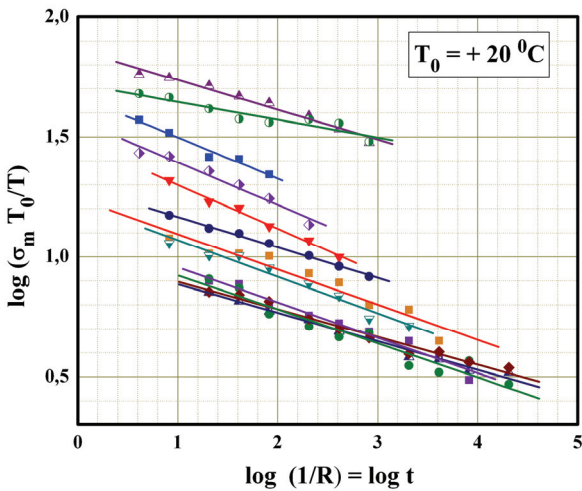


Figure 4. Tensile strength vs. temperature and strain rate.

It can be accepted that the regression lines in Figs. 3 and 4 are approximately linear and parallel. If it is assumed that the hydroxyl-terminated polybutadiene HTPB is a linear-viscoelastic and thermo-rheologically simple material [1,4–7,23], then there exists a correlation between the effects of time and temperature. In this case it is possible to translate all the temperature regression lines horizontally along the time-dimensioned abscissa to meet the reference line, where they overlap to create “a master curve”.

Ultimate strain dependence on temperature and strain rate (Figure 5) is more complex and it is not possible immediately to recognize its final form. Regression lines that correspond to different temperatures do not have proper forms. They are not equidistant as in the cases of modulus and tensile strength.

Distance from an arbitrary line in Figs. 3 and 4 to the line that corresponds to a reference temperature (T_0) is equal to the value of shift $\log a_T$. This feature is known as a time-temperature shift factor, because the

shift from an arbitrary to the reference temperature corresponds to the horizontal shift along the time axis [1,3–9]. Depending on the direction of movement, this value can be positive or negative. The character of time-temperature shift factor a_T [1,5–7,21,23] is universal and it can be theoretically determined from each of the plots in Figs. 3–5. The final result $a_T(T)$ should be same. However, it is much easier to estimate different distances between regression lines using linear plots in Figs. 3 and 4.

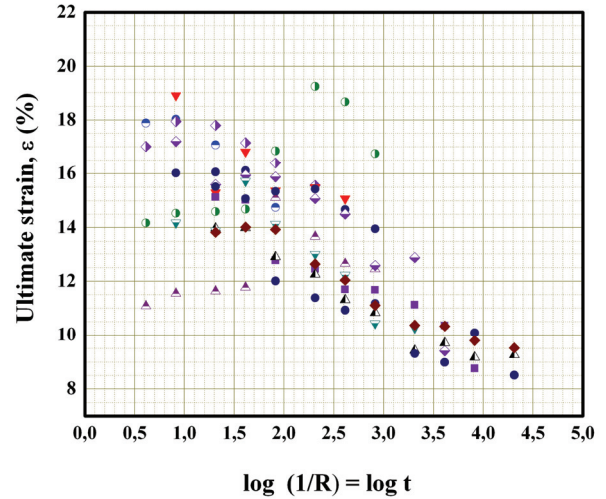


Figure 5. Ultimate strain vs. temperature and strain rate.

Different values of shift correspond to each temperature. When the regression lines are not completely parallel, the distance is determined as in Fig. 6. This way, the functional dependence $a_T(T)$ between time and temperature can be defined, as in Fig. 7.

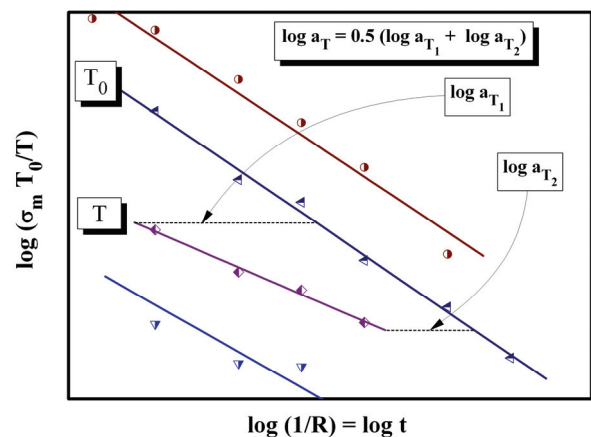


Figure 6. Shift factor a_T - spacing between regression curves.

Regression line that describes the time-temperature dependence can be described in different ways. In

literature, the most commonly used term is Williams-Landel-Ferry (WLF) Equation:

$$\log a_T = -\frac{C_1(T - T_0)}{C_2 + T - T_0} \tag{12}$$

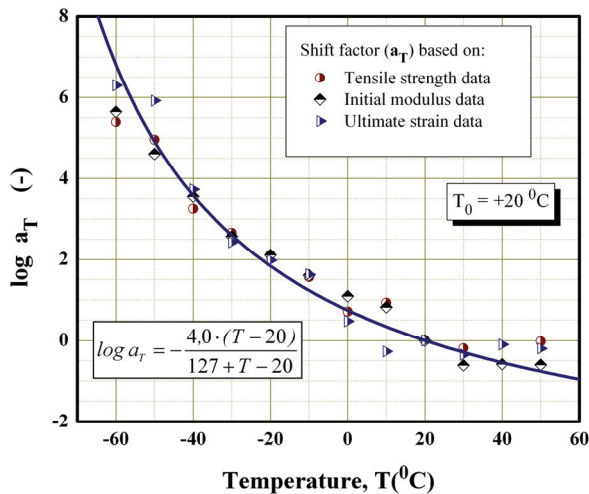


Figure 7. Time-temperature shift factor.

The functional dependence (12) is found to be the same ($C_1 = 8.86$, $C_2 = 101.6$) for a “wide variety of polymers, polymer solutions, organic glass-forming liquids, and inorganic glasses” [24], “after suitable choice of the reference temperature (T_0), about 50 °C above the glass transition temperature T_g , and over the temperature range $T_0 \pm 50$ °C”. Theoretically, this allows the mechanical properties of some materials to be tested only at one single temperature, and the property values at other temperatures are easy to calculate using the expression (12). However, outside this range, the functional dependences $a_T(T)$ for different materials cannot match.

Unfortunately, this rule is not entirely suitable for rocket propellants. Composite rocket propellant is a mixture of approximately one quarter of polymer matrix and three quarters of powdered fillers, and expression (12) does not give completely accurate results if the universal constants C_1 and C_2 are used. In addition, the upper limit temperature of propellant usage does not meet the requirement for using these values of constants, because it comes out from the range $[T_g, T_g + 100$ °C]. For such cases in the same paper [24] it was recommended that “for the practical use, it is more accurate to choose a higher reference temperature (T_0) and use the empirical constants of Eq. (12) in predicting the temperature dependence of mechanical properties”. This requires to conduct the propellant mechanical characterization over the entire operating temperature range and to determine the constants in the expression (12) by fitting the test results.

For the specified propellant, the result is shown in section „Data processing results“, together with other results.

The obtained result represents a regression curve on the basis of tensile strength, initial modulus, and allowable strain data. This regression curve refers to the temperature range in which the measurements were made (–60 to 50 °C), and it is quite enough to cover the whole temperature range of the propellant use.

Finally, the scale of the abscissa in the material property plots (Figs. 3–5) can be corrected, because “there exists the fortunate, although essentially unexplained” [4], association between time and temperature for viscoelastic materials. If any of the regression lines on an arbitrary temperature T , for example $\sigma_m(T, \log t)$, is moved for the value $\log a_T(T)$ to overlap the reference regression line $\sigma_m(T_0, \log t)$, this feature begins to depend not only on time but also on the size of displacement along the timeline:

$$\sigma_m(\log t - \log a_T) = \sigma_m(\log t / a_T) = \sigma_m \log \xi$$

Therefore, instead of real time t which is the reciprocal of the strain rate ($1/R = t$), a “reduced time” (ξ) should be introduced on the abscissa ($\xi = 1/(Ra_T) = t/a_T$). This connection between temperature and time is used to transform the dependence on two variables into the dependence on a single variable ($\log \xi$).

Then, the master curve for a given mechanical property may be plotted against $\log \xi$ that applies to all load conditions. The master curves for tensile strength and initial modulus are of the same type (Figs. 8 and 9):

$$\log \sigma_m \frac{T_0}{T} = a - b \log \xi \tag{13}$$

$$\log E_0 \frac{T_0}{T} = c - d \log \xi \tag{14}$$

A considerable problem in the master curve determination for ultimate strain of the propellant was insufficient recognition (Fig. 5) of individual segments that correspond to different temperatures. Regression curves for these individual segments correspond only to small parts of the final master curve (Figs. 10 and 11) and do not cover the whole time range.

The actual values of the coefficients in linear equations for tensile strength and initial modulus (Eqs. (13) and (14)) are presented in section „Data processing results“, together with other results. For allowable strain the Gaussian regression curve is accepted, in the following form:

$$\varepsilon_m (\%) = \varepsilon_0 + A e^{-2 \left(\frac{\xi - \xi_0}{B} \right)^2} \tag{15}$$

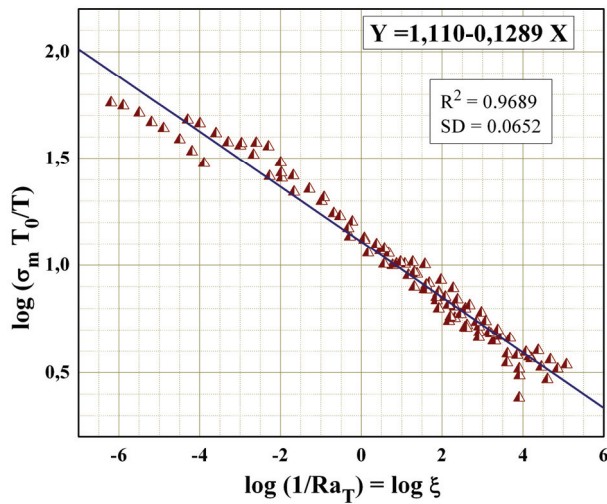


Figure 8. Tensile strength master curve.

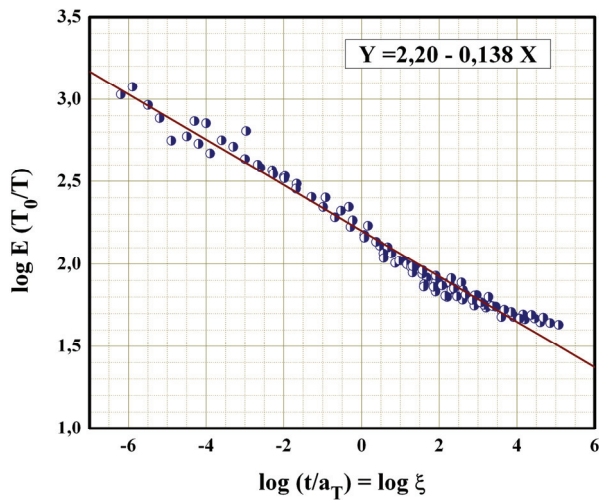


Figure 9. Initial modulus master curve.

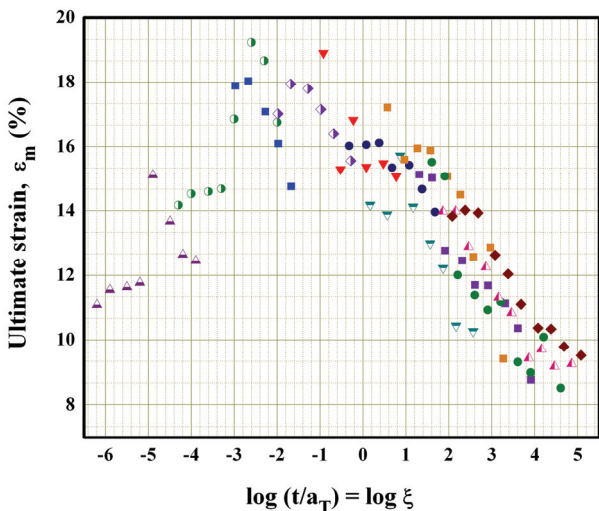


Figure 10. Ultimate strain.

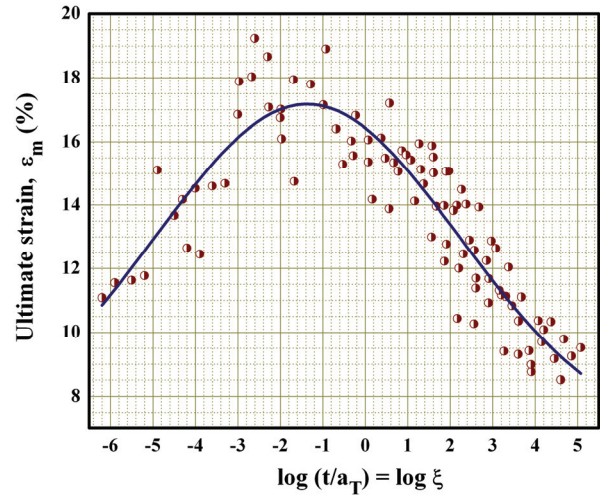


Figure 11. Ultimate strain master curve.

There is no standard form for mathematical description of the ultimate strain curves for different propellant compositions based on HTPB polymer. The Gaussian curve is just an example for an appropriate regression function.

Some individual points in the master plots deviate from the regression lines due to various influences. They are inevitable consequence in the testing of viscoelastic materials. In the probabilistic model [10,11,19], used to estimate a rocket propellant grain reliability, these deviations were compensated because all the features were considered as statistical variables.

Master curves for tensile strength (Fig. 8) and ultimate strain (Fig. 11) are required for failure analysis, as indicators of the material capacity to withstand the loads and stresses.

Before the failure analysis as final stage in the process of reliability determination, the structural analyst has to analyze the stresses acting on the body. For the stress-strain analysis of a viscoelastic body, it is necessary and sufficient to determine the relaxation modulus [1,4,6,9,25–27]. It is very important to make a distinction with respect to the initial modulus of the material which corresponds to the modulus of elasticity in the elastic material.

There are different ways for determination of the relaxation modulus, like DMA tests or long duration relaxation tests. In this study, the relaxation modulus has been determined on the basis of uniaxial constant strain rate tests. Each test mode was sufficient only for one point determination of the master curve, using the following expression [4–7]:

$$E_{rel}(t) = \left[\frac{d\sigma(t)}{d\varepsilon} \right]_{\varepsilon=Rt} \quad (16)$$

The expression (16) represents the relationship between relaxation modulus and the maximum slope

of the stress-strain curve in the constant strain rate test (Fig. 12), in the domain where the strain is proportional to time ($\varepsilon = Rt$). The maximum slope is approximately equal to the initial modulus which is determined in a known manner, like in the case of an elastic material. In the initial region of the curve that corresponds to its elastic part, two pairs of stress and strain values have to be measured:

$$E_i(t) = \frac{d\sigma(t)}{d\varepsilon} \approx \frac{\Delta\sigma}{\Delta\varepsilon} = \frac{\sigma_2 - \sigma_1}{\varepsilon_2 - \varepsilon_1} \quad (17)$$

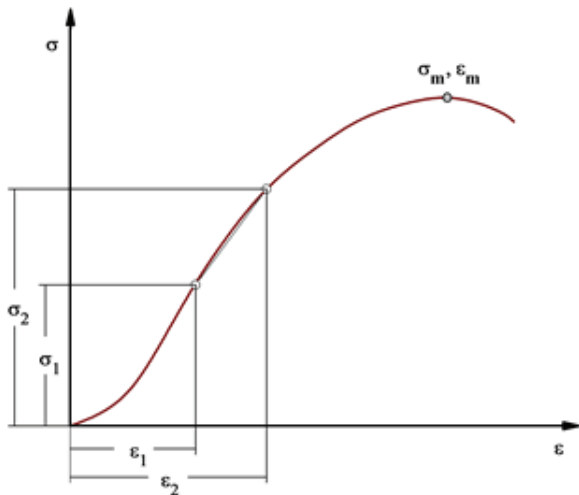


Figure 12. Slope of the stress-strain curve.

It is difficult to determine a rule for measuring the two pairs of stress and strain values. In the paper [28], the authors have measured the values of stress at 3% and 10% strain. However, when the tests are made in a number of different modes, this rule can not be applied.

The method of the relaxation modulus determination is reduced to measuring slopes in different stress-strain test modes. It is important that the value of the relaxation modulus in an exactly defined temperature and speed mode depends not only on the slope of the curve, but also on the position of the measured points on the stress-strain curves ($\sigma_1, \varepsilon_1, \sigma_2, \varepsilon_2$).

Therefore, it is necessary, besides the slope ($\Delta\sigma/\Delta\varepsilon$), to define the position of the measuring points (σ/ε) in each stress-strain plot. Therefore, for the relaxation modulus determination, the following procedure has been applied [5,8,9,19]:

$$E_{rel}(t) = \frac{d\sigma}{d\varepsilon} = \frac{\frac{d\sigma}{\sigma}}{\frac{d\varepsilon}{\varepsilon}} \cdot \frac{\sigma}{\varepsilon} = \frac{\sigma}{\varepsilon} \cdot \frac{d(\ln\sigma)}{d(\ln\varepsilon)} \quad (18)$$

The ratio (σ/ε) defines the position of the measuring point in the stress-strain diagram. If the influence of strain rate (R) and temperature (a_T) is int-

roduced, and the stress is normalized (T_0/T), an expression for the relaxation modulus is obtained:

$$E_{rel}(t, T) = \frac{\sigma}{\varepsilon} \cdot \frac{d(\ln\sigma)}{d(\ln\varepsilon)} = \frac{\frac{\sigma}{Ra_T} \cdot \frac{T_0}{T}}{\frac{\varepsilon}{Ra_T}} \cdot \frac{d\ln\left(\frac{\sigma}{Ra_T} \cdot \frac{T_0}{T}\right)}{d\ln\left(\frac{\varepsilon}{Ra_T}\right)} \quad (19)$$

$$E_{rel}(t, T) = \frac{\sigma_{RED}}{\varepsilon_{RED}} \cdot \frac{d(\ln\sigma_{RED})}{d(\ln\varepsilon_{RED})} \quad (20)$$

$\sigma_{RED}, \varepsilon_{RED}$ – reduced values of stress and strain.

When the values σ_{RED} and ε_{RED} in all stress-strain plots are determined, it is possible to form a log-log plot (Fig. 13), with constant slope, equal to the derivative on the right side of Eq. (20).

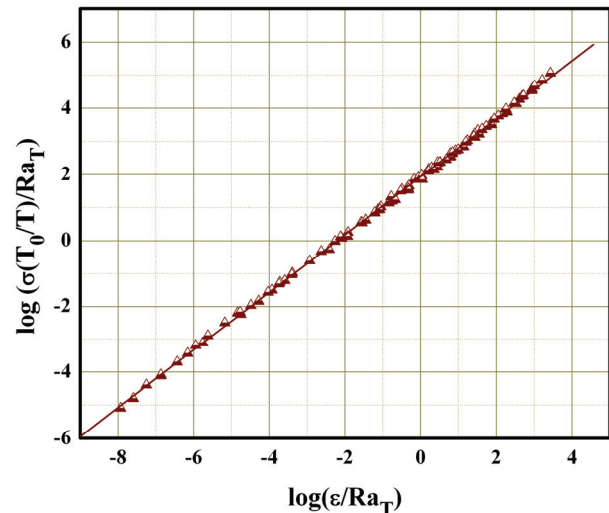


Figure 13. Determination of the relaxation modulus slope.

Finally, it is possible to plot the points defined in Eq. (20). The value $d(\ln\sigma_{RED})/d(\ln\varepsilon_{RED})$ is approximately constant, but the values of the ratio $\sigma_{RED}/\varepsilon_{RED}$ are variables, and an array of points can be formed (Fig. 14), determining the relaxation modulus curve [5,6].

The number of 96 different test regimes at various temperatures and cross-head rates was sufficient to produce a reliable relaxation curve covering the whole area that is interesting for structural analysis of a viscoelastic body.

The distribution of the relaxation modulus “master” curve is represented by Dirichlet or Prony series expansion, which is the most general form of linear viscoelasticity:

$$E_{rel}(t) = E_e + \sum_{i=1}^{i=n} E_i e^{-\frac{t}{\tau_i a_T}} \quad (21)$$

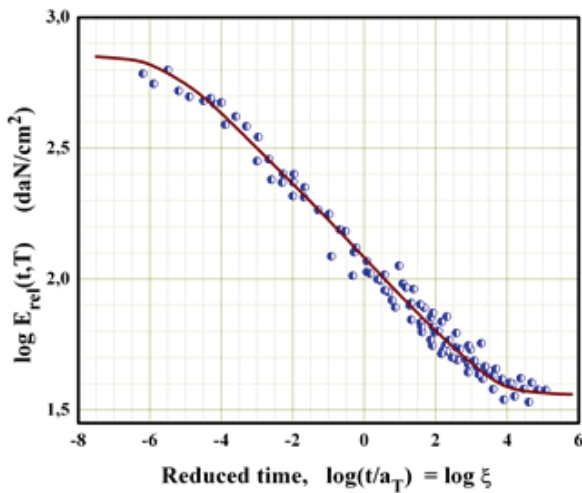


Figure 14. Relaxation modulus.

For the actual HTPB composite propellant, the values of coefficients E_i, τ_i (Table 2) are evaluated by fitting the relaxation modulus master curve (Fig. 14) and presented in Section 3, together with other results.

Expression (21) allows the stress and strain analysis to be conducted in all load cases. Generally, in the structural analysis of a viscoelastic body, due to the complex relation between stress and strain, a method is known which translates the problem into the complex domain, where the viscoelastic problem can be solved on the principles of elastic analysis [1,4]. Expression (21) is suitable for the Laplace transform, because the differential relationship between stress and strain in the expressions (2) and (3) turns into a ratio of two polynomials.

For cyclic loads analysis, the frequency-dependent complex modulus is necessary [1,6,7,11]. This feature may be obtained by dynamic mechanical analyzer (DMA). However, it is also possible to convert uniaxial tensile tests data to dynamic data, according to Williams [1,4].

The dynamic modulus takes the form (22) and (23) which is generally known in the theory of viscoelastic materials [1,4–7,12,25]. The values of coefficients are the same as in Eq. (21).

$$E'(\omega) = E_e + \sum_{i=1}^{i=n} \frac{E_i \omega^2 \tau_i^2 \alpha_T^2}{1 + \omega^2 \tau_i^2 \alpha_T^2} \quad (22)$$

$$E''(\omega) = \sum_{i=1}^{i=n} \frac{E_i \omega \tau_i \alpha_T}{1 + \omega^2 \tau_i^2 \alpha_T^2} \quad (23)$$

Good examples of structural integrity analysis under vibration loads can be found in the studies [8,10–13,15,17,19]. The effects of daily and seasonal temperature fluctuations have been discussed, and their impact on the stress-strain field in viscoelastic bodies.

The accumulation of damage in solid propellant rocket grains has also been discussed. A similar approach can be applied to any arbitrary body exposed to cyclic loads.

The second group of tests was carried out in two different periods, only at standard temperature 20 °C, at different strain rates. Based on the tests on nine different cross-head speeds of the tensile tester (0.5, 1, 2, 5, 10, 20, 50, 100 and 200 mm/min), it was possible to form reliable regression curves for the two considered periods.

For each characteristic feature (Initial modulus, tensile strength and Ultimate strain) one diagram has been prepared for both time periods. In all three cases, two different regression lines apply to the same standard temperature and different periods. In Figs. 15–17 the pairs of regression lines are shown for the initial modulus, tensile strength and ultimate strain.

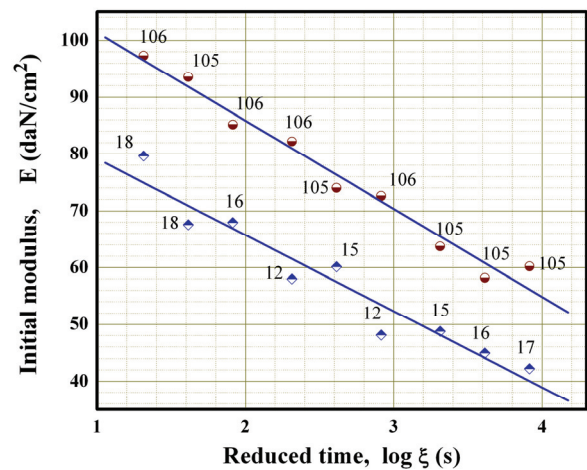


Figure 15. Initial modulus vs. strain rate and aging time.

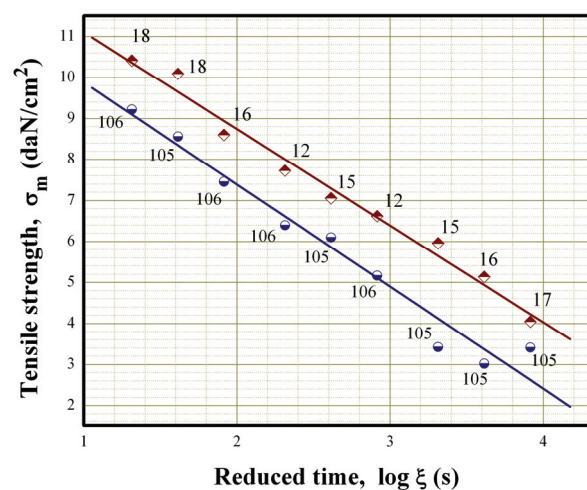


Figure 16. Tensile strength vs. strain rate and aging time.

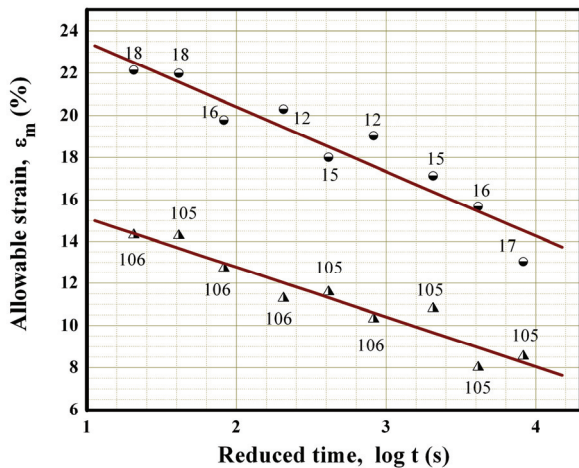


Figure 17. Ultimate strain vs. strain rate and aging time.

Data processing results

After the data processing in a manner presented in section „Processing of measurement results“, the results have been prepared in a form that can be used in the structural analysis. Although this study is concerned with composite rocket propellant, which is very specific viscoelastic material, without a wide application in engineering practice, except in missile technology, the results can be used as a basis for structural analysis of similar types of composite materials with polymer matrix.

1. Tensile strength master curve:

$$\log \sigma_m \frac{T_0}{T} = 1,11 - 0,129 \log \left(\frac{t}{a_T} \right) \tag{24}$$

2. Ultimate strain master curve:

$$\varepsilon_m (\%) = 6.663 + 10.514 e^{-2 \left(\frac{\xi + 1.366}{7.119} \right)^2}; \xi = \frac{t}{a_T} \tag{25}$$

3. Time-temperature shift factor >

$$\log a_T = - \frac{4.0(T - 20)}{127 + T - 20} \tag{26}$$

4. Initial modulus master curve:

$$\frac{T_0}{T} \log E = 2.20 - 0.138 \log \left(\frac{t}{a_T} \right)$$

5. Relaxation modulus master curve, Eq. (21); material constants are shown in Table 2.

In the structural analysis of solid propellant rocket grains, the methods of statistics and probability are usually used, in order to determine or estimate reliability and service life [10–13,19,29]. Therefore, it is often necessary to determine the statistical parameters that define these features. In this paper the statistical

parameters of the propellant mechanical properties haven't been considered.

DISCUSSION

Elastic and viscoelastic analysis of safety factor

The tensile strength of an elastic material is treated in the theory of elasticity as a constant value. In this theory, in simple terms, the safety factor is defined (eq. 4) as the ratio of the tensile strength (σ_m) to the maximum real equivalent stress (σ_0), as a resultant of the simultaneous action of different loads.

For a viscoelastic body, the tensile strength depends on temperature and strain rate, and also on the viscoelastic material age and cumulative damage. When two or more loads act on the body in different manners, it is not possible to define the equivalent tensile strength. In addition, the stresses due to applied forces depend on material properties which are also dependent on temperature and strain rate. The need for detailed mechanical characterization of a viscoelastic material, can be understood in the case of oscillatory temperature loads that act on the body when the material properties continuously change due to temperature.

Let's consider an example: when two different types of loads act on the viscoelastic body simultaneously, at different loading rates, they produce two different stresses, $\sigma_1(t)$ and $\sigma_2(t)$. Since the loads are of different types, the strain rates are also different. Therefore, although it is the same propellant, the tensile strengths $\sigma_{m1}(t)$ and $\sigma_{m2}(t)$ that correspond to different loads are also different, because they depend on the strain rate. Then, the effects of individual loads have to be analyzed separately, using the concept of convolution [7] which is valid for linear-viscoelastic materials. Each of them creates a certain current damage, because it occupies a part of the total capacity of viscoelastic material to withstand loads. The first current damage is equal to the ratio between the first stress $\sigma_1(t)$ and the first tensile strength $\sigma_{m1}(t)$. The same principle applies to the second load. The values of current damages represent the ratios between real stresses and their appropriate ultimate stresses.

In the case considered, the effect of two loads can be represented as the sum of two damage increments, similar to the principle that is used in the Miners cumulative damage law [30]:

$$\begin{aligned} d(t) &= d_1(t) + d_2(t) = \frac{\sigma_1(t)}{\sigma_{m1}(t)} + \frac{\sigma_2(t)}{\sigma_{m2}(t)} = \\ &= \frac{\sigma_1(t)}{(\sigma_{m1})_0 \eta_\sigma(t)} + \frac{\sigma_2(t)}{(\sigma_{m2})_0 \eta_\sigma(t)} \end{aligned} \tag{28}$$

The sum of several individual damages represents the total damage. The possible question could be whether this is just a simple sum of the minor current damages or such amount has to be determined by a geometric principle. It should be a matter of structural analysis.

According to the terminology adopted in the theory of elasticity, the reciprocal of the total damage corresponds to the safety factor of the body.

$$\nu(t) = \frac{1}{d(t)} \quad (29)$$

The above example shows that, unlike elastic material, for the analysis the reliability of a viscoelastic body, it is necessary to make all functional dependences of viscoelastic mechanical properties on temperature and strain rate.

The basic viscoelastic mechanical properties and further required measurements

During the uniaxial mechanical characterization of the composite rocket propellant presented here, the first members of the expressions (6)–(8) are determined: tensile strength (σ_{m0}), strain at maximum stress (allowable strain) (ε_{m0}), and relaxation modulus (E_{rel0}). Based on these results, safety factor of an arbitrary viscoelastic body can be determined at the initial moment of its service life. It is sometimes enough.

In addition, further mechanical characterization as an input for structural analysis of a viscoelastic body should include deterioration of mechanical properties due to the natural aging and the changes due to the cumulative damage.

The effect of natural aging is reflected through the aging factors (η) in expressions (6)–(8). These factors differ for different mechanical properties of materials. For a complete structural analysis it is necessary to define the values of these factors. Changes of the mechanical properties due to the natural aging can be very large in the initial period after the process of polymer curing [10,20,31,32]. An example of the aging factor time-dependence over the period of three years, for the ultimate strain of an HTPB propellant [8,11] is shown in Fig. 18. It indicates an important aging influence, especially in the initial period of the service life.

The initial values of the mechanical properties of viscoelastic materials are displayed as master curves, which represent their functional dependences on temperature and strain rate.

When the changes due to real time are introduced in the form of simple aging functions, in the manner as in expressions (6)–(8), it means that the master curves translationally move through the real aging time, without changing the relations between temperature and strain rate. Otherwise, the master curve could change

their shapes and slopes. At first, it is not possible to estimate in advance whether the influences of temperature and strain rate on the mechanical properties change due to aging in different manners. Second, the abscissas of the master curves have time dimensions, as reciprocals of the strain rate effects. But is there a difference between the impact of real aging-time and strain rate? This dilemma was discussed in the second series of tests in this paper. In Figs. 15–17 the regression curves of modulus, tensile strength and ultimate strain are parallel in all cases for two different time points in an interval of 3 months. Their displacements along the horizontal line (timeline) would lead to their approximate overlap. This means that between the same strain rates in two different time points the horizontal distances are the same, regardless to the values of strain rates. Aging time didn't disrupt the allocation of different strain rate points at the standard temperature. This means intuitively that it was possible to carry out these tests in other circumstances, not only standard conditions (20 °C, 50 mm/min). The same results would probably have been obtained. The conclusion of this review is as follows: due to the natural aging, master curves of the mechanical properties move translationally along the curves represented by the time-distribution of the aging factors.

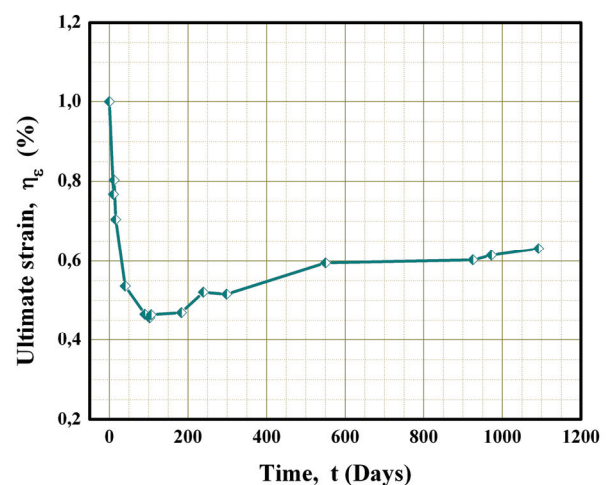


Figure 18. Ultimate strain aging factor.

The effect of cumulative damage is usually neglected because it is less influential at the beginning of service life [6,7]. Some authors believe that cumulative damage becomes significant after a lengthy storage period [12,13,29] or perhaps even earlier [33] but not at the beginning of service life. However, in the Rocket Armament Department in MTI it has been shown in the case of anti-hail propellant grain [10] that this impact can be very large at the beginning of the propellant service life, and shouldn't be neglected.

CONCLUSION

Very often, in engineering practice, structural analysis of viscoelastic materials is done superficially, similar to an elastic material. Despite many papers dealing with this subject, safety factor for a viscoelastic body is sometimes determined based on the data measured under standard conditions (20 °C, tester cross-head speed 50 mm/min). Such a result is often not accurate and gives a completely wrong conclusion about the reliability of the body. During mechanical loading, viscoelastic material behaves quite differently compared to an elastic material. It is not possible to determine the safety factor or reliability of a viscoelastic body without detailed mechanical characterization of the viscoelastic material, because its mechanical properties depend on temperature and strain rate, as well on its age and load history. Therefore, it is also important to carry out the load analysis. Concentrated forces, pressure, acceleration of the body or environmental temperature have completely different effects on the viscoelastic material. Therefore it is necessary to know the behavior of the viscoelastic material in all load conditions.

The principles of test data processing of the mechanical properties of viscoelastic materials are generally known in literature. However, it is almost impossible to find a detailed overview of the data processing. This paper presents an example of simple uniaxial mechanical testing of a composite rocket propellant, as an approximately linear-viscoelastic material. A method of processing constant strain rate tension tests data is presented, in order to obtain the input for the structural analysis of a rocket motor propellant grain reliability and its service life.

In this paper it is also shown that, when a complete mechanical characterization of a viscoelastic material is made in an arbitrary time point, further it is sufficient only to monitor the time distribution of the mechanical properties only in standard test conditions.

Finally, the composite rocket propellant maybe does not have wide application, except in missile technology, but other viscoelastic materials are widely used in engineering practice. The procedure and test results presented in this paper, can be useful as a starting point for analysis of some similar linear-viscoelastic materials.

Nomenclature

A_0	Initial specimen cross-section, cm ²
A, B, C, D, C_1, C_2	Constants
a, b, c, d	Constants
a_T	Time–temperature shift factor
$D, D(t)$	Cumulative damage, time-dependent cumulative damage

$d, d(t)$	Damage, time-dependent current damage
E, E_e, E_{rel}	Modulus, equilibrium modulus, relaxation modulus, daN/cm ²
E_0	Initial modulus, daN/cm ²
E_i	Constant in the Relaxation modulus expression, daN/cm ²
$E(\omega)$	Dynamic modulus, daN/cm ²
$E'(\omega), E''(\omega)$	Storage modulus, Loss modulus, daN/cm ²
F	Force, daN/cm ²
l_0	Effective specimen length, mm
O_1, O_2	Differential operators
P_i, Q_i	Constants
R	Strain rate
T, T_0, T_R	Temperature, reference temperature, °C
T_p	Glass transition temperature, °C
t	Time, s
V	Tensile tester cross-head speed, mm/min
Δ	Increment
ϵ, ϵ_0	Strain, Initial strain, %
$\epsilon_m, \epsilon_{m0}, \epsilon_m(t)$	Ultimate (allowable) strain, initial, time dependent, %
ϵ_{RED}	Reduced strain, %
$\dot{\epsilon} = d\epsilon / dt$	Strain rate, s ⁻¹
ξ	Reduced time, s
$\eta(t)$	Propellant aging factor
$\eta_E, \eta_\sigma, \eta_\epsilon$	Aging factor for modulus, stress, strain
V, V_σ, V_ϵ	Safety factor, safety factors based on stress and strain criteria
σ, σ_m	Stress, strength (ultimate stress), daN/cm ²
$\sigma_{m0}, \sigma_m(t)$	Initial strength, time-dependent strength, daN/cm ²
σ_{RED}	Reduced stress, daN/cm ²
τ_i	Relaxation times, s
ω	Circular frequency, Hz

Acknowledgments

The authors would like to thank MTI's Sector for materials and protection (Composite rocket propellant department), which has produced propellant specimens and provided logistics for testing, as well as the financial support of the project TR 36050 (Research and development of unmanned aircraft in support of traffic infrastructure monitoring).

REFERENCES

[1] M.L. Williams, P.J. Blatz, R.A. Schapery, Fundamental Studies Relating to Systems Analysis of Solid Propellants, Final report GALCIT 101, Guggenheim Aero. Lab., Pasadena, CA, 1961.

- [2] V. Rodić, M. Petrić, The effect of curing agents on solid composite rocket propellant characteristics, *Scientific Technical Review*, LV (2005) 46–50.
- [3] S. Brzić, Lj. Jelisavac, J. Galović, D. Simić, J. Petković, Viscoelastic Properties of hydroxyl-terminated poly (butadiene) – based composite rocket propellants, *Hem. Ind.* **68** (2014) 435–443.
- [4] M.L. Williams, Structural Analysis of Viscoelastic Materials, *AIAA J.* (1964) 785–798.
- [5] R.F. Landel, T.L. Smith, Viscoelastic Properties of Rubberlike Composite Propellants and Filled Elastomers, *ARS J.* **31** (1960) 599–608.
- [6] J.E. Fitzgerald, W.L. Hufferd, Handbook for the Engineering Structural Analysis of solid Propellants, CPIA publication 214, 1971.
- [7] Solid propellant grain structural integrity analysis, NASA Space Vehicle Design Criteria SP–8073, 1973.
- [8] N. Gligorijević, Strukturna analiza pogonskih punjenja raketnih motora sa čvrstim gorivom, Vojnotehnički Institut Beograd, 2013.
- [9] N. Gligorijević, Prilog strukturnoj analizi vezanog pogonskog punjenja raketnog motora sa čvrstom pogonskom materijom, Magistarski rad, Mašinski fakultet u Beogradu, , 1989.
- [10] N. Gligorijević, S. Živković, V. Rodić, S. Subotić, I. Gligorijević, Effect of Cumulative Damage on Rocket Motor Service Life, *J. Energ. Mater.* **33** (2015) 229–259.
- [11] N. Gligorijević, V. Rodić, R. Jeremić, S. Živković, S. Subotić, Structural Analysis Procedure for a Case Bonded Solid Rocket Propellant Grain, *Sci. Tech. Rev.* **61** (2011) 1–9.
- [12] R.A. Heller, M.P. Singh, Thermal Storage Life of Solid–Propellant Motors, *J. Spacecraft Rockets* **20** (1983) 144–149.
- [13] R.A. Heller, M.P. Singh, H. Zibdeh, Environmental Effects on Cumulative Damage in Rocket Motors, *J. Spacecraft Rockets* **22** (1985) 149–155.
- [14] G.P. Sutton, O. Biblarz, *Rocket Propulsion Elements*, 7th ed., Wiley, New York, 2001.
- [15] N. Gligorijević, S. Živković, S. Subotić, S. Kozomara, M. Nikolić, A. Boulahlib, Solving an Irregular Burning Problem in a Small Rocket Motor, *Sci. Tech. Rev.* **64** (2014) 1–11.
- [16] Structural Assessment of Solid Propellant Grains, Agard Advisory Report 350, 1997.
- [17] C.T. Liu, Cumulative Damage and Crack Growth in Solid Propellant, Media Pentagon Report No. A486323, 1997.
- [18] S. Cerri, A.M. Bohn, K. Menke, L. Galfetti, Ageing Behavior of HTPB Based Rocket Propellant Formulations, *Cent. Eur. J. Energ. Mat.* **6** (2009) 149–165.
- [19] N. Gligorijević, Istraživanje pouzdanosti i veka upotrebe raketnih motora sa čvrstom pogonskom materijom (Solid propellant rocket motor reliability and service life research), Ph.D. Thesis, Military Academy, Belgrade, Serbia, 2010.
- [20] N. Gligorijević, S. Živković, S. Subotić, B. Pavković, M. Nikolić, S. Kozomara, V. Rodić, Mechanical Properties of HTPB Propellants in the Initial Period of Service Life, *Sci.Tech. Rev.* **64** (2014) 1–13.
- [21] В.В. Москвитин, Сопротивление вязко-упругих материалов, Наука, Москва, 1972.
- [22] N. Gligorijević, S. Živković, S. Subotić, S. Kozomara, M. Nikolić, S. Čitaković, Side Force Determination in the Rocket Motor Thrust Vector Control System, *Sci.Tech. Rev.* **63** (2013) 27–38.
- [23] K.W. Bills Jr., J.H. Wiegand, Relation of Mechanical Properties to Solid Rocket Motor Failure, *AIAA J.* **37** (1964) 524–541.
- [24] M.L. Williams, R.F. Landel, J.D. Ferry, The Temperature Dependence of Relaxation Mechanisms in Amorphous Polymers and Other Glass-forming Liquids, *J. Am. Chem. Soc.* **77** (1955) 3701–3707.
- [25] N. Gligorijević, V. Rodić, Determination of solid propellant modulus in the process of propellant grain structural analysis, International Symposium on defense technologies, Belgrade, MTI, OTEH, 2009.
- [26] D.J. Ferry, *Viscoelastic Properties of Polymers*, 3rd ed., Wiley, New York, 1980.
- [27] D.I. Thrasher, J.H. Hildreth, Structural Service Life Estimate for a Reduced Smoke Rocket Motor, *J. Spacecraft Rockets* **19** (1982) 564–570.
- [28] L.D. Villar, T. Cicaglioni, M.F. Diniz, M.F.K. Takahashi, L.C. Rezende, Thermal aging of HTPB/IPDI-based polyurethane as a function of NCO/OH ratio, *Mater. Res.* **14** (2011) 372–375.
- [29] H.S. Zibdeh, R.A. Heller, Rocket Motor Service Life Calculations Based on the First Passage Method, *J. Spacecraft Rockets* **26** (1989) 279–284.
- [30] M.A. Miner, Cumulative Damage in Fatigue, *J. Appl. Mech-t Asme* **12** (1945) 159–164.
- [31] L. Gottlieb, S. Bar, Migration of plasticizer between Bonded Propellant Interfaces, *Propell. Explos. Pyrot.* **28** (2003) 12–17.
- [32] H. Shekhar, D.A. Sahasrabudhe, Assessment of Poissons Ratio for Hydroxy-terminated Polybutadiene-based Solid Rocket Propellants, *Defence Sci. J.* **60** (2010) 497–501.
- [33] S. Woei Chyuan, A study of loading history effect for thermoviscoelastic solid propellant grains, *Comput. Struct.* **77** (2000) 735–745.

ИЗВОД**МЕХАНИЧКА КАРАКТЕРИЗАЦИЈА КОМПОЗИТНОГ ЧВРСТОГ РАКЕТНОГ ГОРИВА НА БАЗИ ХИДРОКСИ-ТЕРМИНИРАНОГ ПОЛИБУТАДИЕНА**

Никола И. Глигоријевић, Весна Ж. Родић, Саша Ж. Живковић, Бојан М. Павковић, Момчило М. Николић, Стеван М. Козомара, Средоје Д. Суботић

Војнотехнички Институт, Рајка Ресановића 1, Београд

(Научни рад)

У раду је приказана процедура обраде података једноосне механичке карактеризације композитног чврстог ракетног горива на бази хидрокси-терминираних полибутадиена, као линеарно-вискоеластичног материјала чије механичке особине изразито зависе од температуре и брзине деформације. Разматран је поступак припреме података у облику који је потребан за структурну анализу вискоеластичног тела и процену степена сигурности и поузданости. Епрувете горива су испитиване истезањем константним брзинама клема кидалице, на 96 различитих режима који су обухватили по 12 различитих температура и брзина клема. Приказан је поступак одређивања фактора температурско-временске корекције. Показан је и начин израде јединствених дијаграма зависности механичких особина горива од редукованог времена као величине која обухвата истовремени утицај температуре и брзине деформације. Израђене су тзв. „мастер криве“ затезне чврстоће, дозвољене деформације, иницијалног модула и модула релаксације горива које важе у свим условима оптерећења. Функционалне зависности ових величина представљају улазне податке за структурну анализу и представљене су у математичком облику, погодном за даљу анализу. Овај начин обраде података може да се примени на било које тело од вискоеластичног материјала. Разматране су неке разлике у приступу структурној анализи вискоеластичног и еластичног тела. На једном примеру је показана потреба израде података у облику „мастер кривих“, које показују зависност механичких особина у широком спектру услова оптерећења. Особине ракетног горива могу да послуже као узорак при разматрању неког другог вискоеластичног материјала. У раду су разматране механичке карактеристике горива које одговарају почетном периоду употребе, одмах након израде, када нема утицаја старења или акумулације оштећења услед дејства спољних оптерећења. Ове почетне величине су углавном довољне за процену основне (почетне) поузданости вискоеластичног тела, која се касније мења током времена. Приказан је и поступак праћења утицаја природног старења и извршена експериментална анализа исправности овог поступка. За комплетну структурну анализу и процену века трајања потребне су и вредности фактора акумулације оштећења, које овде нису разматране, јер зависе од реалних услова оптерећења.

Кључне речи: Гориво композитно • Вискоеластичност • Механичка карактеризација • Затезна чврстоћа • Дозвољена деформација • Температурско–временска корелација • Модул релаксације • Степен сигурности • Редуковано време

The influence of thermal treatment on properties of kaolin

Elizabeth Erasmus

Department of Chemistry, University of the Free State, Bloemfontein, Republic of South Africa

Abstract

The kinetics of dehydroxylation of South African kaolin revealed that both the inner and the surface hydroxyl groups disappear according to first order kinetics, however, the surface group disappeared faster than the inner groups, showing that diffusion control kinetics is also important. The temperature dependent transformations of the kaolin was measured by means of fractional conversion of the ratios between $\text{AlO}_6:\text{AlO}_4$ and $\text{Si-O-Al}:\text{Si-O-Si}$, which showed k_{obs} values 0.0168 s^{-1} and 0.0089 s^{-1} for the transformation to the spinel phase and values of 0.0165 s^{-1} and 0.0156 s^{-1} for the transformation to mullite respectively. The pozzolanic activities of the kaolin calcined at different temperatures showed a maximum pozzolanic activity when the kaolin is calcined at 650°C and the pozzolanic activity for mullite is even less than for the uncalcined kaolin. XPS revealed that the atomic ratio between Si and Al did not change from kaolin to metakaolin ($\text{Si}:\text{Al} = \text{ca. } 1.2$) however the mullite showed a atomic ratio of $\text{Si}:\text{Al} = 1.52$, implying that some dealumination occurred during calcination at high temperatures.

Keywords: dehydroxylation, kaolin, metakaolin, infra-red, pozzolanic activity, mullite.

Available online at the Journal website: <http://www.ache.org.rs/HI/>

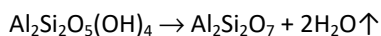
SCIENTIFIC PAPER

UDC 66.094.32.091.8:553.612(6)

Hem. Ind. 70 (5) 595–601 (2016)

doi: 10.2298/HEMIND150720066E

Kaolin is a naturally occurring clay mineral with kaolinite being the main component having a chemical composition of $\text{Al}_2\text{Si}_2\text{O}_5(\text{OH})_4$. It has a layered silicate structure, where oxygen atoms link an octahedral sheet of alumina with a tetrahedral sheet of silica.[1] When kaolinite is calcined at elevated temperatures, dehydroxylation occurs which collapses the crystal structure to produce amorphous metakaolinite ($\text{Al}_2\text{Si}_2\text{O}_7$) [2], according the following proposed reaction scheme:[3]



The thermal transformation of metakaolinite above 1000°C first produces either a Al–Si spinel phase or a aluminasilicate phase [2] which transforms into mullite [4] and above 1150°C cristobalite ($c\text{-SiO}_2$) is formed.

The thermal transformation of kaolin has been the subject of numerous studies, which reported on how the different heating conditions influence the dehydroxylation process.[4–8].

At temperature below 400°C , a reversible dehydroxylation process takes place, upon cooling the hydroxyl peaks reappear in the infrared spectra [9]. Above temperatures of 400°C irreversible loss of hydroxyl groups occur. The temperature at which the highest rate of dehydroxylation occurs is dependent on the original structural state of the kaolin, the particle size, the density of packing, the pressure of water and a few other experimental conditions [10–13].

Metakaolin is used as supplement in cementitious material [14] and the calcination conditions is one of the most important factors influencing the pozzolanic property (which is indicative of the lime-pozzolana reaction or how good and effective the pozzolan is) of the cementitious material produced [4, 15]. A pozzolan is defined as “a siliceous and aluminous material which, in itself, possesses little or no cementitious value but which will, in finely divided form in the presence of moisture, react chemically with calcium hydroxide at ordinary temperature to form compounds possessing cementitious properties” by the American Society for Testing and Materials (ASTM) [16].

The present paper aims to investigate the kinetics dehydroxylation of South African kaolin to metakaolin at temperature between 450 and 650°C . Also Fourier Transformed infra-red spectroscopy was used to study the structural changes of metakaolin heated to different temperatures up to 950°C within metakaolin state as well as the transformation to the spinel transition ($950\text{--}1150^\circ\text{C}$) and eventually the formation of mullite cristobalite (1200°C). The changes in the spectra were studied as the function of fractional conversion of the ratios between $\text{AlO}_6:\text{AlO}_4$ and $\text{Si-O-Al}:\text{Si-O-Si}$. Also to measure the pozzolanic activity of the products that formed at the different thermal treatments, which will be used to determine the optimal calcination temperature for South African kaolin to be used as supplementary cementitious material.

Correspondence: Department of Chemistry, University of the Free State, Bloemfontein, 9300, Republic of South Africa.

E-mail: erasmuse@ufs.ac.za

Paper received: 20 July, 2015

Paper accepted: 10 November, 2015

EXPERIMENTAL

Chemicals and instruments

Kaolin (ALUSIL) was purchased from Serina Trading in South Africa. The chemical analysis as provided by the supplier is tabulated in Table 1. The kaolin used was in powder form and it has 72% minimum particles size less than 2 μm and maximum of 1% moisture content. All solid reagents (Merck, Sigma–Aldrich) were used without further purification and water was double distilled. Attenuated total reflectance Fourier Transformed infra-red (ATR FTIR) spectra were recorded on a Nicolet IS 50 infra-red spectrophotometer equipped with a diamond ATR. The TGA experiment was performed on a TGA/SDTA851^e coupled to a ThermoStarTM Pfeifer vacuum mass spectrometer, at a heating rate of 10 $^{\circ}\text{C}\cdot\text{min}^{-1}$ in air with the final temperature of 750 $^{\circ}\text{C}$. X-ray photoelectron spectroscopy (XPS) data was recorded on a PHI 5000 Versaprobe system, with monochromatic $\text{AlK}\alpha$ X-ray source. Spectra were obtained using the aluminium anode ($\text{AlK}\alpha = 1486.6 \text{ eV}$), operating at 50 μm , 12.5 W and 15 kV energy. The survey scans were recorded at constant pass energy of 187.85 eV, and the detailed region scans at constant pass energy of 29.35 eV, with the analyzer resolution being $\leq 0.5 \text{ eV}$. The background pressure was $2 \times 10^{-6} \text{ Pa}$. The XPS data was analysed, utilizing Multipak version 8.2c computer software [17] applying Gaussian–Lorentz fits (the Gaussian/Lorentz ratios were always $> 95\%$).

Kinetic measurements of kaolin calcination/dehydroxylation

Kaolin was heated in a laboratory furnace at different temperatures (450, 475, 500, 550, 600 and 650 $^{\circ}\text{C}$). Samples were taken at regular time intervals for ATR FTIR measurements. The kinetic rate constants under first order conditions were determined by monitoring formation and disappearance of the selected peaks.

Calculations. Pseudo first-order rate constants, k_{obs} , were calculated by fitting kinetic data to the first-order equation [18] $[A]_t = [A]_0 e^{-k_{\text{obs}}t}$ with $[A]_t$ and $[A]_0$ the absorbance of the indicated species at time t and at $t = 0$ [19].

Calcination/dehydroxylation of kaolin

Kaolin was heated in the laboratory furnace at different temperatures with 50 $^{\circ}\text{C}$ intervals (475, 500, 550, 600, 650, 750, 850, 950, 1050, 1150 and 1200 $^{\circ}\text{C}$) till dehydroxylation was completed. After which ATR FTIR measurements were recorded for structure analysis.

Pozzolanic activity

The pozzolanic activity of the kaolin and metakaolin (kaolin calcined at various temperatures) were evaluated according to the Chapelle test [19]. A sample of either the kaolin or metakaolin (1 g) was mixed with 2 g $\text{Ca}(\text{OH})_2$ in 250 cm^3 water. The suspension was subsequently boiled for 16 h. After which the suspension was cooled, a 250 cm^3 sucrose solution (60 g sugar in 250 cm^3 water) was added to the kaolin suspension and stirred for 15 min. The suspension was filtered and titrated with 0.1 M HCl, using phenolphthalein as indicator.

RESULTS AND DISCUSSION

ATR Fourier Transformed infra-red spectroscopy

The ATR FTIR of the South African kaolin studied is presented in Figure 1, the peak frequencies was allocated in accordance with previously published peak frequency assignments.[20,21] The four peaks observed between 3550 and 3750 cm^{-1} , which are characteristic of kaolinite, correspond to the hydroxyl stretching frequencies. The peak observed at 3620 cm^{-1} is assigned to the inner O–H stretching frequency (Figure 1) which is bound to the octahedral Al. The other three peaks at 3686, 3669 and 3651 cm^{-1} is allocated to the stretching frequency of the surface O–H groups.

The main silica peaks are observed at 1002, 795 and 645 cm^{-1} which are the Si–O stretching, Si–O–Si stretching and bending frequencies respectively. Bands belonging to the alumina are found at 939 and 912 cm^{-1} representing respectively the Al–OH bending vibration and the –OH deformation linked to the 2Al^{3+} .

Since there are no peaks observed between 1620–1642 cm^{-1} , which is the H–O–H bending of water, it can be assumed that there are very little to no free water within the sample. Bands observed at 1125, 1116, 752 and 685 cm^{-1} are attributed to the interference of clay minerals like quartz and muscovite.

The TGA plot of the thermal decomposition of the studied kaolin is shown in Figure 2. The percentage mass loss of the sample of kaolin by thermal dehydroxylation is 12.89%, with the onset and endset temperature being 443.12 and 534.04 $^{\circ}\text{C}$, respectively.

Figure 3 shows the ATR FTIR of the thermal dehydroxylation and further transformation (structural changes) of kaolin at different temperatures. After calcination for prolonged periods of time at the desired temperature, it can clearly be seen that the hydroxyl peaks in the region 3550–3750 cm^{-1} disappeared, indi-

Table 1. The chemical analysis of the kaolin (ALUSIL)

Raw-oxide	SiO_2	Al_2O_3	Fe_2O_3	TiO_2	CaO	MgO	K_2O	N_2O	L.O.I.
Raw-content, mass%	45.20	37.20	0.35	0.90	0.016	0.08	0.20	0.13	13.50

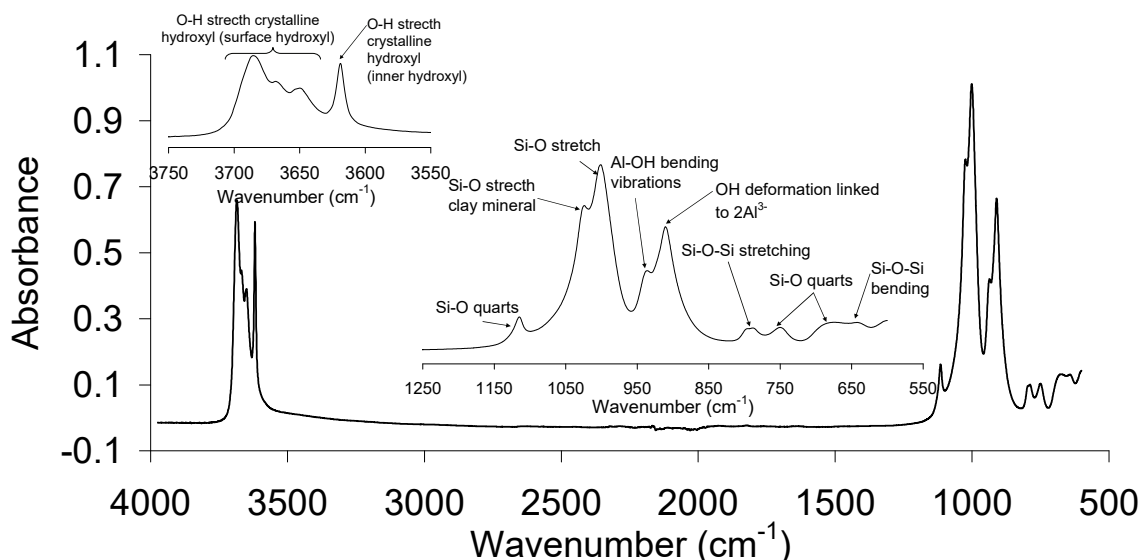


Figure 1. The infra-red spectra of the studied kaolin (Alusil), the insets show the peaks in more detail with their assignments.

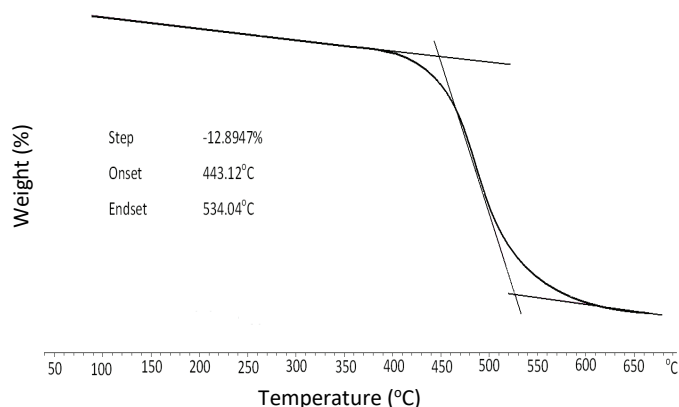


Figure 2. TGA plot of the thermal decomposition of kaolin (Alusil) heated at 10 °C/min.

cating the dehydroxylation of kaolin occurred. Below 450 °C, very little transformation of the silica and alumina occurred, and no dehydroxylation was observed. This result is further confirmed by the TGA data in Figure 2, which shows that below 450 °C very little to no dehydroxylation took place.

The spectra of the thermally treated kaolin shows very broad bands in the region of 600–1300 cm^{-1} with very little fine structure, there is an intense broad band at *ca.* 1100 cm^{-1} ($\nu_{\text{Si-O-Al}}$) with a shoulder at 1200 cm^{-1} ($\nu_{\text{Si-O-Si}}$) and smaller bands at 800 ($\nu_{\text{Al-O}}$) and 667 cm^{-1} ($\nu_{\text{Al-O}}$). Further thermal treatment to produce mullite causes the peak at 1200 cm^{-1} ($\nu_{\text{Si-O-Si}}$) to increase in intensity as well as the appearance of two new bands at 890 ($\nu_{\text{Al-O}}$) and 740 cm^{-1} ($\nu_{\text{Al-O}}$).

The peaks focussed on in this study are listed in Table 2. The formation of the spinel phase and the formation of the mullite are connected to the appearance and disappearance of specific bands within the spectra.

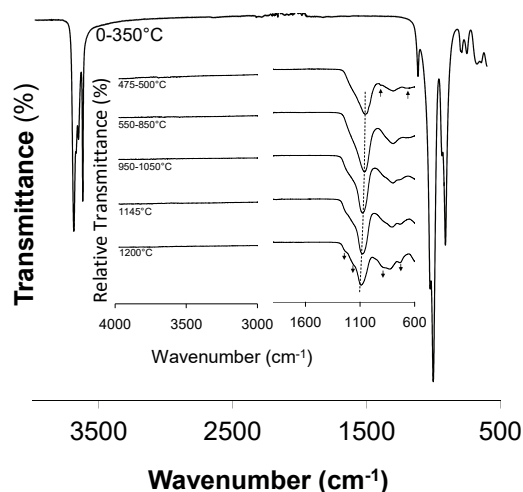


Figure 3. The FTIR ATR of the thermal dehydroxylation and further transformation of kaolin at different temperatures.

The disappearance of the =Al-O- stretching frequency of the octahedral AlO_6 and the antisymmetric stretching frequency of Si-O-Al= at 667 and 1100 cm^{-1}

respectively as well as the appearance of the =Al–O– stretching frequency of the tetrahedral AlO_4 and the antisymmetric stretching frequency of $\equiv\text{Si–O–Si}\equiv$ at 800 and 1200 cm^{-1} respectively were investigated.

Table 2. Fractional conversion of the ratio between AlO_6 (at 667 cm^{-1}) and AlO_4 (at 800 cm^{-1}) and the fractional conversion of the ratio between $\equiv\text{Si–O–Al=}$ (at 1100 cm^{-1}) and $\equiv\text{Si–O–Si}\equiv$ (at 1200 cm^{-1}) at different temperatures during the thermal transformation of metakaolin to the spinel phase, as well as the fractional conversion of the ratio between AlO_6 and AlO_4 at different temperatures during the thermal transformation of the spinel phase to mullite

Temperature, °C	α of $\text{AlO}_6:\text{AlO}_4$	α of $\equiv\text{Si–O–Al=}:\equiv\text{Si–O–Si}\equiv$
475	4.96	3.69
500	4.50	3.26
550	2.19	2.13
600	1.82	1.71
650	1.81	1.45
750	1.58	1.00
850	1.62	0.80
950	1.13	0.56
1050	1.08	0.55
1145	0.96	0.47
1200	0.03	0.01

The changes in the spectra were studied as the function of fractional conversion of the ratios between the AlO_6 and AlO_4 as well as $\equiv\text{Si–O–Al=}$ and $\equiv\text{Si–O–Si}\equiv$, which is shown Figure 4 and defined by the equation below:

$$\alpha = \frac{i_0 - i_t}{i_0 - i_f}$$

where α is the fractional conversion, i_0 is the intensity of the band at time 0, i_t is the intensity of the band at time t and i_f is the intensity of the band at time final.

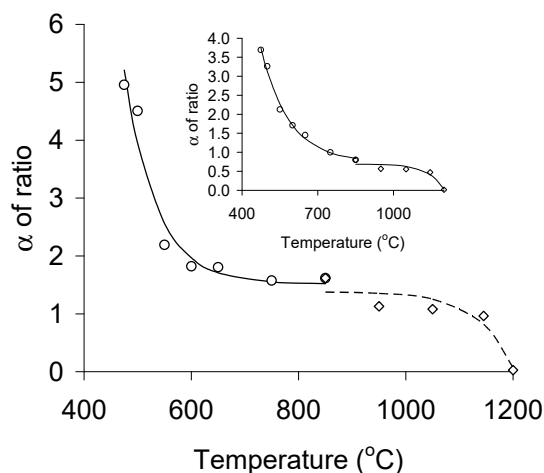


Figure 4. The fractional conversion of the ratio between AlO_6 and AlO_4 . Inset: the fractional conversion of the ratio between $\equiv\text{Si–O–Al=}$ and $\equiv\text{Si–O–Si}\equiv$ (1100 and 1200 cm^{-1} , respectively).

The fractional conversion of the ratio between $\equiv\text{Si–O–Al=}$ and $\equiv\text{Si–O–Si}\equiv$ (1100 and 1200 cm^{-1} respectively) shows a sharp decrease between 475 and 850 °C , it then slightly flattens before going down even further when mullite is formed at 1200 °C . This indicates an increase in the formation of amorphous silica during the transformation to the spinel phase and eventually mullite formation. The fractional conversion decreases for the spinel formation and shows a k_{obs} value (observed rate constant) of 0.0089 s^{-1} for the fractional conversion of the ratio between $\equiv\text{Si–O–Al=}$ and $\equiv\text{Si–O–Si}\equiv$ and a k_{obs} of 0.0168 s^{-1} for the fractional conversion of the ratio between AlO_6 and AlO_4 . The influence on the rate of fractional conversion of the ratio between AlO_6 and AlO_4 is doubled that for the fractional conversion of the ratio between $\equiv\text{Si–O–Al=}$ and $\equiv\text{Si–O–Si}\equiv$, showing that during the formation of the spinel phase the transformation of the Al is more pronounced than that for Si.

Further thermal treatment to produce mullite causes the peak at 1200 cm^{-1} to increase in intensity as well as the appearance of two new bands at 890 and 740 cm^{-1} , which is assigned to the symmetric stretching frequency of $\equiv\text{Si–O–Al=}$ and of $\equiv\text{Si–O–Si}\equiv$ and the the =Al–O– stretching frequency of the tetrahedral AlO_4 in the mullite, as per reported values [22]. The mullite formation showed a k_{obs} value (observed rate constant) of 0.0165 s^{-1} for the fractional conversion of the ratio between $\equiv\text{Si–O–Al=}$ and $\equiv\text{Si–O–Si}\equiv$ and a k_{obs} of 0.0156 s^{-1} for the fractional conversion of the ratio between AlO_6 and AlO_4 . These two k_{obs} values are within experimental error the same and showed that during mullite formation, the transformation of the Al and Si were the same.

A kinetic study of the thermal dehydroxylation of kaolin to metakaolin was studied using ATR FTIR. The disappearance of the surface hydroxyl peaks at 3689 cm^{-1} and the inner hydroxyl peaks at 3620 cm^{-1} were followed (see Figure 5). Table 3 summarises the kinetic data, k_{obs} obtained at the different temperatures.

Numerous reports are available on the kinetics of dehydroxylation of kaolin, there is a debate between first order kinetics and diffusion controlled kinetics. Here we show that the hydroxyl groups on the surface of the kaolin are removed faster than the inner hydroxyls, at a temperature of 773 K , the k_{obs} value obtained for the disappearance of the surface hydroxyl peaks at 3689 cm^{-1} is 0.00128 s^{-1} as compared to the inner hydroxyl peaks at 3620 cm^{-1} is 0.00077 s^{-1} . This shows that even though both disappear with first order kinetics, the inner hydroxyl groups are dependent on diffusion control.

The pozzolanic activity of the thermally treated products (kaolin, metakaolin, spinel and mullite) that formed at the different thermal treatment of the kaolin

was measured using the Chapelle test, which measures amount of lime that can be bound by the metakaolin. It is measured in $\text{Ca(OH)}_2/\text{g}$ and the higher the value the better the pozzolanic activity.

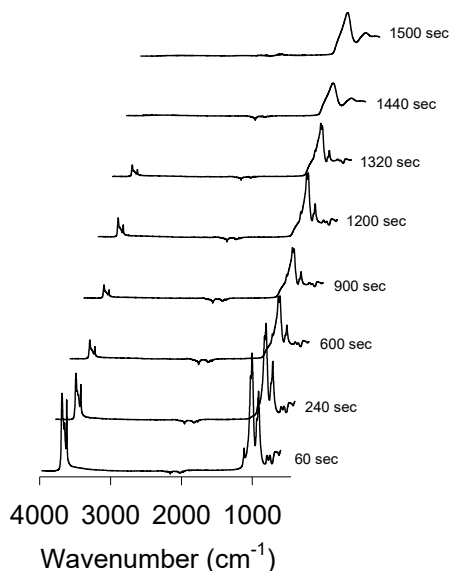


Figure 5. Stacked time scan of the calcination (dehydroxylation) of kaolin to metakaolin at 600°C.

Table 3. Data obtained for the calcination (dehydroxylation) of kaolin to metakaolin

Groups	Wavenumber, nm	T / K	$k_{\text{obs}} / \text{s}^{-1}$
Surface hydroxyls	3689	773	0.00128
		823	0.00159
		873	0.00263
		923	0.00364
Inner hydroxyls	3620	773	0.00077
		823	0.00106
		873	0.00220
		923	0.00291

The comparison of the consumed lime between the products formed at different thermal treatment temperatures are shown in Figure 6. A Bell type curve was formed, with the highest pozzolanic activity found at 650°C calcination temperature. The slope of the curve to the left (lower calcination temperatures) flattens to ca. 0.8 $\text{Ca(OH)}_2/\text{g}$ at 0 °C. The slope of the curve to right (the higher calcination temperatures) slopes down to

zero and eventually flattens to 0.073 $\text{Ca(OH)}_2/\text{g}$ at 1200 °C (where mullite formed).

It was expected that kaolin heated below 400 °C would show the same low pozzolanic activity (0.8 $\text{Ca(OH)}_2/\text{g}$) as the kaolin that has not been subjected to thermal treatment. However, it has been reported that even though no major structural changes occur, there is a slight deformation in the octahedral sheets[23], which could possibly explain the pozzolanic values above 0.8 $\text{Ca(OH)}_2/\text{g}$.

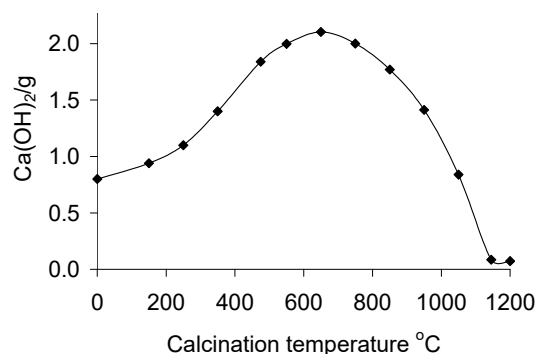


Figure 6. Pozzolanic activity of the calcined kaolin (measured in $\text{Ca(OH)}_2/\text{g}$) vs. calcination temperature.

Only the metakaolin formed at temperature between 350–950 °C had a pozzolanic activity above 1.3 $\text{Ca(OH)}_2/\text{g}$ and only these 7 samples were considered to be pozzolanic. While the products formed at calcination temperature above 1050 °C has an even lower pozzolanic activity than the kaolin itself.

The temperature of the metakaolin prepared by calcination at 650 °C which has the highest pozzolanic activity (2.10 $\text{Ca(OH)}_2/\text{g}$), is slightly higher than other published data that also used this temperature. When metakaolin is used in the formation of geopolymers, the optimum calcination temperature is also reported to be between 500–700 °C [24] while a sharp decrease in strength of the geopolymer is reported above 1000 °C [25], all this corresponds to the pozzolanic activity reported in this publication in Figure 6. These results show that even when kaolin from different sources (different countries) are used, calcination at 650 °C results in the metakaolin with the best pozzolanic activity.

The results of the XPS studies of the kaolin, metakaolin (calined at 650 °C) and mullite (calcined at 1200 °C) are tabulated in Table 4.

Table 4. Results of the XPS studies of the kaolin (not calcined, as recieved), metakaolin (calined at 650 °C) and mullite (calcined at 1200 °C), showing the atomic % of Al, Si, C and O as well as the binding energies (eV) of the Al 2p and Si 2p peaks

Name : temperature of calcination, °C	at.% of Al	at.% of Si	Si:Al ratio	Binding energy, eV	
				Al 2p _{3/2}	Si 2p _{3/2}
Kaolin : 0	10.3	12.5	1.21	75.5	103.1
Metakaolin : 650	9.9	12.5	1.26	75.7	103.3
Mullite : 1200	7.7	11.7	1.52	74.0	102.5

All three of the samples (kaolin, metakaolin and mullite) showed that significant amounts of carbon were adsorbed their surface due to exposure to the atmosphere and this carbon's binding energy was set at 284.8 eV and was used for charge correction.

Firstly, it is important to note that Si:Al ratio obtained from the XPS data in the kaolin (not calcined sample) is 1.21, which is the same as the Si:Al ratio provided by the supplier information in Table 1, $\text{SiO}_2:\text{Al}_2\text{O}_3 = 45.20\%:37.20\% = 1.22$. After calcination at 650 °C the Si:Al ratio slightly increase to 1.26, but could be considered the same within experimental error. However, the sample calcined at 1200 °C (mullite) showed that the Si:Al ratio increase significantly to 1.52.

The binding energies for the Al 2p and Si 2p peaks were found to be at ca. 75.6 and 103.2 eV respectively for kaolin (not calcined sample) and metakaolin (calcined at 650 °C). These results are within experimental error the same, showing that electronic and chemical environment of the Al and Si did not change significantly after being calcined at 650 °C. However, calcination of kaolin at 1200 °C to produce mullite, caused the binding energy of both the Al 2p and Si 2p peaks to decrease by ca. 1.5 and 0.6 eV respectively (see Figure 7). The decrease in binding energy for the Al 2p peak is about three times more than that of the Si 2p peak, which is also accompanied by the decrease in Al content. It is well known that an increase in the Si:Al ratio is accompanied by a decrease in binding energies of both Si and Al.[26,27] This shows that there is a unique structural dissimilarity between the mullite and the metakaolin as well as the kaolin, caused by either a change in the electronic and/or the chemical environment.

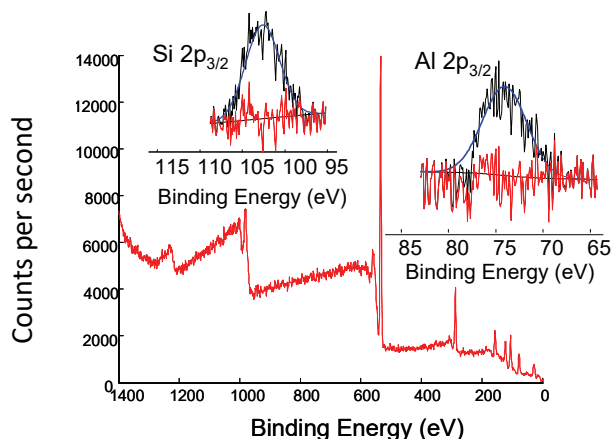


Figure 7. XPS spectra of the mullite, showing the detailed scans of the Si and Al regions.

CONCLUSION

The kinetics of dehydroxylation of South African kaolin at different temperatures (500–650 °C) was fol-

lowed on FTIR ATR monitoring the disappearance of the four hydroxyl peaks between 3550 and 3750 cm^{-1} . The disappearance of the surface hydroxyl groups occurred at an observed rate constant of 0.00128 s^{-1} (at 500 °C) whereas the inner hydroxyl groups disappeared at an observed rate constant of 0.00077 s^{-1} (at 500 °C), which is one order of magnitude lower. This shows that even though both disappear with first order kinetics, it shows that the inner hydroxyl groups are dependent on diffusion control. The transformation of the kaolin to metakaolin, the spinel phase and mullite was investigated by means of FTIR ATR. The fractional conversion of the ratios between $\text{AlO}_6:\text{AlO}_4$ and Si-O-Al:Si-O-Si were calculated to be 0.0168 and 0.0089 s^{-1} , respectively, for the transformation to the spinel phase. The fractional conversion of the ratios between $\text{AlO}_6:\text{AlO}_4$ and Si-O-Al:Si-O-Si for the transformation to mullite were calculated to be 0.0165 and 0.0156 s^{-1} , respectively. The pozzolanic activities of the kaolin calcined at different temperature were tested using the Chappell test, showed that maximum pozzolanic activity is obtained when the kaolin is calcined at 650 °C. When the calcination temperature is above 1050 °C, the pozzolanic activity is even less than for uncalcined kaolin. The XPS of uncalcined kaolin, metakaolin (calcined at 650 °C) and mullite (calcined at 1200 °C) showed that the atomic ratio between Si and Al did not change from kaolin to metakaolin ($\text{Si:Al} \approx 1.2$), but the mullite showed an atomic ratio of $\text{Si:Al} = 1.52$, implying that some deallumination occurred during calcination at high temperatures.

Acknowledgements

The authors acknowledge financial support from University of the Free State during the course of this study.

REFERENCES

- [1] J. Konta, Clay and man: clay raw materials in the service of man, *Appl Clay Sci.* **10** (1995) 275–335.
- [2] P. Ptacek, F. Soukal, T. Opravil, M. Noskova, J. Havlica, J. Brandstetr, Mid-infrared spectroscopic study of crystallization of cubic spinel phase from metakaolin, *J. Sol. State Chem.* **184** (2011) 2661–2667.
- [3] M. Murat, M. Driouche, Chemical reactivity of thermally activated clay minerals estimation by dissolution in hydrofluoric acid, *Cem. Concr. Res.* **18** (1988) 221–228.
- [4] B.R. Ilic, A.A. Mitrovic, L.R. Milicic, Thermal treatment of kaolin clay to obtain metakaolin, *Hem. Ind.* **64** (2010) 351–356.
- [5] G. Kakali, T. Perraki, S. Tsivilis, E. Badogiannis, Thermal treatment of kaolin: the effect of mineralogy on the pozzolanic activity, *Appl. Clay Sci.* **20** (2001) 73–80.
- [6] A. Shvarzman, K. Kovler, G.S. Grader, G.E. Shter, The effect of dehydroxylation/amorphization degree on poz-

- zolan activity of kaolinite, *Cem. Concr. Res.* **33** (2003) 405–416.
- [7] J.A. Kostuch, G.V. Walters, T.R. Jones, High performance concrete incorporating metakaolin – a review, *Concrete*, **2** (1993) 1799–811.
- [8] M. Arikan, K. Sobolev, T. Ertun, A. Yeginobali, P. Turker, Properties of blended cements with thermally activated kaolin, *Constr. Build. Mater.* **23** (2009) 62–70.
- [9] J.J. Fripiat, F. Toussaint, Predehydroxylation State of Kaolinite, *Nature* **186** (1960) 627–628.
- [10] L. Stoch, I. Waclawska, The kinetics of dehydroxylation of kaolinite, *Polska Acad. Nauk. Prace Min.* **1979** (1979) 59–79.
- [11] M. Harman, I. Horvath, Relations between the morphology of particles in structurally and the kinetics of their dehydroxylation, *Geol. Zbor. Geol. Carpath.* **31** (1980) 115–124.
- [12] F. Toussaint, J.J. Fripiat, M.C. Gastuche, Dehydroxylation of kaolinite, *J. Phys. Chem.* **67** (1963) 26–30.
- [13] D. Yeskis, A.F. Koster van Groos, S. Guggenheim, The dehydroxylation of kaolinite, *Amer. Miner.* **70** (1985) 159–164.
- [14] R. Talero, Comparative XRD analysis ettringite originating from pozzolan and from portland cement, *Cem. Concr. Res.* **35** (2005) 1269–1284.
- [15] S. Chandrasekhar, Influence of metakaolinization temperature on the formation of zeolite 4a from kaolin, *Clay Min.* **31** (1996) 253–261.
- [16] American Society for Testing and Materials (ASTM) C-125, Standard terminology relating to concrete and concrete aggregates; 2007.
- [17] F. Moulder, W.F. Stickle, P.E. Sobol, K.D. Bomben, *Handbook of X-ray Photo- 367 electron Spectroscopy*, ULVAC–PHI, Inc., 370 Enzo, Chigasaki 253–8522, Japan, 368 1995, pp. 45, 57, 143.
- [18] J.H. Espenson, *Chemical Kinetics and Reaction Mechanisms*, 2nd ed., McGraw–Hill, New York, 1995, pp. 15, 49, 70–75, 156.
- [19] R. Largent, Estimation de l'activite pouzzolanique, *Bull. Liaison Lab. Pont Chausees* **93** (1978) 61–65.
- [20] J.A. Gadsen, *Infrared Spectra of Minerals and Related Inorganic compounds*, Butterworths, London, 1975.
- [21] B.J. Saikia, G. Parthasarathy, Fourier Transform Infrared Spectroscopic Characterization of Kaolinite from Assam and Meghalaya, *J. Mod. Phys.* **1** (2010) 206–210.
- [22] P. Padmaja, G.M. Anilkumar, P. Mukundan, G. Aruldhas, K.G.K. Warriar, Characterisation of stoichiometric sol–gel mullite by fourier transform infrared spectroscopy, *Int. J. Inorg. Mater.* **3** (2003) 693–698.
- [23] J. Komusinski, L. Stock, Dehydroxylation of kaolinite–group minerals: an ESR study, *J. Thermal Anal.* **29** (1984) 1033–1040.
- [24] A. Elimbi, K.H. Tchakoute, D. Njopwouo, Effects of calcination temperature of kaolinite clays on the properties of geopolymer cements, *Constr. Build. Mater.* **25** (2011) 2805–2812.
- [25] Z. Zhang, X. Yao, H. Zhu, Y. Chen, Role of water in the synthesis of calcined kaolin–based geopolymer, *Appl. Clay Sci.* **43** (2009) 218–223.
- [26] S.L. Yong, D. Feng, G.C. Lukey, J.S.J van Deventer, *Geopolymers: green chemistry and sustainable development solutions*, Geopolymer Institut, Saint-Quintin, 2005, pp. 75–78.
- [27] H. He, T.L. Barr, J. Klinowski, ESCA studies of framework silicates with the sodalite structure: (2) Ultramarine, *J. Phys. Chem.* **98** (1994) 8124–8127.

IZVOD

UTICAJ TOPLOTNE OBRADNE NA SVOJSTVA KAOLINA

Elizabeth Erasmus

Department of Chemistry, University of the Free State, Bloemfontein, Republic of South Africa

(Naučni rad)

Kinetika dehidroksilacije kaolina iz Južne Afrike je pokazala da izdvajanje hidrosilnih grupa iz unutrašnjosti i sa površine, sledi kinetiku reakcije prvog reda, međutim brži nestanak hidrosilnih grupa sa površine u odnosu na nestanak iz unutrašnjosti ukazuje na značaj difuzione kontrole reakcije. Temperaturno zavisna transformacija kaolina, praćenjem odnosa $AlO_6:AlO_4$ i $Si-O-Al:Si-O-Si$, je pokazala da su k_{obs} vrednosti 0,0168 i 0,0089 s^{-1} , za transformaciju u spinel fazu, odnosno da su k_{obs} 0,0165 i 0,0156 s^{-1} za transformaciju u mulit fazu, redom. Kaolin kalcinisan na 650 °C pokazuje maksimalnu pucolansku aktivnost, a pucolanska aktivnost mulita je manja od aktivnosti nekalcinisanog kaolina. XPS ukazuje na to da se atomski odnos Si i Al ne menja pri prelasku kaolina u metakaolin ($Si:Al \approx 1,2$), međutim kod mulita je utvrđen odnos $Si:Al = 1,52$.

Ključne reči: Dehidroksilacija • Kaolin • Metakaolin • Infracrveno • Pucolanska aktivnost • Muilt